Chair of Reservoir Engineering

Master Thesis

Fall-off Test Pressure Derivatives to Weight Geological Model Centroids for Simulation of Polymer Injection

Montanuniversität Leoben

Department of Petroleum Engineering

Written by:
Markus Hofmeister, BSc

University Advisor:
Univ.-Prof. Dipl.-Phys. Dr.rer.nat. Holger Ott
Industrial Advisors:
Dr. Torsten Clemens
Dr. Dominik Steineder

Leoben, September 2017

EIDESSTATTLICHE ERKLÄRUNG

Ich erkläre an Eides statt, dass ich die vorliegende Diplomarbeit selbständig und ohne fremde Hilfe verfasst, andere als die angegebenen Quellen und Hilfsmittel nicht benutzt und die den benutzten Quellen wörtlich und inhaltlich entnommenen Stellen als solche erkenntlich gemacht habe.

AFFIDAVIT

I hereby declare that the content of this work is my own composition and has not been submitted previously for any higher degree. All extracts have been distinguished using quoted references and all information sources have been acknowledged.

Acknowledgement

I would like to take this opportunity to express my deepest and sincere gratitude to my project supervisors Dr. Torsten Clemens and Dr. Dominik Steineder for their continuous guidance and constructive criticism. I am especially grateful to Dominik Steineder for particularly stimulating discussions and sharing his time and insights with me, without which this thesis would not be what it is. It has been a great pleasure working with the Enhanced Recovery Methods team at OMV Exploration & Production GmbH. Furthermore, I am very thankful to Prof. Holger Ott for supporting this external research and his credit of trust throughout this study.

Kurzfassung

Nachdem ein Polymer-Pilot im 8 TH Reservoir des Matzen Feldes eine vielversprechende inkrementelle Ölproduktion aufgezeigt hat, werden gewonnene Erkenntnisse auf eine erste feldweite Implementierung angewandt. Zur Vorausberechnung der inkrementellen Ölproduktion wurde eine probabilistische Methode bestehend aus einer geologischen Sensitivitätsanalyse gefolgt von der Auswahl einer repräsentativen Teilmenge an Modellen (Modell-Zentroide) für vollphysikalische dynamische Simulationen entwickelt. Während die Gruppierung derzeit auf Grundlage virtueller Tracersignale mittels Streamline-Simulationen erfolgt, um eine maximale geologische Vielfalt in der Teilmenge der ausgewählten Modelle zu bewahren, dienen dynamische Parameter bisher als Kalibrierungsgrößen. Ein mangelndes detailliertes Verständnis der in-situ Polymereigenschaften wird derzeit durch breite Verteilungen der relevanten Parameter berücksichtigt.

Die vorliegende Arbeit untersucht die Eignung der Integration von Fall-Off Testdaten zur Gewichtung der Modell-Zentroide während der Gruppierung, um Unsicherheiten in geologischen sowie dynamischen Parametern weiter zu verringern. Der primäre Fokus liegt dabei auf der Untersuchung der in-situ Viskosität der Polymerlösung in Horizontalbohrungen. In-situ Polymereigenschaften stellen einen der größten Unsicherheitsfaktoren in der aktuellen Methodik dar und bilden gleichzeitig einen der wichtigsten Designparameter zur Optimierung der Displacement Efficiency und damit der Gesamtwirtschaftlichkeit eines Polymer-Injektionsprojektes.

Fall-Off Tests wurden für eine Bandbreite generischer Reservoirmodelle simuliert und anschließend mittels Pressure Transient Analysis (PTA) analysiert, wobei der logarithmischen Ableitung des Drucks besondere Aufmerksamkeit zukam. Für Einphasen-Wassermodelle bietet PTA ein zuverlässiges Werkzeug, um sowohl geologische Merkmale als auch wesentliche Polymereigenschaften zu charakterisieren. Es wurde ein Ansatz entwickelt, um die in-situ Polymerviskosität aus der charakteristischen Kurvenform der Pressure Derivative abzuleiten. Das Maß der Heterogenität eines Reservoirs hat einen entscheidenden Einfluss auf die Zuverlässigkeit der Interpretation. Reservoir Quality Index (RQI) abhängiges Adsorptions- und Viskositätsverhalten wurde implementiert, um den Einfluss verschiedener Gesteinsarten zu untersuchen und das strukturviskose Verhalten der Polymerlösung zu approximieren.

Für Mehrphasen-Modelle hat die Analyse von simulierten Fall-Off Tests keine konsistente Reservoirbeschreibung ergeben. Die in-situ Polymerviskosität kann dennoch mit dem vorgeschlagenen Ansatz ermittelt werden, insofern die Druckkurve eines reinen Wassertests als Vergleichsbasis vorliegt. Diese Erkenntnis ist für die operative Planung zukünftiger Fall-Off Tests in Polymer-Injektionsbohrungen von großer Bedeutung. Obwohl die Anwendbarkeit von PTA zur Gewichtung tatsächlicher geologische Modelle in diesem Stadium nicht bestätigt werden konnte, helfen die Ergebnisse dieser Arbeit, die Interpretation geplanter Fall-Off Tests in kürzlich komplettierten Horizontalbohrungen einzugrenzen.

Abstract

After a polymer pilot indicated encouraging incremental oil production in the 8 TH reservoir of the Matzen field, gained insights are deployed for a first field-rollout. A probabilistic workflow was developed to forecast incremental oil production, which comprises a geological sensitivity study followed by the extraction of a representative subset of models (model centroids) for full-physics dynamic simulations. While clustering is currently performed based on virtual tracer responses obtained using streamline simulations in order to select a subset, which preserves maximum geological diversity, dynamic properties are treated as tuning parameters during the model calibration step. Lacking a detailed understanding of in-situ polymer properties, currently broad ranges of the relevant parameters are considered.

This thesis studies the applicability of pressure fall-off test data to be incorporated into the clustering step to weight model centroids and decrease both the uncertainties associated with geological and dynamic parameters. Primary focus is set on investigating the in-situ viscosity of the polymer solution in horizontal well applications. While in-situ polymer properties represent one of the main sources of uncertainty in the current workflow, they constitute one of the key design parameters for optimizing displacement efficiency as well as project’s economics.

Fall-off tests have been simulated for a wide range of generic reservoir models and examined using pressure transient analysis (PTA) with a particular focus on pressure derivatives. For single-phase water models, PTA provides a reliable tool to characterize both geological features and essential polymer properties. An approach is developed to yield the in-situ polymer viscosity based on the characteristic shape of the pressure derivative plot. The degree of reservoir heterogeneity was found to have a strong influence on interpretation reliability. Reservoir quality index (RQI) depending polymer adsorption and viscosity have been implemented to investigate the effect of different rock types and to approximate the pseudoplastic behavior of the polymer solution.

For multi-phase models, the analysis of simulated fall-off tests has not yielded a consistent reservoir description; however, in-situ viscosity can still be approximated with the proposed workflow in case a pure water injection response is provided as baseline. This finding is of importance for the operational planning of future fall-off tests in polymer injection wells. Although the applicability of PTA to weight actual geological models could not be confirmed at this stage, outcomes of this thesis will help to constrain the interpretation of planned fall-off tests to be conducted in recently drilled horizontal polymer injectors.

List of Tables

Table 1 - Reservoir properties derivable from common transient tests [16]............................ 9

Table 2 – Overview of specific flow regimes and related time intervals................................16

Table 3 – Characteristic pressure derivative slopes of various flow regimes in the log-log plot 24

Table 4 - Reservoir and fluid properties used in simulation for the single-phase water model 39

Table 5 – Permeability range and porosity used for model validation 40

Table 6 – Model characteristics and testing schedule for the initial single-phase homogeneous vertical well model...40

Table 7 - PTA results for initial vertical well model with a permeability of 500 mD 41

Table 8 – Comparison of model permeabilities and corresponding values obtained by PTA for the vertical well case 46

Table 9 – Model characteristics and testing schedule for the initial single-phase homogeneous horizontal well model 47

Table 10 - PTA results for initial horizontal well model with a permeability of 500 mD 51

Table 11 - Comparison of model permeabilities and corresponding values obtained by PTA for the horizontal well case 53

Table 12 - Base case model parameters for heterogeneity analysis with the horizontal well 55

Table 13 - Fluid characteristics for heterogeneity analysis..55

Table 14 – Comparison of vertical permeability ratio defined in the model with values derived from PTA in case of vertical permeability anisotropy 56

Table 15 - PTA results for permeability anisotropy parallel to well orientation.......................58

Table 16 - Determination of k_x and k_y based on PTA results..60

Table 17 - PTA results for permeability anisotropy perpendicular to well orientation.............62

Table 18 – Definition of log-normal permeability distributions 66

Table 19 – Comparison of PTA results with statistical reservoir model characterization 69

Table 20 - Initial model set-up for upscaling analysis..70

Table 21 - Comparison of model values and PTA results of highly resolved initial model for narrow permeability distribution cases..72

Table 22 - Comparison of model values and PTA results of highly resolved initial model for wide permeability distribution cases 74

Table 23 - Model set-up for validation of polymer injection cases 79

Table 24 – Comparison of PTA results for polymer and water injection 89

Table 25 - Comparison of viscosity values derived from PTA with statistical model analysis 90

Table 26 – Statistical evaluation of model viscosity (in cP) after 52 weeks of polymer injection 90

Table 27 - Comparison of extracted polymer penetration depths..91

Table 28 - Well test schedule for viscosity and adsorption behavior screening 92

Table 29 – Comparison of polymer viscosity derived from PTA with model distributions for different injection viscosities 94

Table 30 - Effective polymer viscosity calculation for different RRF values 95

Table 31 -Characteristics of different rock types 99

Table 32 - Definition of various polymer viscosity and adsorption allocations to rock types 100

Table 33 – Comparison of PTA results with the statistical evaluation of actual model values for different polymer viscosity to rock type allocations 102

Table 34 - Fluid PVT at the reference pressure of 120 bar 106

Table 35 - Extracted horizontal permeability values from various two-phase models..........109

Table 36 – Comparison of PTA results for different injected polymer viscosities.................111

Table 37 - Comparison of PTA results for different polymer adsorption behavior 113

Table 38 - Permeability distribution of the selected geomodels 118

Table 39 - Water PVT properties as implemented in Eclipse (based on standard correlations) 129

Table 40 - Oil PVT properties as implemented in Eclipse (based on standard correlations)129

List of Figures

Figure 1 – Schematic of a drawdown - build-up sequence [13]....10

Figure 2 – Schematic of a composite system, depicted for a waterflooded reservoir [12] 12

Figure 3 – Two-bank model matched to pressure and derivative type curves [17]....13

Figure 4 – Type curve match for a water injection fall-off test [17] 14

Figure 5 - Compared pressure recordings of a surface and a downhole shut-in test [20]....17

Figure 6 - Overview of possible manifestations of radial flow regimes [21] 18

Figure 7 - Overview of possible manifestations of spherical flow regimes [21]....19

Figure 8 - Overview of possible manifestations of linear flow regimes [21] 20

Figure 9 – Schematic of bi-linear flow regime [21] 21

Figure 10 - Flow regime identification tool [12] 25

Figure 11 – Subsequent flow regimes of a pressure transient test in a horizontal well [12]...26

Figure 12 – Detailed depiction of dominant flow regimes in horizontal wells [27] 27

Figure 13 – Geometrical model description for a horizontal well [13] 28

Figure 14 – Characteristic response of dimensionless pressure and pressure derivative versus dimensionless time for a horizontal well [13] 30

Figure 15 – Non-Newtonian fluid viscosity classification [30] 33

Figure 16 – Matched log-log plot of the initial vertical well model....41

Figure 17 - Semi-log (left) and history (right) plot of the initial vertical well model 42

Figure 18 - Log-log plot of original and time adjusted BHP response of the initial vertical well model 42

Figure 19 - Log-log plot of the BHP response of a vertical well as the result of different horizontal discretization schemes....43

Figure 20 - Semi-log (left) and history (right) plot of the BHP response of a vertical well as the result of different horizontal discretization schemes....44

Figure 21 - Log-log plot of the BHP response of a vertical well as the result of different vertical discretization schemes 45

Figure 22 – The influence of vertical LGR on the BHP response 45

Figure 23 – Log-log plot of homogeneous vertical well model with different permeabilities...46

Figure 24 – Study of various lateral boundary distances for the horizontal well model....48

Figure 25 – Comparison of pore volume multiplication and aquifer attachment to approximate constant pressure boundaries on log-log scale....48

Figure 26 – Influence of horizontal grid coarsening on the log-log pressure response..........49

Figure 27 – The influence of erroneous alignment of the start of the shut-in period..............50

Figure 28 - Matched log-log plot of the initial horizontal well model with a permeability of 500 mD 51

Figure 29 - Semi-log (left) and history (right) plot of the initial horizontal well model with a permeability of 500mD 51

Figure 30 - Log-log plot of homogeneous horizontal well model with different permeabilities53

Figure 31 - Log-log plot of pressure transients with vertical permeability anisotropy.............56

Figure 32 - Log-log plot of pressure transients with horizontal permeability anisotropy parallel to well orientation 57

Figure 33 - Pressure profile in the horizontal well layer for different permeability anisotropy cases after 4 days of injecting 2000 scm/d 58

Figure 34 –Effective permeability as the result of horizontal permeability anisotropy during the three characteristic flow regimes towards a horizontal well [13]...............................60

Figure 35 - Log-log plot of pressure transients with horizontal permeability anisotropy perpendicular to well orientation...61

Figure 36 - The influence of permeability contrast between horizontal layers 63

Figure 37 - The influence of permeability contrast between vertical streaks parallel to the well 64

Figure 38 - The influence of permeability contrast between vertical streaks perpendicular to the well...65

Figure 39 - Log-log plot of lognormally distributed horizontal permeability and $k_z/k_x = 0.1$ 67

Figure 40 - Log-log plot of lognormally distributed horizontal permeability and uniformly distributed k_z...68

Figure 41 - Horizontal permeability distributions for the anisotropic case with $k_z/k_x = 0.1$......68

Figure 42 - Log-normal horizontal permeability distributions (mD) used for upscaling analysis 71

Figure 43 - Orientations of horizontal permeability distributions (depicted for narrow distribution case, bluish color indicates low values)...71

Figure 44 – BHP response of initial and upscaled grids in a vertical well (narrow distribution) 72

Figure 45 - BHP response of initial and upscaled grids in a horizontal well (narrow distribution) 73

Figure 46 - BHP response of initial wide distributions as observed in a vertical well.............74

Figure 47 - BHP response of initial wide distributions as observed in a horizontal well.........75

Figure 48 – BHP response of initial and upscaled grids in a vertical well (broad distribution)75

Figure 49 - BHP response of initial and upscaled grids in a horizontal well (broad distribution) 76

Figure 50 – Permeability distribution (mD) shifts associated with various permeability upscaling methods 77

Figure 51 – Grid size influence on BHP response due to polymer injection in a vertical well 80

Figure 52 - Grid size influence on BHP response due to polymer injection in a horizontal well 80

Figure 53 – BHP response of the vertical well on the 10m x 10m x 1m grid model 82

Figure 54 – Water viscosity (cP) distribution on the 10m x 10m x 1m grid after polymer injection 83

Figure 55 - Water viscosity after 16 weeks of injecting 500 scm/d of 5.5 cP polymer solution 84

Figure 56 – The influence of polymer injection duration prior to fall-off test (negligible polymer adsorption) 85

Figure 57 – The influence of polymer adsorption behavior on variable polymer injection durations prior to shut-in 87

Figure 58 – Match of the pure water response as baseline for the viscosity determination ...88

Figure 59 – Match of linear flow response with diagnostic tool (negligible polymer adsorption) 88

Figure 60 – Match of linear flow response with diagnostic tool (considerable polymer adsorption) 89

Figure 61 - Polymer viscosity correlations used for investigation 91

Figure 62 - Polymer adsorption correlations used for investigation 92

Figure 63 – The influence of different polymer viscosities 93

Figure 64 – Injected polymer viscosity versus apparent viscosity from PTA 94

Figure 65 – The influence of different magnitudes of polymer adsorption 95

Figure 66 – The influence of different residual resistance factors 96

Figure 67 – The influence of combined adsorption and permeability reduction behavior 96

Figure 68 – Maximum adsorbed polymer concentration versus apparent viscosity from PTA 97

Figure 69 – The challenge of response ambiguity 97

Figure 70 - Sensitivity of polymer viscosity with regards to interpreted effective well length .98

Figure 71 - Implementation of rock type heterogeneity in the simulation model 99

Figure 72 – Water fall-off responses for the homogeneous and heterogeneous model 100

Figure 73 – The influence of vertical permeability anisotropy in the layered model............101

Figure 74 – The influence of different polymer viscosity to rock type allocations 102

Figure 75 – Pore volume weighted viscosity distribution (cP) for viscosity allocation 1 in the layered reservoir case 103

Figure 76 - Different penetration behavior associated with different model heterogeneities104

Figure 77 – The influence of different polymer adsorption allocations................................105

Figure 78 - Relative permeability curves as implemented into the reservoir model 107

Figure 79 – Comparison of pressure responses from single- and two-phase reservoir models 108

Figure 80 – Pressure transient responses of models with different producing water cuts ...108

Figure 81 - Average water saturation versus obtained permeability ratio from PTA 109

Figure 82 – The influence of different in-situ oil viscosities 110

Figure 83 – The influence of different injection fluids 111

Figure 84 - Permeability derived from PTA versus water mobility 112

Figure 85 – The influence of different polymer viscosities..112

Figure 86 – The influence of different average water saturations during polymer injection .113

Figure 87 – The influence of different polymer adsorption and permeability reduction 114

Figure 88 – The influence of stratified rock types on the pure water fall-off test pressure derivative for reservoirs producing at different water cuts 115

Figure 89 – The influence of different polymer viscosities and adsorption behaviours in a stratified reservoir..116

Figure 90 – The challenge of pressure response ambiguity..116

Figure 91 – Horizontal permeability layering in geomodel 1635..117

Figure 92 – Water injection fall-off test responses observed in the initial geomodels..........118

Figure 93 – The influence of LGR and different boundary implementations........................119

Figure 94 – The influence of differnet well geometries..120

Figure 95 - Distribution of horizontal and vertical permeability (mD) in geomodel 1635 120

Figure 96 – The influence of vertical permeability on well following the reservoir layer.......121

Figure 97 – The influence of polymer viscosity on simulated fall-off tests (geomodel 1635)122

Figure 98 – The influence of polymer adsoprtion on simulated fall-off tests (geomodel 1635) 123

Figure 99 – Effect of thin horizontal streak of low permeability (k*/k = 0.01) 130

Figure 100 - Effect of thin horizontal streak of low permeability (k*/k = 0.1) 130

Figure 101 – Effect of thin horizontal streak of high permeability (k*/k = 10)........................131

Figure 102 – Effect of thin horizontal streak of high permeability (k*/k = 100).....................131

Figure 103 – Influence of thickness of low permeability streak concentrically encompassing the horizontal well (k*/k = 0.01) 132

Figure 104 - Influence of thickness of low permeability streak concentrically encompassing the horizontal well (k*/k = 0.1) 132

Figure 105 – Influence of thickness of high permeability streak concentrically encompassing the horizontal well (k*/k = 10) 133

Figure 106 - Influence of thickness of high permeability streak concentrically encompassing the horizontal well (k*/k = 100) 133

Figure 107 – Effect of thin vertical streak of low permeability parallel to the well (k*/k = 0.01) 134

Figure 108 - Effect of thin vertical streak of low permeability parallel to the well (k*/k = 0.1) 134

Figure 109 – Effect of thin vertical streak of high permeability parallel to the well (k*/k = 10) 135

Figure 110 – Effect of thin vertical streak of high permeability parallel to the well (k*/k = 100) 135

Figure 111 – Influence of width of parallel oriented low permeability streak concentrically encompassing the horizontal well (k*/k = 0.01)..136

Figure 112 - Influence of width of parallel oriented low permeability streak concentrically encompassing the horizontal well (k*/k = 0.1)..136

Figure 113 – Influence of width of parallel oriented high permeability streak concentrically encompassing the horizontal well (k*/k = 10)...137

Figure 114 - Influence of width of parallel oriented high permeability streak concentrically encompassing the horizontal well (k*/k = 100)..137

Figure 115 – Vertical low permeability streak perpendicularly intersecting the well (k*/k = 0.01)...138

Figure 116 - Vertical low permeability streak perpendicularly intersecting the well (k*/k = 0.1) 138

Figure 117 – Vertical high permeability streak perpendicularly intersecting the well (k*/k = 10) 139

Figure 118 – Vertical high permeability streak perpendicularly intersecting the well (k*/k = 100).......139

Figure 119 – Influence of width of perpendicularly intersecting low permeability streak concentrically encompassing the horizontal well (k*/k = 0.01) 140

Figure 120 - Influence of width of perpendicularly intersecting low permeability streak concentrically encompassing the horizontal well (k*/k = 0.1) 140

Figure 121 – Influence of width of perpendicularly intersecting high permeability streak concentrically encompassing the horizontal well (k*/k = 10) 141

Figure 122 - Influence of width of perpendicularly intersecting high permeability streak concentrically encompassing the horizontal well (k*/k = 100) 141

Figure 123 – Pressure response alteration for a vertical well due to arithmetic upscaling...142

Figure 124 – Pressure response alteration for a horizontal well due to arithmetic upscaling 142

Figure 125 – Pressure response alteration for a vertical well due to harmonic upscaling....143

Figure 126 – Pressure response alteration for a horizontal well due to harmonic upscaling143

Figure 127 – Pressure response alteration for a vertical well due to geometric upscaling...144

Figure 128 – Pressure response alteration for a horizontal well due to geometric upscaling 144

Figure 129 – Influence of different polymer viscosity correlations within a layered reservoir 151

Figure 130 - Influence of different polymer viscosity correlations within a sliced reservoir ..151

Figure 131 – The influence of vertical permeability anisotropy in a layered reservoir..........152

Figure 132 – The influence of vertical permeability anisotropy in a sliced reservoir 152

Figure 133 – The influence of spatial orientation of rock and PVT heterogeneities (k_V/k_H = 1) 153

Figure 134 – The influence of spatial orientation of rock and PVT heterogeneities (k_V/k_H = 0.1).......153

Figure 135 – The influence of different adsorption behavior allocation in a layered model..154

Figure 136 – The influence of different adsorption behavior allocation in a sliced model 154

Abbreviations

BHP	Bottom hole pressure
CDF	Cumulative distribution function
EOR	Enhanced oil recovery
HRF	Horizontal radial flow
LF	Linear flow
LGR	Local grid refinement
MAPE	Mean average percentage error
OF	Objective function
PTA	Pressure transient analysis
ROI	Radius of investigation
RRF	Residual resistance factor
VRF	Vertical radial flow
WBS	Wellbore storage

Nomenclature

Roman Symbols

A	Cross-sectional area	ft²
B	Formation volume factor	RB/STB
C	Wellbore storage coefficient	Bbl/psi
C_P^a	Adsorbed polymer concentration	$\mu g/g_{rock}$
c_t	Total compressibility	psi^{-1}
h	Formation thickness	ft
k	Absolute permeability	mD
kh	Permeability-thickness product	mD·ft
k_H	Horizontal permeability	mD
k_r	Relative permeability	-
$k_{ro}(S_{wc})$	Oil end-point relative permeability	-
$k_{rw}(S_{or})$	Water end-point relative permeability	-
k_s	Spherical permeability	mD
k_x, k_y, k_z	Permeability in the denoted direction	mD
k_V	Vertical permeability	mD
L	Distance	ft
L_a	Apparent wellbore half-length	ft
L_w	Effective wellbore half-length	ft
M	Mobility ratio	-
n_o	Corey exponent with respect to oil	-
n_w	Corey exponent with respect to water	-
p	Pressure	psia
p_D	Dimensionless pressure	-
p_i	Initial pressure	psia
p_{wf}	Bottom hole flowing pressure	psia
p_{ws}	Bottom hole shut-in pressure	psia
q	Flow rate	STB/d
q_s	Sand face flow rate	STB/d
r	Radius	ft
r_D	Dimensionless radial distance	-
r_e	Drainage radius	ft
R_k	Actual permeability reduction factor	-
R_{rf}	Residual resistance factor	-
r_w	Wellbore radius	ft
S	Skin	-
S_{or}	Residual oil saturation	-
S_w	Wellbore mechanical skin	-
S_{wc}	Connate water saturation	-
S_z	Partial penetration skin	-
t	Time	hr
t_D	Dimensionless time	-

t_p	Duration of production time before shut-in	hr
x_f	Fracture half-length	ft

Greek Symbols

γ	Total compressibility ratio	-
η	Diffusivity constant	mD/cP·psi
λ	Mobility	mD/cP
ϕ	Porosity	-
μ	Viscosity	cP
μ_{app}	Apparent viscosity	cP
μ_P	Effective polymer viscosity	cP
τ	Superposition time	-

Table of content

Page

1 INTRODUCTION 1

2 FUNDAMENTALS OF PRESSURE TRANSIENT ANALYSIS 6

2.1 Basic Principle 6

2.2 Diffusivity Equation 7

2.3 Classification of Transient Tests 9

2.3.1 Drawdown Test...10

2.3.2 Build-Up Test...10

2.3.3 Injectivity and Fall-Off Tests...11

2.4 Characteristic Flow Regimes 14

2.4.1 Wellbore Storage Effect..16

2.4.2 Radial Flow..17

2.4.3 Spherical Flow 19

2.4.4 Linear Flow 20

2.4.5 Bilinear Flow 21

2.5 Radius of Investigation...21

2.6 Pressure Derivative...22

3 PRESSURE TRANSIENT ANALYSIS FOR HORIZONTAL WELLS 26

3.1 Early Time Radial Flow 28

3.2 Intermediate Time Linear Flow 29

3.3 Late Time Radial Flow 29

3.4 Interpretation Procedure 30

3.5 Model Limitations...31

4 POLYMER INJECTION 32

4.1 Rheology of Polymer Solutions..32

4.2 Polymer Viscosity..33

4.3 Polymer Retention 34

5 METHODOLOGY...36

5.1 Geological Modelling...36

5.2 Fluid Modelling...36

5.3 Well Test Design..37

5.4 Pressure Transient Analysis 37

6 SINGLE-PHASE RESERVOIR MODELS 39

6.1 Model Validation 39
6.1.1 Vertical Well Model 40
6.1.2 Horizontal Well Model 47
6.2 The Influence of Reservoir Heterogeneity 54
6.2.1 Permeability Anisotropy 54
6.2.2 Discontinuous Permeability Heterogeneity 62
6.2.3 Continuous Permeability Heterogeneity 66
6.2.4 The Influence of Permeability Upscaling 69

7 THE EFFECT OF POLYMER INJECTION 78

7.1 Model Validation 79
7.2 Viscosity Determination in Horizontal Wells 84
7.3 The Influence of Polymer Viscosity and Adsorption 91
7.4 The Influence of Various Rock Types 98

8 TWO-PHASE RESERVOIR MODELS 106

8.1 Model Set-up 106
8.2 The Effect of Reservoir Heterogeneity 114

9 APPLICABILITY FOR GEOMODEL SCREENING 117

9.1 Geological Screening 117
9.2 Polymer Injection 121

10 CONCLUSION 124

11 REFERENCES 126

APPENDICES 129

Appendix A – Eclipse fluid PVT data 129
Appendix B – Horizontal permeability plane type curves 130
Appendix C – Vertical permeability plane type curves (parallel to well) 134
Appendix D – Vertical permeability plane type curves (perpendicular to well) 138
Appendix E – Influence of various upscaling techniques on the pressure response for a log-normally distributed permeability (μ = 3, σ = 1.5) 142
Appendix F – Polymer viscosity correlations as implemented into Eclipse 145
Appendix G – Polymer adsorption correlations as implemented into Eclipse 146
Appendix H – Reservoir models for layered heterogeneity investigation 147
Appendix I – Reservoir models for sliced heterogeneity investigation 149

Appendix J – The influence of reservoir and PVT heterogeneity.................................151

1 Introduction

Significant water production is a major concern of mature oil reservoirs and well known throughout the petroleum industry. Decreasing hydrocarbon production in conjunction with the disposal of excessive amounts of underground water, which causes complex environmental problems, adversely affects recovery economics and might result in premature abandonment of a field. The heterogeneous nature of most oil and gas reservoirs causes channeling and disproportionate water production through high permeability zones, leaving considerable amounts of movable hydrocarbons bypassed and trapped in low permeability regions. Better mobility control of the injected fluid can be achieved by applications of polymer solution and help to recover a significant part of the remaining oil. Two main mechanisms dominate incremental oil production: (1) Increased viscosity of the polymer augmented injection water lowers the mobility ratio with respect to the resident viscous oil, hence increasing the oil production, and (2) improves the volumetric sweep efficiency [1]. The flow of oil along its flow paths is accelerated by the reduction of the mobility ratio itself as well as a reduction of the relative permeability of water due to polymer adsorption, while leaving the relative permeability of oil unaltered.

After a polymer injection pilot indicated encouraging incremental oil production in the 8 TH reservoir of the Matzen field, the pilot project is extended and field-rollout considered. Like any other Enhanced Oil Recovery (EOR) method, polymer flooding requires a structured approach to minimize economic and technical uncertainties while improving operational capabilities [2]: After a profound portfolio screening, both laboratory and field testing are crucial steps to be conducted for the selected candidates before sector and field roll-out. Compliance with that sequence ensures that evaluations based on theoretical considerations as well as observations of tests under laboratory conditions are transferred adequately into real-field situations. Pilot projects are used to assess the effect of reservoir geology on process performance and to calibrate models for full-field predictions. There is agreement between simulations and field results, which indicate that the change in sweep efficiency due to polymer injection is significantly impacted by reservoir heterogeneity, especially permeability contrast and distribution [1] [3] [4]. Hence, a comprehensive reservoir characterization is the crucial prerequisite to successfully simulate the response of a polymer pilot and eventually optimize an entire field roll-out.

While the traditional reservoir simulation workflow is based on calibrating one single static geological model to an observed production history (history matching), it is nowadays well accepted in the scientific community that uncertainty inherent in all geological models should be incorporated in a more general manner. Increased awareness that various geological models might yield equally acceptable history matches, depending on the set of dynamic parameters used, has replaced the single-model with an ensemble based approach. This non-uniqueness of geological realizations has to be taken into account, while interpreting field test data as well as forecasting incremental oil production. Possible geological representations can be screened and ranked based on a wide range of techniques, such as tracer responses [5], reservoir connectivity [6], the Dynamic Lorenz Coefficient [7], and streamline simulations [8].

Within OMV, a tailored probabilistic workflow has been developed to forecast incremental oil production due to polymer injection based on a distance kernel model developed by Scheidt and Caers [8]. While initially a dissimilarity distance calculated from streamlines has been applied for model selection by Scheidt and Caers, tracer responses are used to extract a representative sub-set of models from the entire population and to weight different model realizations to estimate the probabilistic forecast of incremental oil associated with the polymer injection pilot. This approach honors the uncertainty associated with both geological models as well as dynamic parameters and is detailed in [9].

Initially, a large number of different static geomodel realizations are generated taking into account the uncertainty inherent in correlations of geological layers, facies, logs, and cores as well as different geological concepts and parameter ranges for geo-algorithms. Generalized Sensitivity Analysis has been found to be an appropriate tool to ensure sufficient variability between the geomodel realizations to account for a realistic degree of uncertainty and heterogeneity [9]. In a subsequent step, streamline simulations are performed to assess the dissimilarity between the dynamic tracer responses of the various models. A dissimilarity matrix, which describes the “distance” between any two realizations in a multi-dimensional variable space, is constructed and forms the basis for clustering the entire population into a significantly lower number of representative realizations (centroids), which are carried forward for full-physics dynamic simulation and history matching. This approach helps to minimize computational costs compared to history matching all models, while preserving geological diversity.

Having selected the sub-set of representative model centroids, Latin Hypercube Sampling is applied to populate these geological representations with ranges of dynamic parameters to create comprehensive models for the history matching step. Special attention has been paid to average oil saturation before the secondary water flooding, relative permeability curves and polymer properties, as these properties are associated with a high degree of uncertainty. The dynamic responses of all history matched reservoir models are subsequently evaluated by a predefined Objective Function (OF) based on observed total liquid rate, historic oil production data, and measured tracer responses, if available. While the tracer concentration captures the dependency on geological connectivity, the liquid rate ensures that the productivity of the wells is sufficient to allow for the historically observed total volumes. Differential Evolution is applied as a global optimization methodology to improve the OF, in order to ensure that geomodels with a similar historic tracer response are stronger weighted in the forecasting step.

To forecast the economic benefit of a potential polymer injector, the incremental oil production for each realization is calculated after differential evolution for history matching is finalized. These individual forecasts are weighted according to the OF to derive a probabilistic forecast according to their mismatch with the observed production history. In the sense of a classical Bayesian framework, each forecast can be understood as the posterior probability given the historical data.

The current workflow is based on the OF solely comprising total liquid and oil rate as well as tracer concentration in the back-produced fluids to weight different geological realizations in the dynamic simulation step. Polymer viscosity has been used as a calibration parameter to align the P50 forecast of incremental oil production as derived from simulation with values obtained from Decline Curve Analysis of adjacent wells. These calibrated models then form the basis to assess incremental oil production potential by further polymer injectors using the proposed probabilistic workflow.

While tracer concentration in the back-produced fluid stream is particularly sensitive to the geological set-up of the model, one of the key design parameters for optimizing the displacement efficiency of an injected polymer solution is the in-situ viscosity. Although polymer viscosity can easily be measured at the surface, the viscosity within the reservoir is difficult to estimate due to degradation during the injection process. In addition, polymers exhibit non-Newtonian behaviors introducing a functional behavior between experienced shear rate in the reservoir and actual viscosity.

Pressure transient analysis (PTA) is a practical method to investigate reservoir properties and to obtain information on the size and shape of a formation as well as its ability to produce fluids. Comprehensive interpretation of acquired well test data is critical for all stages throughout the life of a reservoir from optimal development to efficient management, as it assists in quantifying the parameters determining the dynamic response during hydrocarbon recovery. Introduced as a rational to interpret interference tests using the line source solution, pressure response type curves have evolved quickly to illustrate features like near-wellbore geometry, reservoir heterogeneity and outer boundaries, which are typically presented as entire families of type curves. Since the advent of the pressure derivative, new models have been introduced in the literature as type curve pairs of pressure change and its derivative. Well test analysts have learned to recognize models for observed transient data as identifiable trends in the pressure derivative.

Advances in computing techniques have facilitated the development of custom curves representing a major advance in well test interpretation. Computer generated models are displayed simultaneously with the observed data and rigorously matched to produce precise estimates for the reservoir parameters. It is now possible to screen an almost unlimited number of reservoir models with the observed data due to much greater flexibility. However, real transient data often contains behavior dominated by effects, which cannot easily be captured in analytical models. Multi-phase and non-Darcy flow as well as distinct model heterogeneity and complex boundary configurations are typical reasons for corresponding deviations from analytical type curves, which could easily be addressed using screening procedures with numerical models.

Possessing the ability to provide considerable insight beyond that possible from analytical models, makes numerical simulation a tool to refine the interpretation process. One main issue is the tailored design of commercial simulators towards full-field applications with multiple wells and larger time horizons. Such a set-up does not readily adapt to single-well focus and highly resolved short-term transient behavior. If sufficient information is available to support the level of complexity required to set-up a numerical reservoir model, incorporation of transient data may enable the quantification of areal permeability anisotropy, with successive tests even being able to determine the in-situ characterization of multi-phase fluid flow properties.

Pressure derivative data obtained from fall-off tests was shown to be appropriate to elucidate the polymer effective permeability [10]. Hence, pressure derivative studies represent a promising approach to determine the in-situ polymer properties within a reservoir and to further constrain the OF to enhance the weighting procedure in the current workflow by further reducing the overall uncertainty.

In this thesis, PTA is used to investigate both geological characteristics and essential polymer properties, mainly the residual resistance factor (RRF) and the in-situ viscosity. The major objective of this research is to elaborate how much information in terms of polymer characterization, reservoir heterogeneity and two-phase flow can be obtained using PTA. Until now, no thorough understanding of transient pressure analysis in two-phase flow has been attained. Therefore, the influence of multi-phase flow as well as heterogeneity will be investigated using classical well test analysis tools, which were developed based on the assumption of single-phase flow. Eventually this investigation helps to understand to which extend traditional PTA might be applied to EOR projects.

In the first two chapters, a brief introduction into the terminology used in well testing and interpretation is presented, characteristic well pressure behavior is illustrated, and the corresponding analysis methods are introduced. Primary focus is set on the interpretation of data acquired in horizontal wells and the analysis of pressure derivative responses. The fourth chapter provides an overview of relevant effects of polymer flooding to ensure thorough understanding of associated aspects during the interpretation of affected pressure transient tests in the subsequent chapters.

Initially, highly resolved homogeneous models are simulated in order to verify the consistency between simple hypothetical geological models and their responses obtained using PTA. These verified models form the basis for subsequent steps, in which the pressure responses according to various geological features such as permeability heterogeneity, permeability anisotropy, spatial property distribution, and property averaging effects due to upscaling are analyzed for a horizontal well configuration.

In a second stage polymer solution is injected into single-phase water models with an increasing geological complexity. The effect of different fluid mobilities on the pressure transient response in a horizontal well is investigated and an interpretation technique to yield the in-situ polymer viscosity in relatively homogeneous geological settings is developed. The influence of different rock - polymer interaction is investigated by defining various rock types with different polymer adsorption behavior in the simulation model. The effect of shear-thinning, typically observed for polymers under reservoir conditions, is approximated by implementing various polymer PVT regions in the model.

The last phase of this study is dedicated to the incorporation of multi-phase flow. All investigated models are initialized to yield certain water cuts before fall-off tests are simulated. Considerable differences between the pressure responses from single- and two-phase simulations are observed. The influence of relative permeability and mobility is studied and the applicability of the proposed approach to obtain the in-situ polymer viscosity is confirmed. Eventually, an actual geological realization currently considered in the probabilistic workflow is investigated. Gained insights from prior analyses on simplified models are shown not to be readily transferable due to inherent geological complexity.

Transient tests provide several parameters critical to traditional nodal analysis, which helps determine the cost effectiveness of different treatments under consideration and assists in making an optimal completion decision. This methodical approach optimizes oil and gas well deliverability by identifying major sources of flow restrictions and performing sensitivity studies regarding optimal debottlenecking. Insights regarding the in-situ polymer properties from PTA might be applied in a similar manner to optimize the design of future polymer injection schemes, where this thesis will make a small contribution.

2 Fundamentals of Pressure Transient Analysis

From its modest beginnings as a rudimentary productivity test, well testing has progressed to become one of the most powerful tools for determining complex reservoir characteristics. Pressure transient testing constitutes one primary source of dynamic reservoir data and is performed at various stages of drilling, completion, and production of oil and gas wells. Test objectives can range from a simple reservoir pressure measurement to complex characterization of reservoir features. Most pressure transient tests can be classified as either (1) productivity tests or (2) descriptive reservoir tests.

While productivity tests are mainly focused on determining well deliverability, formation damage and skin effect, and identifying produced fluids as well as their respective volume ratios in order to evaluate completion efficiency and workover or stimulation treatments, descriptive reservoir tests provide information about reservoir extend and geometry, reservoir heterogeneity, and parameter estimations.

Compared to other techniques, PTA features some unique advantages, which range from its large radius of investigation to tailored testing procedures depending on specific parameters to be analyzed. The ability of well tests to investigate much larger volumes of a reservoir provides an exceptional possibility to interpret boundaries; however, in heterogeneous reservoirs the responses of different zones might be convolved and complicated to interpret. PTA can be applied to monitor both well and reservoir behavior and provide insights into causes of unexpected performance deviation. In cases of injection wells, PTA can help to limit excessive fracture growth and maintaining cap rock integrity.

2.1 Basic Principle

The principal concept of any well test is sending a pressure signal into the reservoir and recording the corresponding response from the formation. During a transient well test, changes in production rate induce pressure disturbances in the wellbore and the surrounding rock, which subsequently extend into the formation while being affected in various ways by certain rock features. Since a pressure disturbance will have difficulty entering a tight reservoir zone, while passing unhindered through areas of high permeability, recording wellbore pressure response over time produces a curve, which shape is defined by the unique characteristics of the reservoir. Monitoring the propagation of the pressure discontinuity through the reservoir provides information about the in-situ mobility as well as the distance of certain features like fractures or boundaries, which can be estimated from the time delay of the recording.

Input data required for a detailed well test analysis comprises the test data itself, which consists of flow rate and bottom hole pressure (BHP) as a function of time, well data, such as wellbore radius, well geometry and depths of the gauges, and eventually reservoir and fluid parameters, which covers formation thickness, porosity, compressibility of both rock and fluids, saturations, and a few more. While well evaluation tests are frequently achieved in less than two days, reservoir limit testing may require several months of pressure data. The pressure response is analyzed versus the elapsed time since the start of the test period.

Transient well testing constitutes a typical inverse problem, for which input and output are well defined by the applied step function of rate and the measured pressure response, respectively. The reservoir can be understood as a simple transfer function between these two. Therefore, well test interpretation models are only capable of describing the behavior of a reservoir (homogeneous or heterogeneous, bounded or infinite acting) and often differ from real geological or log models due to the averaging of reservoir properties.

Analytical solutions are used to generate pressure responses to a specific production rate history until model and observed behavior are identical. The typical interpretation work flow consists of (1) model identification, followed by (2) model parameter calculation, and eventually (3) model validation. Model identification is basically a pattern recognition and non-unique solution problem, which has the objective to find a general model able to match the obtained pressure response in consistency with geophysics, geology, and petrophysics. Major considerations are characteristic shapes created by well-defined flow regimes and identifying possible superpositions of these basic regimes, which could create the given type of data. The subsequent model parameter calculation step is again a direct problem and focused on adjusting the parameters of the selected model in order to minimize the discrepancy between the theoretical and the measured pressure data. The model verification step assures that the obtained model honors meaningful parameter ranges and is in agreement with other related knowledge. The model parameters are then regarded as a good representation of those of the actual reservoir.

To unlock the information contained in pressure transient curves, three different coordinate systems are applied: Log-Log plots are mainly used for model recognition and are also called diagnostic plots, while semi-log plots are applied for parameter computation, and Cartesian plots help to verify both the selected model and the calculated parameters. Typical pressure responses that might be observed due to different formation characteristics have been described in numerous publications and can be found elsewhere [11] [12] [13]. This chapter is designed to provide only a brief overview of relevant aspects for later discussed analyses.

2.2 Diffusivity Equation

Considering a drawdown test, immediately after the start of production the pressure in the wellbore drops sharply and fluid near the well starts to expand and to move against this imposed pressure gradient. While friction against the pore walls as well as the fluid’s own inertia and viscosity retard this movement, the propagating pressure imbalance induces adjacent fluid particles to also move towards the wellbore. This process continues until the initial pressure disturbance is dissipated throughout the reservoir. The physical process behind this pressure propagation through the reservoir can be described by the diffusivity equation.

Well tests are modelled with the diffusivity equation expressed in radial coordinates assuming fluid flow towards a cylindrical well positioned normally between two parallel, impermeable, and planar barriers. Combining the law of mass conservation and Darcy's law for the isothermal flow of fluids of small and constant compressibility yields the radial diffusivity equation as provided in eq. (1) [14].

$$\frac{\partial^2 p}{\partial r^2} + \frac{1}{r}\frac{\partial p}{\partial r} = \frac{1}{\eta}\frac{\partial p}{\partial t} \tag{1}$$

The hydraulic diffusivity constant η is defined by eq.(2).

$$\eta = \frac{0.0002637\, k}{\phi\, c_t\, \mu} \tag{2}$$

In the derivation of this equation, it has been assumed that compressibility of the total system c_t is small and independent of pressure. Permeability k and porosity Φ are assumed constant with k furthermore considered isotropic. The viscosity μ is assumed independent of pressure. Both initial and boundary conditions are required to yield a unique solution to the diffusivity equation.

The so-called infinite acting radial model (well situated in a porous medium of infinite radial extend) represents the most relevant case considered in fundamental well testing theory. Assuming uniform pressure distribution equal to the initial reservoir pressure p_i before production, the pressure at the infinite outer boundary also being equal to p_i, and a fluid withdrawal at a constant sand face flow rate q_s given by eq. (3), the solution of the diffusivity equation in its approximate form yields eq. (4).

$$q_S = \frac{2\,\pi\, k\, h}{\mu}\, (r\frac{\partial p}{\partial r})_{r_w} \tag{3}$$

$$p_D(r_D, t_D) = 0.5\; (ln\frac{t_D}{r_D^2} + 0.80907) \tag{4}$$

Dimensionless time t_D and dimensionless radial distance r_D are provided by eq. (5) and eq.(6), respectively.

$$t_D = \frac{0.0002637\, k\, t}{\mu\, \phi\, c_t\, r_w^2} \tag{5}$$

$$r_D = \frac{r}{r_w} \tag{6}$$

Dimensionless pressure p_D is given by eq. (7), where the well flowing pressure p_{wf} refers to the pressure, where r_D yields unity.

$$p_D = 0.00708 \frac{k\,h}{q_s\,\mu}(p_i - p_{wf}) \tag{7}$$

In cases of reservoirs with regular, straight boundaries or off-centered well locations the same set of equations as for the infinite reservoir solution can be used, applying the principal of superposition of well images in space. This approach is of particular value to investigate pressure responses associated with faults and changes in reservoir size.

As it can be obtained from the solution given in eq. (4), a plot of pressure versus time on a semi-log scale will be characterized by a straight line. This relationship provides an easy to use graphical interpretation procedure for calculating permeability from the slope of the portion of the curve possessing a straight line and forms the basis for most of the analysis procedures discussed later.

2.3 Classification of Transient Tests

Pressure transient tests can be conducted in manifold modes, with specific test configurations dedicated to certain stages of reservoir exploitation. While drill stem and wireline formation tests are mostly run in exploration and appraisal wells, conventional transient well tests are typical during primary, secondary, and tertiary recovery stages. Step-rate, injectivity, fall-off, interference, and pulse tests are commonly used to further delineate certain aspects of the target formation during secondary and enhanced recovery phase [15]. Although the same formation property can often be derived from various transient tests, different analyses are typically associated with different levels of accuracy. It has been found that built-up tests yield higher accuracy for permeability estimation compared to drawdown test, while suffering from lower reliability regarding skin calculation and vice versa. Table 1 provides an overview of common pressure transient tests together with derivable formation properties.

Table 1 - Reservoir properties derivable from common transient tests [16]

Drill Stem Tests	Reservoir behavior, reservoir pressure, fluid samples, permeability, skin, fracture length, reservoir boundaries
Wireline Formation Tests	Reservoir pressure, fluid samples
Drawdown Tests, Build-up Tests	Reservoir behavior, permeability, skin, fracture length, reservoir boundaries
Step-rate Tests	Permeability, skin, formation parting pressure
Fall-off Tests	Reservoir pressure, skin, mobility in various banks, fracture length, front location, reservoir boundaries
Interference Tests, Pulse Tests	Reservoir behavior, communication between wells, permeability, porosity
Layered Reservoir Tests	Average pressure, skin, permeabilities of individual layers, vertical permeability, reservoir boundaries

2.3.1 Drawdown Test

A drawdown test records the BHP evolution during a period of constant production rate. Before putting the well on production, the pressure within the formation of interest should ideally be equalized and uniform. Hence, drawdown tests are often conducted in virgin reservoirs or after extended shut-in periods (due to work-overs, …).

Drawdown data is normally noisy, as it is difficult to ascertain a constant flow rate, which is why these types of tests are typically conducted, when there are some uncertainties or limitations associated with build-up interpretations. It is not untypical to conduct drawdown and build-up tests for comparative analysis.

During the flowing period, the drawdown pressure response Δp is defined by eq. (8), where Δt denotes the elapsed time since the start of the flow period. Figure 1 depicts a typical drawdown – build-up sequence as observed during well testing and illustrates the typical notations for time and pressure.

$$\Delta p = p_i - p(\Delta t) \tag{8}$$

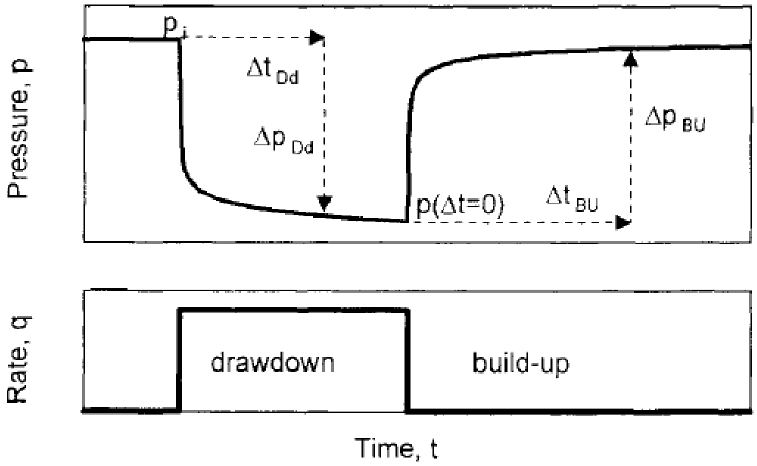

Figure 1 – Schematic of a drawdown - build-up sequence [13]

2.3.2 Build-Up Test

A build-up test records the BHP evolution during a shut-in, after the well has been on (constant) production for an extended period of time. The pressure builds up, because it is recovering from the reduced level during drawdown and associated production. Build-up tests represent the preferred means to determine well flow capacity, permeability thickness, skin and further reservoir properties. Compared to drawdown tests, build-up tests usually reach quiescent states quickly after shut-in, so that the BHP rises smoothly, ensuring easy measurements, high data quality and interpretable test results.

After shutting in the well, the build-up pressure change Δp can be calculated by eq. (9), where $p(\Delta t = 0)$ characterizes the last flowing pressure.

$$\Delta p = p(\Delta t) - p(\Delta t = 0) \tag{9}$$

2.3.3 Injectivity and Fall-Off Tests

Fall-off and injectivity testing is conducted to elaborate parameters for modelling injection schemes, since the success of both water- and polymer flooding largely depends on adequate prediction of the reservoir response. In addition to parameters, which could also be obtained by conventional transient tests, specific time dependent insights might be gained, such as front location, injectivity, and average interwell pressure.

During an injectivity test, the well is initially shut-in until pressure is stabilized followed by injection at a constant rate while recording BHP. Given the case that the injection fluid possesses exactly the same properties (density, viscosity, compressibility, wetting characteristics) as the in-situ reservoir fluid, the only difference to a drawdown test would be the negative flow rate. In case of a difference in density, the injection profile would be uneven with the injected fluid experiencing gravity under- or override depending on higher or lower density compared to the reservoir fluid, respectively. The effective net pay thickness to be used during PTA should be reduced accordingly. If the fluids differ in terms of viscosity, compressibility, or wetting characteristics, an interface or front will form in the reservoir requiring more elaborate analyses approaches. Relative permeability becomes important for immiscible fluids. A pressure fall-off test is typically preceded by a long injectivity test, which is stopped while BHP is continued to be recorded. Hence, fall-off tests can be considered as analogues to build-up tests.

Although conceptually the only mathematical difference between injection and production well testing is the sign associated with the rate, there are many more complications in water injection wells. Since water injection into hydrocarbon reservoirs is an immiscible displacement process, multiphase flow has to be considered during interpretation. Furthermore, reservoir conditions will likely not be isothermal, since the injected fluid will inevitably possess a different temperature than the formation of interest. As a result, several effects have to be taken into account, in order to ensure a meaningful interpretation of the test results: (1) Viscosity differences between the displaced and the displacing fluids, (2) relative permeability differences between the flushed and the unflushed zones, and (3) saturation and compressibility differences between the flushed and the unflushed zones.

From a mathematical point of view, an injection well can be interpreted as a radial discontinuity in both mobility and diffusivity with an additional complication of a time dependent moving boundary. If cold water is injected or high pressures are yielded, the necessary consideration of the occurrence of fractures adds further complexity. Just considering radial matrix flow, two displacement models are commonly used for analysis: If the properties of the injected and in-situ reservoir fluid are identical, the resulting piston-like displacement does not show any discontinuity across the flood front. This case is referred to as (1) unit mobility case and the governing equations reduce to the single-phase, homogeneous fluid case. (2) Buckley Leverett displacement concepts are applied in case of mobility differences between the in-situ and the injected fluid. Piston-like displacement results in the establishment of three generic zones around the saturation discontinuity: The invaded zone is located adjacent to the injector. The oil saturation in this zone is assumed being equal to residual saturation. The invaded zone, in which oil saturation increases from residual to initial, contains the discontinuity, also known as saturation front. Behind the front, the uninvaded zone is located and assumed to show initial water saturation. Since Buckley Leverett theory was developed for one-dimensional problems, undisturbed radial flow is a necessary assumption to be made during the analysis of fall-off test data, which significantly restricts its applicability.

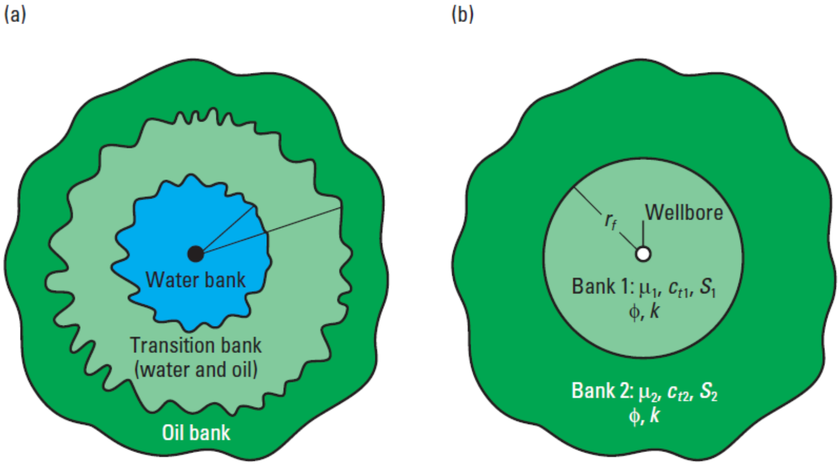

Figure 2 – Schematic of a composite system, depicted for a waterflooded reservoir [12]

Due to differences in fluid properties, the pressure transient response in a reservoir exposed to multi-phase flow differs from single-phase flow behavior. Figure 2 depicts the schematic formation of a saturation gradient within the reservoir as the result of fluid injection exemplarily for a waterflooding case. The region of high water saturation around the well is termed water bank (invaded zone), while the oil bank (uninvaded zone) refers to the region ahead of the injection front possessing initial water saturation. PTA for injection tests in vertical wells is often conducted based on radial composite reservoir models (Figure 2 a), which assume the reservoir to be comprised of various distinct annuli within which the fluid properties are considered constant but change sharply at an interface. The two-bank model (Figure 2 b) is the simplest version of a radial composite model and honors the necessary condition for an analysis incorporating Buckley Leverett theory.

After WBS effects have vanished, the characteristics of each fluid bank may be retrieved from PTA by means of a two-bank model for vertical well cases as depicted in Figure 3. The early time response is governed by the rock and fluid properties of the bank closely around the well and appears as a horizontal line identical to single-phase flow. The subsequent response represents the transient travelling through the transition bank, experiencing a certain saturation distribution and the corresponding displacement mobility ratio M. The mobility ratio is defined as the mobility of the displacing fluid divided by the mobility of the displaced fluid. The derivative curve yields a hump for $M > 1$ and a dip for $M < 1$. The storativity ratio of the banks determines the duration of the transition period. Having passed the transition zone, the pressure transient becomes solely controlled by the properties of the outer bank. A second pressure derivative plateau can be observed in the diagnostic plot with the level of stabilization now being related to the mobility of the exterior bank.

The definition of fluid mobility for both water and oil is provided by eq. (10) and their relationship to yield the mobility ratio is stated by eq. (11). A mobility ratio of less than unity will yield a stable and piston-like displacement with a rather narrow transition zone. A mobility ratio exceeding unity characterized unstable displacement with water channeling, fingering, and bypassed oil. A significantly larger transition zone establishes.

$$\lambda_w = \frac{k\, k_{rw}}{\mu_w} \qquad \lambda_o = \frac{k\, k_{ro}}{\mu_o} \tag{10}$$

$$M = \frac{\lambda_w}{\lambda_o} = \frac{k_{rw}\, \mu_o}{k_{ro}\, \mu_w} \tag{11}$$

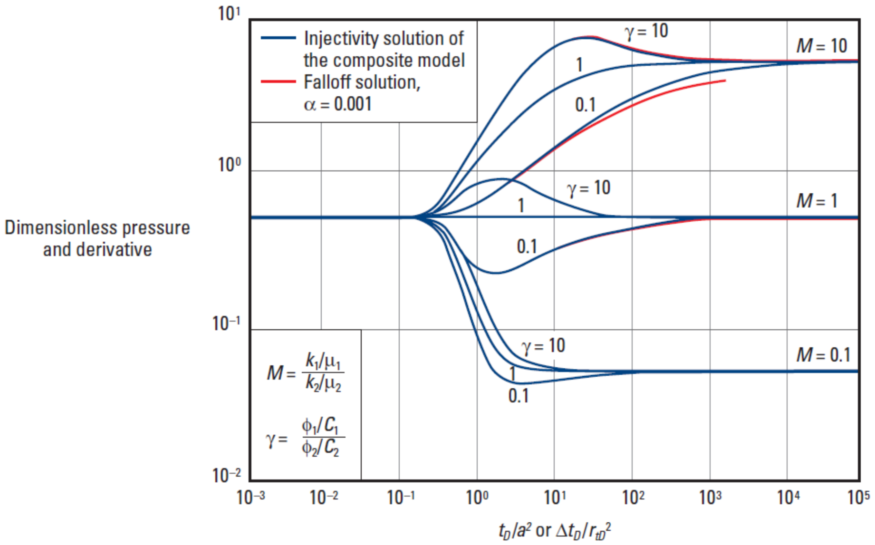

Figure 3 – Two-bank model matched to pressure and derivative type curves [17]

Matching observed field data with type curves as depicted in Figure 3 provides all parameters of the system. The mobility of the inner fluid bank and the mobility of the outer fluid bank can be obtained by the first and second radial flow regime, respectively. The intermediate flow regime yields the location of the propagating fluid front, if combined with a simple material balance calculation.

A more elaborate approach is the interpretation based on a multi-bank model (Figure 2 a), which explicitly incorporates the saturation distribution within the transition zone. Based on a certain relative permeability behavior as well as individual rock and fluid compressibility values, customized and field specific type curves are constructed. As depicted in Figure 4, a subsequent match with one of these customized type curves is able to yield both the location of the fluid front and the mobility of unaffected region ahead of the front. Providing such insights, fall-off tests are of great value for reservoir monitoring.

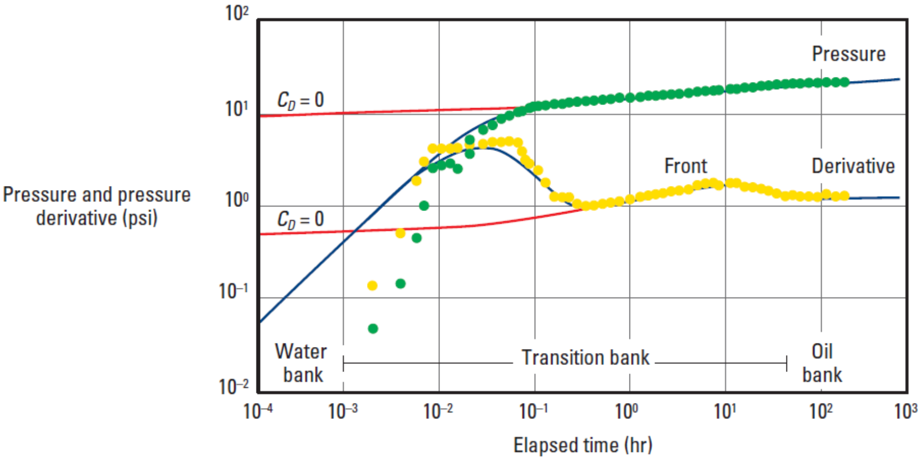

Figure 4 – Type curve match for a water injection fall-off test [17]

2.4 Characteristic Flow Regimes

The flow of fluid within a reservoir is dominated by changing boundary conditions over time, depending on the shape and the size of the reservoir. Hence, well test responses follow a chronological characteristic behavior at different times, providing insights into the well and reservoir configuration.

The mathematical representations to describe the flow of reservoir fluids in porous media will vary depending upon the characteristics of the reservoir. Primary reservoir characteristics to be considered include types of reservoir fluids, flow regimes, reservoir geometry, and the number of flowing phases in the reservoir. Hence, a clear identification of predominant flow regimes is important to conduct a meaningful interpretation with the corresponding mathematic model.

Before providing a more detailed classification, the three principle flow regimes will be described, which are usually classified in terms of rate of change of pressure with respect to time.

Steady State Flow

During steady state flow, the pressure in the well drainage volume does not vary in time at any point. The existing pressure profile remains constant and the pressure derivative with respect to time vanishes (eq.(12)). This behavior is typically observed, if some form of pressure maintenance, either naturally existing as a gas cap or an aquifer or artificially imposed by water interjection, dominates the reservoir performance.

$$\frac{\partial p}{\partial t} = 0 \tag{12}$$

Pseudo Steady State Flow

During pseudo steady state flow, pressure changes uniformly with time. The incremental change in the pressure profile becomes constant for each unit of time (eq. (13)). This behavior is typically observed as response from closed systems, when all boundaries have been reached.

$$\frac{\partial p}{\partial t} = constant \tag{13}$$

During pseudo steady state, the BHP is a linear function of the elapsed time and the reservoir pore volume ΦhA might be calculated based on straight line approach presented in [18].

Transient State Flow

During transient flow, the pressure variation with time is a function of well geometry and reservoir properties, primarily permeability and heterogeneity (eq.(14)). This behavior is typically observed before constant pressure or closed boundary effects are reached. Higher compressibility of the fluid leads to a more pronounced transient flow behavior [19].

$$\frac{\partial p}{\partial t} = f(x, y, z, t) \tag{14}$$

The transient flow regime is the primary focus of well test interpretation. During PTA, wellbore conditions dominate the early time response and make way for a pressure response determined by reservoir properties as the drainage area expands, before boundary effects are seen at late times, when the flow regime transitions to pseudo steady or steady state.

A limited number of flow line geometries produce a characteristic pressure behavior, following a well-defined time function. Straight line techniques have been developed to obtain reservoir properties from specialized pressure versus time plots. A complete well response consists of a sequence of flow regimes, which define the appropriate interpretation model for each time interval. An overview of specific flow regimes is provided in Table 2.

Table 2 – Overview of specific flow regimes and related time intervals

Wellbore Configuration	**Early Time**	**Middle Time**	**Transition**	**Late Time**
Vertical well	Wellbore Storage Linear Flow Bilinear Flow Spherical Flow	Radial Flow	Single No Flow Boundary Linear Channel Flow	Pseudo Steady State Flow Steady state Flow
Horizontal well	Wellbore Storage Vertical Radial Flow Linear Horizontal Flow Elliptical Flow	Horizontal Radial Flow	Linear Channel Flow	Pseudo Steady State Flow Steady state Flow

2.4.1 Wellbore Storage Effect

Since rate measurements are conducted at surface, expansion or compression of fluid in the wellbore as well as moving fluid interfaces may result in a discrepancy between the recorded production and the effective reservoir flow rate immediately after a rate change. The phenomenon of this time lag between the surface production and the sand face rate after any change in the well flowing conditions is called wellbore storage (WBS) effect.

Assuming it is possible to keep the surface flow rate perfectly constant during a drawdown test, the initial production is associated with fluid expansion in the wellbore and not related to any reservoir inflow, while the sand face flow rate only slowly builds up to equalize with the surface flow rate. Hence, the pressure signal does not reflect any reservoir properties during this period. On the contrary, it is impossible to gain perfect control of the reservoir flow rate in build-up tests, since fluid will continue to flow into the wellbore driven by the imposed pressure gradient immediately after shut-in. This afterflow yields a pressure increase in the wellbore due to fluid compression. The effect of afterflow may be minimized by a downhole shut-in and combined downhole flow and pressure measurements, which reduces the volume of compressed fluid dramatically and allows analyzing reservoir-dominated flow at earlier times.

The wellbore storage coefficient C defines the rate of pressure change during the pure WBS regime, which describes the well acting as a closed volume and with a constant surface rate condition. For single-phase fluid applications WBS becomes a compressibility term and pressure changes linearly with time. While traditional type curve matching techniques rely on the assumption of constant WBS, numerous circumstances like wellbore phase redistribution and increasing or decreasing fluid level violate this presumption.

Figure 5 depicts the superimposed log-log plots for two build-up tests conducted on the same vertical well. It can be obtained that radial flow is barely reached after 200 hours in the surface shut-in test, while the radial stabilization can be detected almost immediately after shut-in in the downhole shut-in test due to the elimination of a large fraction of the wellbore volume. This significant effect of WBS on the establishment of a distinct radial flow regime becomes especially relevant for wells with large volumes such as deviated and horizontal ones.

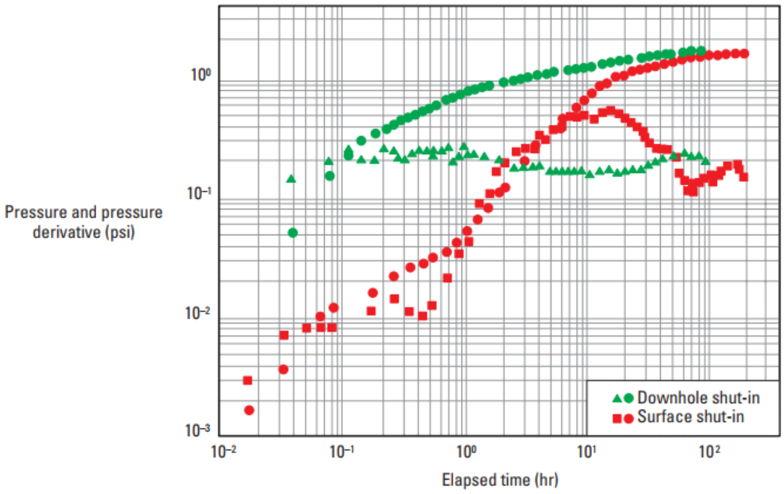

Figure 5 - Compared pressure recordings of a surface and a downhole shut-in test [20]

By minimizing both WBS effects and the duration of the afterflow period, the value of information gained from a well test can be maximized by the application of downhole shut-in tools. However, flow into the well does not immediately cease after shut-in, but continues to enter the remaining chamber below at an exponentially decreasing rate. This continued inflow undermines the assumption of perfect flow control while deriving the solution of the diffusivity equation applicable for well testing in Chapter 2.2, where effects of fluid flow on the shape of the pressure transient were discounted. To overcome this issue, a solution accounting for flow rate effects has to be developed by understanding the declining flow rate curve as a series of step changes. Hence, the combined pressure transient curve can be obtained by integrating infinitely small flow rate steps, which can individually be described using the developed standard equation.

2.4.2 Radial Flow

Radial flow represents the most important flow regime during PTA and can easily be recognized as an extended constant or flat trend in the derivative plot. Radial flow enables the determination of permeability and skin as well as extrapolated reservoir pressure if occurring in late time. As illustrated by Figure 6, this flow geometry is characterized by flow streamlines converging towards a circular cylinder.

For vertical well applications, this cylinder may represent the fully penetrating vertical well length (Figure 6 b) or be limited to the early time response for partially completed wells (Figure 6 a). Stimulation treatments as well as horizontal completion schemes enlarge the effective radius for the radial flow (Figure 6 c, e). Horizontal wells exhibit vertical radial flow behavior oriented normally to the well at early times (Figure 6 d). The proximity to a fault or other flow barrier, might yield a transient response indicating the radial flow to the well at early time, followed by radial flow to the actual well plus an image well across the boundary (Figure 6 f). A situation in which a well is adjacent to a sealing fault can mathematically be modeled by removing the fault, and placing an image well with a flow rate equivalent to the producing well in an equivalent distance.

Slope doubling is triggered by the succession of two radial flow regimes, where the slope of the second is exactly twice that of the first. Such a behavior typically arises from a sealing fault, but can also be attributed to permeability heterogeneity, particularly in laminated reservoirs.

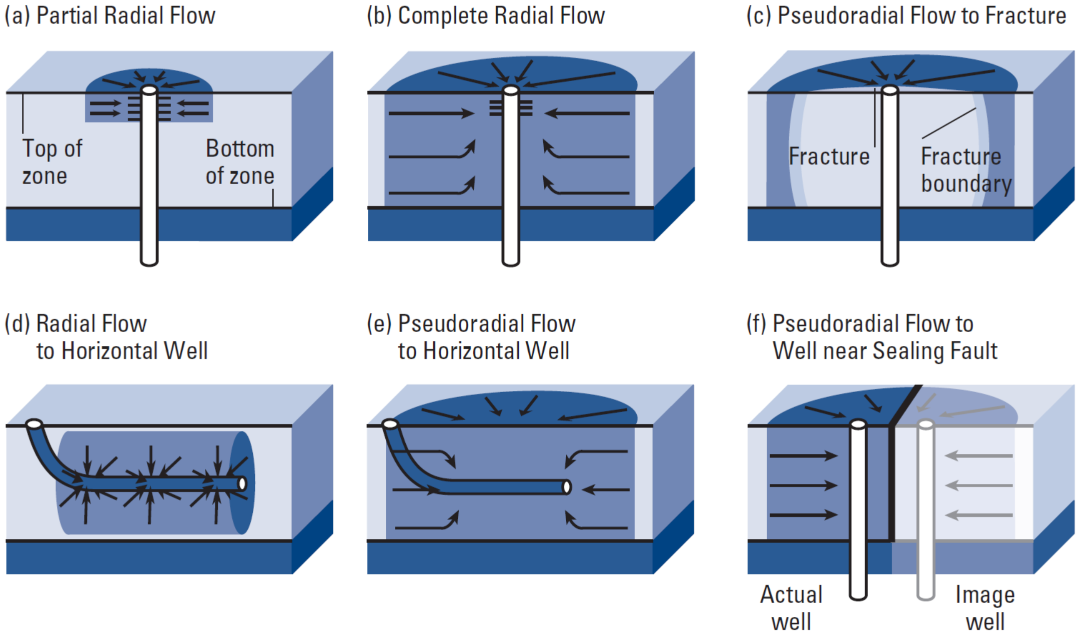

Figure 6 - Overview of possible manifestations of radial flow regimes [21]

Assuming an infinite acting homogeneous reservoir with a single-phase slightly compressible fluid and a constant production during the period Δt, the pressure during the radial flow regime is a function of the logarithm of the elapsed time as depicted in eq. (15) [22]. A semi-log plot of the BHP versus $\log \Delta t$ (referred to as MDH plot) yields a straight line with slope m after all WBS transitional effects are vanished, from which the permeability-thickness product (flow capacity) can be derived according to eq. (16).

$$\Delta p = 162.6\,\frac{q\,\mu\,B}{k\,h}\left[log\frac{k\,\Delta t}{\phi\,\mu\,c_t\,r_w^2} - 3.23 + 0.87\,S\right] \qquad (15)$$

$$kh = 162.6\,\frac{q\,\mu\,B}{m} \qquad (16)$$

As the production time increases, the well flowing pressure p_{wf} decreases and the circular drainage area of radius r_i, which is discussed in chapter 2.5, expands further into the reservoir. The concept applies vice versa for pressure build-up after shut-in.

2.4.3 Spherical Flow

Spherical flow denotes the flow geometry, where streamlines converge to a single point as depicted in Figure 7. This configuration is typical for partially completed wells (Figure 7 a). Hemispherical flow refers to a geometry, where an impermeable bed suppresses all-round fluid inflow, which is typical for partially penetrated formations (Figure 7 b) or partial completion near the upper or lower boundary. Both flow regimes show the same negative half-slope on the derivative plot, since pressure was found to change with the reciprocal of the square root of time $1/\sqrt{\Delta t}$ [23].

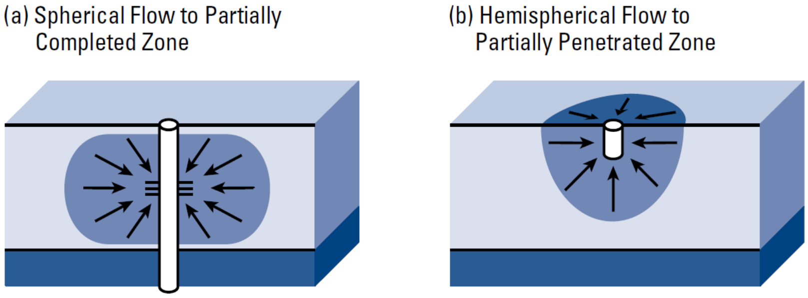

Figure 7 - Overview of possible manifestations of spherical flow regimes [21]

An analysis of this flow pattern yields the spherical permeability k_s, which is defined in eq. (17), and provides insights into permeability anisotropy. In conjunction with the horizontal permeability obtained from a radial flow period in another portion of the data, the vertical permeability might be determined. Furthermore, a complete analysis may provide a decomposition of the skin effect into its components indicating which portion is associated with limited entry and which portion is attributed to the actively flowing interval. A detailed analysis of the spherical flow regime can be found in [23].

$$k_S = \sqrt[3]{k_x k_y k_z} = \sqrt[3]{k_H^2 k_V} \qquad (17)$$

A well in partial penetration typically shows radial flow in front of the perforated interval, before the flow lines are established in both the horizontal and vertical directions, until top and bottom boundaries are reached. Hence, spherical flow can be observed before radial flow establishes over the entire formation thickness.

2.4.4 Linear Flow

Linear flow is characterized by strictly parallel flow vectors and exhibits a positive half slope in the derivative plot. Figure 8 illustrates the dominance of this flow pattern in vertically fractured (Figure 8 a) as well as horizontal drain holes (Figure 8 b). Furthermore, elongated reservoir geometries might impose linear flow patterns (Figure 8 d).

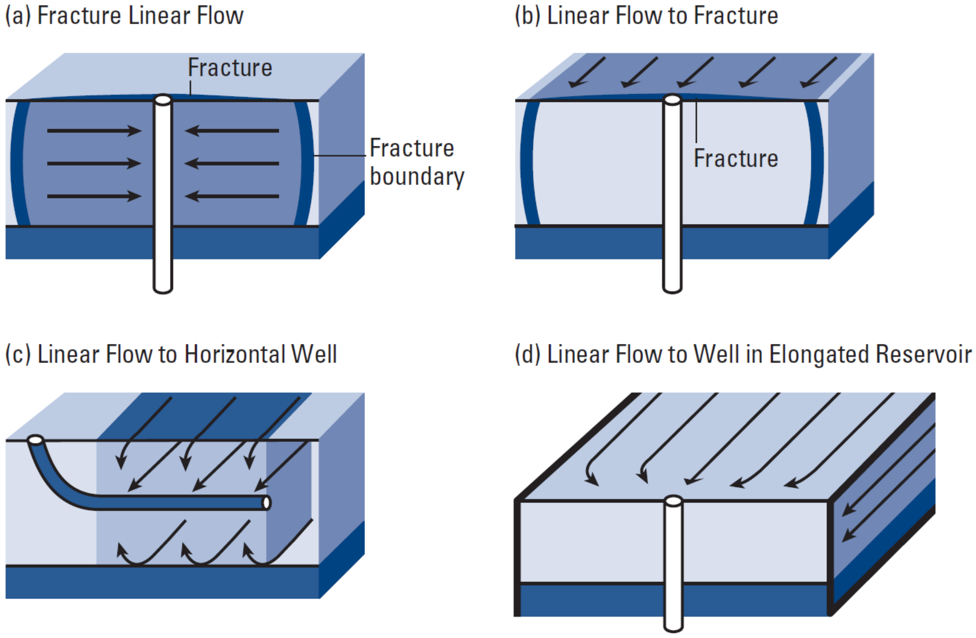

Figure 8 - Overview of possible manifestations of linear flow regimes [21]

Due to the perfect alignment of the streamlines in parallel planes, the parameters associated with the linear flow regime are the formation's permeability in the direction of the streamlines and the flow area normal to the streamlines. The fracture half-length of a vertically fractured well or the effective production length in case of a horizontal well can be obtained by incorporating the kh value determined by another flow regime to yield the width of the effective flow area. Combining linear with radial flow data can provide parameter estimations for both horizontal and vertical permeabilities within the bedding planes.

During linear flow within an infinite conductivity fracture, the pressure change was found to be proportional to the square root of the elapsed time [24] according to eq. (18), where x_f denotes the effective fracture half-length. A specialized Cartesian plot of pressure change Δp versus the square root of elapsed time $\sqrt{\Delta t}$ exhibits a characteristic straight line of slope m, which can be applied to yield the fracture half-length x_f based on the relationship given in eq. (19), in case the reservoir permeability is known from the analysis of the subsequent radial flow as discussed earlier.

$$\Delta p = 4.06 \, \frac{q\,B}{h\,x_f} \sqrt{\frac{\mu\,\Delta t}{\phi\,k\,c_t}} \tag{18}$$

$$x_f = 4.06 \, \frac{q\,B}{h\,m} \sqrt{\frac{\mu}{\phi\,k\,c_t}} \tag{19}$$

2.4.5 Bilinear Flow

The term bilinear denotes the simultaneous occurrence of two linear flow regimes oriented perpendicular to each other (Figure 9). This specific flow geometry is caused by the imposed pressure drop towards the well inside a fracture, which leads to a parallel alignment of the streamlines within the fracture, while at the same time streamlines in the formation also orientate in parallel to each other as they converge towards the fracture. Hence, the second linear flow regime establishes as the pressure drop along the fracture extension is not negligible.

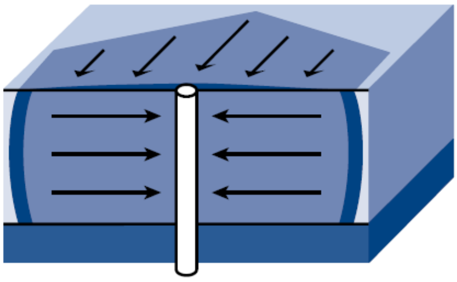

Figure 9 – Schematic of bi-linear flow regime [21]

This flow regime is primarily prone to hydraulically fractured wells with finite conductivity and shows a positive quarter-slope in the derivative plot. A specialized analysis is discussed in [25].

2.5 Radius of Investigation

The radius of investigation (ROI) is a concept, which relates the elapsed time Δt of well test to a certain distance away from the well, which is likely to be the origin of the recorded transient pressure signal. Hence, the ROI tentatively describes the distance that the pressure transient has moved into the formation after a given time. Several definitions have been proposed, however in general the ROI is defined with the relationship given by eq. (20) [13].

$$r_i = 0.029\sqrt{\frac{k\,\Delta t}{\phi\,\mu\,c_t}} \tag{20}$$

The ROI has a great significance for both planning and analyzing a well test. For a certain ROI needed, the minimum duration of a test can be estimated. If the ROI is set equal to the drainage radius of a certain well r_e, the required time to reach the reservoir boundaries and hence stabilized pseudo steady or steady state flow can be obtained.

It is important to note that this concept assumes a homogeneous and isotropic formation with a cylindrical shape. Pronounced heterogeneity significantly reduces the accuracy of obtained estimations. Furthermore, the idea of describing the investigated area by one characteristic length only, namely a radius, assumes radial flow with a cylindrical propagation into the reservoir. This concept fails for horizontal wells showing a distinct three-dimensional nature of the assessed reservoir volume.

2.6 Pressure Derivative

While the pressure curve refers to the pressure change associated with an abrupt production rate perturbation, the pressure derivative curve indicates the rate of pressure change with respect to time. Being highly sensitive to transient features originating from well and reservoir characteristics, which are often too subtle to be recognized in the pressure change response, makes the derivative curve the single most effective interpretation tool. However, both curves are always presented in the same plot on a log-log scale, since skin effects cannot be recognized and quantified from the derivative response alone.

The major advantage of pressure derivatives is their greater diagnosis and verification capability compared to the pressure change itself, while possessing the accuracy of straight line methods. By definition, the derivative is the slope of the pressure data plotted versus time on a semi-log scale. By defining the pressure derivative with respect to the natural logarithm of the elapsed time, the radial flow regime is emphasized and the derivative can be expressed as the time derivative multiplied by the elapsed time as shown in eq. (21).

$$\Delta p' = \frac{dp}{dln(\Delta t)} = \Delta t\frac{dp}{dt} \tag{21}$$

The computation of the pressure derivative $\Delta p'$ depends on the nature of the conducted test to ensure that the same features become identifiable from the final plot regardless of the type of data. Equations (8) and (9) depict the definitions for the pressure change for drawdown and build-up tests, respectively. The pressure derivative of drawdown test data is computed according to eq. (22) as the derivative of the pressure change with respect to the natural logarithm of the elapsed time interval Δt, where t_0 denotes the start of the transient data (eq. (23)).

$$\left(\frac{d\Delta p}{dln(\Delta t)}\right)_i = \frac{p(t_{i+1}) - p(t_{i-1})}{ln(t_{i+1}) - ln(t_{i-1})} \tag{22}$$

$$\Delta t_i = t_i - t_0 \tag{23}$$

The preferred derivative computation for build-up transient data is given by eq. (24) and introduces a simplified superposition time (Horner time) τ_i as defined by eq. (25). The derivation of these derivative equations as well as an evaluation on computational accuracy of each approach is elaborated in [26].

$$\left(\frac{d\Delta p}{d\tau}\right)_i = \frac{p(t_{i+1}) - p(t_{i-1})}{\tau_{i+1} - \tau_{i-1}} \tag{24}$$

$$\tau_i = ln\frac{t_p + \Delta t_i}{\Delta t_i} \tag{25}$$

The parameter Δt denotes the elapsed time since the start of the transient test and t_p represents the duration of production prior to the shut-in, which is calculated by dividing the cumulative production before the build-up test by the last flow rate immediately before shut-in. It has to be noted that several definitions of a build-up time correction have been proposed to account for the pressure response originating from the prior draw down period, with the effective Agarwal time (superposition time) and the Horner time (simplified superposition time) being the most common ones [13]. While effective Agarwal time results in a compression of the time scale, this compression becomes negligible for the Horner time method due to the numerator in eq. (25) being independent of actual production period.

The log-log presentation of the pressure derivative is the most reliable tool to distinguish predominant flow regimes in a pressure transient response. Each flow regime appears as a characteristic pattern according to the geometry of the flow streamlines in the tested formation. Hence, for each identified flow regime, certain well or reservoir parameters can be computed based on only the portion of the transient data exhibiting the specific pattern. The eight most common flow regime patterns observed in transient data are radial, spherical, linear, bilinear, and steady state flow as well as WBS (compression/expansion), dual-porosity or dual-permeability, and slope doubling behavior.

Wellbore Storage

During pure WBS, the pressure change Δp and its derivative become identical and follow a single straight line of unit slope on log-log scales as depicted in eq. (26).

$$\Delta p = \Delta p' = \frac{q\,B}{24\,C}\Delta t \tag{26}$$

Radial Flow

The derivative of an established infinite-acting radial flow regime is constant as shown in eq. (27), which provides a clear identification on a log-log plot, although this regime does not produce any characteristic shape in the pressure change curve. The derivative response is even more pronounced in dimensionless terms, where radial flow can be distinguished by a characteristic stabilization at a pressure value of 0.5 (eq. (28)). The dimensionless pressure p_D has been introduced by eq. (4).

$$\Delta p' = 70.6 \, \frac{q \, \mu \, B}{k \, h} \tag{27}$$

$$p_D' = \frac{dp_D}{d \, ln(t_D/C_D)} = 0.5 \tag{28}$$

Other Characteristic Flow Regimes

As discussed in chapter 2.4, except the radial flow, all different flow regimes experience a pressure change as a function of the elapsed time to the power of $1/n$. A generalized formulation of this behaviour is shown in eq. (29) and differentiated with respect to the natural logarithm of elapsed time in eq. (30).

$$\Delta p = A \, (\Delta t)^{1/n} + B \tag{29}$$

$$\Delta p' = \frac{dp}{d \ln \Delta t} = \frac{A}{n} \, (\Delta t)^{1/n} \tag{30}$$

$$\log \Delta p' = \frac{1}{n} \log \Delta t + const \tag{31}$$

Equation (31) represents the logarithmic form of the generalized pressure derivative equation. As it can easily be obtained, the derivative will plot as straight line with slope $1/n$ in a log-log coordinate system. Table 3 provides an overview of characteristic slope values and associated flow regimes.

Table 3 – Characteristic pressure derivative slopes of various flow regimes in the log-log plot

$1/n$	**Flow Regime**
1	WBS, pseudo steady state
1/2	Linear flow
1/4	Bi-linear flow
-1/2	Spherical flow

The flow regime identification tool, as depicted in Figure 10, can be used to differentiate these eight common subsurface flow regimes on log-log plots. A constant or flat derivative represents radial flow, while spherical flow, which might arise from a limited entry well configuration, possesses a characteristic negative half-unit slope. WBS effects exhibit a typical unit slope, which with progressing time bend over in a characteristic hump shape. Linear flow, as observed by flow to a high conductivity fracture or a long horizontal well, shows a half-unit slope, while bilinear flow can be observed with a quarter-unit slope. In build-up and fall-off tests, a steeply falling derivative may represent either pseudo steady or steady state. A rather smooth declining trend in the derivative response is likely to be associated with three-dimensional flow effects as observed in wells, where only a small fraction is well connected to the formation.

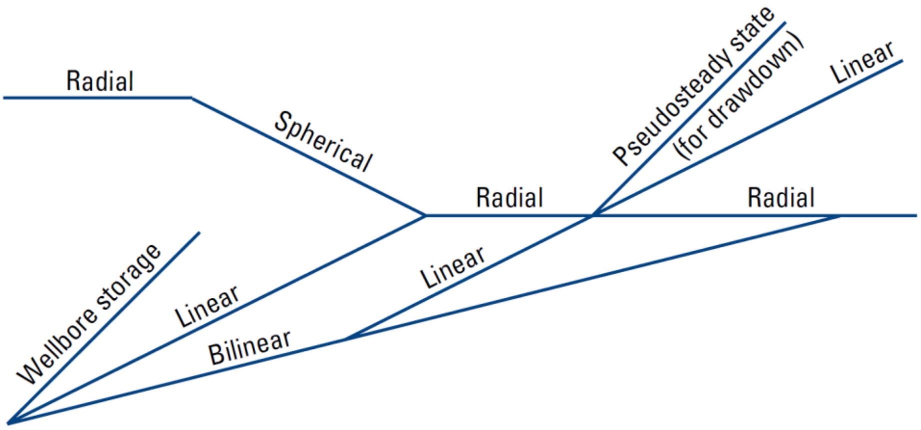

Figure 10 - Flow regime identification tool [12]

Due to the fact that the derivative is often noisy and information might be lost by over-smoothening the data, it is recommended practice to fine tune derived parameters with established standard analyses or to at least cross-check obtained values from derivative analysis.

3 Pressure Transient Analysis for Horizontal Wells

Although, pressure transient behavior observed in a horizontal well test is considerably more complex than in a conventional vertical well due to its three-dimensional nature, its thorough description has received substantial attention as the result of a significant increase in horizontal drilling activity in the recent years.

In comparison to the single radial flow regime of a conventional vertical well, three different flow geometries may occur after WBS effects have vanished. An overview of these different phases is provided in Figure 11. The early time response is characterized by radial flow in the vertical plane towards the drain hole and obtainable as first plateau on the log-log pressure derivative representation. This period is referred to as early-time pseudo radial flow due to the elliptical flow pattern triggered by the vertical to horizontal permeability anisotropy. As soon as the transient reaches the upper and lower no-flow boundaries, the flow pattern transitions into linear flow towards the well within the horizontal plane. Denoted as intermediate or middle time linear flow this period exhibits a half-slope trend in the derivative plot. As the transient propagates deeper into the reservoir, despite the extended horizontal length, the well can progressively be understood as a point source compared to the accessed reservoir volume. This yields a second plateau in the derivative curve due to the transition into the late time radial flow regime in the horizontal plane.

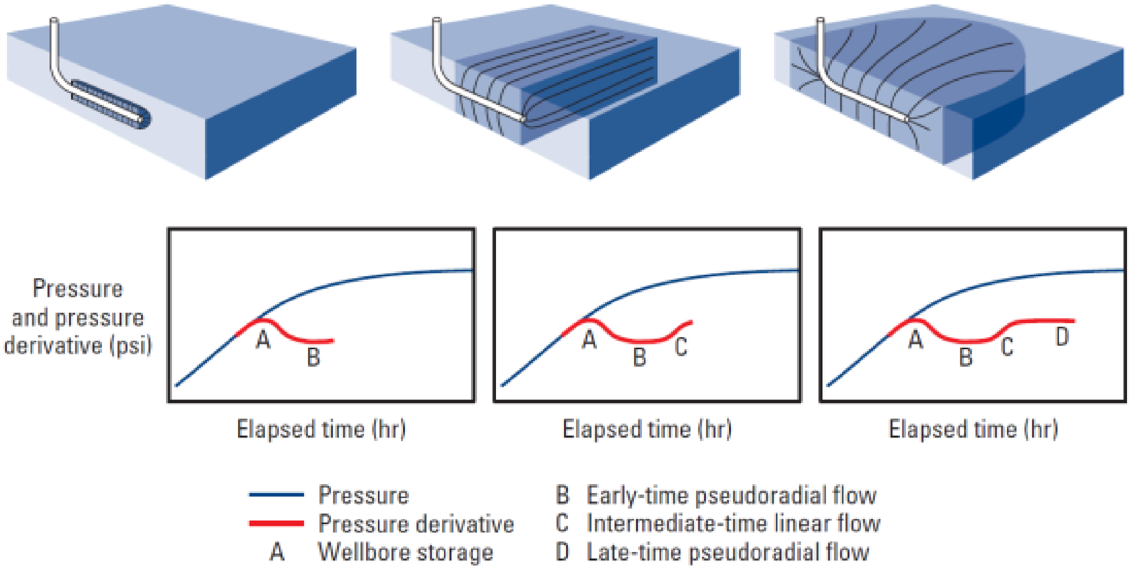

Figure 11 – Subsequent flow regimes of a pressure transient test in a horizontal well [12]

While the early time radial flow provides insights into the mechanical skin factor and the geometric average of vertical and horizontal permeability, the middle time linear flow is used to estimate the effective well length, given the horizontal plane can be considered isotropic. The late time radial flow reveals the average permeability in the horizontal plane as well as the total skin factor of the well configuration. Three parameters significantly affect the transient behavior of a horizontal well test, which are the effective well length, the formation thickness, and the ratio of horizontal to vertical permeability.

It has been found that both thick formations and a high contrast between horizontal permeability k_H and vertical permeability k_V are likely to suppress the establishment of early time radial and middle time linear flow [12]. Furthermore, first pseudo radial flow, which is the only source of formation damage information, is often masked by the unavoidably large WBS effect in horizontal wells. This emphasizes the need for full control of the downhole environment with simultaneous measurements of flow rate and either pressure or downhole shut-in to assure successful interpretation.

Deriving the effective well length solely from transient analysis has been found very challenging due to the superposition of various interlinked effects on the pressure data. Therefore, supplementing the transient data with flow profile measurements along the well trajectory facilitates identifying the producing zones and determining the effective flowing interval. Furthermore, flow profile information is particular valuable to recognize and localize crossflow, which seriously distorts interpretability of recorded transient data. Since crossflow is more likely to occur during build-up tests, drawdown tests are recommended for producing fields where pressure differentials have already developed and may cause crossflow.

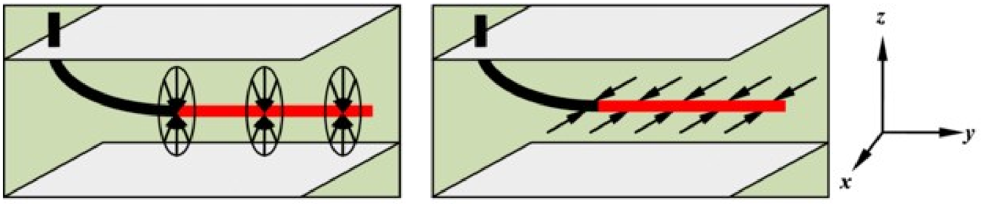

(a) early radial flow (b) early-linear flow

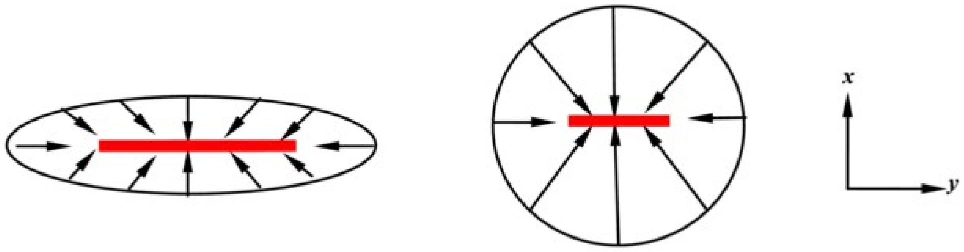

(c) elliptical flow (d) late pseudo-radial flow

Figure 12 – Detailed depiction of dominant flow regimes in horizontal wells [27]

In the following each flow regime will quickly be described together with applicable computations to determine relevant reservoir characteristics. The calculation of skin has been discussed elsewhere [13] [28] and will be neglected here, due to its limited value for the subsequent discussion of conducted analyses. Relevant geometrical parameters in the following equations are defined in Figure 13. The well is strictly horizontal with a penetration half-length L_w and possesses infinite conductivity with the reservoir being assumed homogeneous.

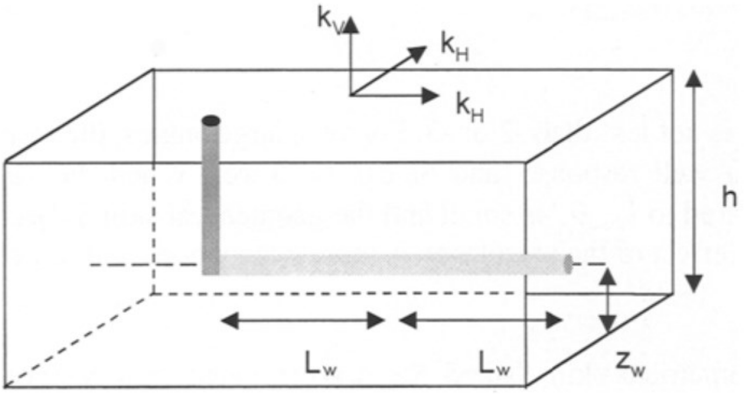

Figure 13 – Geometrical model description for a horizontal well [13]

3.1 Early Time Radial Flow

The early time radial flow is also referred to as radial flow in the vertical plane and behaves identically with infinite-acting radial flow as observed in a vertical well penetrating the entire reservoir thickness. The pressure transient propagates radially away from the wellbore, while not being influenced by any boundary effects yet. The time at which a first boundary is reached, represents the end of the early time radial flow regime.

Its analogy to the radial flow in a conventional vertical well allows for the principle applicability of eq. (15) to describe the BHP evolution during the test for both drawdown and build-up cases. However, the permeability term has to be adjusted to represent the geometric mean of vertical and horizontal permeability according to the observed flow geometry.

During the vertical flow regime, the pressure difference can be expressed by eq. (32) [13]. It can be obtained that the product of the effective wellbore half-length L_w and the geometrically averaged permeability can be derived from a semi-log pressure analysis. Equation (33) states the relationship typically applied for the appropriate analysis with m denoting the slope obtained from the semi-log plot.

$$\Delta p = 162.6\,\frac{q\,\mu\,B}{2\sqrt{k_V k_H}L_w}\left[\log\frac{\sqrt{k_V k_H}\,\Delta t}{\phi\,\mu\,c_t\,r_w^2} - 3.23 + 0.87S_w - 2\,log\frac{1}{2}\left(\sqrt[4]{\frac{k_V}{k_H}} + \sqrt[4]{\frac{k_H}{k_V}}\right)\right] \quad (32)$$

$$\sqrt{k_V k_H}\,L_w = 81.3\,\frac{q\,\mu\,B}{m_{VRF}} \quad (33)$$

3.2 Intermediate Time Linear Flow

The intermediate-time linear flow is dominated by fluid movement in a horizontal plane perpendicular to the orientation of the horizontal well and identical to behavior observed in vertically fractured wells. The end of this flow geometry is reached when considerable flow in the y-direction (Figure 12) starts to contribute. High vertical permeability accelerates the clear establishment of this flow geometry with dominating also the early time behavior as limiting case for permeability ratios greatly larger than unity.

During the linear flow regime, the pressure changes with the square root of the elapsed time as stated by eq. (34). The analogy to linear flow within a fracture proposes the quantitative analysis based on a Cartesian plot of Δp versus $\sqrt{t}$ yielding a straight line for parameter determination. The obtained slope m can then be applied to yield the product of horizontal permeability perpendicular to the well with effective wellbore length according to eq. (35). During PTA it is often assumed that permeability behaves isotropically, so that the observed permeability is treated as horizontal permeability k_H. Strictly speaking, k_x is seen during this flow regime, considering the coordinate system provided in Figure 12.

.

$$\Delta p = 8.128 \frac{q\,B}{2\,L_w\,h} \sqrt{\frac{\mu\,\Delta t}{\phi\,c_t\,k_H}} + \frac{141.2\,q\,B\,\mu}{2\sqrt{k_V k_H} L_w} S_w + \frac{141.2\,q\,B\,\mu}{k_H h} S_z \tag{34}$$

$$k_H\,L_w^2 = 16.52 \left(\frac{q\,B}{m_{LF}\,h}\right)^2 \frac{\mu}{\phi\,c_t} \tag{35}$$

3.3 Late Time Radial Flow

This flow regime is also known as horizontal radial flow (HRF) and describes a geometry with considerable flow across the tips of the well. With progressing time, the horizontal length of the drain hole becomes sufficiently small compared to the lateral extent of the pressure transient, so that streamlines from all directions converge towards the wellbore and a point source approximation becomes valid. The end of this flow period is marked by reaching the lateral boundaries of the reservoir.

Similar to the early time radial flow evaluation, eq. (15) can be applied to yield the permeability thickness product representative for the prevalent flow geometry. Using the well half-length L_w as the reference for semi-log analysis of horizontal radial flow, pressure changes with time according to eq. (36). The slope m of pressure change Δp versus time t in a semi-log plot provides the basis for the qualitative analysis shown in eq. (37). The characteristic length is the height of the reservoir h and the observed permeability is the horizontal permeability k_H, which is often approximated by the geometric mean of k_x and k_y.

$$\Delta p = 162.6\,\frac{q\,B\,\mu}{k_H\,h}\left[\log\frac{k_H \Delta t}{\phi\,\mu\,c_t\,L_w^2} - 2.53\right] + \frac{141.2\,q\,B\,\mu}{2\sqrt{k_V k_H} L_w} S_w + \frac{141.2\,q\,B\,\mu}{k_H h} S_z \qquad (36)$$

$$k_H\,h = 162.6\,\frac{q\,\mu\,B}{m_{HRF}} \qquad (37)$$

As a result of limited standard test durations, the late time radial flow is not always present in the recorded data, which complicates comprehensive analyses significantly [13].

3.4 Interpretation Procedure

The increased complexity compared to vertical wells renders the applicability of standard type curves. Instead, derivative log-log plots are used to identify characteristic flow regimes, while the analysis is conducted by generating pressure and derivative responses with a computer or based on specialized straight line plots.

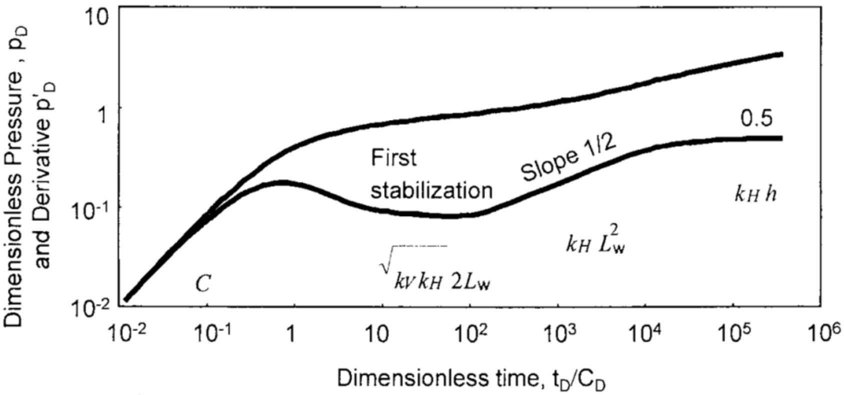

Figure 14 – Characteristic response of dimensionless pressure and pressure derivative versus dimensionless time for a horizontal well [13]

Having identified all three flow regimes discussed earlier from the pressure derivative response, parameters can be determined based on specialized analyses. After matching time and pressure, the early time unit slope straight line and the level of final pressure stabilization yield the wellbore storage coefficient C and the horizontal permeability thickness product $k_H h$, respectively. With an approximate formation thickness h as additional input, the equivalent isotropic horizontal permeability k_H can be estimated. A match of the half-unit slope straight line at intermediate time linear flow reveals the product of horizontal permeability and effective well half-length squared $k_H L_w^2$. According to the prior determined k_H, the effective length of the well can be assessed. Having predicted both L_w and k_H, the permeability ratio k_V/k_H as well as mechanical skin s become retrievable from the first derivative stabilization, which corresponds to the permeability-thickness product $2\sqrt{k_V k_H} L_w$ with the average permeability in the vertical plane k_V. An overview is provided in Figure 14. The early time radial flow will stabilize at a lower level than the late time pseudo-radial behavior only if either the ratio of vertical to horizontal permeability $k_V/k_H \gg 1$ or the ratio of effective horizontal well length to reservoir thickness $L_w/h \gg 1$ significantly exceeds unity.

In case of distinct WBS, the vertical radial flow will be masked. Hence, the permeability anisotropy k_V/k_H cannot be determined. In case the late time pressure derivative stabilization is not reached, horizontal permeability k_H estimations become very unreliable. In consequence, a consistent description of the effective horizontal well length from the middle time response becomes very questionable.

3.5 Model Limitations

Actual well examples indicate that the assumed ideal configuration described in Figure 13 is often too simple. The majority of horizontal drain holes are neither perfectly straight, nor parallel to the upper and lower boundaries. On the contrary, several oscillations over the formation thickness are not unlikely. Furthermore, it has been repeatedly reported that only a few segments of horizontal wells considerably contribute to hydrocarbon production, which results in a difference between actual and effective well length. An increasing pressure gradient in the wellbore violates the infinite conductivity hypothesis and finite conductivity behavior might dominate pressure transients. It has to be noted, that horizontal well solutions are approximate, due to their derivation based on the line-source assumption.

It has been shown that effective well length and average vertical permeability k_V from PTA are significantly distorted if the basic horizontal well model is applied to describe more complex well or reservoir configurations [13]. While k_V is frequently underestimated for complex wellbore conditions, layered systems have shown an inverse effect.

4 Polymer Injection

Initially, crude oil is displaced from porous sandstone or carbonate rock formations into the wellbore and up to the surface under its own reservoir energy. After depletion of these natural occurring driving forces, such as gas cap drive, water drive due to aquifer influx, or gravity drainage, external fluids are injected for pressure maintenance and displacing hydrocarbons towards the production wells. The most common technique applied during this secondary recovery stage is water flooding. After secondary oil recovery processes have been exhausted, a total recovery of as low as one third of the original oil in place (OOIP) is not uncommon [29]. EOR methods aim to recover the entire movable OOIP. Polymer flooding has established as one of the most successful EOR methods, especially for medium and high viscous crude oils. The injection of polymer solutions reduces the mobility of the aqueous phase and increases volumetric sweep efficiency by increasing the stability of the flood front. Enhanced mobility control origins from two main mechanisms: (1) increased viscosity and (2) reduced permeability of the polymer augmented aqueous phase. The mobility ratio defined by eq. (11) is one of the key design factors determining the efficiency of a polymer injection project. The lower the mobility ratio, the more efficient is the polymer flood.

The position of the polymer front is crucial in determining the swept reservoir volume. It is desired to maintain a stable flood front to avoid early break through and maximize recovery. The increased viscosity of polymer solution helps to reduce the disproportional injection into high permeable zones, diverting the flow into lower permeable regions. By plugging high conductivity zones at the injector, performance is improved by producing from lower permeable zones.

4.1 Rheology of Polymer Solutions

Polymers usually applied in the oilfield range from water soluble polyacrylamide and xanthan gum to associative polymers. On the contrary to pure water, polymer solutions exhibit non-Newtonian rheological behavior characterized by both shear-thinning and shear-thickening depending on the shear rate. Hence, rheological properties measured at the surface differ significantly from in-situ polymer properties and contradict their direct applicability to predict pressure-to-flow relationships in porous media. However, there is agreement between lab experiments, numerical simulation, and field application results that the influence of polymer rheology reaches far beyond impacting only polymer injectivity. On the contrary, polymer rheology dominates the entire oil displacement process as well as the final recovery of a polymer flood project. This supports ongoing effort to yield a better understanding of in-situ polymer rheology in porous media [10] [29].

Polymer rheology primarily depends on polymer type, molecular weight, concentration, and salinity of the water it is exposed to. During injection into a porous media, polymer solutions experience changing flow velocities, which are related to shear rates, and will exhibit different viscosity properties at different locations within the reservoir. Being furthermore governed by reservoir permeability, tortuosity and polymer retention behavior, makes polymer flow through porous media a complex topic, of which no comprehensive understanding has yet been attained. Although, polymer viscosity can easily be measured at reservoir conditions, its apparent equivalent within the reservoir remains unknown due to the mentioned effects.

4.2 Polymer Viscosity

As non-Newtonian fluids, polymer solutions do not exhibit a linear relationship between shear stress and shear rate. As depicted in Figure 15 this results in a shear rate dependent viscosity. Furthermore, polymer degradation due to excessive shear rates in the near wellbore region during injection is of major concern. Although the effect of unsnagging polymer chains due to elongation in shear flow is partially reversible below a critical shear rate, this effect induces a shear rate history dependent behavior. To account for a spatially varying viscosity within in the reservoir, a macroscopic in-situ apparent viscosity μ_{app} is often used to design polymer floods and is defined based on Darcy's law for an average flow rate in the field q by eq. (38) [29].

$$\mu_{app} = k\frac{A\ \Delta p}{q\ L} \tag{38}$$

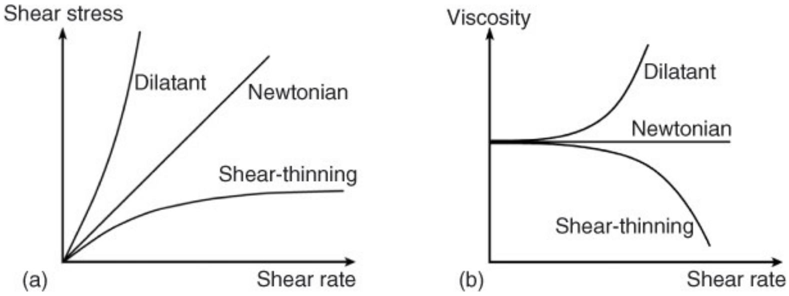

Figure 15 – Non-Newtonian fluid viscosity classification [30]

While apparent viscosity μ_{app} describes macroscopic rheology based on Darcy's law, effective viscosity μ_{eff} refers to the general definition of viscosity as the ratio of shear stress over shear rate on a microscopic scale for a single capillary channel based on Poiseuille's law. A clear distinction between effective and apparent viscosity needs to be maintained, especially when porous media is described by capillary bundle models. While the apparent viscosity can be understood as an average polymer property, local flow and oil displacement capabilities are governed by the effective viscosity in each capillary. Nevertheless, as the effective viscosity cannot be controlled on a local scale, an accurate apparent viscosity determination is essential to design a stable polymer injection by adjusting the concentration of the injected polymer stream at surface.

The apparent shear rate, a polymer is exposed to, during its flow through porous media depends on permeability, porosity, and actual fluid velocity. Several representative models have been proposed to calculate apparent shear rate and are summarized in [29]. These relationships form the basis to couple apparent viscosity and Darcy velocity to yield applicable approaches to incorporate non-Newtonian behavior into reservoir simulators.

4.3 Polymer Retention

Core flood tests conducted with polymer solution revealed a permanent permeability reduction of the core [31]. This observation is the effect of polymer retention due to mechanical trapping, polymer adsorption on solid surfaces, and hydrodynamic retention. Mechanical trapping describes the influence of smaller pore throats getting blocked by flowing large polymer molecules. Hydrodynamic retention refers to polymer molecules becoming temporarily trapped in stagnant flow regimes and is more significant in low permeability formations. The major cause of polymer retention is attributed to adsorption effects, with physisorption being more pronounced than chemisorption [32]. Besides permeability reduction with respect to the aqueous phase, adsorption of polymers results in a lag of the polymer injection front and the generation of a stripped water bank. Since adsorption of the polymer from the leading edge of the polymer bank can cause a deterioration of the entire slug, reliable information regarding the magnitude of adsorption is essential to optimize the slug size. The magnitude of polymer adsorption depends on the polymer type, its concentration, and rock surface. Experimental studies furthermore indicate that the adsorption behavior is strongly affected by salinity and solution pH value [33].

Polymer adsorption causes a characteristic pressure build-up, which is often observed during polymer flooding, even after the polymer solution itself has been displaced by brine. A resistance factor has been introduced to describe this effect with a corresponding reduction of permeability to the aqueous phase. Due to negligibly low polymer desorption rates, this reduction in permeability is mostly assumed irreversible and will dominate subsequent water flooding. Hence, the RRF is defined as the ratio of mobility of the aqueous phase before and after the polymer flood as given by eq. (39). It has been shown that polymer floods significantly alter the permeability with respect to the aqueous phase, while the relative permeability for the oil phase remains practically unaltered. The relationship between apparent and effective polymer viscosity is stated by eq. (40).

$$R_{rf} = \frac{\lambda_w^{before\ polymer\ contact}}{\lambda_w^{after\ polymer\ contact}} = \frac{k_w^{before\ polymer\ contact}}{k_w^{after\ polymer\ contact}} \tag{39}$$

$$\mu_P = \frac{\mu_{app}}{R_{rf}} \tag{40}$$

In water-wet reservoirs, the oil phase flows inside the pores while the water occupies the annulus between the pore walls and the oil-water interface [34]. As a certain fraction of the available pore space is inaccessible for relatively large polymer molecules compared to the pore sizes, an acceleration of the polymer solution can be observed. This increased polymer velocity tends to compensate the effect of polymer retention to a certain extend. Decreased permeabilities and higher flow velocities further lead to higher shear rates, which favor the injection of shear-thinning polymer solutions.

5 Methodology

In order to investigate the influence of various geological as well as dynamic model parameters on the pressure response behavior of a fall-off test, reservoir models with respective properties have been created in Petrel (Schlumberger) and simulated using ECLIPSE 100 (Schlumberger). The simulated BHP profiles have been exported and evaluated with the PTA software package Saphir (KAPPA Engineering). Subsequently, the consistency between the imposed reservoir model in Petrel and the interpreted model using Saphir has been assessed with regards to specific parameters, in order to evaluate the applicability of PTA to yield a reliable reservoir description under various conditions.

Since the ultimate objective of this thesis is the enhancement of the existing probabilistic workflow to evaluate the potential of an extension of the polymer pilot in the 8 TH of the Matzen field, all considered models have been set up according to real geological insights and reported fluid characteristics; however, strong simplifications regarding heterogeneity and property distribution have been implemented in order to investigate various aspects of reservoir behavior individually.

5.1 Geological Modelling

The 8 TH reservoir consists of sandstone deposited in a shallow marine environment with porosities ranging from 20 % to 30 % and an average permeability of 500 mD, spanning a range between 10 mD and 3000 mD. The reservoir is located at a depth of approximately 1150 m and possesses a net thickness of about 20 m. A weak aquifer has been identified at the northern edge of the reservoir.

5.2 Fluid Modelling

The initial reservoir conditions are reported as 120 bar initial pressure and an average temperature of 50 °C. The reservoir contains oil with a density of about 20 °API and an in-situ viscosity of approximately 19 cP. The formation water shows a salinity in the order of 20000 ppm. Close attention has to be paid to ensure consistency between the fluid models implemented in Eclipse and Saphir. While Saphir uses constant fluid properties for its analytical interpretation, pressure tables are required for numerical simulation. Hence, an initial screening of available input options and correlations in both software packages has been necessary.

5.3 Well Test Design

All simulated well tests start with an initialization period during which the injection well is shut-in, in order to assure successful equilibration of the reservoir model before conducting the test. In case model initialization has not yielded a state of equilibrium, inter-cell flow will be observed during this simulation period. In case of successful initialization, the well is opened and water injection starts at a constant rate for a predefined period of time. The injection duration has been adjusted to yield a stable pressure plateau for pure water injection cases before the well is shut-in. Depending on the case to be investigated, tracers and polymer are added to the injection stream. The flow rate of each test is adjusted to yield a sufficiently high pressure increase to ensure meaningful test interpretation, while limiting the risk of exceeding the formation parting pressure. This pressure constraint has no superior relevance for theoretical test interpretation; however, plays a crucial role for the extrapolation of the study outcomes to real operations, since formation fracturing has not been investigated as part of this thesis.

Since the shape of the pressure transient curve is affected by the reservoir's injection and production history, respectively, only single injection periods with a subsequent shut-in have been considered to ensure consistent interpretation. As each change in production rate generates a new pressure transient passing into the reservoir merging with the previous pressure effects, the observed pressures at the wellbore represent a superposition of all these pressure changes.

After injection the well is shut-in for an extended period of time until pressure equilibration is reached. In order to provide sufficient resolution of the simulated gauge data, logarithmic time stepping has been used for the simulation of the shut-in period. As finer grid resolution was found to be very sensitive at early times, when the well test evaluates the near the wellbore region, Local Grid Refinement (LGR) has been implemented into some of the screened models [28].

In order to maximize the range of interpretable data from the simulated well test, the wellbore volume has been set to a marginal value resulting in negligible WBS effect. WBS is disregarded due to its distorting effects on the analysis of important features as described earlier. Although this approach might not be very realistic, it provides valuable insights especially in the early time which will normally be masked in observed data. Similarly, all wells are assumed to possess zero skin.

5.4 Pressure Transient Analysis

The first and very crucial step during PTA is the identification of individual flow periods within the data set. The exact start and end of each flow period has to be specified. According to the nature of the pressure disturbance propagation, a logarithmic sampling rate is preferred and has been specified in the Eclipse input.

Due to the primary focus on polymer injection in horizontal wells, an analysis with composite models, which have extensively been applied to model EOR processes, is hardly applicable. The sequence of various flow regimes with progressing time would require a reliable estimation of front propagation in all three dimensions, which is extremely cumbersome. Therefore, all pressure transient studies in Saphir have been conducted as single domain analyses with water as the testing fluid. Necessary changes to this set-up will be discussed in the according chapters.

The general procedure for horizontal wells starts with matching the late time response to yield the horizontal permeability, followed by the analysis of the middle time linear flow to obtain the effective wellbore length and eventually estimating permeability anisotropy from early time behavior.

6 Single-Phase Reservoir Models

In a first step, a single-phase water model has been investigated. Starting from a very simplistic homogeneous case, an increasing number of characteristic geological features have been incorporated. This increasing level of geological complexity comprises different porosity and permeability distributions as well as high and low permeability streaks in all principal directions. Table 4 summarizes all relevant model parameters, which have been kept constant throughout all simulations. It has to be mentioned that fluid properties are specified as constant values in Saphir, but are treated as pressure tables in Eclipse. The input for Saphir corresponds exactly to the values provided in Table 4, while Eclipse inputs have been adjusted to match these values at the reference pressure of 120 bar. Typical pressure build-ups due to water injection have been observed in the order of 5 bar to 10 bar. Excerpts of the used PVT tables can be found in Table 39 in the appendix. Parameters, which have been modified for different cases will be detailed at the appropriate point further below.

Table 4 - Reservoir and fluid properties used in simulation for the single-phase water model

Parameter	**Value**
Reservoir pressure, bar	120.0
Reservoir temperature, °C	50.0
Net reservoir thickness, m	20.0
Water density, kg/m^3	1013.0
Water viscosity, cP	0.55
Water formation volume factor, -	1.007
Rock compressibility, bar^{-1}	$3.0 \cdot 10^{-5}$
Water compressibility, bar^{-1}	$4.0 \cdot 10^{-5}$
Total system compressibility, bar^{-1}	$7.0 \cdot 10^{-5}$
Well radius, m	0.09525

The primary objective of this initial step was to study the influence of certain geological features on the recorded pressure signal and the applicability of PTA to evaluate them. It could be shown that PTA in capable of obtaining reservoir permeability with reasonable accuracy for both vertical and horizontal wells.

6.1 Model Validation

In order to verify the principal applicability of the proposed workflow of generating synthetic pressure test data using reservoir simulation and subsequently tracing back the imposed properties by PTA, a simple homogeneous model has been analyzed for both a vertical and a horizontal well. Permeability and porosity have both been assumed homogeneous and isotropic, with horizontal and vertical permeability being equal. The primary focus has been to obtain the permeability defined in the reservoir model using PTA. Table 5 provides an overview of the investigated permeability range.

Table 5 – Permeability range and porosity used for model validation

Parameter	**Value**
Permeability, mD	100 … 900
Porosity, -	0.25

Furthermore, the influence of various gridding schemes on the simulated BHP response has been investigated to assure the interpretation of meaningful results without distortion of numerical artefacts as a result of discretization. For the horizontal well case a boundary screening has been conducted to exclude superposition of the late radial flow pressure response with early boundary effects.

6.1.1 Vertical Well Model

Initially, a fully penetrating vertical well has been implemented in the center of a homogenous reservoir domain with isotropic horizontal as well as vertical permeability of 500 mD. The model has been initialized with reference pressure of 120 bar at a depth of 1160 m. The top of the reservoir is located at a depth of 1150 m. The negligible WBS effect specified in the simulation translates the surface shut-in at the injector into a bottom hole shut-in, increasing the range of interpretable data. Table 6 summarizes relevant model characteristics as well as the testing schedule used for the initial vertical well screening.

Table 6 – Model characteristics and testing schedule for the initial single-phase homogeneous vertical well model

Parameter	**Value**
Reservoir depth, m	1150
Dimension in X, m	1050
Dimension in Y, m	1050
Discretization in X, m	2
Discretization in Y, m	2
Discretization in Z, m	1
Permeabilities k_H and k_V, mD	500
Initialization duration, d	1
Injection duration, d	1
Shut-in duration, d	4
Water injection rate, scm/d	500

Figure 16 depicts the matched log-log pressure response, which can be characterized by a well-established radial flow stabilization followed by a clear constant pressure boundary indication. As expected, WBS effects are negligible. Relevant results of the PTA are summarized in Table 7. As one can see, both total permeability and the distance of the aquifer (the well is located in the middle of a square) can be obtained with reasonable accuracy. The initial reservoir pressure of approximately 119 bar corresponds exactly to the reference pressure specified at the middle of the formation at a depth of 1160 m reduced by the hydrostatic pressure of the water column between the midpoint of the most upper perforated reservoir cell and the reference depth of 1160 m. This matches perfectly the definition of the BHP used in Petrel, which reports the simulated pressure at the cell containing the very first perforation along the well path as BHP.

Table 7 - PTA results for initial vertical well model with a permeability of 500 mD

Parameter	**Value**
Permeability, mD	495
Skin, -	0
Reservoir pressure, bar	119.06
Boundary distance (rectangular model), m	525

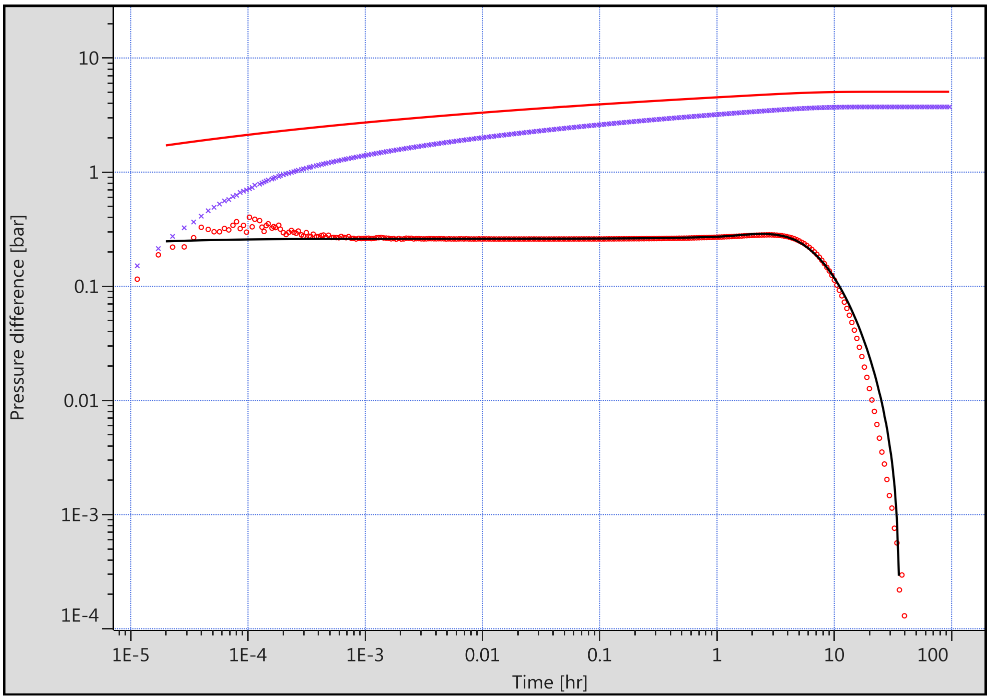

Figure 16 – Matched log-log plot of the initial vertical well model

While the pressure derivative can be matched almost perfectly, the pressure behavior itself is far off the calculated model response, while both the semi-log plot and the history plot also indicate close agreement between the simulated data and analytical model response using Saphir (Figure 17).

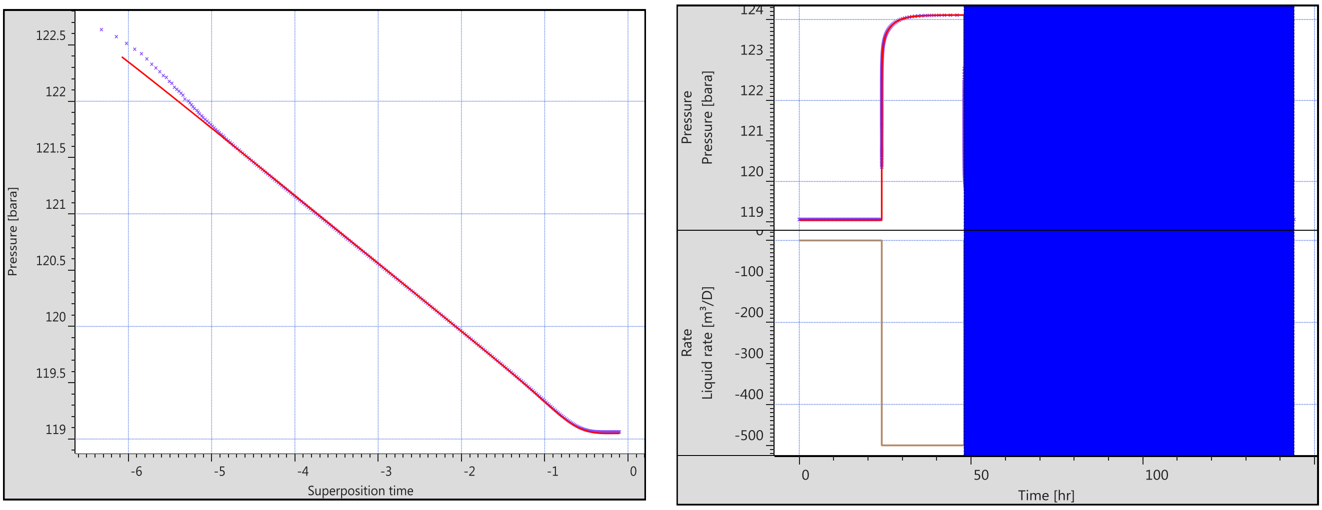

Figure 17 - Semi-log (left) and history (right) plot of the initial vertical well model

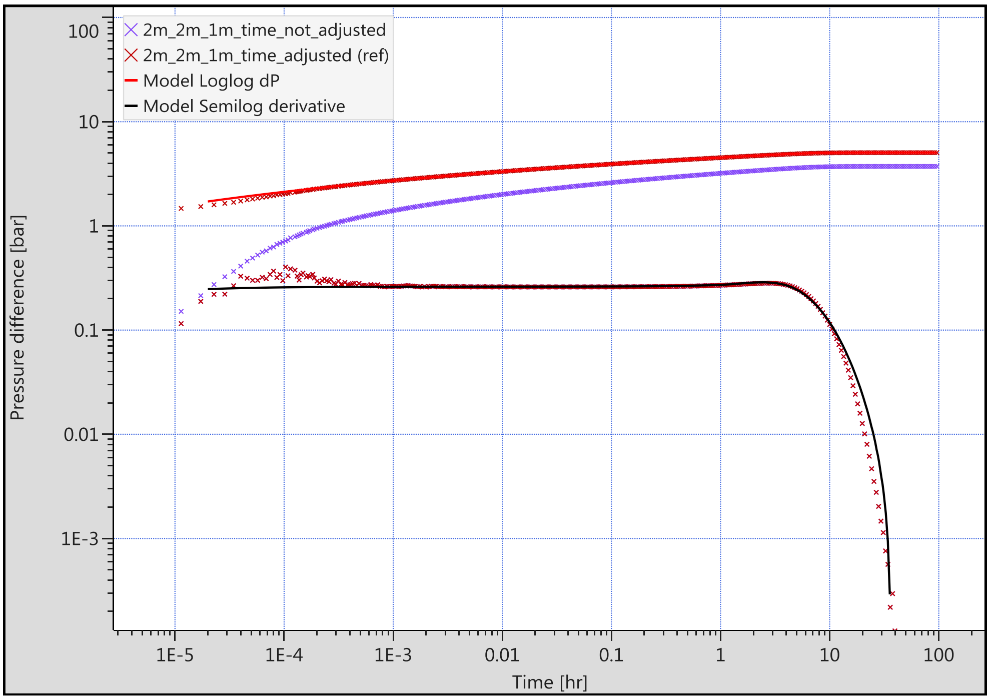

Figure 18 - Log-log plot of original and time adjusted BHP response of the initial vertical well model

Analyzing the pressure series exported from Petrel revealed a misalignment of the initial shut-in pressure between Petrel and Saphir to cause this discrepancy: Unfortunately, Petrel is not capable of reporting BHP according to a predefined highly-resolved time stepping as required for early time recordings during well tests, but exports the data based on a time series, which only approximates the requested reporting frequency. As a result, the first BHP data point after shut-in has erroneously been assigned as initial reservoir pressure before shut-in. Adjusting this inconsistency manually yields a pressure response in perfect agreement with the model determined by PTA (Figure 18). Both semi-log and history plot are unaltered by this marginal adjustment.

As it can be obtained from Figure 18, the pressure at the beginning of the shut-in period significantly affects the shape of the pressure difference plots, while its effect on the derivatives is negligible. As the primary focus of my analysis is centered on pressure derivatives, manually adjusting the reported time series is disregarded in the majority of the subsequent analyses.

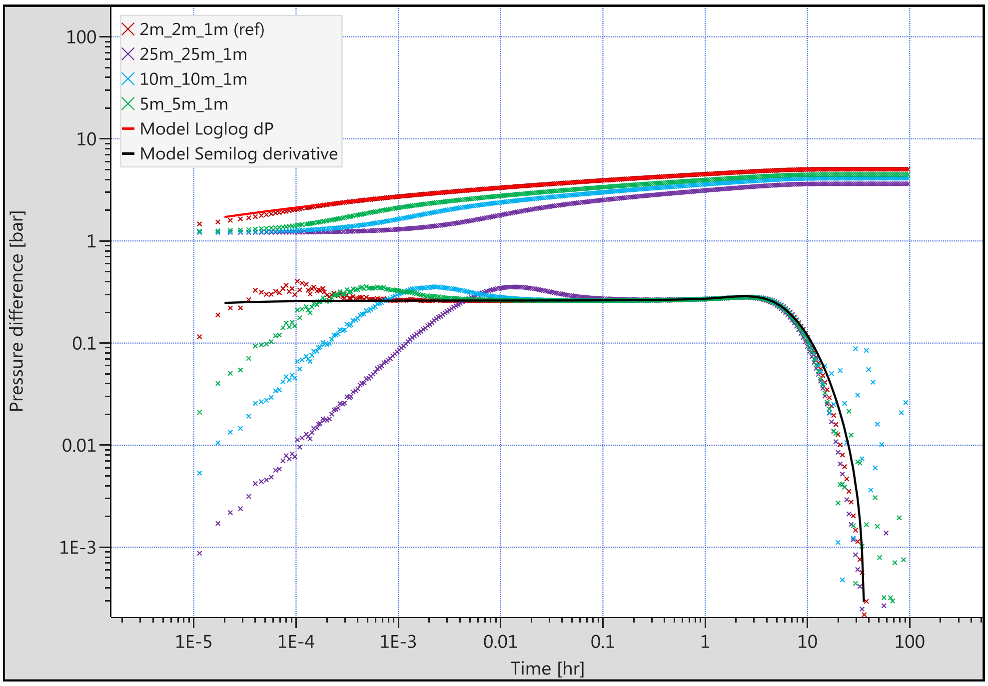

Figure 19 - Log-log plot of the BHP response of a vertical well as the result of different horizontal discretization schemes

Having obtained reasonable matches of all three plots for a highly-resolved numerical model, the influence of various discretization schemes has been investigated. Figure 19 depicts the pressure and pressure derivative log-log plots for four different grid sizes in the horizontal direction. The notation in the legend is structured as follows: The first two items denote the discretization distances in the horizontal direction, while the last one describes the grid resolution along the vertical axis. The plot clearly indicates that grid coarsening decreases the level of BHP stabilization and shifts the stabilization of the derivative forward in time. Both can be attributed to the internal calculation procedure of a reservoir simulator, which assigns average property values of a given grid cell to the location of the cell center. Hence, the same incremental fluid flow over the cell boundaries will yield a larger pressure change in smaller grid cells than in larger ones, as the conceptual incremental pressure change in one portion of the control volume is compensated by an almost unaffected portion, which increases in size with decreasing grid resolution. Tracing the hump of the derivative curve using the Radius of Investigation tool provided by Saphir, almost perfectly reproduces the increasing distance between the cell centers the fluid has to flow in order to trigger a pressure change between the four discretization schemes.

Since the permeability determination is of primary concern, a horizontal grid resolution of 10 to 25 m is found to be sufficient, since all derivative curves stabilize on the exact same level and early time responses are very likely to be masked by WBS and skin effects in real data sets anyway. Figure 20 shows the semi-log and history plot of the respective models, illustrating that all cases coincide with the same slope in the semi-log plot, but yielding different initial pressures before shut-in as a result of the prior discussed averaging.

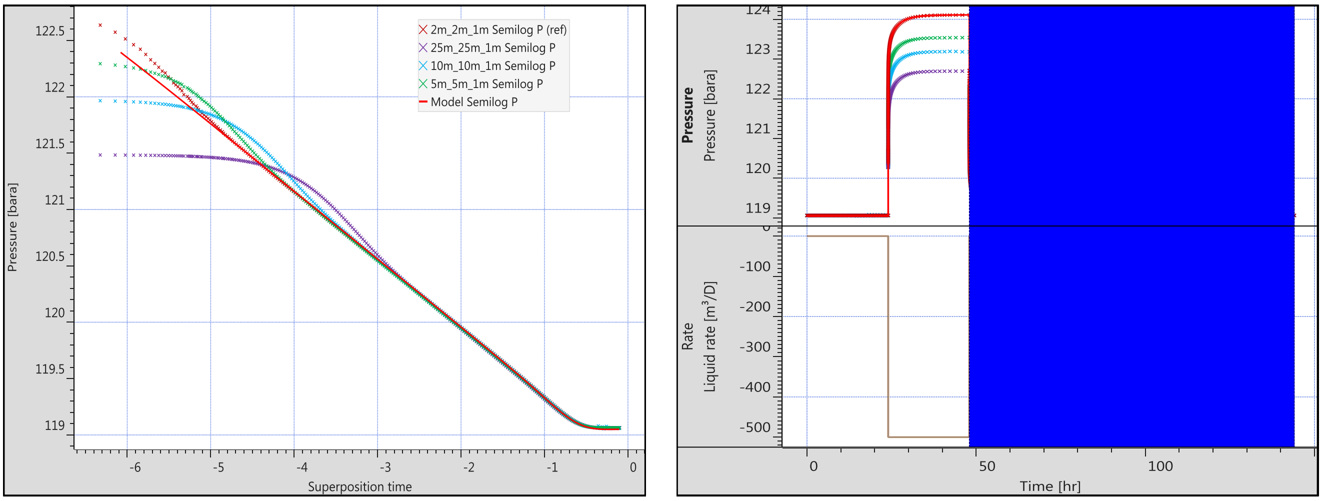

Figure 20 - Semi-log (left) and history (right) plot of the BHP response of a vertical well as the result of different horizontal discretization schemes

Investigating the sensitivity with respect to vertical discretization revealed that the pressure derivative curves again stabilize on the very same level, irrespectively of grid resolution. As one can obtain from Figure 21, the derivative of the BHP responses in case of a 25 m horizontal and 1 m or 2 m vertical grid resolution, respectively, exactly coincides. Same applies for the case with a 50 m horizontal and 2 m or 5 m vertical resolution, respectively.

The deviation in pressure difference can again be explained by a BHP decrease due to an increasing influence of dynamic property averaging with decreasing horizontal resolution. On the contrary, decreasing vertical grid resolution results in an upward shift of the pressure curve. This trend can be explained by considering the exact treatment of the BHP in Eclipse, which sets the reference depth of the BHP equal to the center depth of the grid block containing the first connection defined for this well. Hence, as a result of the downward movement of the grid cell center with decreasing vertical resolution the required BHP during injection is increased, which yields an elevated pressure difference stabilization during shut-in.

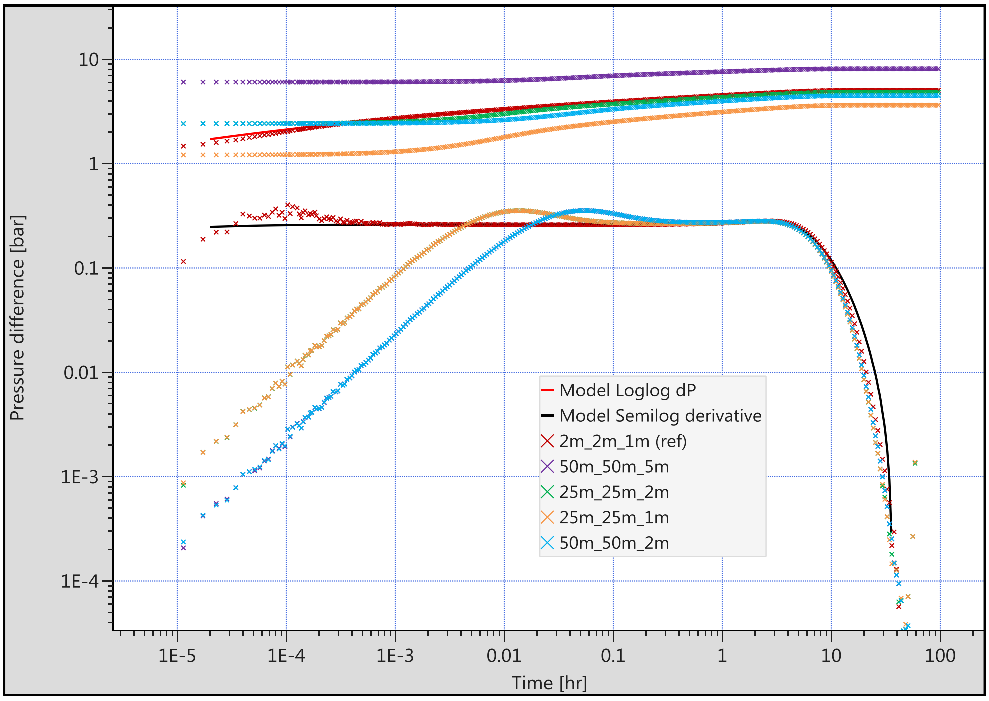

Figure 21 - Log-log plot of the BHP response of a vertical well as the result of different vertical discretization schemes

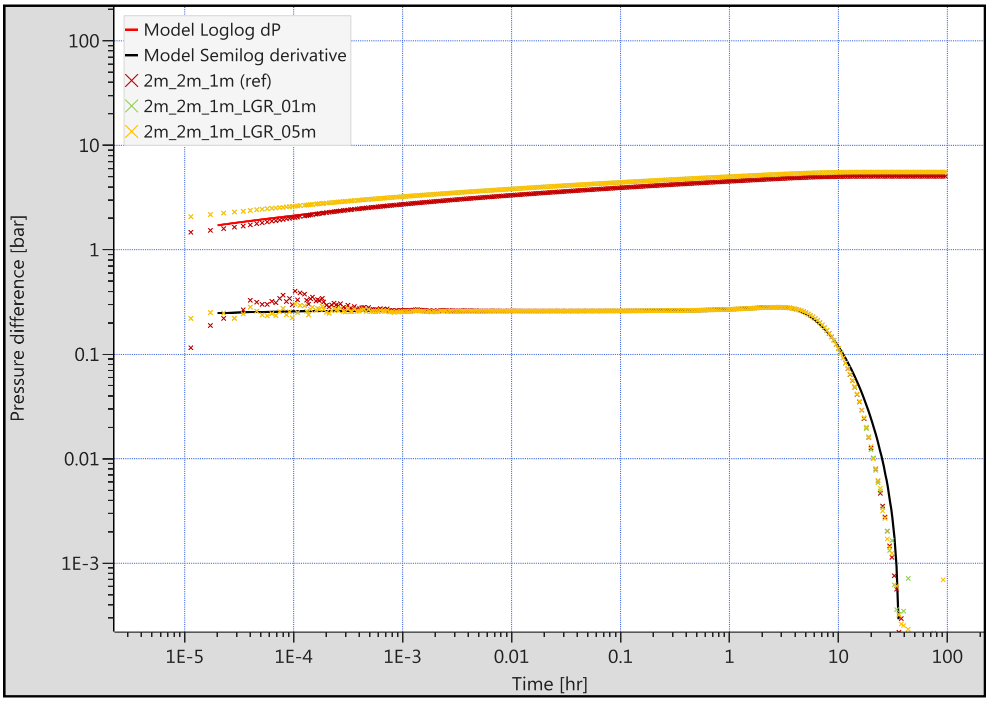

Figure 22 – The influence of vertical LGR on the BHP response

In a last step, the influence of LGR has been investigated. As depicted in Figure 22, the pressure derivative is again hardly affected, while the pressure difference plot exhibits a slight increase as the result of decreasing averaging with decreasing grid block pore volume near the cell. *LGR_05m* and *LGR_01m* refer to a vertical resolution of 0.5 m and 0.1 m, respectively. In conclusion, a horizontal grid resolution between 10 m and 25 m and a vertical resolution of 1 m have been found most appropriate for the desired investigations. However, reservoir heterogeneity will have significant effects on these values.

Finally, the numerical model has been populated with homogeneous permeability values between 100 mD and 900 mD. Respective pressure responses on log-log scale are depicted in Figure 23 and a qualitative analysis in provided in Table 8. It is shown that the input permeabilities of the numerical model are almost perfectly retrievable from PTA. Furthermore, it can be seen that the humps on both sides of the derivative stabilization increase with decreasing permeability.

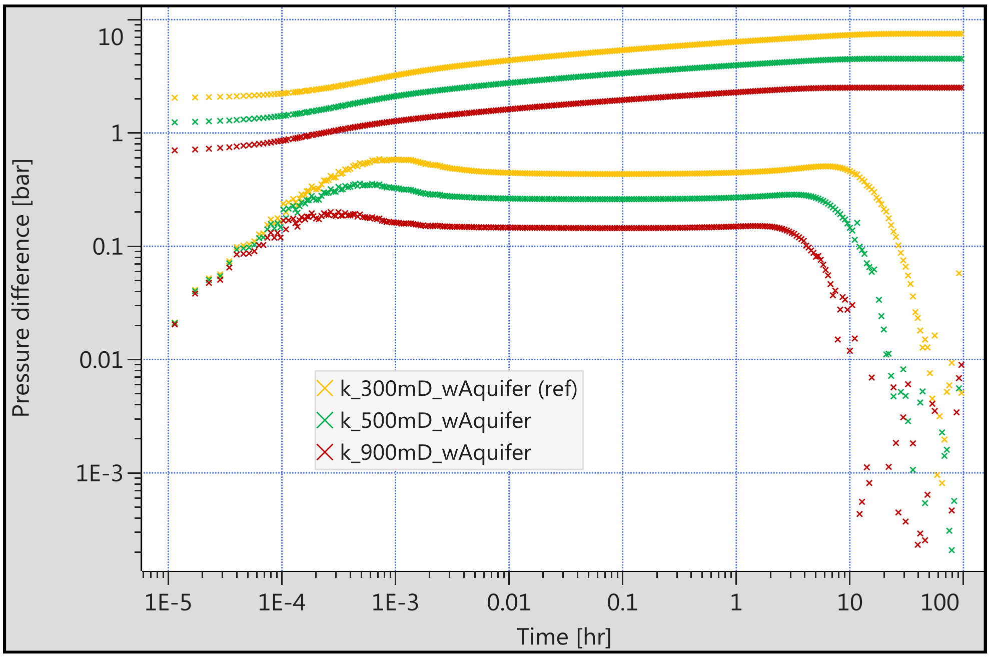

Figure 23 – Log-log plot of homogeneous vertical well model with different permeabilities

Table 8 – Comparison of model permeabilities and corresponding values obtained by PTA for the vertical well case

Permeability, mD		**Error**, %
Model	*PTA*	
100	100	0.0%
300	297	1.0%
500	495	1.0%
700	690	1.4%
900	885	1.7%
	Average	1.0%

6.1.2 Horizontal Well Model

After the proposed workflow of retrieving imposed permeability values of the numerical reservoir model from PTA of simulated fall-off tests could be confirmed for homogenous single-phase models, the same initial investigations have been conducted for a horizontal well case. Initial gridding of the domain has been conducted according to the insights gained from the vertical well analysis. In order to place the horizontal well exactly in the middle of the reservoir domain by maintaining a vertical grid resolution of 1 m around the well, the reservoir thickness has been adjusted to 21 m. The far field has been discretized by a 25 m increment in the horizontal and a 3 m increment in the vertical direction. LGR with horizontal resolution of 5 m and vertical resolution of 1 m has been applied to encompass the near wellbore region with sufficient distance.

Table 9 – Model characteristics and testing schedule for the initial single-phase homogeneous horizontal well model

Parameter	**Value**
Reservoir depth, m	1150
Permeabilities k_H and k_V, mD	500
Well length, m	800
Initialization duration, d	1
Injection duration, d	7
Shut-in duration, d	28
Water injection rate, scm/d	2000

Table 9 provides an overview of relevant model parameters and the defined well test schedule. The horizontal length of the well has been set to 800 m, which approximates the actual horizontal departure of the current polymer pilot as well as further planned injectors. By exceeding the perforated interval of the vertical well by a multiple, both rate and duration of the injection had to be adjusted for the horizontal well application.

The very first analysis has been dedicated to investigating the influence of various model dimensions. Compared to vertical wells, the pressure transient in horizontal drain holes subsequently experiences three distinct flow regimes, with radial flow in the horizontal plane being observed only after sufficiently deep propagation into the reservoir. This boundary screening is depicted in Figure 24 and reveals that rectangular models with edge lengths larger than 5000 m exhibit satisfactorily clear late time pseudo radial flow stabilization before being overlaid by boundary features to assure interpretation using PTA. An approach to match the deviation from the late time pseudo radial flow as an effect of reaching the boundaries using the rectangular boundary model implemented in Saphir reproduced the model dimensions with sufficient accuracy. Hence, further analyses are conducted assuming infinite acting late time responses to ease interpretation.

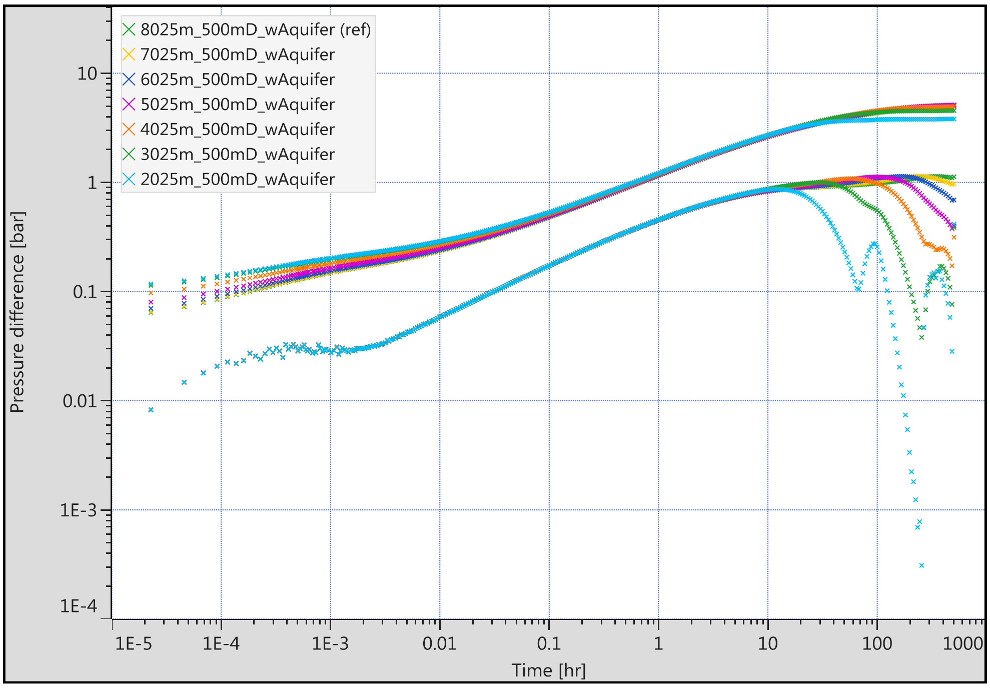

Figure 24 – Study of various lateral boundary distances for the horizontal well model

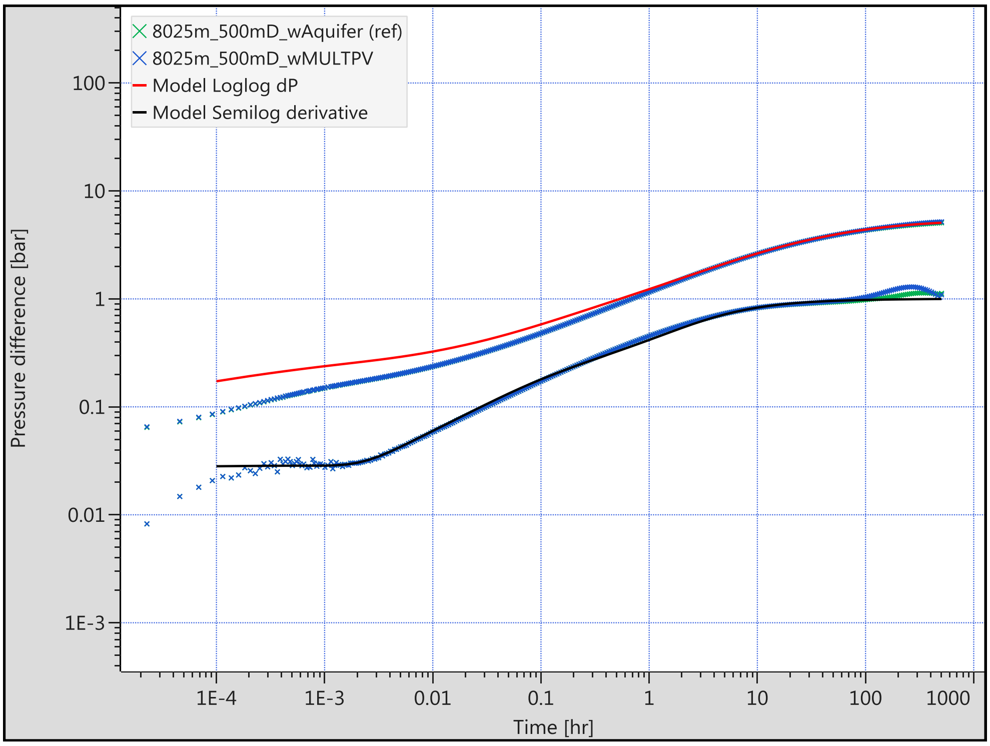

Figure 25 – Comparison of pore volume multiplication and aquifer attachment to approximate constant pressure boundaries on log-log scale

A comparison of two different approaches to treat the reservoir's outer boundary is shown in Figure 25. Both multiplying the pore volume of the most outer cells and attaching an aquifer to the edges of the domain are common approaches to approximate constant pressure boundary conditions. To investigate possible effects of either procedure, a pore volume multiplier (denoted as suffix *MULTPV* in the figure) of 10^6 has been implemented and compared to the response of an analytical Carter-Tracy aquifer attached to the entire circumference (labelled as *Aquifer* in the figure), which is initially in equilibrium with the reservoir and possesses an external radius of 10^4 m. Rock and fluid properties are identical between reservoir and aquifer.

The late time response of the pressure derivative appears smoother for the aquifer case; however, the difference is minor and negligible if a clear pseudo radial flow stabilization can be observed. In cases of smaller lateral extend and earlier boundary influence the hump imposed by the pore volume multiplier approach might be misinterpreted as extended linear flow. Hence, boundaries are modelled by attached aquifers for all following investigations to avoid misleading data interpretation.

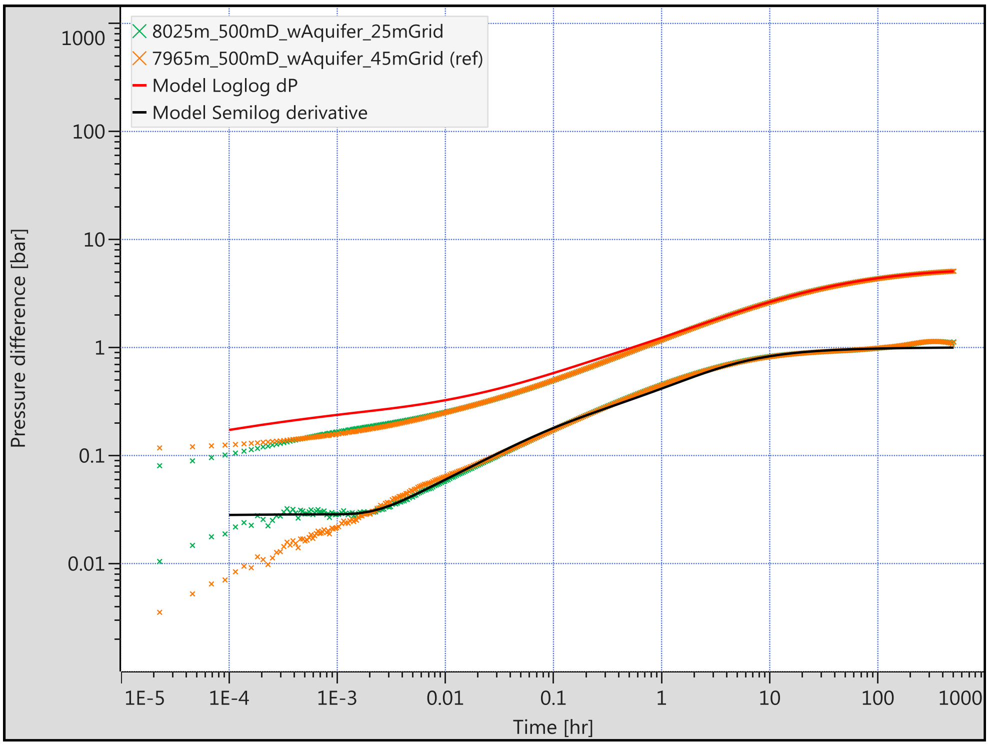

Figure 26 – Influence of horizontal grid coarsening on the log-log pressure response

A study on the influence of vertical grid coarsening has revealed that early time radial flow cannot be observed on coarser grids. As depicted in Figure 26, the pressure derivative continuously follows the linear flow straight line from the very beginning for a horizontal grid increment of 45 m (inner LGR increment 15 m), whereas a 25 m (inner LGR increment 5 m) grid resolution is capable of resolving the early time radial flow stabilization. This effect might be explained by the pressure transient information being transported faster in the horizontal direction due to increased grid size, thus yielding linear flow geometry much quicker.

The influence of inconsistent exporting of the BHP time series from Petrel has again been studied for horizontal wells and the same conclusion could be drawn: Although the shape of the actual pressure change curve is considerably affected, especially during early times, the derivate plots congruently for the prior shut-in pressure being taken as the first reported time step shortly after shut-in as well as prior shut-in pressure being exactly adjusted to the last observed pressure during injection (Figure 27).

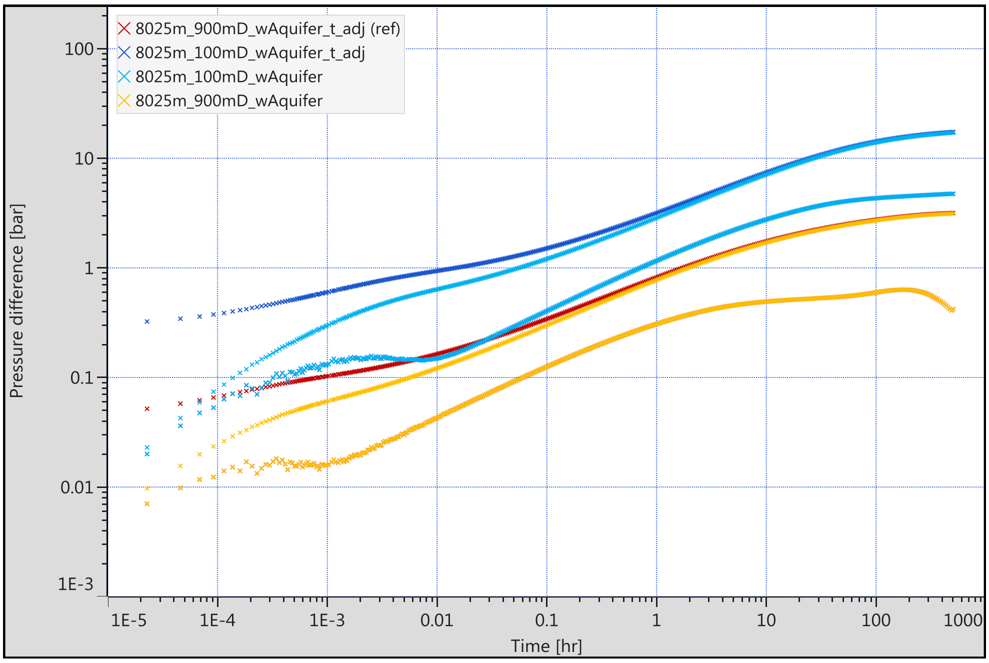

Figure 27 – The influence of erroneous alignment of the start of the shut-in period

Having discussed the influence of several aspects of the model set-up, the pressure response for a homogenous reservoir with 500 mD has been investigated. Using the analytical toolkit provided by Saphir, all three flow regimes could easily be identified and successfully matched by respectively derived parameters. The quality of the match is illustrated in Figure 28 and Figure 29 by showing very close agreement between observed data and the analytical model in all three characteristic plots. The computed parameters of the analytical well model are presented in Table 10. The permeability has been calculated as being 490 mD, which is in very good agreement with the actual 500 mD. The permeability ratio has been found to be 0.85 according to PTA, although permeability has been defined equally in all three dimensions. This discrepancy might be attributed to insufficient grid resolution for very early time responses; however, further analyses with finer grid resolution have yielded only minor improvements.

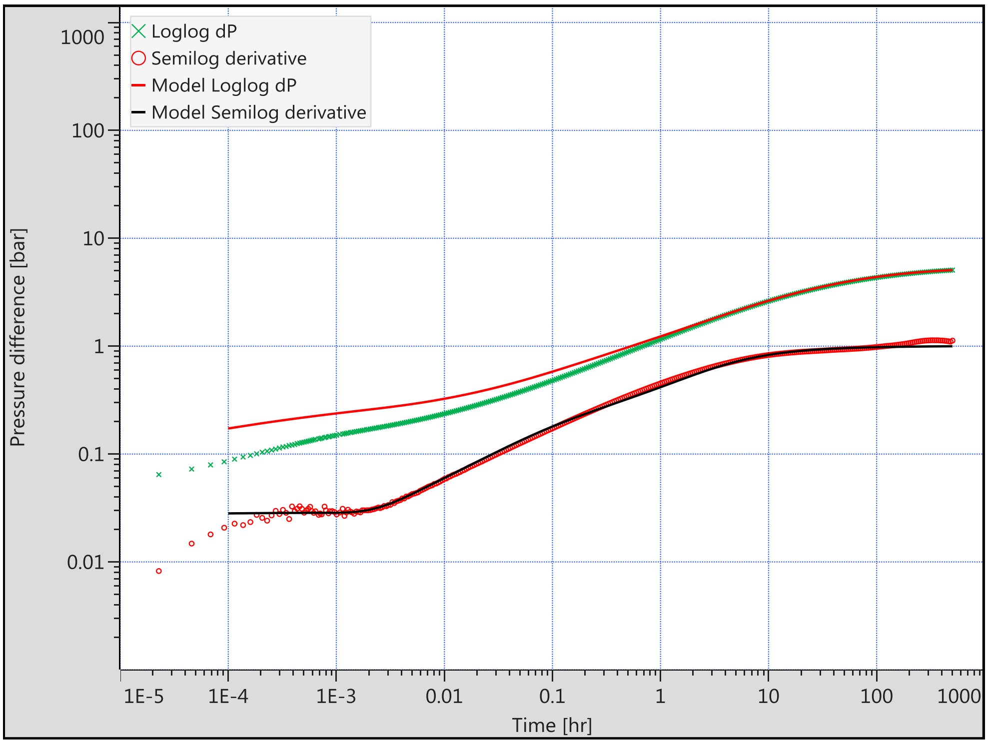

Figure 28 - Matched log-log plot of the initial horizontal well model with a permeability of 500 mD

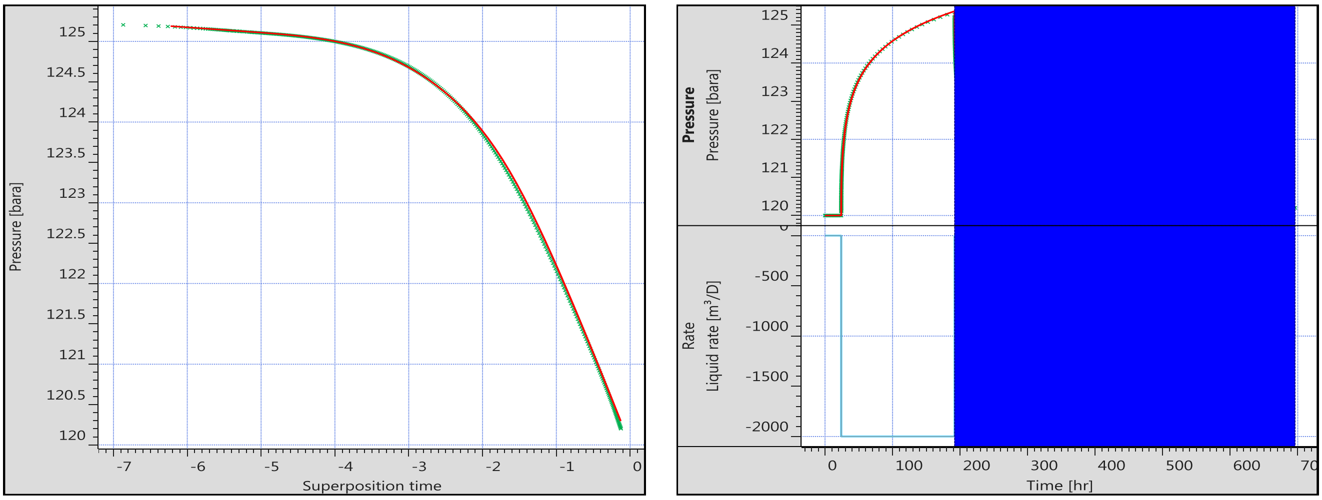

Figure 29 - Semi-log (left) and history (right) plot of the initial horizontal well model with a permeability of 500mD

Table 10 - PTA results for initial horizontal well model with a permeability of 500 mD

Parameter	**Value**
Permeability, mD	490
Permeability ratio k_V/k_H, -	0.85
Skin, -	0
Reservoir pressure, bar	120

During the matching procedure the boundary effects have been disregarded and primary focus has been centered on determining the horizontal permeability. Hence, the late time response is fitted assuming infinite acting behavior of the reservoir. The principle capability of retrieving model permeability in homogeneous horizontal well applications is confirmed by Figure 30 depicts the permeability analysis conducted for the horizontal well for 300 mD, 500 mD, and 900 mD exemplarily. Increasing permeability values result in a simple downward shift of both the pressure change and derivative curve, while leaving the characteristic shape unaltered. This is in accordance with a constant well length as well as permeability ratio between all models, since changing permeability values should then simply affect the level of the stabilization plateau for radial flow geometries according to the changed fluid mobility.

In a last step, the influence of an extended injection duration has been assessed. Therefore, the injection schedule has been adjusted to comprise 6 weeks of injection with subsequent 3 months of shut-in. Although this adjustment resulted in a more pronounced pressure stabilization before shut-in than depicted in Figure 29, no effect on the permeability values obtained from PTA could be distinguished.

Table 11, which summarizes five different permeability values defined in the reservoir simulation case together with the respective values obtained from PTA. An average error of 2.2 % emphasizes almost perfect agreement and underlines the applicability of the proposed workflow. The permeability ratio suffers from a poorer match. An average offset of approximately 15 % indicates that permeability anisotropy between the horizontal and vertical plane cannot be constrained with similar confidence as horizontal permeability itself using PTA. This finding is supported by studies discussed in [13], which found the vertical permeability to be one of the most uncertain parameters to be computed from a pressure transient match.

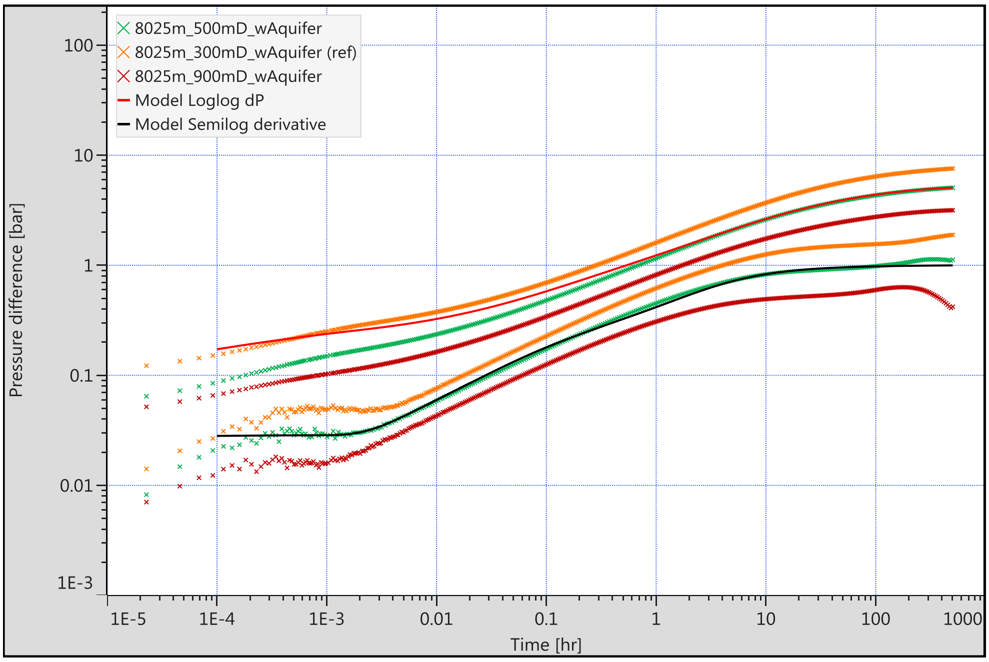

Figure 30 - Log-log plot of homogeneous horizontal well model with different permeabilities

Figure 30 depicts the permeability analysis conducted for the horizontal well for 300 mD, 500 mD, and 900 mD exemplarily. Increasing permeability values result in a simple downward shift of both the pressure change and derivative curve, while leaving the characteristic shape unaltered. This is in accordance with a constant well length as well as permeability ratio between all models, since changing permeability values should then simply affect the level of the stabilization plateau for radial flow geometries according to the changed fluid mobility.

In a last step, the influence of an extended injection duration has been assessed. Therefore, the injection schedule has been adjusted to comprise 6 weeks of injection with subsequent 3 months of shut-in. Although this adjustment resulted in a more pronounced pressure stabilization before shut-in than depicted in Figure 29, no effect on the permeability values obtained from PTA could be distinguished.

Table 11 - Comparison of model permeabilities and corresponding values obtained by PTA for the horizontal well case

Permeability, mD		**Error**, %	**Permeability ratio k_V/k_H**		**Error**, %
Model	*PTA*		*Model*	*PTA*	
100	96	4.0%	1	0.85	15.0%
300	294	2.0%	1	0.83	17.0%
500	490	2.0%	1	0.85	15.0%
700	689	1.6%	1	0.85	15.0%
900	887	1.4%	1	0.88	12.0%
	Average	2.2%		Average	14.8%

The confidence of PTA representing a strong tool to characterize reservoir features could be confirmed for single-phase flow in simple homogenous reservoir models. The subsequent chapter will introduce an increasing level of geological complexity and investigate possible limitations of the proposed workflow.

6.2 The Influence of Reservoir Heterogeneity

On the contrary to common model assumptions, most reservoirs exhibit a considerable degree of geological complexity. Reservoirs are of inherently heterogeneous nature consisting of various depositional facies and sub-facies with differing sediment textures and bedding architectures. Post-depositional alteration of the strata due to compaction, cementation, and tectonic deformation induce further variability in properties influencing fluid flow through the porous media. A common classification of geological reservoir heterogeneity with respect to scale comprises (1) wellbore, (2) interwell, and (3) field wide heterogeneity.

Heterogeneities at wellbore scale affect the matrix permeability, various rock-fluid interactions, and the distribution of residual oil due to directional flow of fluids. The flow pattern as well as vertical and horizontal sweep efficiency of secondary and tertiary recovery projects is affected by interwell heterogeneity. Heterogeneities at field scale determine spatial property distributions affecting the in-place hydrocarbon estimation and determine areal trends in hydrocarbon production.

6.2.1 Permeability Anisotropy

The results of a horizontal well test do not only depend on reservoir characteristics, but also on well geometry and orientation. To take full advantage of horizontal drilling by maximizing the inflow into the wellbore, a horizontal drain hole is often oriented along the minimum principle permeability direction [35]. Hence, the characteristic flow regimes are controlled by different permeabilities. This effect is investigated for permeability anisotropies in all principle directions and conclusions regarding the analyzability of the generated data are drawn.

The reservoir has been initialized with 120 bar at a reference depth of 1160 m, which exactly equals the constant depth of the horizontal well. Skin is defined with zero and the wellbore volume has been assigned a marginal value to assure negligible WBS effects, which might distort the analysis. The well possesses a 800 m perforated interval, is oriented along the X axis and placed in the middle of the domain. The distance to any boundary is approximately 4000 m, which yields model dimensions of approximately 8000 m in both X and Y, to assure sufficient late time flow stabilization for most cases of interest. The near wellbore area has been resolved by LGR to ensure sufficient data also during early times.

Table 12 and Table 13 summarize relevant reservoir, well, fluid and testing schedule data. It has to be mentioned that all listed parameters refer to the homogeneous base case, which acts as the basis for the following analysis.

Table 12 - Base case model parameters for heterogeneity analysis with the horizontal well

Parameter	**Value**
Dimension in X, m	8025
Dimension in Y, m	8025
Dimension in Z, m	21
Discretization in X (LGR resolution around well), m	25 (5)
Discretization in Y (LGR resolution around well), m	25 (5)
Discretization in Z ((LGR resolution around well), m	3 (1)
Permeability, mD	500
Porosity, -	0.25
Rock compressibility, bar^{-1}	$3.0 \cdot 10^{-5}$
Well length, m	800
Wellbore radius, m	0.09525
Initialization duration, d	1
Injection duration, d	7
Shut-in duration, d	28
Water injection rate, scm/d	2000

Table 13 - Fluid characteristics for heterogeneity analysis

Parameter	**Value**
Water density, kg/m^3	1013.0
Water viscosity, cP	0.55
Water formation volume factor, -	1.007
Water compressibility, bar^{-1}	$4.0 \cdot 10^{-5}$
Total system compressibility, bar^{-1}	$7.0 \cdot 10^{-5}$

The first investigation has been focused on vertical permeability anisotropy, which inherently is a crucial feature of most reservoirs due to depositional history of the formation. Figure 31 depicts the diagnostic plot of the pressure transient of a horizontal well for various permeability ratios k_z/k^*. The parameter k^* refers to the unaltered permeability in all remaining directions of 500 mD, while k_z denotes vertical permeability. According to the figure, only cases with a vertical permeability equal or smaller than its horizontal equivalent yield a distinct early time flow stabilization, which allows for the determination of the permeability ratio. The two cases characterized by a vertical permeability clearly exceeding its horizontal equivalence show linear flow behavior from very early time on, which is in agreement with previous findings as discussed in chapter 3.2.

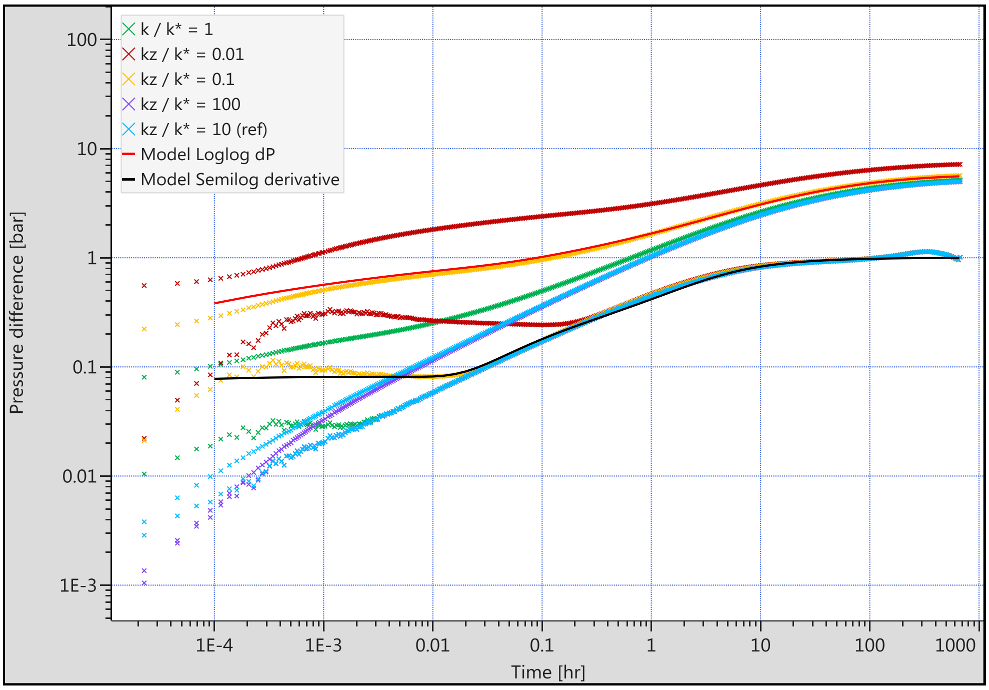

Figure 31 - Log-log plot of pressure transients with vertical permeability anisotropy

Table 14 contrasts the vertical permeability ratio as implemented in the reservoir model with the values obtained from PTA. In case of a permeability ratio smaller than unity, a match on the log-log plot resulted in reasonable estimates. However, for permeability ratios larger than unity, this approach becomes increasingly questionable, since no distinct early time match can be obtained. Properties denoted with an asterisk could not be retrieved from PTA.

Table 14 – Comparison of vertical permeability ratio defined in the model with values derived from PTA in case of vertical permeability anisotropy

Permeability ratio k_z / k*		**Error**, %
Model	*PTA*	
0.01	0.011	10.00%
0.1	0.105	5.00%
1	0.85	15.00%
10	16	60.00%
100	*	*

Subsequently, horizontal permeability anisotropy has been investigated, starting with the direction parallel to well orientation (X direction). As it can be observed from Figure 32, all cases possess the same early time plateau defined by radial flow in the vertical plane followed by linear flow of varying duration. The earlier deviation towards the late time pseudo radial flow stabilization for cases with an elevated horizontal permeability ratio is attributed to an earlier contribution of inflow from the sides into the pure linear flow regime. Increased permeability along the well affects the flow geometry to yield quickly an elliptical shape as depicted in Figure 33.

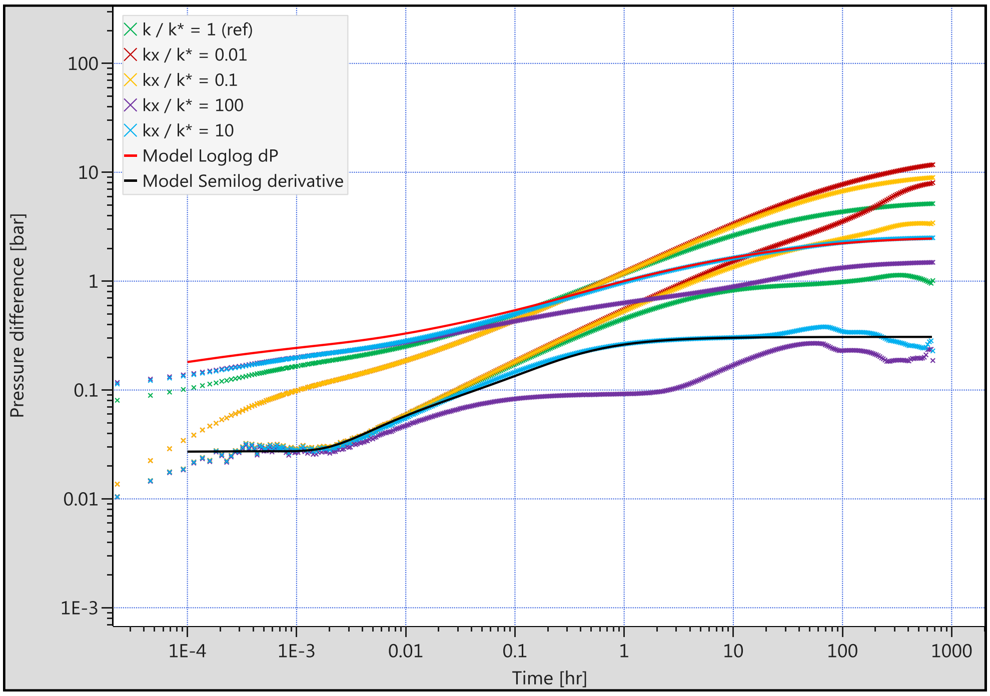

Figure 32 - Log-log plot of pressure transients with horizontal permeability anisotropy parallel to well orientation

A reduction of the permeability in well orientation emphasizes the establishment of a clear linear flow regime, by postponing considerable inflow from the sides or suppressing it at all. The result can be seen as extended linear flow slope in the log-log plot. Late time radial flow stabilizations could not be matched for these cases due to a limited shut-in duration. However, it remains questionable whether clear plateau behavior might be observed for an adjusted schedule, as boundaries are likely to be reached already during linear flow even before significant inflow from parallel to the well can establish.

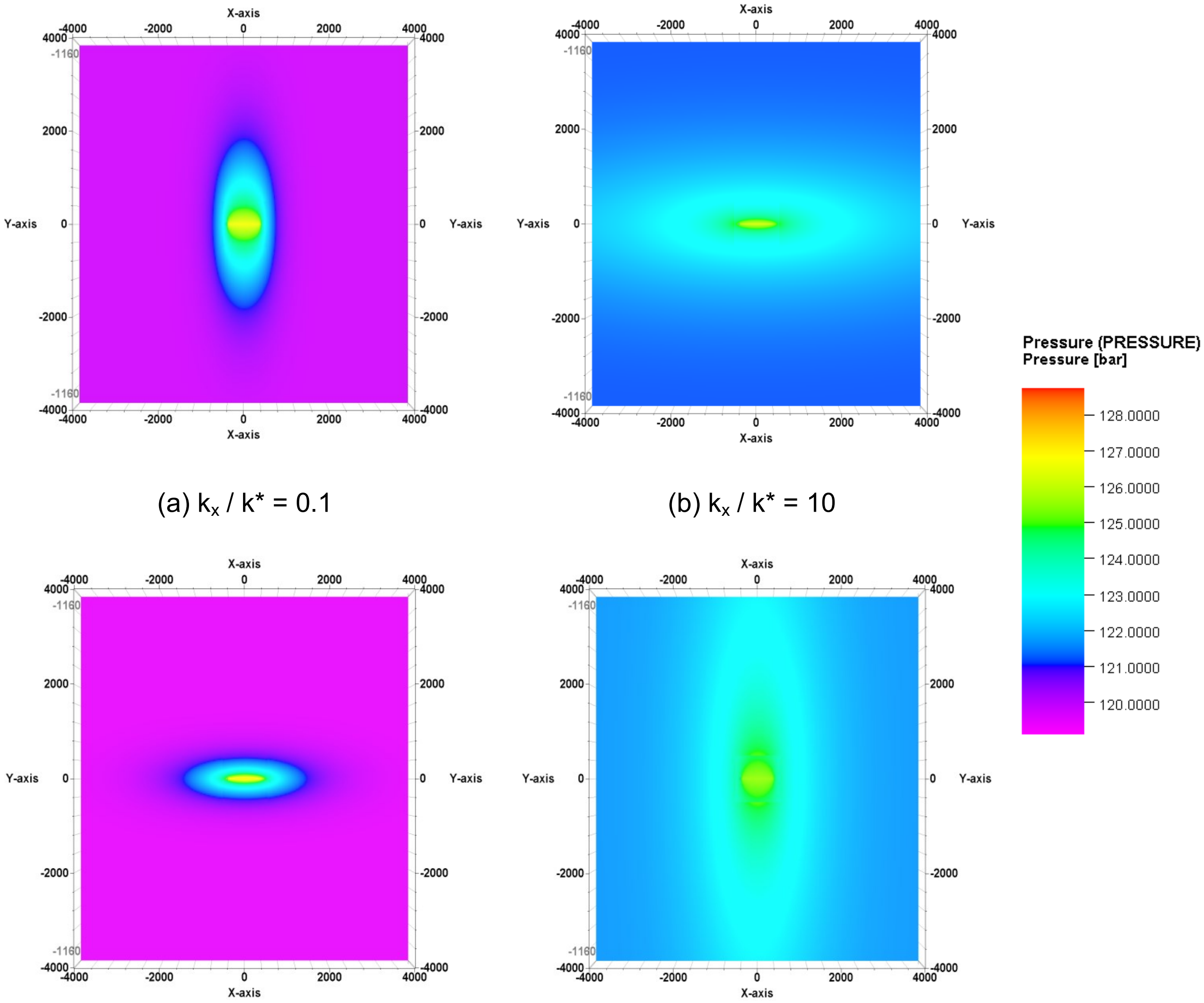

(a) $k_x / k^* = 0.1$

(b) $k_x / k^* = 10$

(c) $k_y / k^* = 0.1$

(d) $k_y / k^* = 10$

Figure 33 - Pressure profile in the horizontal well layer for different permeability anisotropy cases after 4 days of injecting 2000 scm/d

Table 15 - PTA results for permeability anisotropy parallel to well orientation

Model					**PTA**		
k_x / k^*	k^*	k_x	$k_{H,geom}$	$k_V / k_{H,geom}$	k	k_V / K_H	$2\ L_w$
-	mD	mD	mD	-	mD	-	m
0.01	500	5	50	10.00	*	*	*
0.1	500	50	158	3.16	*	*	*
1	500	500	500	1.00	490	0.85	800
10	500	5000	1581	0.32	1600	0.30	430
100	500	50000	5000	0.10	5260	0.11	199

Table 15 summarizes permeability data defined in the simulation model and the results from PTA. The comparison shows that neither permeability nor the effective well length of 800 m can be reproduced directly with sufficient accuracy using PTA. However, a thorough post-processing of the results provides meaningful insights.

It has been shown that the pressure behavior of a reservoir with horizontal permeability anisotropy can be described by an equivalent isotropic reservoir model of average radial permeability $\bar{k}$ defined by eq. (41) with $k_{H,min}$ and $k_{H,max}$ denoting the minimum and maximum permeability oriented perpendicular to each other, respectively [35]. This finding is supported by the current study when comparing the geometric mean of the permeabilities defined in the model with the values obtained from PTA. Contrasting PTA and the computed equivalent isotropic values demonstrates good agreement for both horizontal permeability and permeability anisotropy. This clearly indicates that PTA yields the geometric mean of horizontal permeability, from which no distinct indications of the individual magnitudes of k_x and k_x can be derived. Furthermore, the effective well length, to obtain a close match between the pressure data and the model response, differs significantly compared to the model input.

$$\bar{k} = \sqrt{k_{H,min}\, k_{H,max}} \tag{41}$$

Although the overall well behavior is apparently homogenous, permeability anisotropy has to be taken into account during the entire interpretation. If the analysis is conduced based on an isotropic permeability model, the vertical permeability k_z remains unaltered while adjusting the apparent half-length of the well to account for differences between k_x and k_y. Equation (42) refers to the coordinate system depicted in Figure 34 and indicates that the apparent effective length increases for wells oriented in the minimum permeability direction and vice versa.

$$L_a = \sqrt[4]{\frac{k_y}{k_x}} L_w \tag{42}$$

A consequence of substituting actual with equivalent isotropic permeability values is the necessary transformation of dimensions in the two main directions of permeability. Accordingly, the wellbore appears as ellipse with the major axis oriented in the low permeability direction and not circular anymore. The cross-sectional area of the well is kept constant between the original and the transformed system, which yields an increased perimeter. The behavior of such an elliptical well is identical to a cylindrical hole, whose equivalent radius is the arithmetic mean of the major and minor axis [13]. In other words, the behavior of a cylindrical well in anisotropic media can be described by an elliptical well of certain dimensions in an isotropic formation. This approach is only valid if the well is strictly drilled along one principle permeability orientation. Otherwise, errors are introduced with a magnitude depending on the permeability contrast.

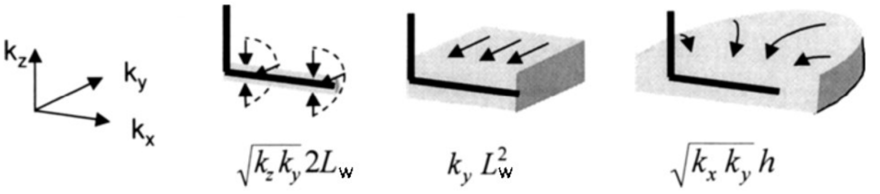

Figure 34 –Effective permeability as the result of horizontal permeability anisotropy during the three characteristic flow regimes towards a horizontal well [13]

Incorporating the concept of apparent well half-length into the post-processing of direct PTA results is shown in Table 16. The required inputs for k_x and k_y in eq. (42) have been taken respectively from the reservoir model. A comparison of well length L_w obtained from PTA and its computed apparent equivalent L_a illustrates promising consistency. Hence, combining eq. (41) and eq. (42) with results obtained from PTA can be used to estimate k_x and k_y to yield a more profound description of actual reservoir heterogeneity according to eq. (43) and (44). Errors with respect to permeability estimation of less than 5 % indicate the principle applicability of this interpretation workflow to constrain horizontal permeability anisotropy from PTA data.

$$k_x = \bar{k}\left(\frac{L_w}{L_a}\right)^2 \tag{43}$$

$$k_y = \frac{\bar{k}^2}{k_x} \tag{44}$$

Table 16 - Determination of k_x and k_y based on PTA results

Model		**PTA**		**Analytical Model Evaluation**			**Error in k**
k_x	k_y	k	$2\,L_w$	$2\,L_a$	k_x	k_y	
mD	mD	mD	m	m	mD	mD	%
500	500	490	800	800	490	490	2.0
5000	500	1600	430	450	5059	506	1.2
50000	500	5260	199	253	52600	526	5.2

Eventually, this interpretation workflow has been applied to reservoirs models with permeability anisotropy perpendicular to the well direction (Y direction). As depicted in Figure 35, early radial flow can only be observed for cases with sufficiently large permeability perpendicular to the well, in order to establish an all-around flow geometry encompassing the well. Except for the case possessing the highest permeability in the Y direction, all cases could be matched for late time pseudo radial as well as intermediate time linear flow to yield horizontal permeability and well length values from PTA. The discrepancy for the high permeability case might be explained by reaching the boundaries parallel to well already during linear flow, which would be consistent to the conclusions drawn from the cases exhibiting low permeability ratios while investigation horizontal permeability anisotropy in the X direction. The figure clearly shows that the most efficient horizontal well crosses perpendicularly to the high permeability direction.

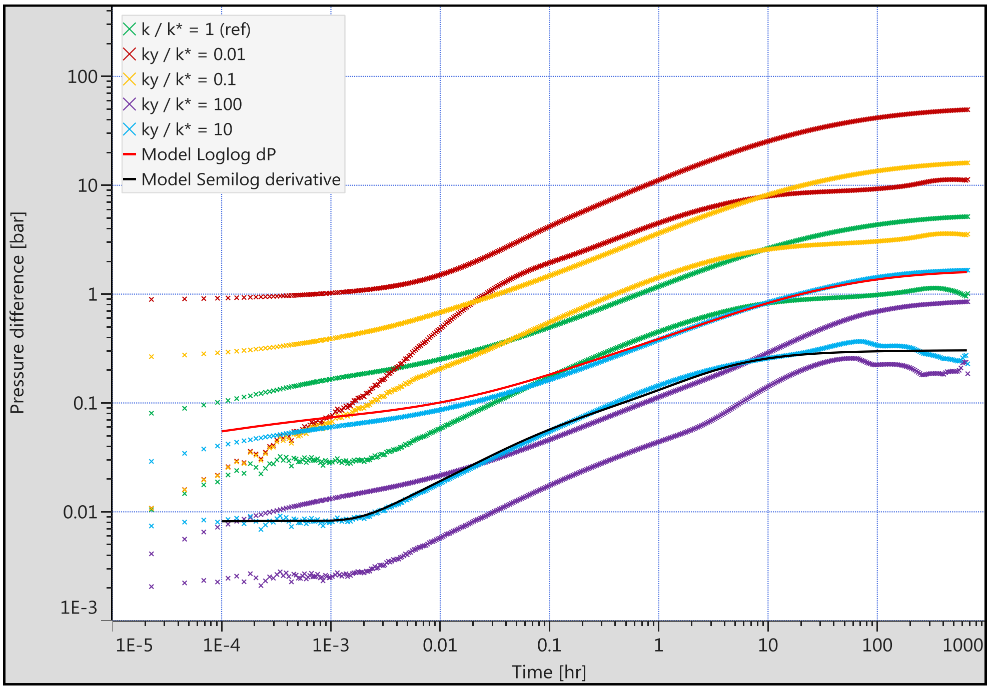

Figure 35 - Log-log plot of pressure transients with horizontal permeability anisotropy perpendicular to well orientation

By understanding the permeability obtained from PTA as the geometric mean of the horizontal permeabilities in the two principle directions and the determined well length as its apparent equivalent, k_x and k_x can be approximated. Although the results shown in Table 17 show some deviation from the actual model values, this analysis provides a useful tool to constrain horizontal permeability contrast. One shortcoming of this approach is that the effective well length L_w has to be known. For the current synthetic models, the producing interval equals the total well length; however, this might not be the case for actual wells, which imposes the need for further input data to conduct this evaluation.

Table 17 - PTA results for permeability anisotropy perpendicular to well orientation

Model			PTA			Analytical Model Evaluation			
k_y / k^*	k_x	k_y	k	k_V / K_H	$2\,L_a$	$k_{H,geom}$	$k_V / k_{H,geom}$	k_x	k_y
-	mD	mD	mD	-	m	mD	-	mD	mD
0.01	500	5	52	*	270	50	10.00	457	5
0.10	500	50	156	*	462	158	3.16	468	53
1.00	500	500	490	0.85	800	500	1.00	490	510
10.00	500	5000	1611	0.32	1379	1581	0.32	542	4611
100.00	500	50000	*	*	*	5000	0.10	*	*

6.2.2 Discontinuous Permeability Heterogeneity

Although a homogeneous reservoir model is commonly used to analyze well tests, most reservoirs are stratified and permeability varies with depth. While variations of horizontal permeability with depth have been found to exhibit only minor effects on the horizontal radial flow regime, pressure transient responses of horizontal wells are sensitive to changes in vertical permeability [13]. Ultimately, change of permeability in the vertical direction can reduce the ability of vertical flow during the early time response.

After global permeability anisotropy has been studied in the previous chapter, the effect of low and high permeability streaks on the behavior of the pressure transient from a horizontal well has been investigated. Therefore, the permeability in all directions has been adjusted in individual planes of specific width at distinct positions. Hence, the influence of distance between well and permeability discontinuity as well as thickness of a certain permeability layer can be analyzed. Their effect has been studied for all three principle orientations: horizontal bedding planes, vertical permeability streaks parallel to the wellbore, and vertical permeability streaks perpendicularly intersecting the wellbore. The permeability contrast between the adjusted plane and the unaltered rest of the domain has been varied between 0.01 and 100. Given the discontinuous behavior evoked by the implemented permeability streaks, a quantitative analysis of pressure transient behavior with respect to evaluating permeability and permeability contrast is not feasible. However, a qualitative study provides valuable insights into principle responses of potential fractures or sealing layers within the reservoir.

The reservoir model used for this analysis is the same as for the previous analysis and described in Table 12. The stated model dimensions and grid sizes divide the domain into 321 slices in both the X and Y direction and 7 layers in the Z direction. The thickness of each X- or Y- slice equals 25 m and each Z-layer accounts for 3 m. The well is oriented along the X axis and located in Y-slice 161 and Z-layer 4, representing the centerline of the reservoir domain. The 800 m long well spans X-slice 146 to X-slice 177. This explanation is important to understand the legends in the following three tables. Each data series is labelled by three individual parts. The first section denotes the ratio of altered permeability *k** in the layer of interest to the permeability of the initial homogeneous model *k*, which has been defined as 500 mD. The middle term starts with *x, y,* or *z* denoting the orientation of the permeability plane with the subsequent number stating the first layer or slice to be adjusted. The last part describes the thickness of the respective permeability plane stated in layers or slices, respectively. Following this notation, *k*/ k = 0.01, z_s = 3, h_s = 2* translates into a low permeability layer with a permeability contrast of 0.01 and a thickness of 2 layers with layer 3 being the upper one of the two. The effects evoked by a low permeability layer with a permeability contrast of 0.01 have been found to be most pronounced, which is why this case will be discussed in detail in the following. All remaining cases can be found as type curves in appendices B, C and D.

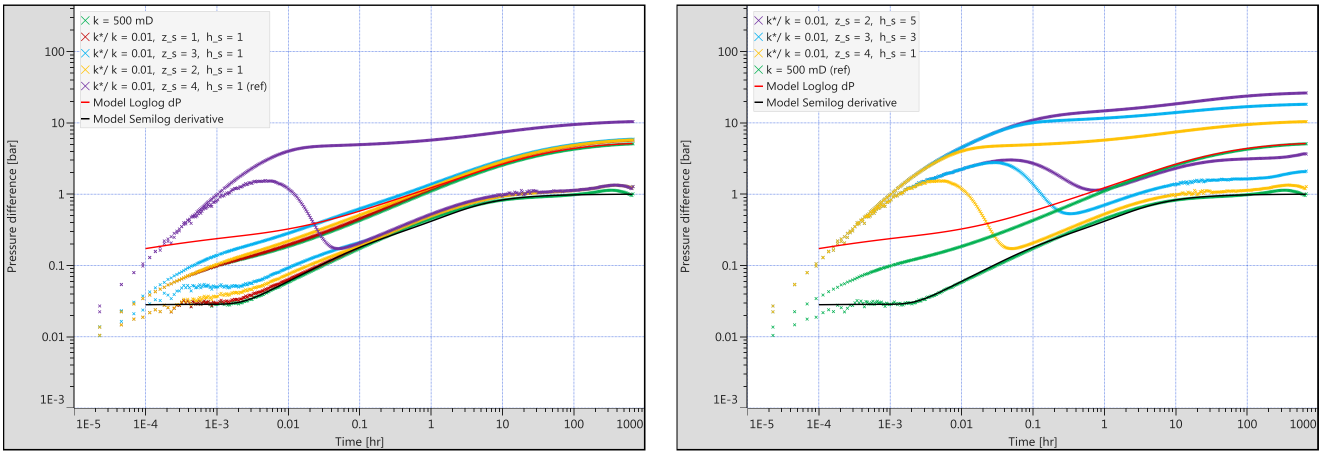

(a) Influence of distance to layer

(b) Influence of layer thickness

Figure 36 - The influence of permeability contrast between horizontal layers

The presence of interbeds with very low vertical permeability in an otherwise homogeneous reservoir, affects the shape of the horizontal well response and consequently the production. Figure 36 depicts the influence of distinct horizontal permeability layers on the pressure transient behavior of a horizontal well. It can be observed from Figure 36 (a) that the early time vertical radial flow stabilization plateau shifts upwards with the low permeability layer approaching. Which might erroneously be interpreted as a decreased ratio of vertical to horizontal permeability, is actually attributed to the diversion of flow by the low permeability layer suppressing fluid movements to the upper part of the formation. In case the well is perforated in the low permeability layer, the early time pressure response becomes similar to a vertical well with considerable skin. This is consistent with theory, since the concept of skin models wellbore damage by introducing an artificial pressure drop to account for the difference from the pressure predicted by Darcy's law. In the given example, this additional pressure drop is created by an area of decreased permeability encompassing the well. The late time pseudo radial flow stabilizes on a slightly elevated level for the non-homogeneous reservoir models, yielding decreased values for equivalent isotropic permeability. However, the value of this stabilization could not be reproduced by any general mathematical relationship combining initial model permeability with the adjusted low permeability streak value, due to the discontinuous nature imposing a rather complex flow geometry.

Considering low permeability layers of increasing thickness, which all encompass the well in their middle, the pressure derivative responses become similar to dual-permeability systems. This observation becomes obvious by drawing an analogy to a vertical well radial composite model. If the layer of altered permeability is sufficiently thick, its characteristics dominate all three subsequent flow regimes while experiencing inflow from the upper and lower part of the reservoir. This conceptually matches exactly the assumptions of a dual-permeability model. In case of short shut-in times, the horizontal well response could not be distinguished from a typical vertical response.

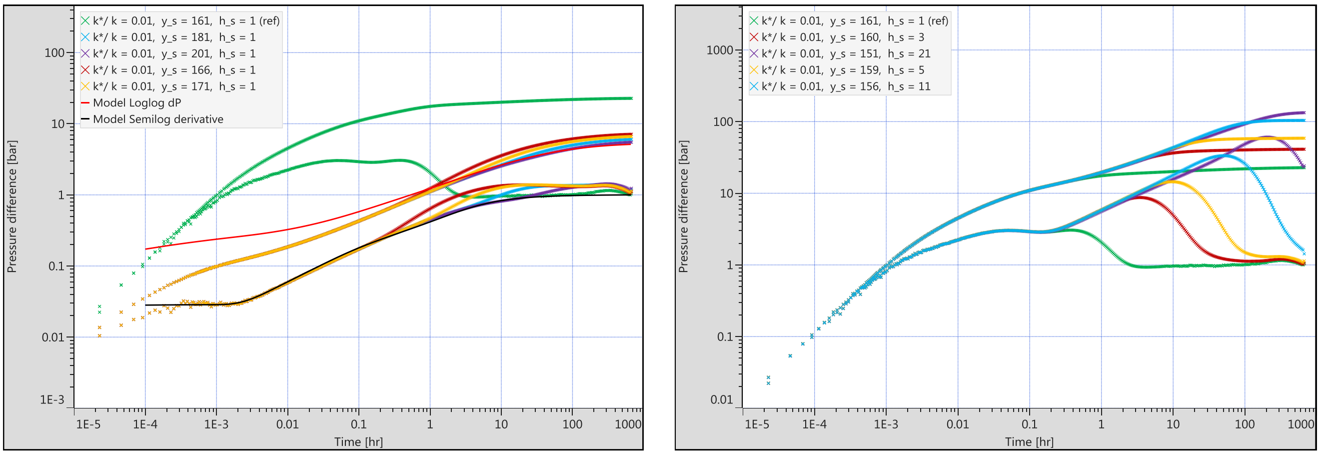

(a) Influence of distance to slice (b) Influence of slice thickness

Figure 37 - The influence of permeability contrast between vertical streaks parallel to the well

The influence of a low permeability slice oriented parallel to the horizontal well is illustrated in Figure 37. Focusing on the effect of changing distance between the well and the low permeability streak (Figure 37 (a)) reveals that the initial model permeability of 500 mD can only be retrieved from the case containing the low permeability slice directly intersecting the well. Keeping the reservoir away from the well undisturbed assures the thorough establishment of horizontal radial flow. Matching the early time vertical flow stabilization for that case, yields approximately the imposed permeability contrast of 0.01; however, the length of the well is significantly underestimated. This discrepancy origins again from the permeability discontinuity, possessing different values only in slice containing the well. All other cases can be matched with reasonable agreement for both early time radial and linear flow, as the permeability disturbance is shifted away from the well. Being located at a certain distance to the well, the low permeable nature of the altered slice acts as a barrier to fluid flow. Hence, a pressure response similar to a single sealing fault, which is characterized by a doubling of the radial flow stabilization level, can be observed.

Placing the well in the middle of a larger low permeable streak aligned with the well, results in the pressure responses depicted in Figure 37 (b). All pressure derivatives exhibit the same early time stabilization and converge towards a common plateau again for the late time response. This can be explained by early time vertical radial flow within the low permeability streak, followed by a linear flow geometry until the boundary of the altered domain is reached, and the eventual establishment of horizontal pseudo radial flow determined by the unaltered reservoir permeability. Lacking a clear relation between the observed linear flow period and the subsequent late time derivative stabilization due to a significant drop in the derivative, common PTA tools developed for horizontal wells cannot readily be applied to evaluate such responses. Instead of using equivalent homogenous models, radial composite models should be applied.

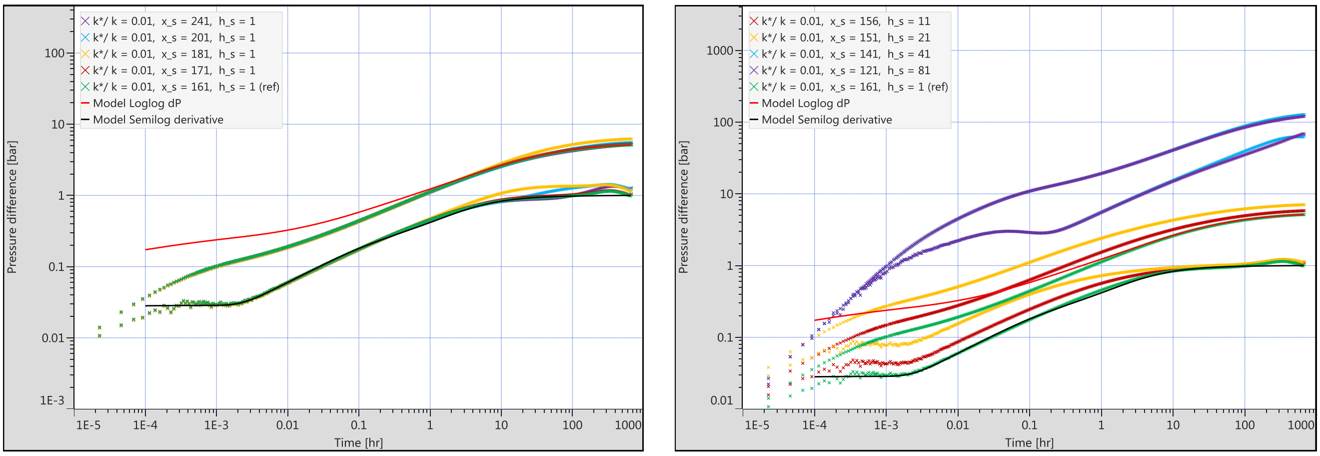

(a) Influence of distance to slice

(b) Influence of slice thickness

Figure 38 - The influence of permeability contrast between vertical streaks perpendicular to the well

Eventually, the influence of permeability slices intersecting the horizontal well have been investigated and respective responses are depicted in Figure 38 for the low permeability case. Compared to the previous observations, the influence of a single slice cutting the well has been found marginal, which can easily be explained by averaging effects. As the majority of the well is connected to relatively high permeable parts of the formation, a shorter section possessing low permeability does not have a significant affect. On the contrary, a single high permeability slice intersecting the well changes the pressure response towards a typical infinite conductivity fracture response and disappearing early time radial flow by significantly diverting the flow into one reservoir slice. Low permeability slices perpendicular to the well, which do not intersect with the well show similar single sealing fault features as observed earlier.

If the thickness of the low permeability slice does not exceed the well length, increasing thickness results in a lower vertical to horizontal permeability ratio. While horizontal permeability is obtained from late time radial flow obtained outside the altered permeability zone and constant for all cases, vertical permeability is averaged along the well and decreases with increasing contribution of the low perm streak. For low permeability streaks significantly exceeding well length, the responses become perfectly homogeneous again. However, only early time radial and linear flow can be observed in that case due to small permeability values and limited shut-in time.

6.2.3 Continuous Permeability Heterogeneity

To deepen the understanding of the influence of more realistic property heterogeneity, continuous parameter distributions have been investigated and are discussed in this chapter. Compared to the sharp permeability discontinuities described in the previous chapter, random parameter distributions will result in smooth pressure derivative responses, which can be described and analyzed by an equivalent isotropic media approach. Hence, the main focus of the current analysis is to reveal which parameter of a certain distribution is characteristic for it pressure transient response.

The basis for this study is again the simulation model as introduced in chapter 6.1.2 and 6.2.1. However, porosity and permeability are not assumed constant, but honor predefined distributions. These distributions have been developed according to observations stated in chapter 5.1 and are provided in Table 18. Two different permeability distributions have been defined to investigate the effect of horizontal permeability anisotropy, while both distributions yield log-normally distributed values between 10 mD and 3000 mD. Porosity has been constrained to values between 0.05 and 0.4 and a respective porosity-permeability relationship has been defined based on distribution 1. The shut-in period has been extended to allow for an equilibration of the higher pressure build-up due to increased heterogeneity and to assure a clear late time radial flow stabilization.

Table 18 – Definition of log-normal permeability distributions

	μ	**σ**	Poro-perm relationship
	ln(mD)	ln(mD)	
Distribution 1	5.8	0.3	$\ln k = 4.196 + 8.035\Phi$
Distribution 2	6	0.4	

In total, four different model set-ups have been considered: Horizontal permeability in both directions is computed according to distribution 1 for isotropic cases, while k_x and k_y are characterized by distribution 1 and 2, respectively, for the anisotropic case. Both set-ups have then been combined with a vertical permeability of exactly one tenth of k_x or randomly assigned values of a uniform distribution ranging from 1 mD to 100 mD. The porosity field has been calculated depending on k_x as denoted in Table 18. Petrel workflows have been developed to generate multiple simulation cases honoring the principle set-ups.

Subsequent analyses have revealed that BHP transients of different realizations of the same set-up cannot be distinguished by PTA. This observation is caused by property averaging, which is an inherent effect of PTA, and meets prior expectations. Figure 39 depicts the BHP responses for both set-ups characterized by the vertical permeability being one tenth of the horizontal permeability in one direction. The cases with a uniformly distributed vertical permeability between 1 mD and 100 mD are shown in Figure 40. The BHP responses from both isotropic (Figure 39) and anisotropic (Figure 40) models can be matched closely by analytical models, including an accurate estimation of the boundary distance for a rectangular configuration. Permeability and permeability ratio determined by PTA are listed in Table 19 for each of the four considered cases.

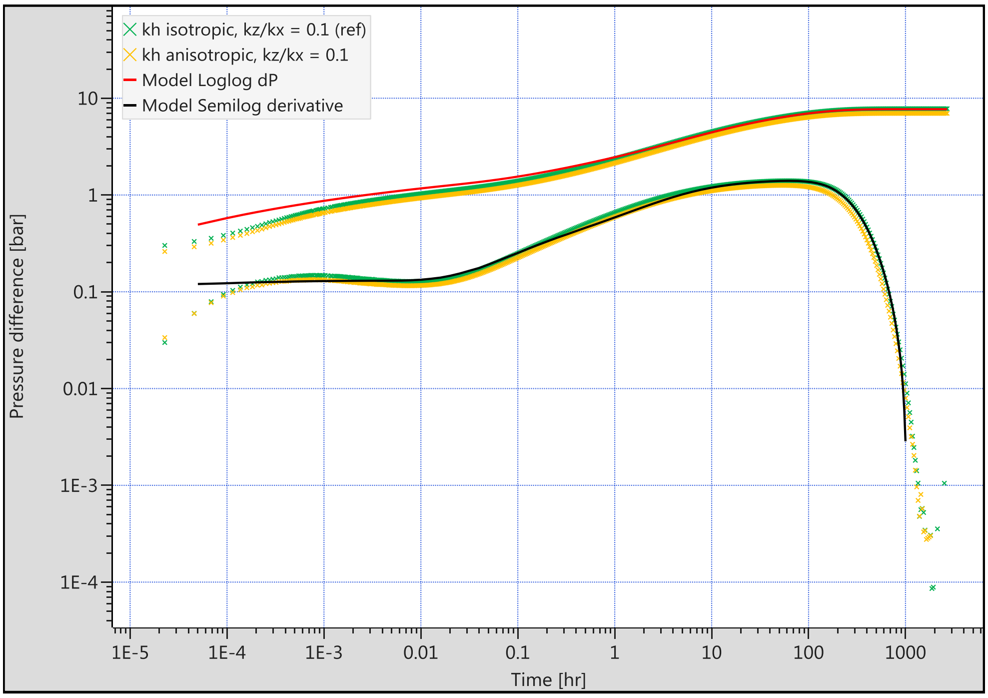

Figure 39 - Log-log plot of lognormally distributed horizontal permeability and $k_z/k_x = 0.1$

Although one might argue that the investigated permeability anisotropy has not been very pronounced, the PTA results in Table 19 indicate a distinct difference between the horizontal permeability value for the isotropic and anisotropic cases. This demonstrates the sensitivity of PTA with respect to minor changes in permeability and emphasizes the need for an accurate match of the late time radial flow stabilization. The different vertical to horizontal permeability ratios cannot be distinguished from the PTA response.

To gain thorough understanding of the meaning of the obtained permeability values, the permeability fields of all cases have been analyzed statistically. For this purpose, the actual generated distributions have been exported from Petrel and evaluated with R to compute the gross rock volume weighted mode, median, and arithmetic mean for each distribution. The volume weighting accounts for different grid block sizes in the model. Figure 41 illustrates the actual permeability distribution for one of the anisotropic cases.

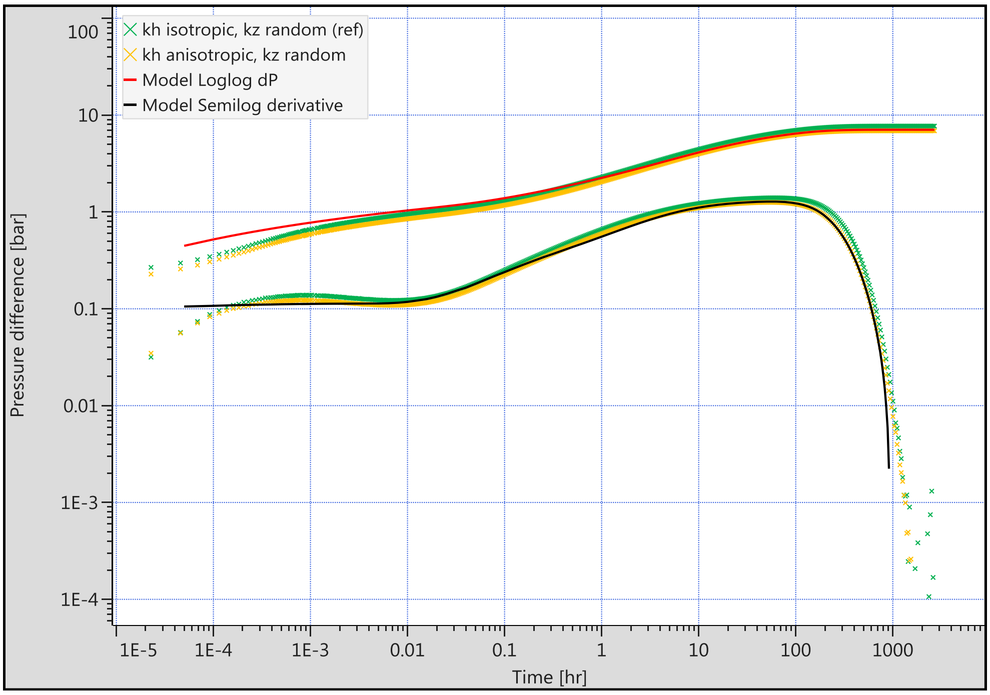

Figure 40 - Log-log plot of lognormally distributed horizontal permeability and uniformly distributed k_z

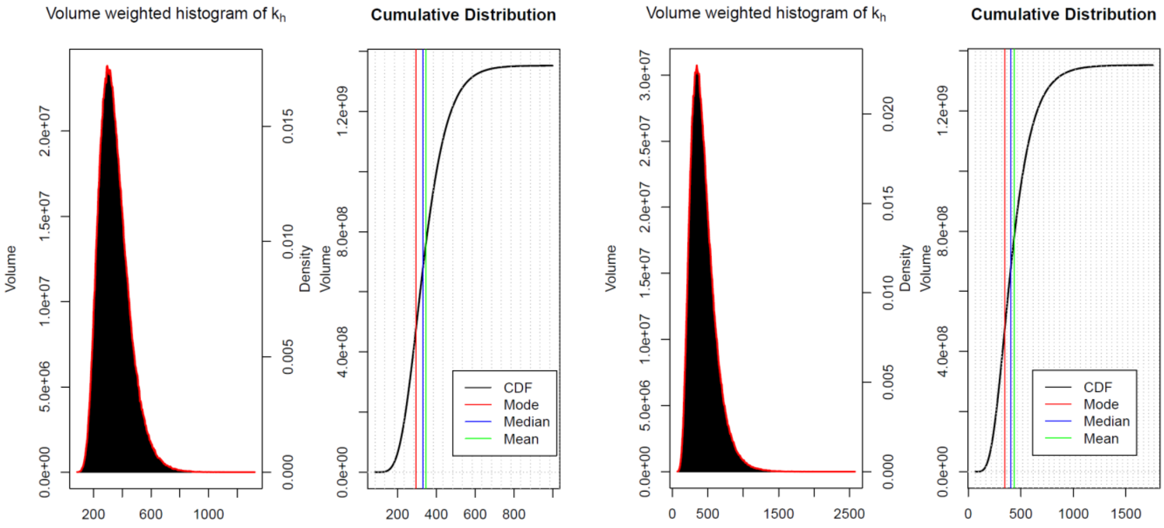

(a) Permeability parallel to well k_x (mD) (b) Permeability normal to well k_y (mD)

Figure 41 - Horizontal permeability distributions for the anisotropic case with $k_z/k_x = 0.1$

Table 19 – Comparison of PTA results with statistical reservoir model characterization

		k_H isotropic		**k_H anisotropic**	
		$k_z/k_x = 0.1$	k_z random	$k_z/k_x = 0.1$	k_z random
	PTA using Saphir				
	k_H	**330**	**330**	**359**	**360**
	k_V/k_H	**0.09**	**0.1**	**0.09**	**0.1**
	Statistical evaluation				
Mode	k_x	296.4	303.2	295.4	301.1
	k_y	296.4	303.2	344.6	341.1
	k_z	29.6	63.9	29.5	89.9
	k_H	296.4	303.2	319.1	320.5
	k_V/k_H	0.10	0.21	0.09	0.28
Median	k_x	330.4	330.3	330.3	330.3
	k_y	330.4	330.3	403.7	404
	k_z	33	50.5	33	50.5
	k_H	**330.4**	**330.3**	**365.2**	**365.3**
	k_V/k_H	**0.10**	**0.15**	**0.09**	**0.14**
Mean	k_x	345.5	345.6	345.6	345.4
	k_y	345.5	345.6	437.4	437.3
	k_z	34.5	50.5	34.6	50.5
	k_H	345.5	345.6	388.8	388.6
	k_V/k_H	0.10	0.15	0.09	0.13

The statistical evaluation with R has revealed that the median permeability almost perfectly coincides with the estimate from PTA for each of the respective cases. The horizontal permeability k_H has been calculated as the geometric mean of k_x and k_y according to eq. (41). This finding emphasizes that the recorded pressure response is dominated by the most “typical” permeability value. While the arithmetic mean of a distribution is largely influenced by extremely small or large values, the median is typically less skewed due to its nature of separating the lower half of a distribution from the upper half. Furthermore, the median does not depend on an arbitrary bin size, such as the mode. It has to be mentioned that the vertical to horizontal permeability ratio cannot be estimated with similar confidence from PTA as horizontal permeability itself.

6.2.4 The Influence of Permeability Upscaling

After PTA has been shown to be capable of identifying even minor differences in field-wide permeability distribution, the influence of upscaling on the pressure transient response has been investigated. This study is aimed to provide insights how local resolution of permeability heterogeneities affects the results obtained from PTA. Although a proper upscaling method should ideally be based on the actual reservoir character and consider flow directions, the three basic upscaling methods discussed in this chapter are limited to arithmetic, harmonic and geometric averaging of permeability values of the merged cells.

Arithmetic averaging is applicable when the dominating portion of flow occurs parallel to the main permeability change as observed in layered formations. Since high permeability values have a larger impact on fluid flow than small values, this approach is prone to overestimate the upscaled permeability. If the flow direction is oriented perpendicular to the main permeability change, the harmonic average is often used for upscaling, since low permeability values control resulting flow rates. The geometric average is primarily applied when there is no distinct preference for vertical or horizontal flow, meaning the reservoir does not possess any significant permeability anisotropy. This technique tries to retain both high and low values.

Table 20 - Initial model set-up for upscaling analysis

Parameter	**Value**
Dimension in X, m	1000
Dimension in Y, m	1000
Dimension in Z, m	21
Discretization in X, m	2
Discretization in Y, m	2
Discretization in Z, m	1
Porosity, -	0.14
Horizontal well length, m	500
Initialization duration, d	1
Injection duration, d	7
Shut-in duration, d	21
Water injection rate, scm/d	1000

Initially, a highly resolved rectangular model has been set up according to the parameters summarized in Table 20. To maintain a manageable number of grid cells, the reservoir extend had to be reduced to 1000 m. Reservoir, well, and fluid parameters, which are not explicitly presented in the stated table, are kept from the previous study. The permeability fields have been defined according to the distributions depicted in Figure 42. Both a very narrow log-normal distribution in a region of reasonably high permeability values and a wide distribution ranging from 0.1 mD to 10 D have been considered. The first one basically corresponds to distribution 1 in Table 18. For each distribution three different scenarios have been developed: The permeability values can either be randomly distributed throughout the entire reservoir domain (referred to as *RanDist*) or follow a certain spatial correlation, which is geologically more meaningful. This geostatistical effect has been modeled using spherical Variogram models supported by Petrel. The anisotropy range in the major direction has been defined with 300 m, whereas in the minor direction the data is correlated only within 100 m. The azimuth of the major direction has been oriented perpendicularly to the horizontal well (referred to as distribution *Spatial 1*) as well as aligned parallel with the well (denoted as *Spatial 2*).Figure 43 illustrates both realizations.

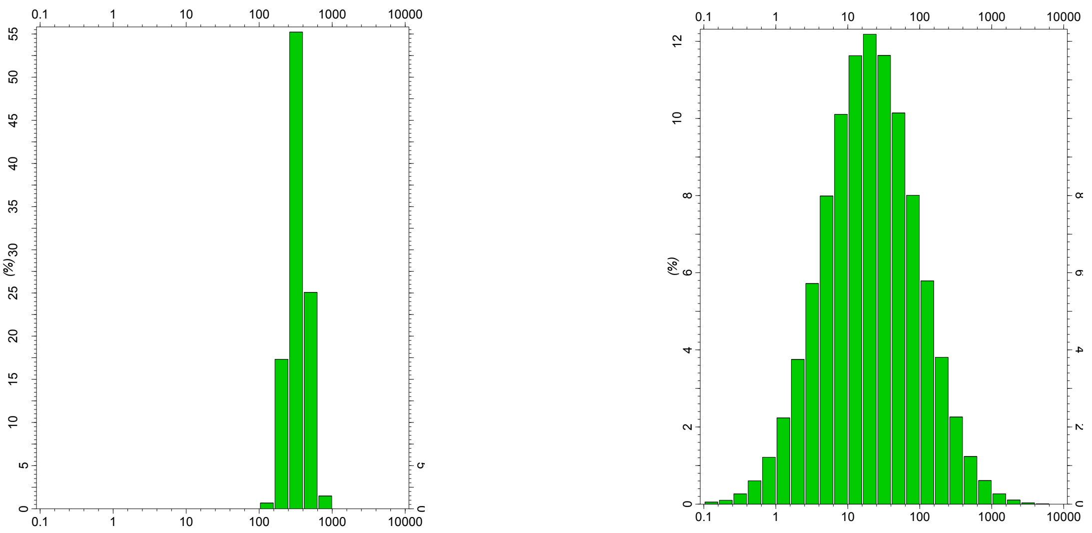

Figure 42 - Log-normal horizontal permeability distributions (mD) used for upscaling analysis

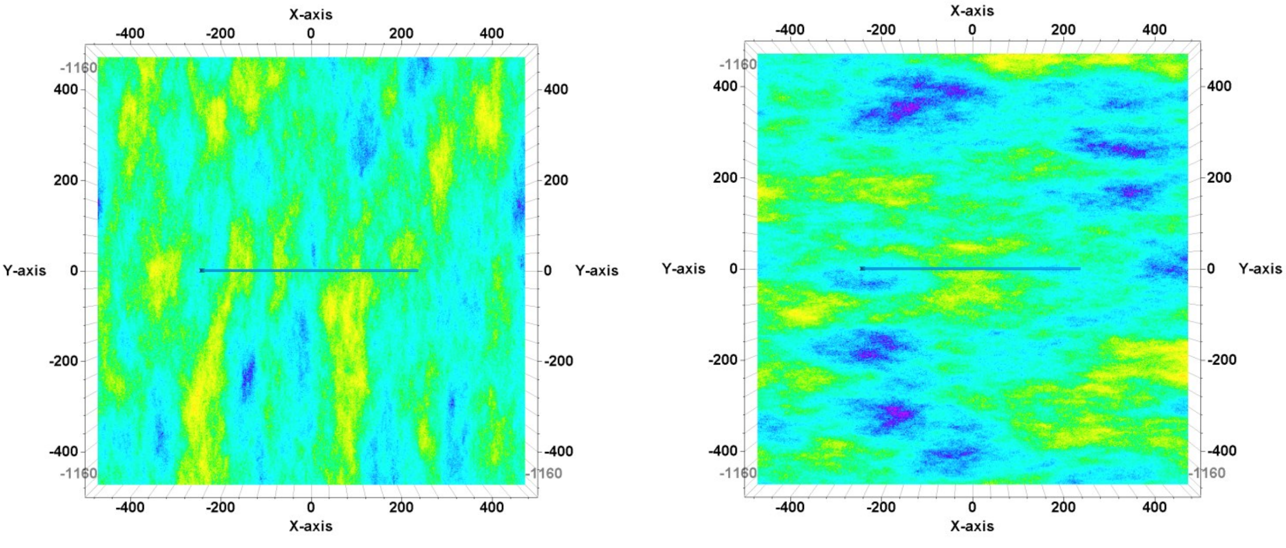

(a) Spatial Distribution 1

(b) Spatial Distribution 2

Figure 43 - Orientations of horizontal permeability distributions (depicted for narrow distribution case, bluish color indicates low values)

Horizontal permeability is assumed isotropic. Vertical permeability is modelled independently and centered around one tenth of its horizontal equivalent. Both a vertical and a horizontal well have been considered for each model to enhance understanding of effects associated with spatial parameter distribution as well as upscaling. Table 21 shows that for the narrow permeability distribution, PTA provides a reliable tool to characterize in-situ permeability.

Although, no information regarding spatial distribution can be obtained, the resulting permeability tends to reproduce once more the median of the actual distribution. The slight increase in permeability obtained for models possessing spatially oriented permeability fields might be explained by the establishment of preferred flow paths, which is suppressed in case where permeability is assigned as random noise. However, all three cases exhibit very similar behavior. It is important to note that horizontal permeabilities obtained from the vertical and horizontal well analysis are in close agreement and that the pressure transients can be reproduced with sufficient accuracy, including boundary effects. Since no extended late time horizontal radial flow stabilization can be observed due to reduced reservoir dimensions, this consistency is a crucial prerequisite for meaningful further analyses.

Table 21 - Comparison of model values and PTA results of highly resolved initial model for narrow permeability distribution cases

		Petrel model			*PTA using Saphir*					
		Permeability, mD			**Boundary distance**, m					
	Well type	min	max	median	South	East	North	West	k_H	k_V/k_H
Random distribution	vertical	0.1	10^4	330.2	500	500	500	500	**319**	-
	horizontal				500	250	500	250	**316**	0.110
Spatial distribution 1	vertical	0.1	10^4	325.5	500	500	500	500	**328**	-
	horizontal				500	250	500	250	**320**	0.115
Spatial distribution 2	vertical	0.1	10^4	327.7	500	500	500	500	**325**	-
	horizontal				500	250	500	250	**316**	0.115

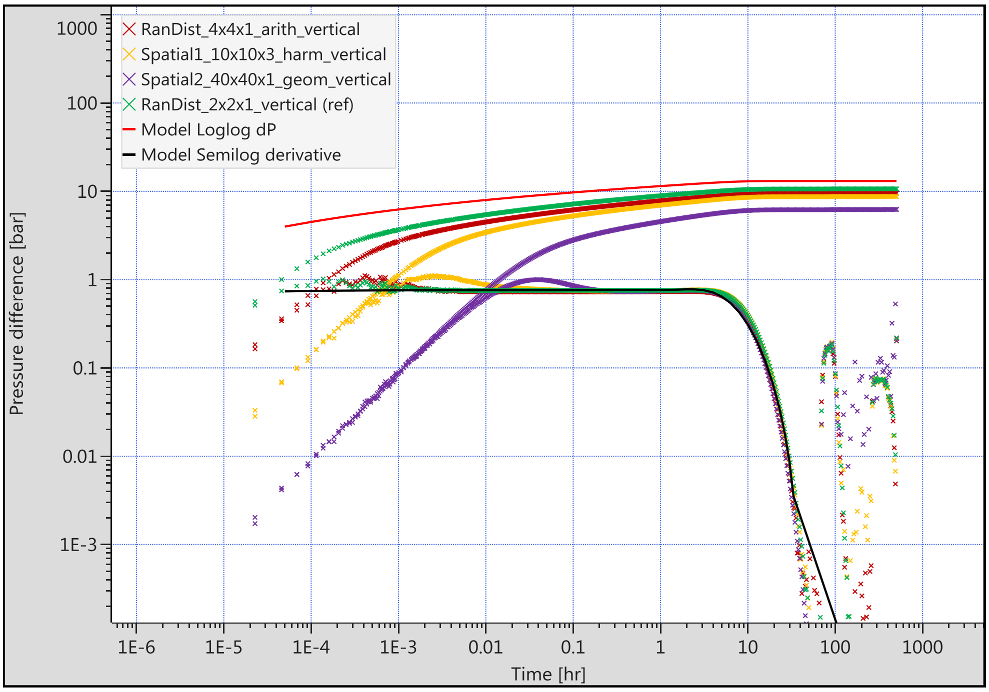

Figure 44 – BHP response of initial and upscaled grids in a vertical well (narrow distribution)

Figure 44 and Figure 45 depict the pressure responses for all three distributions and upscaling techniques in a very condensed manner for a vertical and a horizontal well, respectively. The legend is organized as follows: The first part denotes the permeability distribution to be studies, where the explicit statement of *wide* refers to the wide distribution. The grid resolution of the current model in meters is stated in the middle. The last two parts characterize the applied upscaling method and the type of well, respectively. One can see that neither different initial distributions nor different averaging methods during upscaling can be distinguished from PTA. The observed time-shift of the early time radial flow stabilization is an effect of increasing grid size, as discussed in 6.1.1 and 6.1.2.

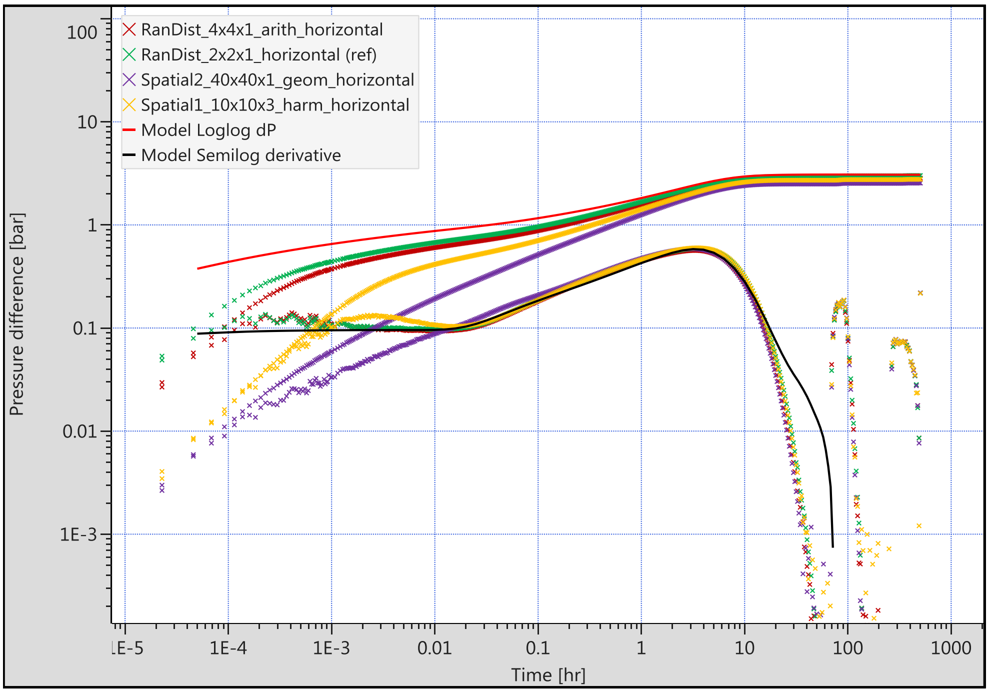

Figure 45 - BHP response of initial and upscaled grids in a horizontal well (narrow distribution)

To account for a broader permeability distribution comprising an essential range of small values, the water injection rate has been decreased to avoid excessive pressure build-up. 100 scm/d and 10 scm/d are assumed as constant injection rate for the horizontal and vertical well implementation, respectively. Table 22 contrasts permeability as defined in each initial reservoir model before upscaling and its respective value based on PTA. The log-log plots of the matched models are depicted in Figure 47 and Figure 48. A clear discrepancy between the values of horizontal permeability obtained from a vertical and a horizontal well of 500 m can be observed. Furthermore, both set-ups are not capable of reproducing a representative value of the actual permeability distribution.

Since pressure tests from vertical and horizontal wells theoretically yield a consistent reservoir description, most likely the assumption of an effective well length of 500 m is violated. Penetrating low permeability regions can cause a reduction of the effectively drained length of a horizontal section, which would need to be accounted for by reducing the well length during PTA. A reduction of the effective length would yield an increase in horizontal permeability according to eq. (35).

Table 22 - Comparison of model values and PTA results of highly resolved initial model for wide permeability distribution cases

		Petrel model			*PTA using Saphir*					
		Permeability, mD			**Boundary distance**, m					
	Well type	min	max	median	South	East	North	West	k_H	k_V/k_H
Random distribution	vertical	0.1	10^4	20	500	500	500	500	**19.0**	-
	horizontal				500	250	500	250	**5.1**	0.35
Spatial distribution 1	vertical	0.1	10^4	21.1	500	500	500	500	**44.0**	-
	horizontal				500	250	500	250	**11.1**	0.15
Spatial distribution 2	vertical	0.1	10^4	19.5	500	500	500	500	**44.0**	-
	horizontal				500	250	500	250	**9.6**	0.15

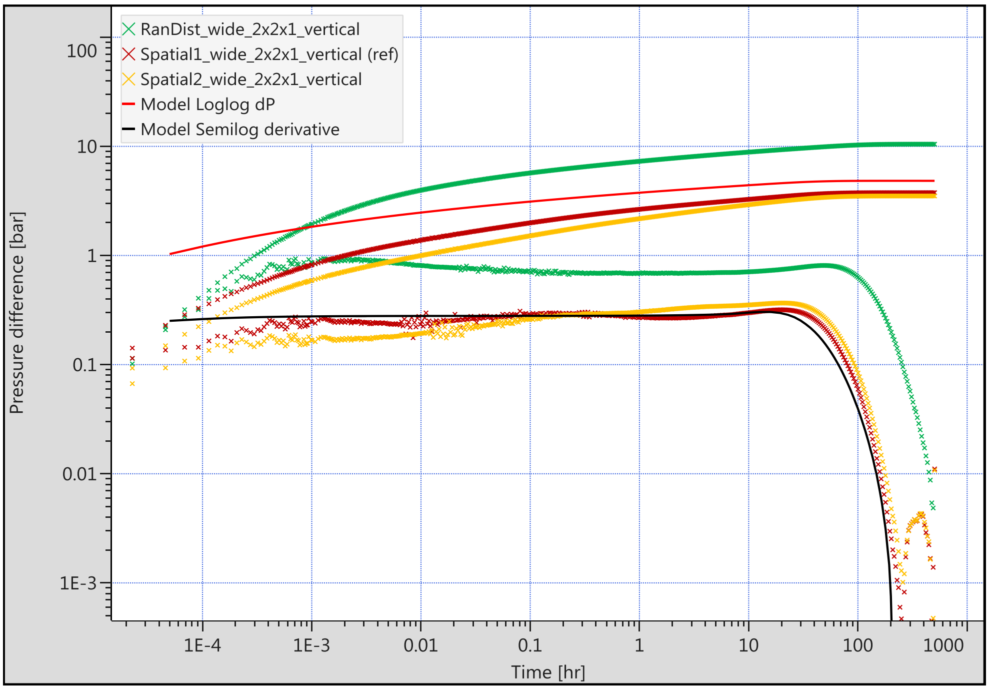

Figure 46 - BHP response of initial wide distributions as observed in a vertical well

The general discrepancy between permeability values obtained from PTA and any representative statistical parameters of the actual distribution within the reservoir model is attributed to the establishment of preferred flow paths. By following the path of least resistance, higher permeable regions are over proportionally penetrated, while bypassing low permeable regions. Being based on an equivalent isotropic media approach, PTA is dominated by higher permeable regions and does not yield a consistent description of the actual reservoir in cases of distinct spatial heterogeneity. This explanation is supported by PTA being capable of retrieving horizontal permeability with reasonable accuracy from the vertical well test simulated on the grid initialized with a randomly distributed permeability field.

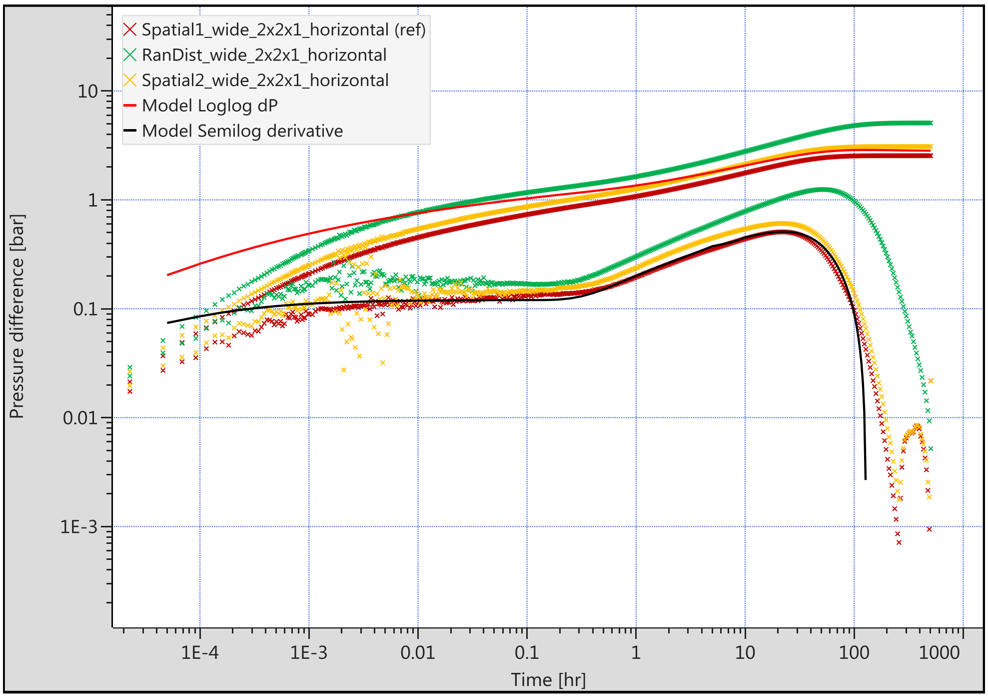

Figure 47 - BHP response of initial wide distributions as observed in a horizontal well

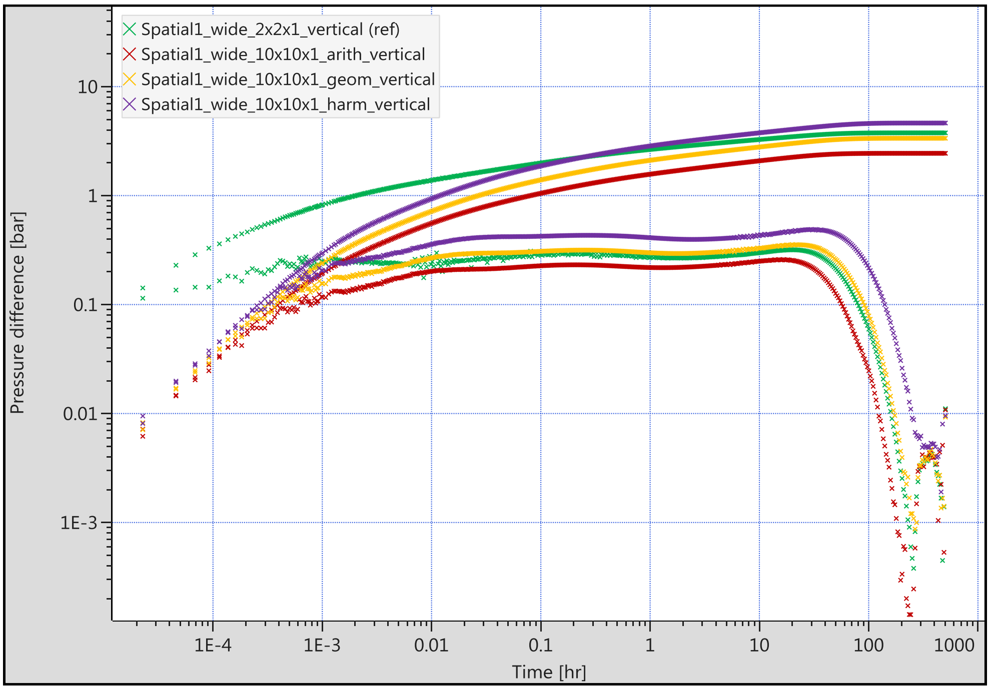

Figure 48 – BHP response of initial and upscaled grids in a vertical well (broad distribution)

Upscaling data, which spans several orders of magnitude, is significantly more challenging than upscaling narrow distributions. Figure 48 and Figure 49 illustrate changes in the pressure response as a result of various upscaling methods. It can be observed that upscaling based on harmonic averaging shifts the pressure derivative stabilizations upwards for both a vertical and a horizontal well. On the contrary, arithmetic averaging results in a downward shift of the pressure derivative. Both can be explained by the arithmetic and the harmonic mean to favor larger or smaller values during the computation of the representative average, respectively. This effect is well-known and depicted in Figure 50. Therefore, the assumption of actual permeability being constrained by the harmonic average as lower and arithmetic average as upper bound is often applied. As expected, the geometric mean has resulted in the most appropriate averaging technique to be used during upscaling. Although the distribution is significantly narrowed down, the respective change in the pressure derivative is rather minor, which is attributed to the absence of a severe shift of the distribution. The origin of the noise in the pressure data depicted in Figure 49 has not been fully understood.

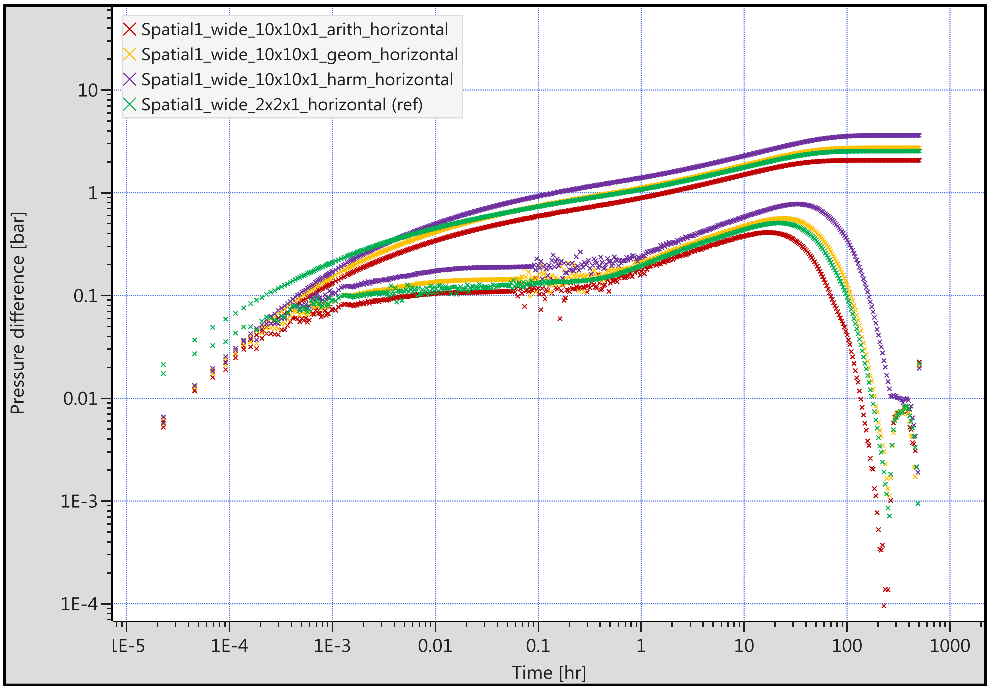

Figure 49 - BHP response of initial and upscaled grids in a horizontal well (broad distribution)

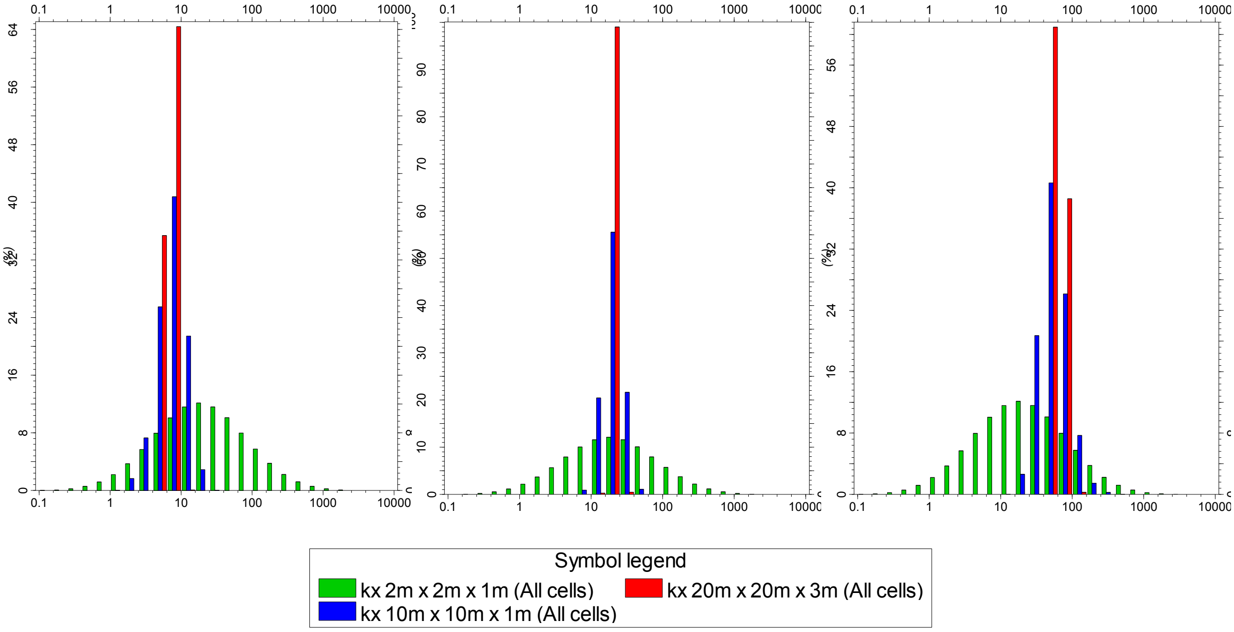

(a) Harmonic upscaling (b) Geometric upscaling (c) Arithmetic upscaling

Figure 50 – Permeability distribution (mD) shifts associated with various permeability upscaling methods

7 The Effect of Polymer Injection

To comprehensively model polymer injection, it is necessary to include conservation equations for the polymer and to represent the adsorption behavior of polymer molecules, the reduction of rock permeability to the aqueous phase after contact with the polymer, the dispersion of the polymer slug, and the non-Newtonian behavior of the polymer solution. Furthermore, certain polymers exhibit strong sensitivities to the presence of certain salts, which influence the viscosity characteristics of the polymer solutions. The flow of polymer solution through the porous media is assumed to take place within the water phase. Hence, a slightly modified black oil model can be applied to simulate polymer injection.

For the current study, the consideration of non-Newtonian behavior and salinity effects is excluded and polymer solutions are modeled as Newtonian fluids. Effects of physical dispersion at the leading edge of the slug as well as viscous fingering at the rear edge are minimized by suppressing any segregation between the water and the injected polymer solution. The simulator represents the polymer as a fully miscible component included in the aqueous phase. The viscosity of the polymer solution increases with polymer concentration and is calculated by applying certain factors to the water viscosity in the respective grid block. These factors are required input to the simulator in the form of look-up tables of viscosity multiplier as a function of cell polymer concentration.

Polymer adsorption describes the loss of polymer molecules to the rock formation, resulting in a stripped polymer region at the leading edge of the slug. The adsorption model assumes that the reservoir rock instantaneously strips polymer from the solution upon contact until the rock is saturated. The maximum amount of adsorption possible is required as input. Polymer adsorption is considered irreversible and permeability reduction is accounted for by the permeability resistance factor. In Eclipse, the permeability reduction to the aqueous phase in a certain grid block is proportional to the amount of polymer adsorbed on the rock. The actual permeability reduction factor is given by eq. (45) and increases from unity to the RRF as the grid block becomes saturated with adsorbed polymer. The fraction in the equation denotes the ratio of the actual amount of polymer adsorbed in a grid block to the block's adsorptive capacity.

$$R_k = 1.0 + (R_{rf} - 1.0)\frac{C_P^a}{C_P^{a,max}} \tag{45}$$

During PTA the responses of all simulated models are analyzed as single-phase water models. Although radial composite models have been established to evaluate pressure transients associated with radial flow origination from vertical wells, horizontal wells exhibit spatially less confined pressure propagation. Since this complicates the moving boundary problem of a composite model into a changing geometry problem, a more applicable and general approach had to be developed. Furthermore, gained insights will possess a higher likelihood of being transferrable to other cases compared to composite models, which are prone to fail for heterogeneous reservoirs.

7.1 Model Validation

Before the influence of varying polymer viscosity and adsorption behavior is investigated in detail, a homogenous model is used to determine a proper grid resolution for the subsequent analyses. For this initial screening, rock polymer interaction has been suppressed by defining a negligible polymer adsorption value and a RRF of unity. WBS has been assigned a negligible value as well and skin is defined with zero. The model set-up as well as the injection schedule are provided in Table 23. The injection rate has been set to 500 scm/d and 2000 scm/d for the vertical and horizontal well, respectively. For both wells polymer injection has been simulated on three different grids. Using a constant cell thickness of 1 m, horizontal grid increments of 40 m, 20 m, and 10 m have been studied. Pure water injection on the 10 m grid has been simulated as reference case. A comparison of the total pressure build-up on the high resolution grid shows a pressure increase of 5.4 bar for the water and 34.7 bar for the polymer injection into the vertical well. For the horizontal well a total pressure increase of 6.9 bar has been observed for pure water injection and 11.5 bar during polymer injection.

Table 23 - Model set-up for validation of polymer injection cases

Parameter	**Value**
Dimension in X, m	6000
Dimension in Y, m	6000
Dimension in Z, m	21
Porosity, -	0.2
Horizontal well length, m	800
Initialization duration, d	7
Injection duration, d	115
Shut-in duration, d	115
Injected polymer viscosity, cP	5.5

Figure 51 and Figure 52 depict the pressure transients as result of the stated polymer injection schedule together with the pure water base case for the vertical and horizontal well, respectively. For both well types, all late time radial flow responses coincide on the same plateau, emphasizing that the horizontal permeability of the far field can be estimated from each single response. Matching the late time radial flow stabilization reveals a value of 487 mD and 495 mD for the vertical and the horizontal case, respectively. Both values are in very good agreement with the defined 500 mD.

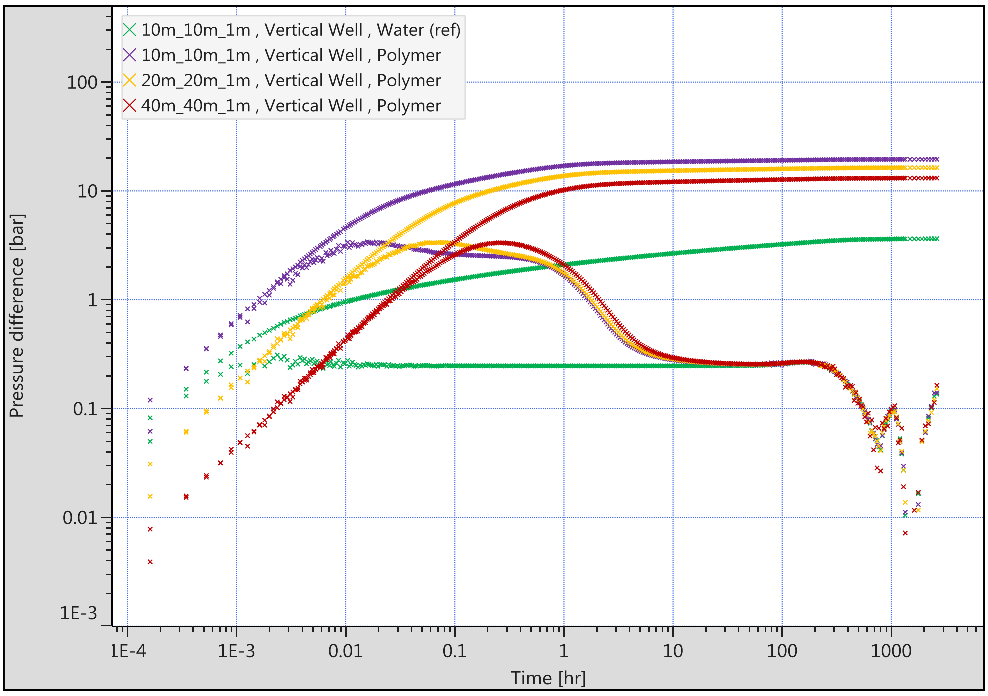

Figure 51 – Grid size influence on BHP response due to polymer injection in a vertical well

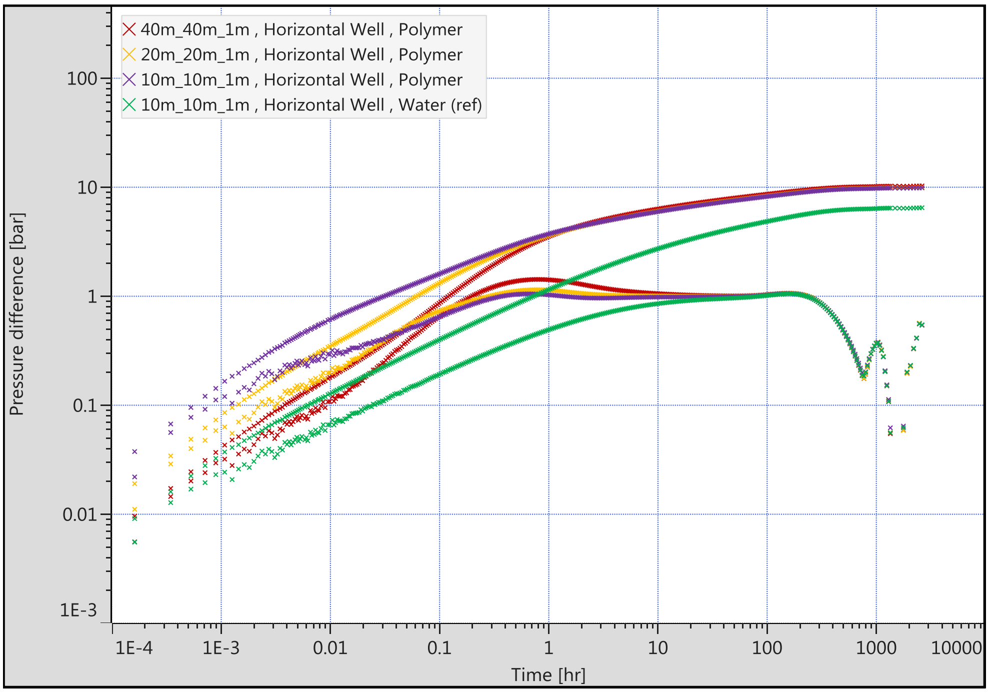

Figure 52 - Grid size influence on BHP response due to polymer injection in a horizontal well

As one can obtain form Figure 51, the pressure transient experiences a clear transition between two different radial flow stabilizations during the middle time. While the early-time response is characterized by the near wellbore region flooded with polymer, the outer region is still filled with brine. Since the early-time stabilization is only clearly established on the 10m resolution grid, this marks the maximum resolution to ensure reliable PTA analysis for polymer injection in a vertical well. For the horizontal well, the early-time derivative experiences a decreasing slope with increasing grid refinement and no distinct common feature to be used as an indicator for a systematic analysis. However, the rather noisy part of the very early data exhibits a common slope, which will be discussed later. In order to explicitly refine this feature, a LGR will be applied around the horizontal well for more detailed analysis. The rest of the grid can be discretized by 20 m increments, because no distinct difference between the 10 m and 20 m response can be obtained.

Matching the early time radial flow of the highly resolved polymer case in the vertical well (Figure 53) yields a horizontal permeability of 49 mD. As already mentioned, this region refers to the polymer bank, which means that PTA results obtained for water as analysis fluid cannot directly be used. As discussed in chapter 2.4.2, the permeability-thickness product during horizontal radial flow can be calculated using eq. (16), which can be rearranged to yield the mobility of the investigated zone according to eq. (46).

$$\frac{k}{\mu} = \lambda = 162.6\,\frac{q\,B}{h\,m} \tag{46}$$

Assuming consistent mobility between the actual reservoir model and the analytical description generated during PTA, eq. (47) can be used to convert differences in permeability derived from PTA into the actual differences in viscosity between the polymer in the reservoir and the analysis fluid. The viscosity $\mu_{PTA,W}$ refers to the water viscosity specified in the analytical model used for PTA and $k_{PTA,W}$ represents the permeability directly derived from matching the observed polymer pressure response based on the defined water properties. The viscosity μ_P denotes the effective in-situ polymer viscosity and k_P refers to the absolute permeability with respect to water in the presence of polymer.

$$\frac{k_P}{\mu_P} = \frac{k_{PTA,W}}{\mu_{PTA,W}} \tag{47}$$

To capture the effect of polymer adsorption and associated permeability reduction, the absolute permeability, to which the polymer solution is exposed to, k_P can be related to the absolute permeability of the formation $k_{H,abs}$ by incorporating the actual permeability reduction factor R_k according to eq. (48).

$$k_P = \frac{1}{R_k} k_{H,abs} \tag{48}$$

The unaltered absolute rock permeability $k_{H,abs}$ can either be obtained directly from the reservoir model for the synthetic cases discussed within the scope of this thesis or, more practically, be determined by a prior conducted single-phase water injection fall-off test. The apparent viscosity of the polymer within the reservoir can eventually be determined based on the permeability ratio of the absolute rock permeability $k_{H,abs}$ and the matched permeability with a known water viscosity from PTA as given by eq. (49).

$$\mu_{app} = \mu_P \, R_k = \mu_{PTA,W} \frac{k_{H,abs}}{k_{PTA,W}} \tag{49}$$

Considering the 487 mD obtained from the pure water base case as representative horizontal permeability of the model, the in-situ polymer viscosity yields 5.47 cP according to eq. (50), which is in reasonable agreement with further analyses of model data.

$$\mu_{app} = \frac{487 \; mD}{49 \; mD} \, 0.55 \; cP = 5.47 \; cP \tag{50}$$

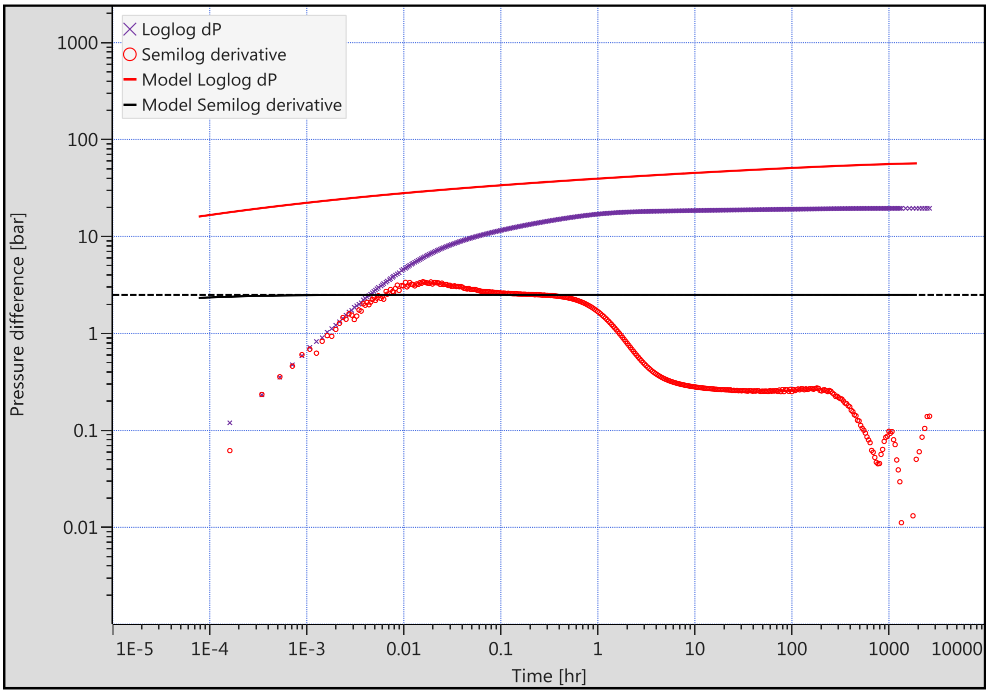

Figure 53 – BHP response of the vertical well on the 10m x 10m x 1m grid model

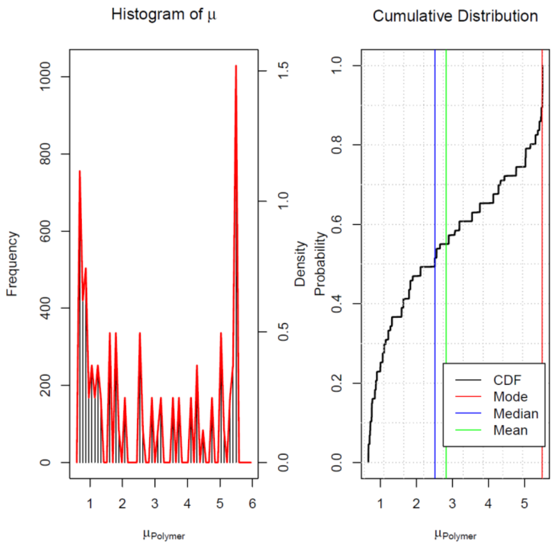

Figure 54 – Water viscosity (cP) distribution on the 10m x 10m x 1m grid after polymer injection

Figure 54 depicts the distribution of water viscosity of all cells containing a polymer concentration of more than 20 ppm. Since polymer is modelled as a fully miscible aqueous component altering viscosity, water viscosity actually corresponds to the viscosity of the polymer solution. As one can obtain, the value of 5.47 cP is in good agreement with the mode of the distribution. Although, the mode is often of little value due to its significant dependency on the underlying bin size, Figure 55 (c) reveals the formation of a well-defined polymer bank around the well of similar viscosity. The influence of the establishment of a clear bank with constant viscosity can be sufficiently matched between the actual distribution in the grid and the pressure transient responses depicted in Figure 51.

(a) 40 m horizontal grid size

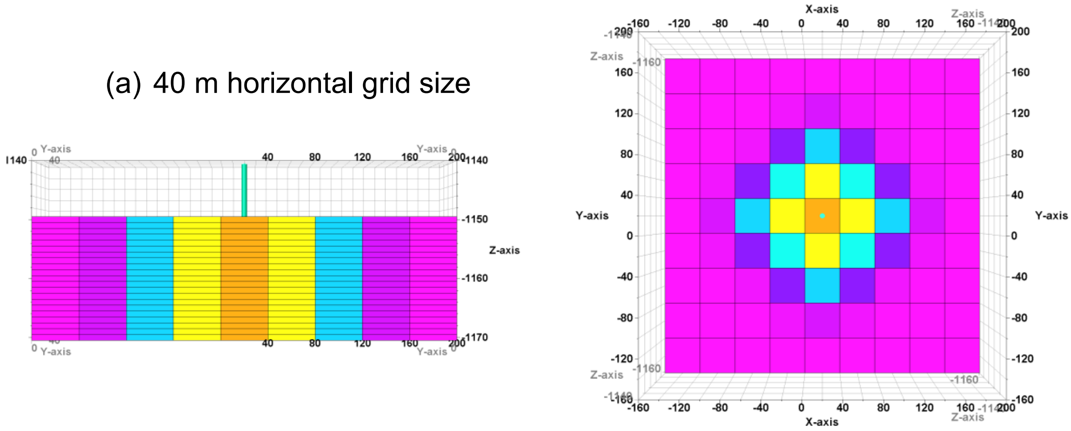

(b) 20 m horizontal grid size

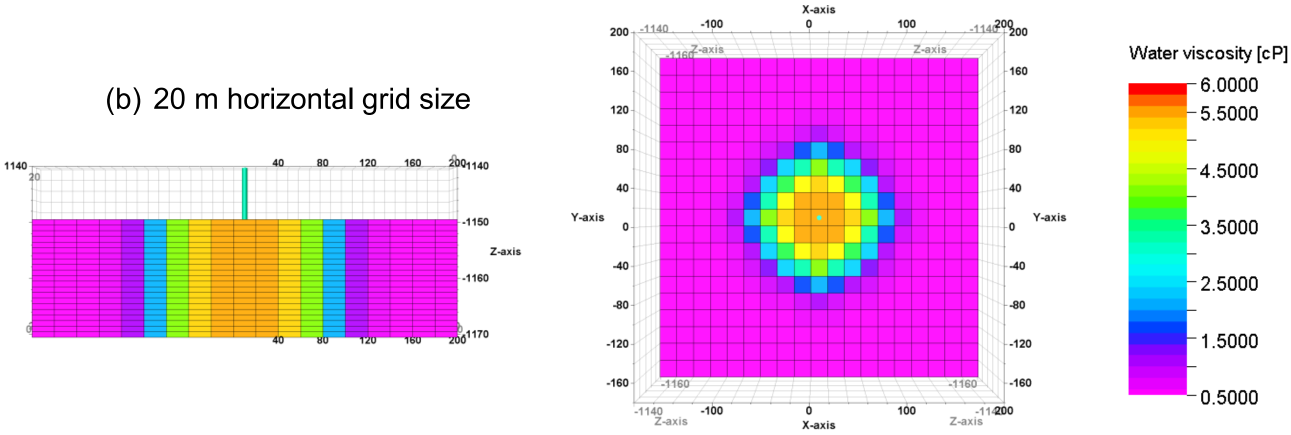

(c) 10 m horizontal grid size

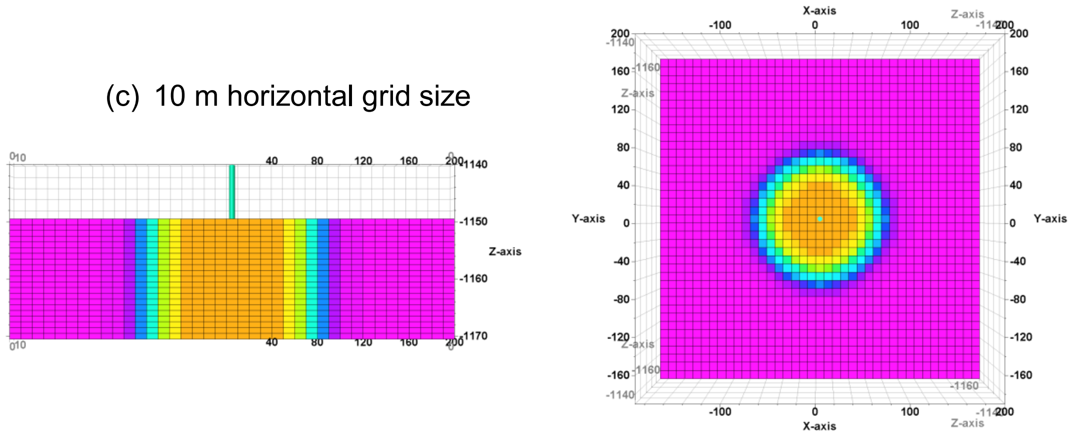

Figure 55 - Water viscosity after 16 weeks of injecting 500 scm/d of 5.5 cP polymer solution

7.2 Viscosity Determination in Horizontal Wells

With the objective of deriving a similar relationship to eq. (47), which yields in-situ viscosity from PTA conducted on horizontal well pressure responses, a variety of further simulation cases have been run and analyzed. As a starting point, the reservoir model introduced in the previous chapter has been discretized by 20 m increments in both horizontal directions, and 1 m increments in the vertical direction. The near wellbore region has been locally refined with a horizontal grid size of 4 m all-around the well reaching 150 m into the reservoir. LGR has been applied to assure proper interpretation of the early time vertical radial flow regime. Polymer injection has been modeled for durations of 8, 16, 26, and 52 weeks with a viscosity of the injection stream of 5.5 cP. Polymer adsorption and permeability reduction is considered for some of the cases, but will not be explained in detail here. The influence of various adsorption behaviors is elaborated in the subsequent chapter 0.

Figure 56 depicts the pressure transients for all four injection periods assuming negligible polymer adsorption. It is clearly shown that all responses coincide for the early time vertical radial flow period and stabilize late on the same plateau during horizontal radial flow. This emphasizes that the near wellbore region is sufficiently high resolved to capture relevant early time effects and that all analytical PTA models would be capable of retrieving horizontal permeability. Furthermore, one can obtain that all cases follow the exact same straight line during the linear flow regime, regardless of injection duration. Hence, subsequent analyses have been focused on evaluating this characteristic line.

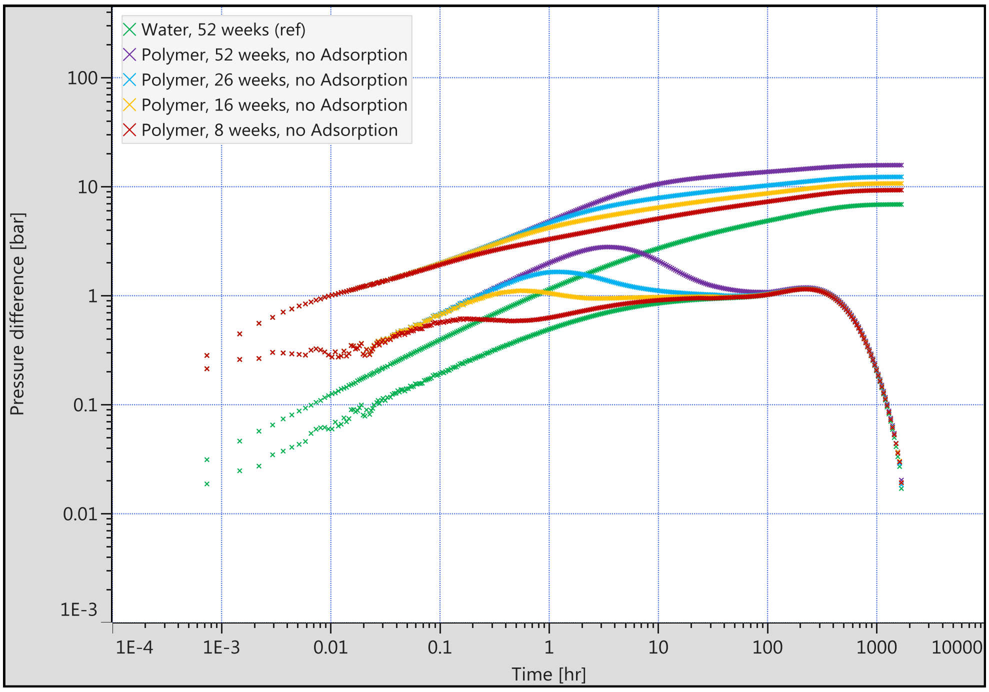

Figure 56 – The influence of polymer injection duration prior to fall-off test (negligible polymer adsorption)

Matching the linear flow straight line correctly, provides insights about effective well length and horizontal permeability according to eq. (35). Rearranging yields eq. (51) with the right-hand side being solely dependent on rock properties, the well test schedule, and the extracted slope, which can be assumed constant for a certain test setting. Hence, the influence of different fluid properties can be compensated by a proper scaling of the PTA results as denoted in eq. (52). The subscript *PTA,W* refers to values obtained from single-phase water PTA conducted on pressure transients originating from polymer injection. The permeability denoted as $k_{H,Poly}$ describes the horizontal permeability, to which the polymer solution is exposed to. The parameter $L_{w,Poly}$ refers to the effective well length and effective in-situ polymer viscosity is given by μ_P.

$$\frac{k_H\, L_w^2}{\mu} = \frac{16.52}{\phi\, c_t}\left(\frac{q\, B}{h\, m_{LF}}\right)^2 \tag{51}$$

$$\mu_P = \mu_{PTA,W}\, \frac{k_{H,Poly}}{k_{PTA,W}}\left(\frac{L_{w,Poly}}{L_{PTA,W}}\right)^2 \tag{52}$$

Equation (52) implies that both the polymer affected horizontal permeability and the effective well length have to be extracted from the linear flow match to yield the effective in-situ polymer viscosity. The effective well length $L_{w,Poly}$ is mostly fixed and known or has to be determined by matching a prior water injection fall-off test. The very same test can be used to derive the absolute permeability of the formation denoted as $k_{H,abs}$. If the shut-in duration of the polymer injection fall-off test is sufficiently long, $k_{H,abs}$ can also be obtained directly from matching the polymer unaffected late time radial flow of the polymer injection case. The permeability, which dominates the linear flow of the polymer solution $k_{H,Poly}$ can be related to the formation's absolute permeability according to eq. (48). Incorporating the effect of considerable permeability reduction in the polymer flooded zone yields the apparent polymer viscosity according to eq. (53).

$$\mu_{app} = \mu_P\, R_k = \mu_{PTA,W} \frac{k_{H,abs}}{k_{PTA,W}}\left(\frac{L_{w,Poly}}{L_{PTA,W}}\right)^2 \tag{53}$$

Since the determination of both horizontal permeability and effective well length is not feasible from solely matching the observed linear flow straight line, one of the parameters has to be constrained to yield an applicable version of eq. (53). The fact that all pressure responses converge towards the same late time radial flow stabilization coinciding with the pure water pressure derivative suggests constraining horizontal permeability. By matching the polymer unaffected late time plateau of the derivative, it is assumed that $k_{PTA,W} = k_{H,abs}$. Hence, the difference of the effective well length derived from PTA reveals the difference in apparent polymer viscosity. This approach allows the determination of apparent polymer viscosity based on the ratio of the actual and the apparent effective well length during PTA. It has to be noted that this approach is based on the assumption that the observed far field equivalent isotropic permeability value is also representative to characterize the reservoir region dominating the linear flow regime.

A left shift of the linear flow straight line corresponds to a decrease in effective well length, assuming constant horizontal permeability. Hence, the increasing apparent viscosity as a result of polymer adsorption and permeability reduction can be observed by the pressure response plotting further left compared to a case assuming negligible adsorption, as depicted in Figure 57. The duration of polymer injection affects the length of the straight line. An increasing thickness of the polymer bank due to extended injection time yields a longer linear flow straight. Hence, the deviation of the pressure response from the straight line can be matched qualitatively to the penetration depth of the polymer into the reservoir. However, no thorough quantitative description could be attained. As it can be observed from the trend depicted in the figure, a polymer injection extending into the late time radial flow geometry will plot as a pressure derivative stabilization on an elevated plateau as an effect of higher viscosity and permeability reduction. The viscosity of the polymer can be determined based on the mobility ratio as explained above by eq. (47). The actual permeability in that case can either be determined from PTA by matching the derivative stabilization or a scaling of the polymer unaffected permeability in the far-field with the actual permeability reduction factor.

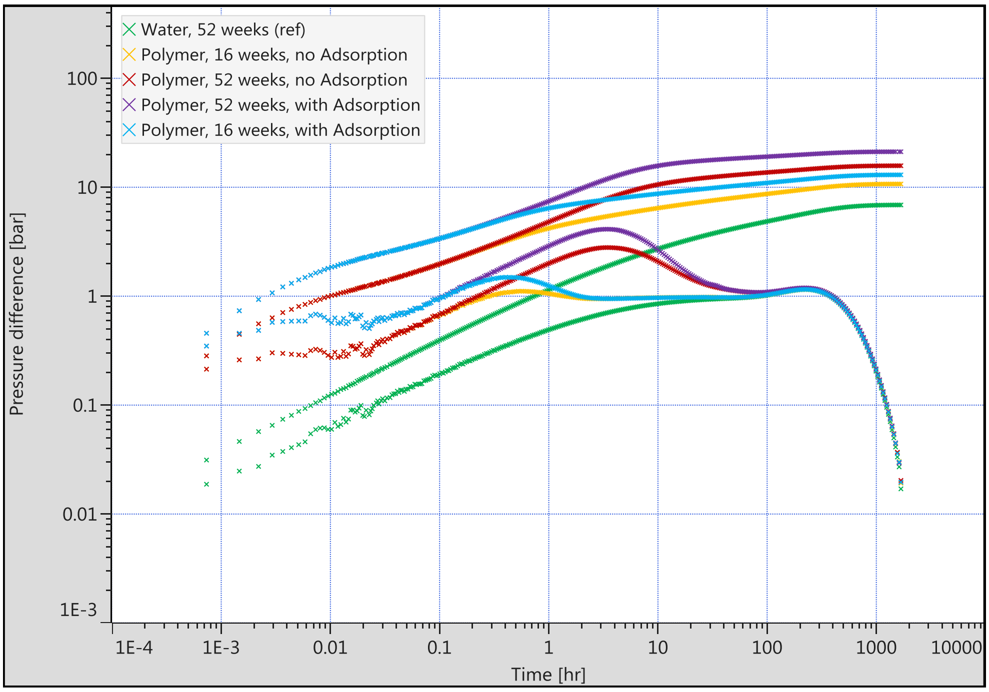

Figure 57 – The influence of polymer adsorption behavior on variable polymer injection durations prior to shut-in

The proposed workflow is briefly explained in this paragraph. Figure 58 depicts the match of the pressure transient data for the pure water baseline, which yields a horizontal permeability of 490 mD. This value is in good agreement with the predefined 500 mD. The extracted model provides the basis for the analysis of the polymer cases. Therefore, only the linear straight line of the diagnostic tool (dotted line) in Saphir needs to be aligned with the linear flow straight lines of the respective pressure responses (Figure 59 and Figure 60). This shift influences the extracted well length L_w as well as the vertical to horizontal permeability ratio k_V/k_H, while keeping horizontal permeability unaltered. Table 24 summarizes the analytical model parameters for the pure water base case as well as polymer cases with and without polymer adsorption effects enabled. It has to be mentioned that the extracted k_V/k_H ratios yield meaningless values. This is attributed to the pure water base case not resolving the early time radial flow as a result of large vertical permeability as discussed earlier.

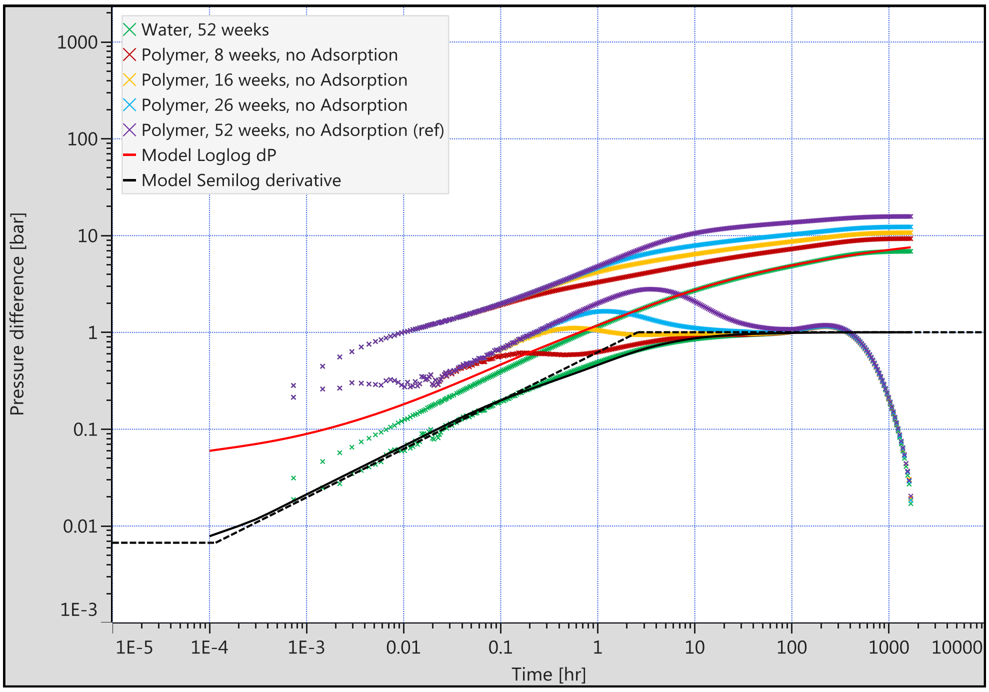

Figure 58 – Match of the pure water response as baseline for the viscosity determination

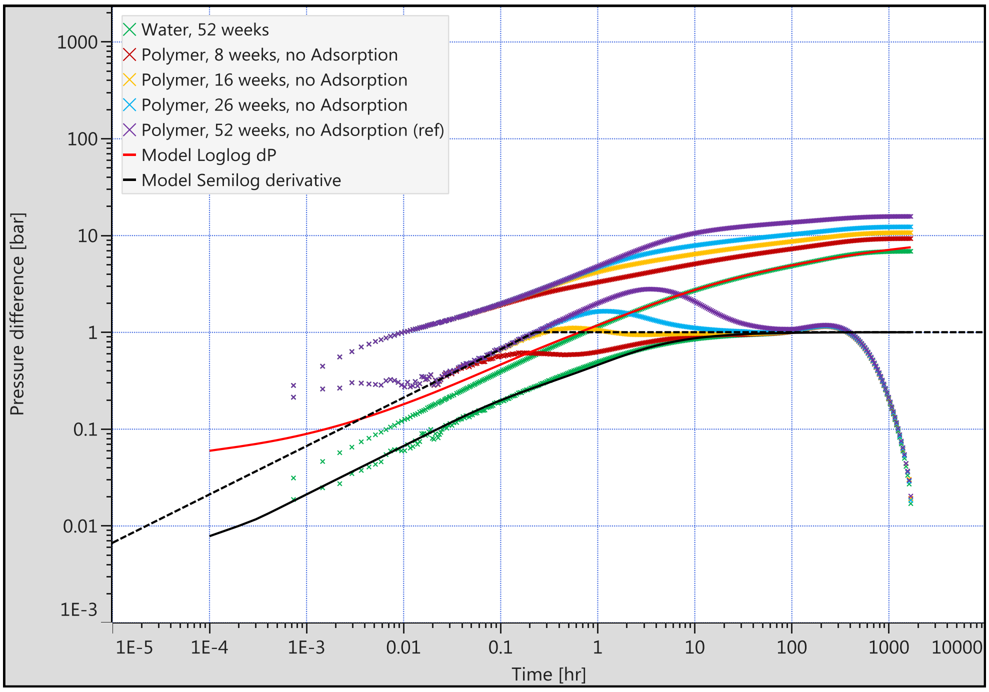

Figure 59 – Match of linear flow response with diagnostic tool (negligible polymer adsorption)

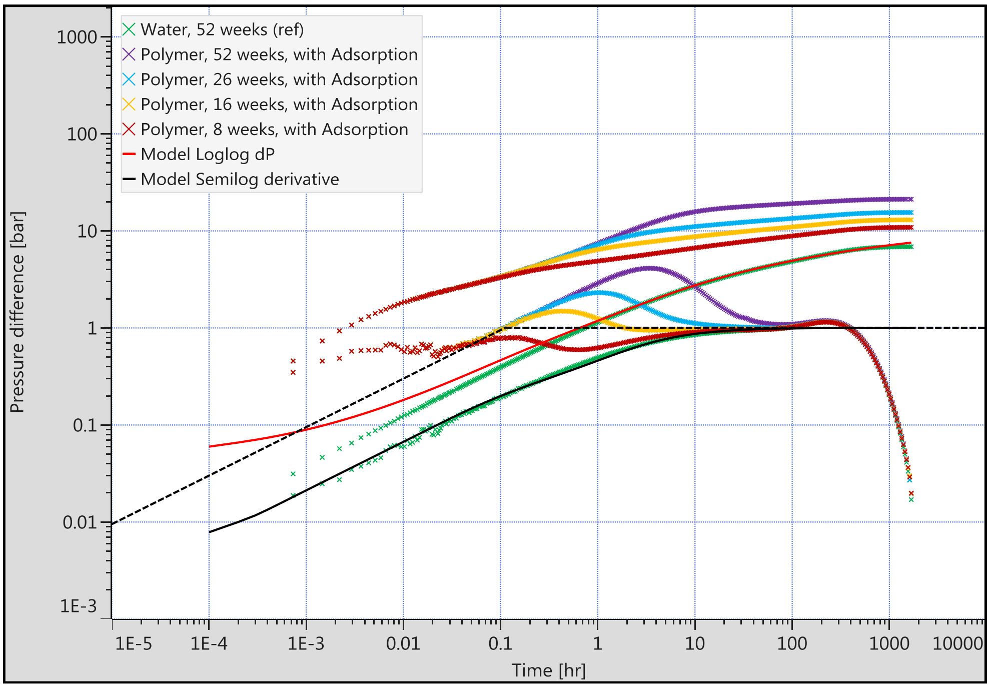

Figure 60 – Match of linear flow response with diagnostic tool (considerable polymer adsorption)

Table 24 – Comparison of PTA results for polymer and water injection

		Water Base Case	**Polymer injection**	
			Negligible adsorption	*Considerable adsorption*
k_H	mD	490	490	490
$2\ L_w$	m	800	254	178
k_V/k_H	-	10	154	155
skin	-	0	0	0

Although the vertical to horizontal permeability ratios possess little value, the extracted effective well lengths are capable of reproducing the polymer apparent viscosity with reasonable accuracy. The calculation is depicted exemplarily for the case of negligible polymer adsorption by eq. (54), while all the results are presented in Table 25. As one can obtain, the distribution of viscosity values in the numerical model narrows down with increasing injection duration. This can be explained by the establishment of a dominating polymer bank around the injector. The calculated apparent viscosity based on PTA tends to characterize the upper range of the distribution, which emphasize the dominating behavior of the polymer bank. After 52 weeks of injection, the extracted viscosity value is located between the median and the mode of the entire distributions.

$$\mu_{app} = 0.55\ cP \left(\frac{800\ m}{254\ m}\right)^2 = 5.46\ cP \qquad (54)$$

Table 25 - Comparison of viscosity values derived from PTA with statistical model analysis

μ, cP		**Negligible adsorption**				**Considerable adsorption**			
		Polymer Injection Duration, weeks							
		8	16	26	52	8	16	26	52
PTA		**5.46**				**11.11**			
Model	Min	0.68	0.56	0.68	0.69	0.86	0.71	0.77	0.72
	Mode	0.87	0.58	5.95	5.95	1.22	11.71	11.71	11.92
	Median	2.69	2.31	3.79	4.50	4.12	7.10	9.04	11.02
	Mean	3.02	2.84	3.60	3.89	5.14	6.35	7.41	7.87
	Max	5.95	5.99	5.99	5.99	11.49	11.80	11.81	11.80

The viscosity distributions have been generated by analyzing the grid properties exported from Petrel. During the analysis only cells containing a polymer cell concentration of more than 20 ppm have been considered. Knowing the mutual distribution of viscosity and actual permeability reduction factor, the apparent viscosity can be calculated according to eq. (40). The extracted distributions are illustrated in Table 26 for the case of 52 weeks of polymer injection.

Since PTA results are limited to yield the apparent viscosity of a fluid, effective polymer viscosity can only be computed, if the adsorption behavior of the polymer is properly understood, so that the RRF can effectively be constrained.

Table 26 – Statistical evaluation of model viscosity (in cP) after 52 weeks of polymer injection

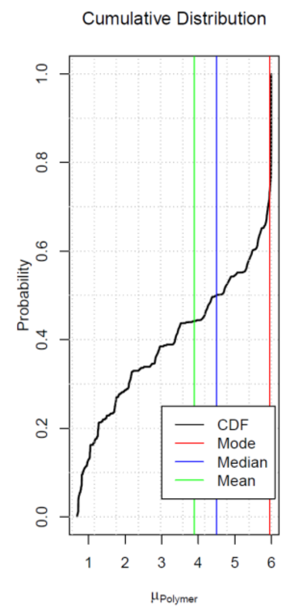

(a) Negligible adsorption

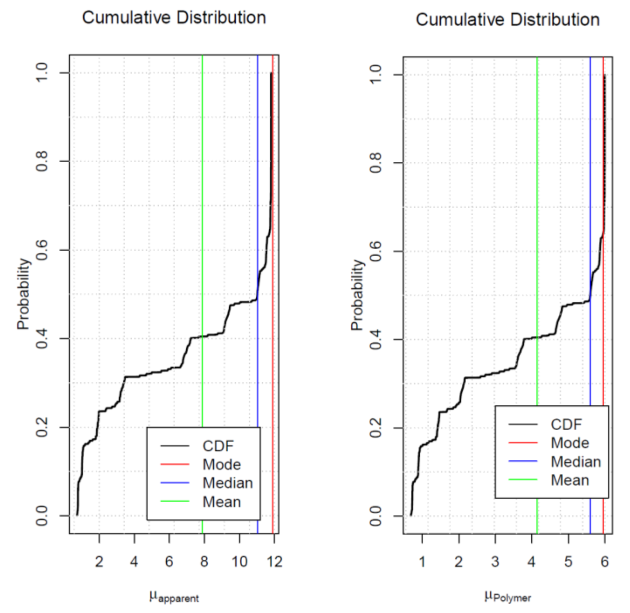

(b) Considerable adsorption

In a last step the applicability of the ROI function in Saphir to localize the polymer front within the reservoir has been investigated. Therefore, the deviation of the pressure response from the straight line has been identified by the ROI tool and the respective result has been compared to the penetration depth simulated in Eclipse. While for cases with negligible polymer adsorption reasonable agreement could be obtained, this approximation fails for cases with significant adsorption as presented in Table 27. The investigation radius provided by Saphir is computed according to eq. (20), which has been developed for drawdown analyses during radial diffusion of a line source well in an infinite homogenous reservoir. For any deviations from this geometry, this value will only be an indicative approximation. However, an accurate prediction of the location of the polymer front has not been investigated further under the scope of this thesis.

Table 27 - Comparison of extracted polymer penetration depths

Injection duration, weeks	**Negligible adsorption**		**Considerable adsorption**	
	ROI	*Model*	*ROI*	*Model*
52	137	145	136	103
26	92	85	93	55
16	58	55	64	39
8	32	30	30	23

7.3 The Influence of Polymer Viscosity and Adsorption

In this chapter, the influence of different polymer viscosity and adsorption behavior is investigated. Therefore, five different correlations between polymer concentration and solution viscosity have been implemented. The same approach has been taken to model variable adsorption tendencies. The used correlations are depicted in Figure 61 and Figure 62 and are provided in detail in the appendices F and G.

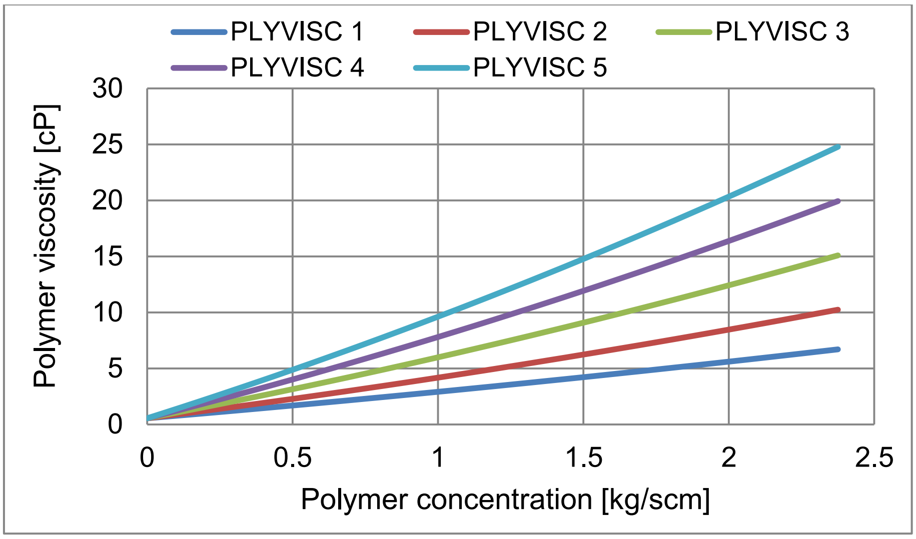

Figure 61 - Polymer viscosity correlations used for investigation

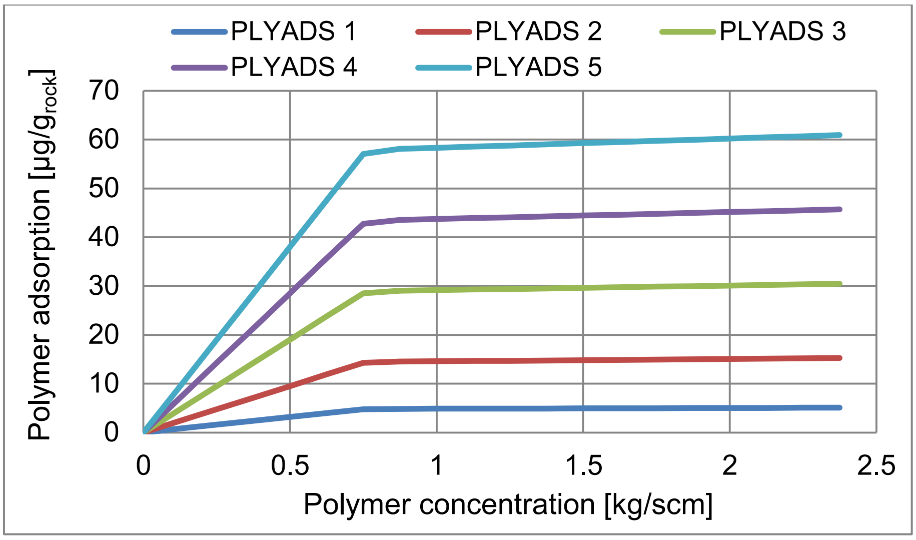

Figure 62 - Polymer adsorption correlations used for investigation

The solution viscosity correlations have been constrained to values between 4 cP and 10 cP for a polymer concentration of 1000 ppm. Although polymer adsorption behavior is hard to quantify accurately, a study conducted with hydrolyzed-polyacrylamide polymers revealed that 80 % of the adsorption data can be characterized by values below 60 µg/g$_{rock}$ [36]. The input correlations have been designed accordingly and span the range from 5 µg/g$_{rock}$ to 60 µg/g$_{rock}$ with a linear concentration dependency in the lower and an asymptotical behavior in the higher concentration range. The rock formation has been assigned a density of 2600 kg/m^3.

For the analysis, polymer solution with a concentration of 1000 ppm has been injected for 26 weeks through a 800 m long horizontal well into the homogeneous reservoir model described in the previous chapter. As summarized in Table 28, the well has subsequently been shut in for 10 weeks. To assure optimal resolution of the outset of the linear flow straight line, the area around the well is again locally refined.

Table 28 - Well test schedule for viscosity and adsorption behavior screening

Parameter	**Value**
Injection duration, weeks	26
Shut-in duration, weeks	10
Injected polymer concentration, kg/scm	1

Figure 63 depicts the pressure transients associated with the injection of polymer solution honoring different viscosity correlations. Each correlation can be understood as a different injection viscosity. Polymer adsorption has been disabled to study the sole influence of viscosity. It can be obtained that all responses yield the same late time radial flow stabilization as the pure water baseline, which is an important prerequisite for the proposed workflow to determine in-situ polymer viscosity. The pressure derivative of the water case has been matched again by 490 mD horizontal permeability, a vertical to horizontal permeability ratio of 10 and zero skin. Subsequently, the linear flow straight line of the analytical model has been aligned with the responses of the polymer cases, while leaving all other parameters unaltered. The extracted values for the effective well length are listed in Table 29 and provide the input for the calculation of apparent polymer viscosity according to eq. (53). The computed values are compared to actual viscosities present in the numerical model. Therefore, the statistical description of the permeability distribution within the grid is presented next to the post-processed PTA result in Table 29.

Mode, median, and mean have been calculated based on all cells with a polymer concentration exceeding 20 ppm. The mean average percentage error (MAPE) of the viscosity derived from PTA has been calculated to assess the level of conformity with each location parameter of the distribution. As one can obtain, the mode manifests as the most representative characteristic with respect to influencing the pressure response. This can be explained with the establishment of a distinct polymer bank around the injector, dominating the transient behavior, which is in good agreement with prior findings. The pressure response from the transition zone ahead of the polymer front might already deviate from the straight line and plot as part of the observed hump in Figure 63.

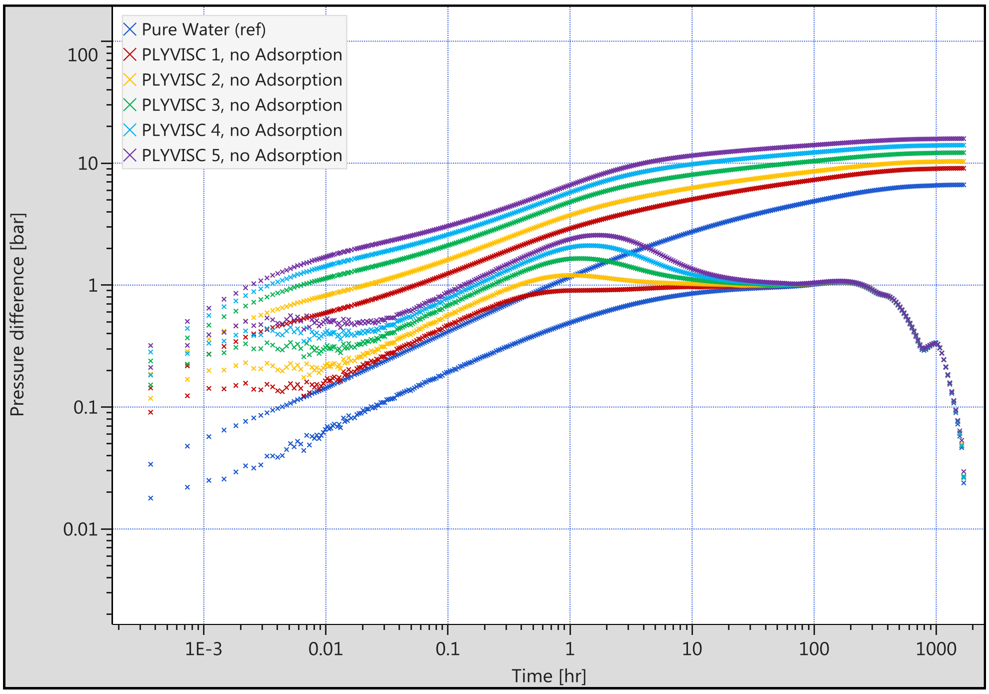

Figure 63 – The influence of different polymer viscosities

It is important to note that the statistical evaluation of the polymer distribution within the numerical grid significantly depends on the applied cut-off and bin size. After assessing the influence of cut-off values between 10 ppm and 50 ppm, excluding all cells with a polymer concentration of less than 20 ppm has been found most applicable for polymer viscosity and permeability reduction factor evaluation. While smaller cut-off values tend to skew the distribution quickly towards values of hardly affected cells, larger cut-off values exclude parts of the transition zone ahead of the polymer bank. Since the mode is essentially influenced by the bin size of the histogram, an initial screening has been conducted and revealed that sampling with a resolution of 100 bins provides most insights. Coarser sampling results in unwanted averaging effects, while too small bins might hide an actual accumulation of similar values.

Table 29 – Comparison of polymer viscosity derived from PTA with model distributions for different injection viscosities

		PTA		**Model μ_{Poly} distribution,** cP		
Case	*μ_{inj}, cP*	*2 L_w, m*	*μ_{app}, cP*	*mode*	*median*	*mean*
PLYVISC 1	2.9	355	2.8	2.9	1.6	1.7
PLYVISC 2	4.2	295	4.0	4.2	2.0	2.2
PLYVISC 3	6.0	248	5.7	6.0	2.8	3.1
PLYVISC 4	7.8	219	7.3	7.8	3.6	3.9
PLYVISC 5	9.6	196	9.2	9.6	3.0	4.6
			MAPE	4.5%	118.1%	84.0%

Plotting viscosity of the polymer injection stream against extracted apparent in-situ viscosity for all cases yields a straight line, as depicted in Figure 64. Hence, in-situ viscosity can be determined from measurements in the injection stream in cases of negligible polymer adsorption.

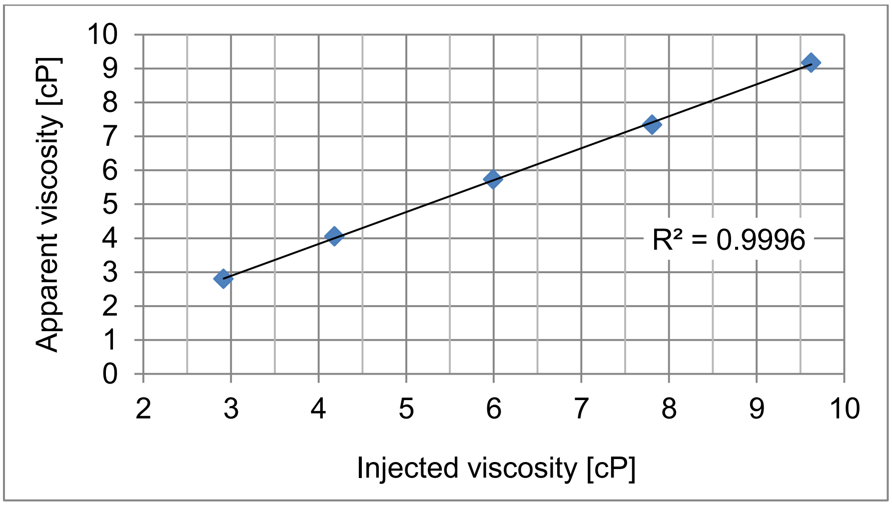

Figure 64 – Injected polymer viscosity versus apparent viscosity from PTA

Figure 65 depicts the pressure response for cases of identical viscosity of the injected polymer and varying adsorption behavior. Permeability reduction due to polymer adsorption is disabled by defining a RRF of unity. It is shown that an increase in adsorptive capacity yields an earlier flow stabilization, which can be translated into a decreased penetration of the polymer into the reservoir. The weaker the adsorption, the deeper the penetration and the more pronounced appears the hump during the transition period. All responses plot on the exact same linear flow straight line. This meets prior expectations, since adsorption is decoupled from permeability reduction, leaving the apparent viscosity unaltered.

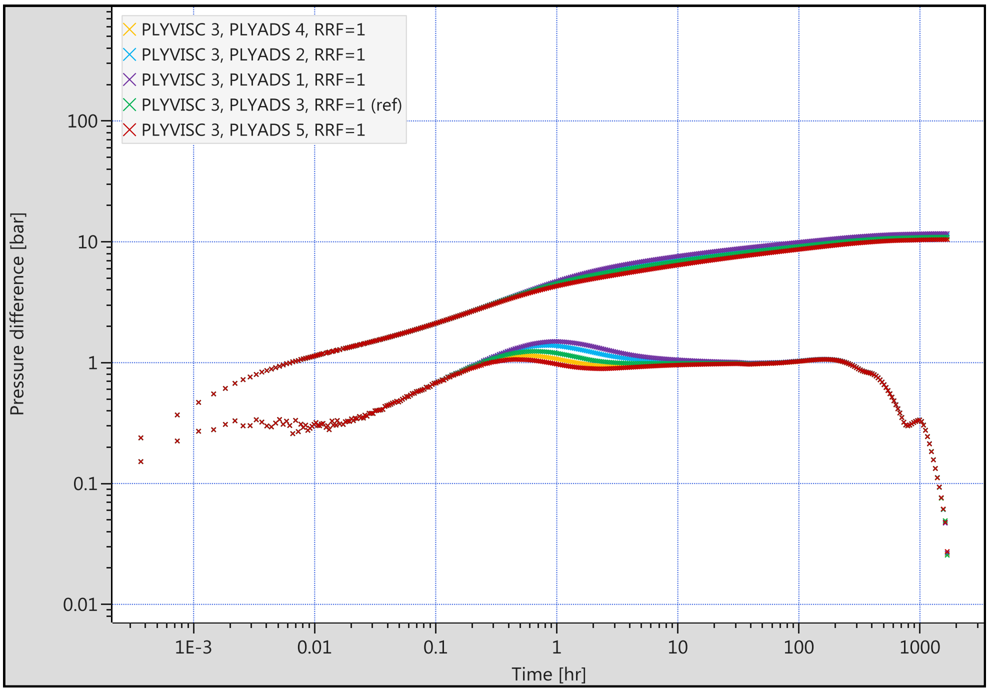

Figure 65 – The influence of different magnitudes of polymer adsorption

Table 30 - Effective polymer viscosity calculation for different RRF values

		PTA		Model	
RRF	*μ_{inj}, cP*	*2 L_w, m*	*μ_{app}, cP*	*R_k (mode)*	*μ_{eff}, cP*
1	6.00	247	5.77	1.00	5.77
2	6.00	176	11.36	1.97	5.77
3	6.00	144	16.98	2.94	5.77
4	6.00	128	21.48	3.91	5.49

Figure 66 depicts the influence of varying RRFs. All cases are simulated with the same viscosity of the injected polymer and show identical adsorption behavior. The larger the RRF, the more significant is the permanent reduction of permeability with respect to the aqueous phase after the contact with polymer. Hence, apparent polymer viscosity is proportional to the permeability reduction factor, which is clearly supported by the plot indicating an increasing upward shift of the derivative curve with an increasing RRF. Table 30 summarizes the calculation of apparent viscosity based on the extracted effective well lengths from PTA.

By incorporating the mode of the actual permeability reduction factor according to eq. (40), the effective polymer viscosity can be computed. The final values are consistent and in good agreement with injected viscosity as well as results listed in Table 30.

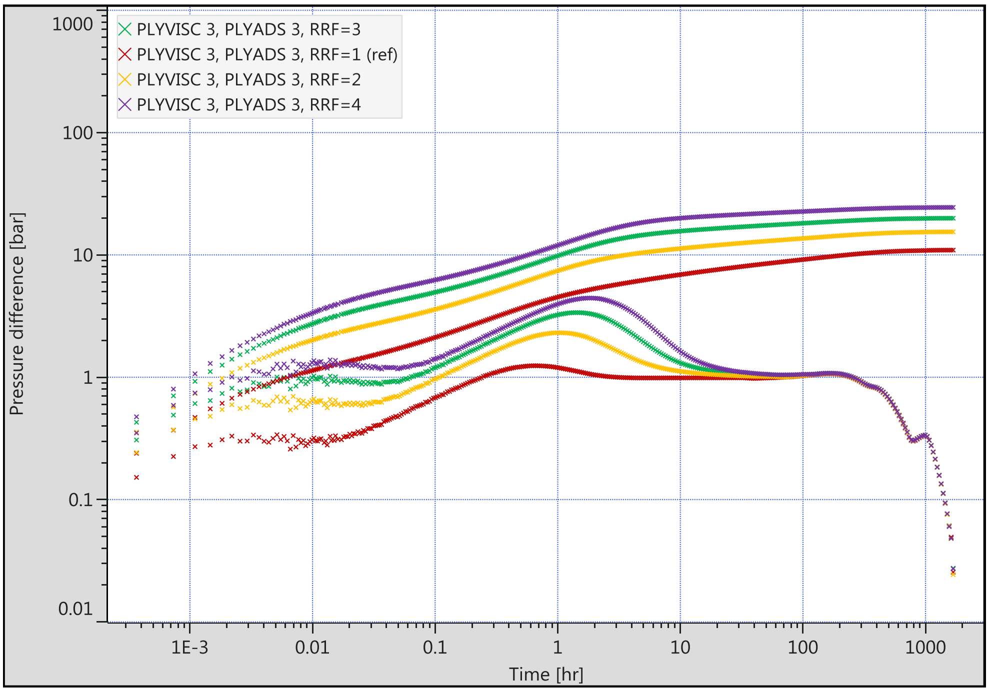

Figure 66 – The influence of different residual resistance factors

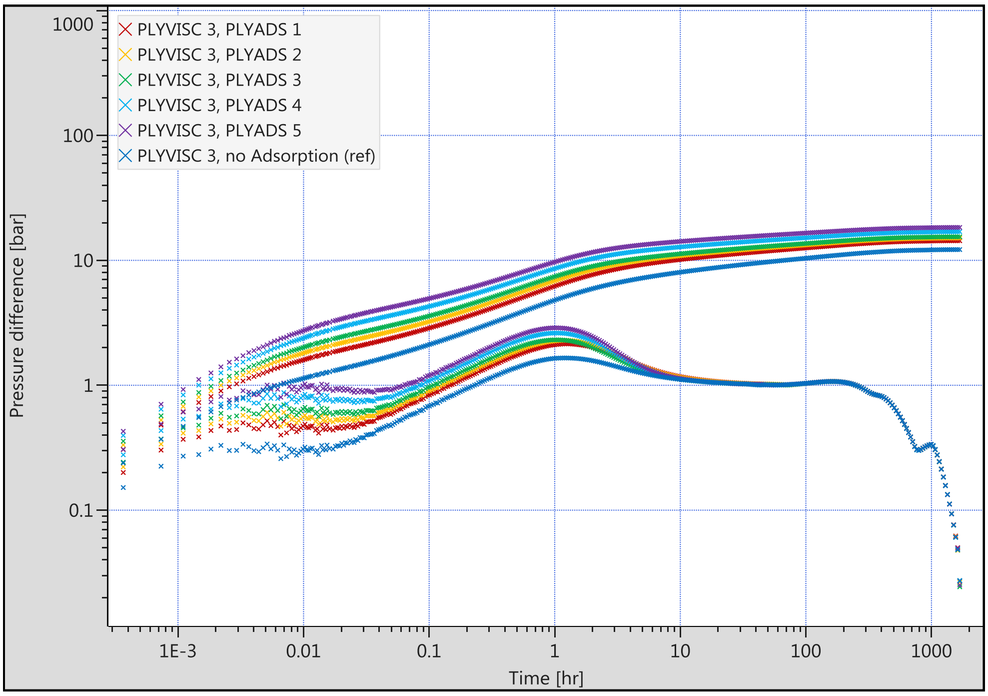

Figure 67 – The influence of combined adsorption and permeability reduction behavior

In a last analysis, different magnitudes of polymer adsorption have been aligned with corresponding permeability reduction. The influence on the pressure transients is depicted in Figure 67 and illustrates a clear increase of apparent viscosity with an increasing adsorption level by shifting the linear flow straight further left. The extracted apparent polymer viscosity can be correlated with the maximum adsorbed concentration of the polymer as shown in Figure 68.

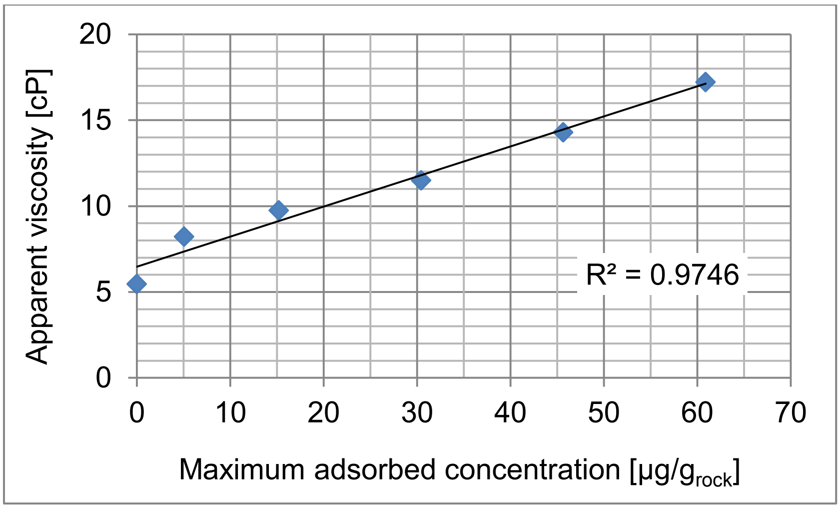

Figure 68 – Maximum adsorbed polymer concentration versus apparent viscosity from PTA

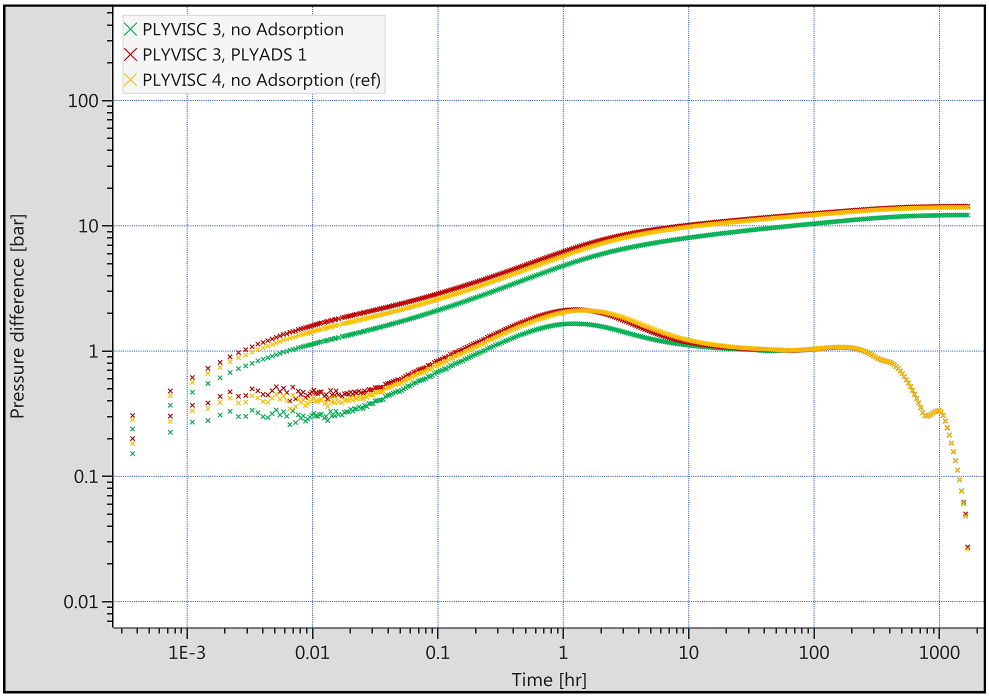

Figure 69 – The challenge of response ambiguity

Figure 69 emphasizes that the interpretation of a match of the linear flow straight line is not unambiguous. Since the retrievable effective well length can only be translated into an apparent viscosity, polymer solutions with different viscosity and adsorption behavior might result in the same response. A reliable determination of effective viscosity requires further knowledge about the in-situ permeability reduction.

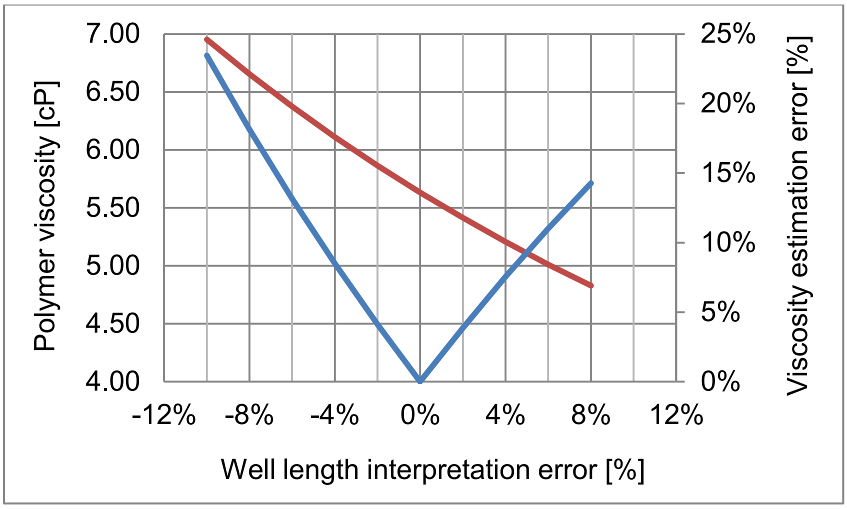

Figure 70 - Sensitivity of polymer viscosity with regards to interpreted effective well length

During the analyses, small deviations in the extracted effective well lengths have been found to exhibit a significant influence on the subsequent viscosity estimation. This is emphasized by Figure 70, which depicts the computed polymer viscosity as a function of effective well. The show case is based on 250 m constituting the correct length value. This sensitivity further increases towards smaller well lengths and underlines the necessity for LGR around the well to ensure most reliable pressure derivative interpretation.

7.4 The Influence of Various Rock Types

After PTA results have successfully been used to compute apparent polymer in-situ viscosity for a homogeneous single-phase water model, both rock and fluid heterogeneity is considered for this concluding analysis. Therefore, five different rock types have been incorporated into the homogeneous model described in the previous chapter. The specified rock types differ in porosity and permeability and are presented in Table 31. Besides the definition of various rock types and an increased polymer concentration of 2000 ppm in the injection stream, all other model parameters have been left unaltered.

Although the majority of real reservoirs is dominated by heterogeneity in the vertical direction due to their depositional history, both horizontal layers and vertical slices of different rock types have been considered. Figure 71 illustrates the implementation of the rock type heterogeneities into the model. The heterogeneous models have been set up to yield a thickness-weighted average porosity and a total permeability-thickness product equal to the homogeneous model. This ensures equal fluid in place, which is important for the pressure build-up, and principally comparable flow behavior.

Table 31 -Characteristics of different rock types

	Rock type				
	1	*2*	*3*	*4*	*5*
φ	0.1	0.15	0.2	0.25	0.3
k_H, mD	100	300	500	700	900

(a) Layered heterogeneity

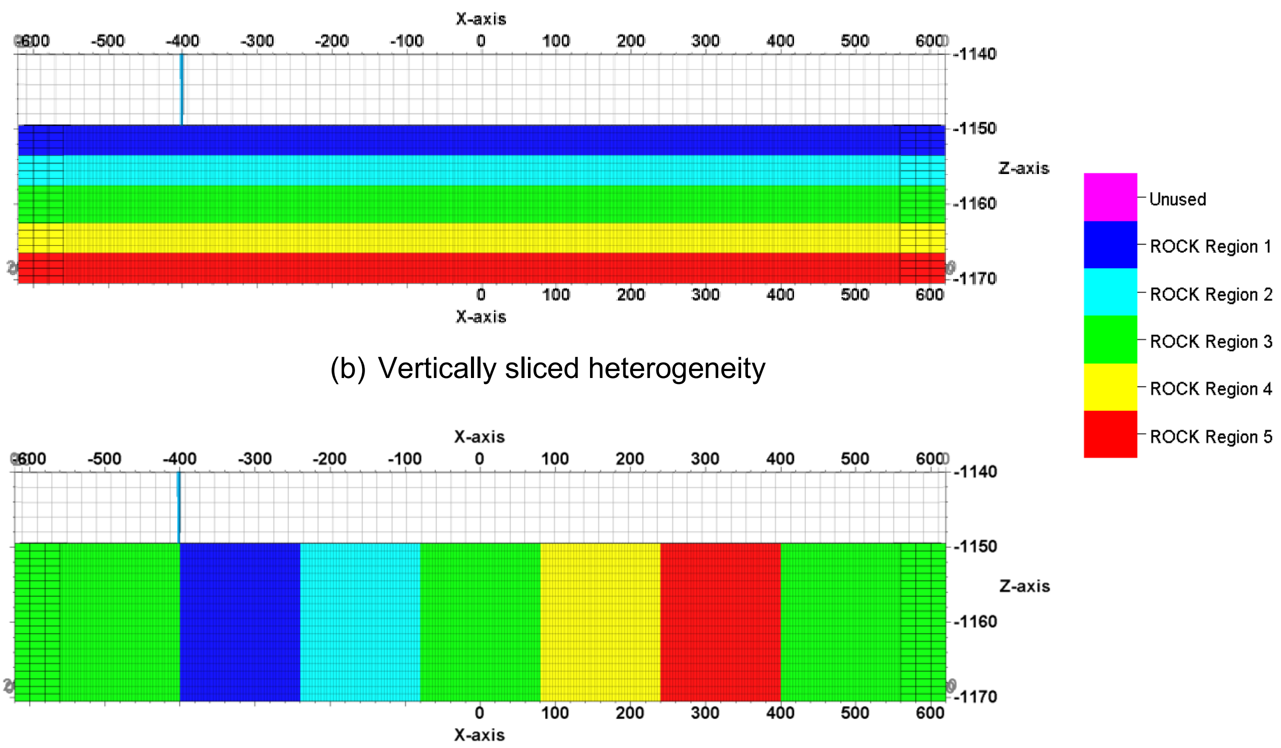

(b) Vertically sliced heterogeneity

Figure 71 - Implementation of rock type heterogeneity in the simulation model

Different rock types have been assigned different polymer adsorption behavior to investigate the respective influence on the pressure derivative. Polymer adsorption is especially challenging to quantify and no comprehensive understanding has yet bet attained. High adsorption has been observed for high clay concentrations and carbonates often exhibit higher adsorption values than silicates [36]. Since no clear correlation between formation porosity or permeability and the magnitude of polymer adsorption has been found in the literature, polymer adsorption has been assigned to the various rock types in both an increasing and a decreasing order. That means that for adsorption allocation 1, lower porosity correlates with a lower adsorption level, while for adsorption allocation 2, adsorption increases with decreasing porosity. An overview is provided in Table 32, which refers to adsorption correlations introduced in Figure 62.

To account for differences in polymer viscosity within the reservoir, the same approach has been applied by assigning different polymer PVT regions to the predefined rock types. The objective of this consideration is to approximate the non-Newtonian rheological behavior of the polymer solution. By incorporating various PVT regions with distinctly different viscosities, possible shear-thinning and shear-thickening effects within the reservoir can be replicated and help to answer the question, to which extend these effects will influence the pressure transient response. An overview of all investigated set-ups is provided in the appendices H and I, with associated BHP responses being summarized in appendix J.

Table 32 - Definition of various polymer viscosity and adsorption allocations to rock types

	Rock type				
	1	*2*	*3*	*4*	*5*
Viscosity allocation 1	PLYVISC 1	PLYVISC 2	PLYVISC 3	PLYVISC 4	PLYVISC 5
Viscosity allocation 2	PLYVISC 5	PLYVISC 4	PLYVISC 3	PLYVISC 2	PLYVISC 1
Adsorption allocation 1	PLYADS 1	PLYADS 2	PLYADS 3	PLYADS 4	PLYADS 5
Adsorption allocation 2	PLYADS 5	PLYADS 4	PLYADS 3	PLYADS 2	PLYADS 1

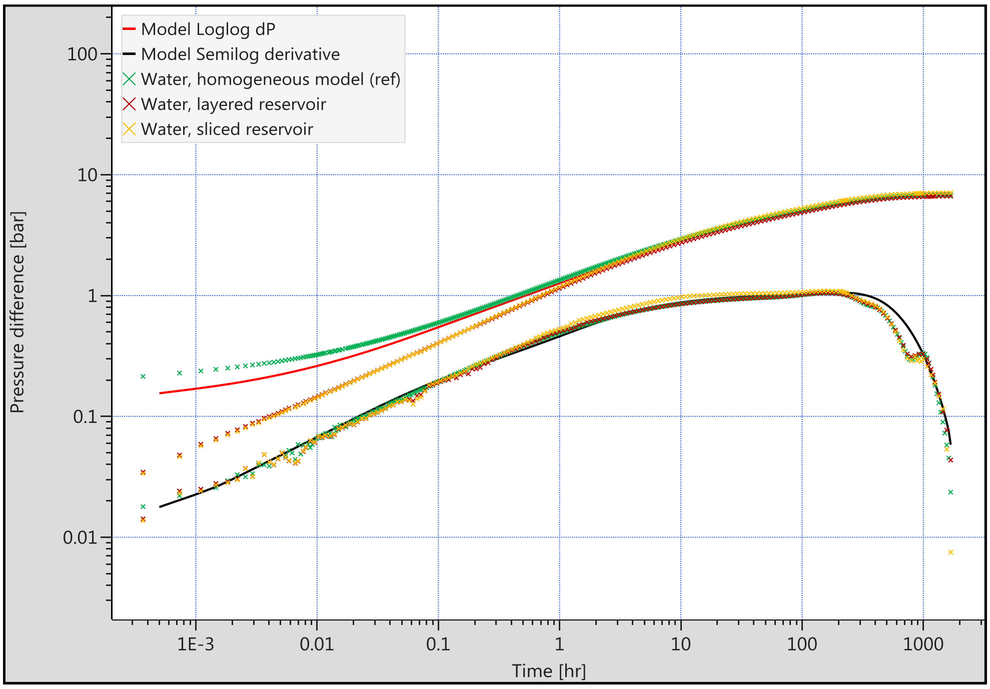

Figure 72 – Water fall-off responses for the homogeneous and heterogeneous model

Initially, pure water fall-off tests have been simulated for the layered and the sliced reservoir to generate the baselines for subsequent polymer analyses. The obtained pressure transients are depicted in Figure 72 and exhibit almost identical behavior. Matching the late time radial flow stabilization reveals a horizontal permeability of 480 mD and 460 mD for the layered and the sliced reservoir case, respectively. Both responses are in good agreement with a fall-off test conducted in the entirely homogenous initial reservoir.

Figure 73 depicts the pressure response for the layered reservoir model initialized as one singe polymer PVT region. The ratio of vertical to horizontal permeability has been defined by 1 and 0.1, respectively. The plot emphasizes that vertical permeability anisotropy does not distort the PTA result, since the transient honors the same linear flow straight line. However, the elevated early time radial flow stabilization shortens the length of the linear flow straight line available for interpretation significantly. Although being principally capable of retrieving the effective well length, this will cause serious interpretability issues for pronounced vertical permeability anisotropy.

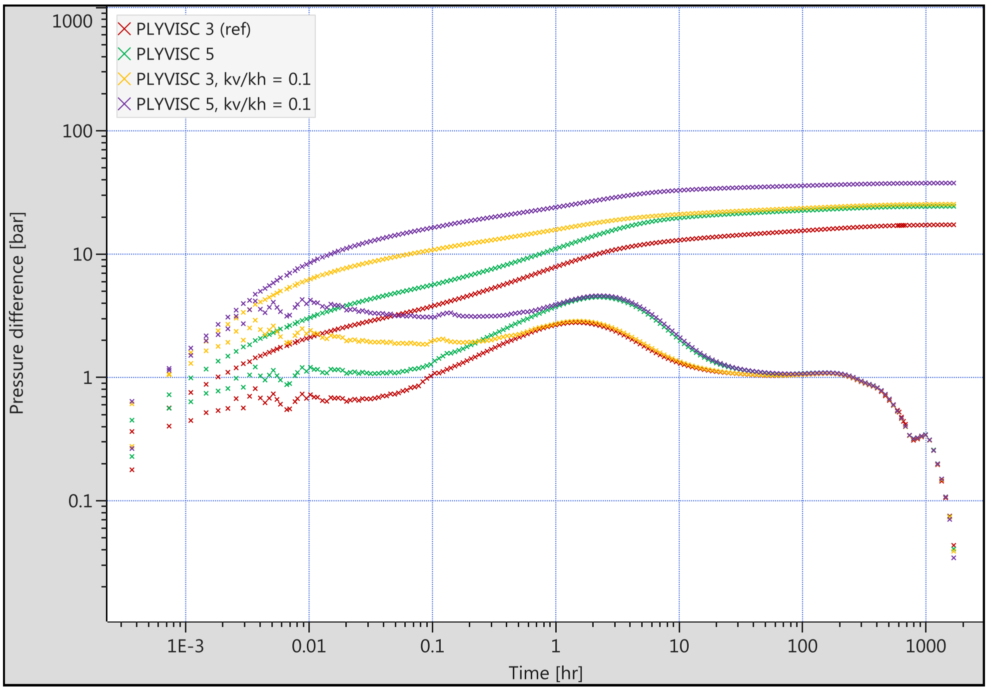

Figure 73 – The influence of vertical permeability anisotropy in the layered model

Figure 74 compares the pressure responses of the layered with the sliced model for three different polymer viscosity conditions. It can be obtained, that the transients of both models plot on an identical linear flow straight line for each polymer representation, while diverging only slightly during the transition towards late time radial flow. That means that based on the diagnostic plot solely, the underlying geological model cannot be distinguished. This emphasizes that the orientation of inherent model heterogeneity cannot be obtained from PTA.

The interpretation of the linear flow straight line according to the prior developed workflow yields reasonable agreement between the results from PTA and actual model viscosity values for the case of one consistent polymer PVT region. For cases, where various polymer viscosity correlations have been allocated to different rock types, a distinct discrepancy has been obtained. The comparison of the results based on PTA and actual model values is listed in Table 33. The statistical evaluation is based on a viscosity cut-off of 0.75 cP and divides the observed polymer range into 60 bins. Applying a viscosity instead of a concentration cut-off ensures a more coherent extraction of viscosity values depending on different concentration correlations.

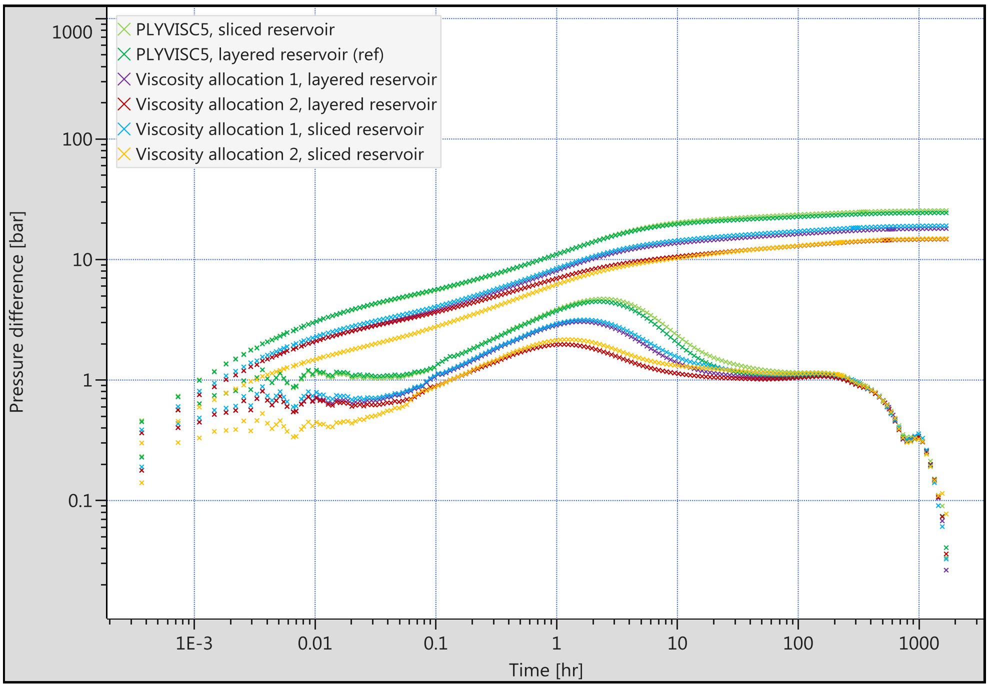

Figure 74 – The influence of different polymer viscosity to rock type allocations

Table 33 – Comparison of PTA results with the statistical evaluation of actual model values for different polymer viscosity to rock type allocations

Viscosity allocation	**Heterogeneity orientation**	**μ_{inj},** cP	**PTA**		**Model μ_{Poly} distribution,** cP		
			2 L_w, m	*μ_{app}, cP*	*mode*	*median*	*mean*
PLYVISC 5	layered	20.35	134	19.60	20.34	17.88	12.49
PLYVISC 5	sliced	20.35	139	18.22	20.35	17.68	13.11
Allocation 1	layered	12.43	169	12.32	16.32	8.47	9.20
Allocation 1	sliced	12.43	169	12.32	0.72	8.16	9.15
Allocation 2	layered	12.43	198	8.98	5.57	5.61	6.80
Allocation 2	sliced	12.43	201	8.71	5.58	5.60	6.07

Figure 75 illustrates the pore volume weighted polymer viscosity distribution for the case of viscosity allocation 1 in the layered reservoir. The distribution can be characterized by distinct spikes, representing the dominating viscosity values in each of the region. This erratic behavior has a strong influence on the computation of statistical location parameters, through to undermining their representative meaning at all. Since real reservoirs will exhibit gradual fluid viscosity changes resulting in a rather smooth cumulative distribution function (CDF), PTA results are likely to yield more meaningful results. Considering the shape of the CDF, polymer viscosity based on PTA has been found to be located in the upper quarter for all cases.

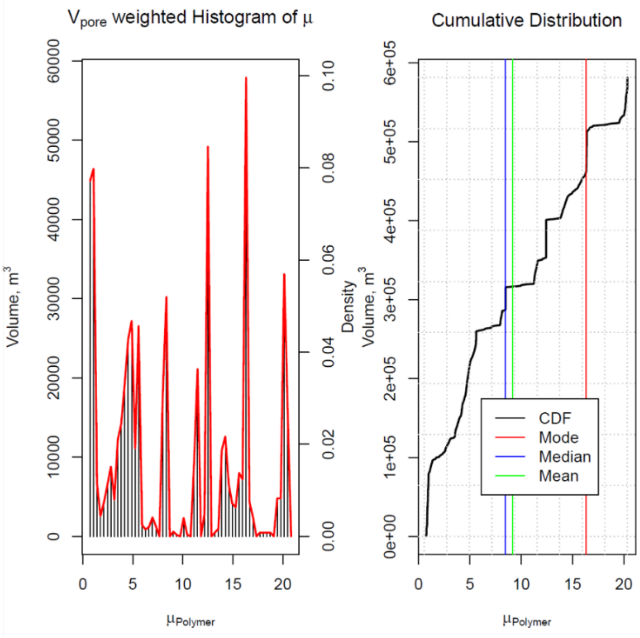

Figure 75 – Pore volume weighted viscosity distribution (cP) for viscosity allocation 1 in the layered reservoir case

Figure 76 depicts the penetration of the injected polymer solution into the reservoir for the case of polymer allocation 1 in the layered and the sliced reservoir, respectively. Although both cases exhibit identical linear flow behavior, they experience distinctly different shapes of the polymer propagating into the reservoir. Hence, it becomes obvious that no information about the contacted area can be inferred from PTA.

(a) Layered heterogeneity

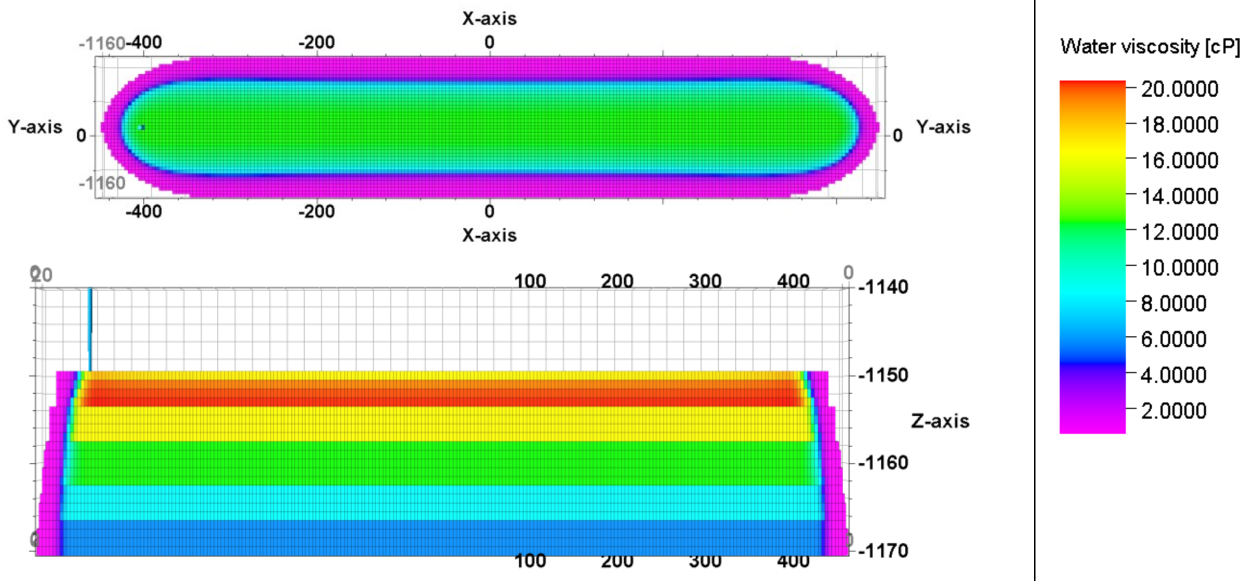

(b) Vertically sliced heterogeneity

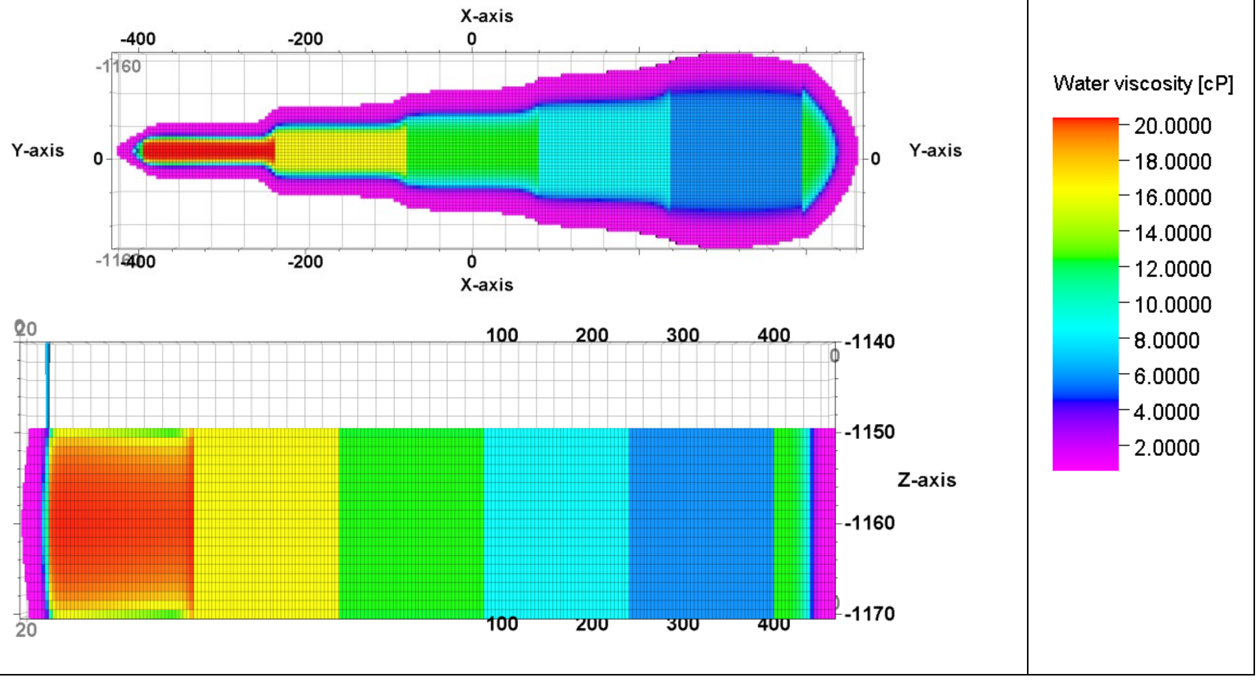

Figure 76 - Different penetration behavior associated with different model heterogeneities

In conclusion, Figure 77 depicts that the principle shape of the pressure transients is not altered in the presence of viscosity and adsorption heterogeneity compared to homogeneous behavior. High adsorption in high porous and high permeable media has been found to have a higher influence on the pressure response than high adsorption in low porous and low permeable formations. The fact that pressure responses caused by different viscosity and adsorption behavior allocations cannot be distinguished in the diagnostic plot once more emphasizes that comprehensive knowledge of in-situ polymer viscosity can only be obtained for reservoirs, where adsorption behavior is well understood. This ambiguity represents one of the major shortcomings of the developed method to constrain in-situ polymer viscosity.

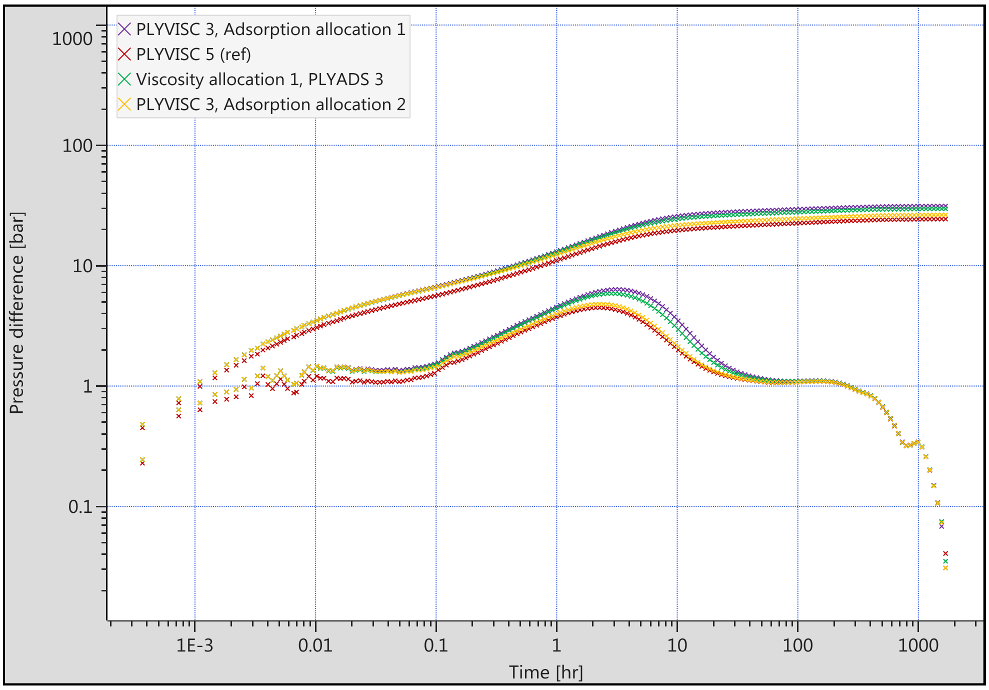

Figure 77 – The influence of different polymer adsorption allocations

8 Two-Phase Reservoir Models

Actual fall-off tests are exposed to multi-phase flow phenomena due to the presence of multiple fluids within the reservoir. After PTA has been applied to retrieve in-situ polymer viscosity for a range of single-phase water models, several fall-off tests have been simulated to investigate the behavior of two-phase reservoirs. The reservoirs have been initialized to produce at certain constant water cuts. Therefore, distinct water saturation and pressure distributions have been predefined as inputs. While the pressure experiences a significant change during the test, water saturation only changes in the near wellbore region, but remains practically unaltered on field scale.

Water and polymer injection represent immiscible displacement processes. While drawdown tests conducted under multi-phase flow conditions are typically analyzed by combining the surface rates of multiple fluids into one single equivalent reservoir extraction rate, this assumption of a homogeneous fluid is not applicable for injection tests. The main problem is that, on the contrary to drawdown tests, where the production of different phases is measured and can be related to one another, no information about the allocation of the total flow to the various phases can be obtained. Hence, it is hard to quantify to which extend each phase contributes to the obtained pressure transient.

8.1 Model Set-up

To simulate multi-phase flow, relative permeability and capillary pressure have to be defined in the reservoir model. Relative permeability is described based on Corey's correlation and is provided in Figure 78. The typical relative permeability behavior of a water wet formation has been selected to account for observations from the 8 TH reservoir. Capillary pressure has been considered with a function possessing a thin transition zone and a free water level below the model domain.

The homogeneous reservoir model introduced in chapter 7.1 provides the basis for the subsequent analysis. The in-situ oil phase is described by standard correlations implemented in Petrel, while the water properties remain unaltered. Relevant parameters are summarized in Table 34. During the simulated fall-off test, polymer solution with a concentaion of 2000 ppm has been injected for 26 weeks, followed by a shut-in period of 20 weeks.

Table 34 - Fluid PVT at the reference pressure of 120 bar

	Water	**Oil**
Viscosity, cP	0.55	3.07
Formation volume factor, -	1.007	1.105
Compressibility, bar^{-1}	$4.1 \cdot 10^{-5}$	$8.6 \cdot 10^{-5}$

Prior to conducting the well tests, the reservoir models have been initialized to produce at a constant water cut (WC) of 95 % according to conditions present in the 8 TH reservoir. Therefore, fractional flow theory has been used to yield a first estimate for the average water saturation in the model. Since capillary pressure and gravity effects cause a redistribution of the approximate water saturation, this first estimate has been refined by simulating production for an extended period of time to allow for equilibration within the reservoir. After a satisfactory water cut stabilization has been obtained, the actual fall-off test has been simulated.

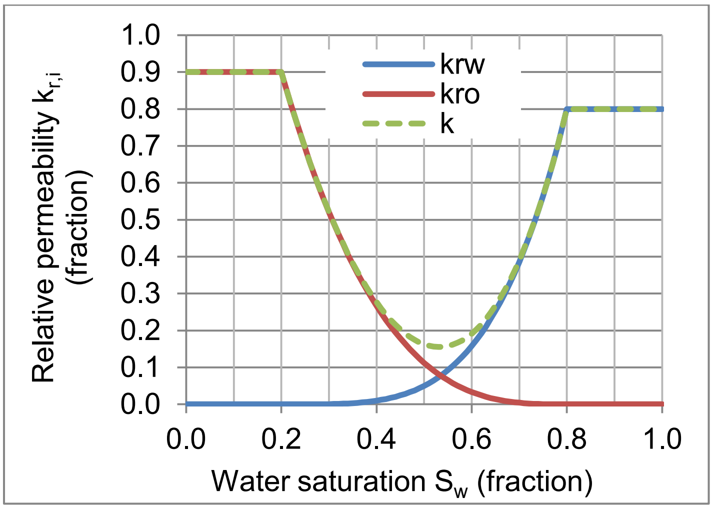

Corey parameters

S_{or}	0.2
S_{wc}	0.2
$k_{ro}(S_{wc})$	0.9
$k_{rw}(S_{or})$	0.8
n_o	3
n_w	4

Figure 78 - Relative permeability curves as implemented into the reservoir model

Figure 79 depicts the pressure transients originating from fall-off tests conducted with pure water in the single-phase water model described in the previous chapter and the two-phase model initialized with a producing water cut of 95 %, respectively. It can be observed that the pressure response in the two-phase model stabilizes at a significantly higher plateau. Furthermore, the response from the two-phase model exhibits a distinct discontinuity associated with an elevation of the derivative. This phenomenon might be explained by the formation of a saturation front as the result of immiscible displacement according to Buckley Leverett theory. Since the concept of a well-defined investigation radius has been shown to be inapplicable for horizontal wells, this interpretation could not be correlated with the actual Petrel model. However, the analysis of further models producing at different water cuts supports this finding. As depicted in Figure 80, models with a considerable amount of both the oil and the water phase flowing, exhibit a comparable discontinuity or change in the pressure derivative at a similar time.

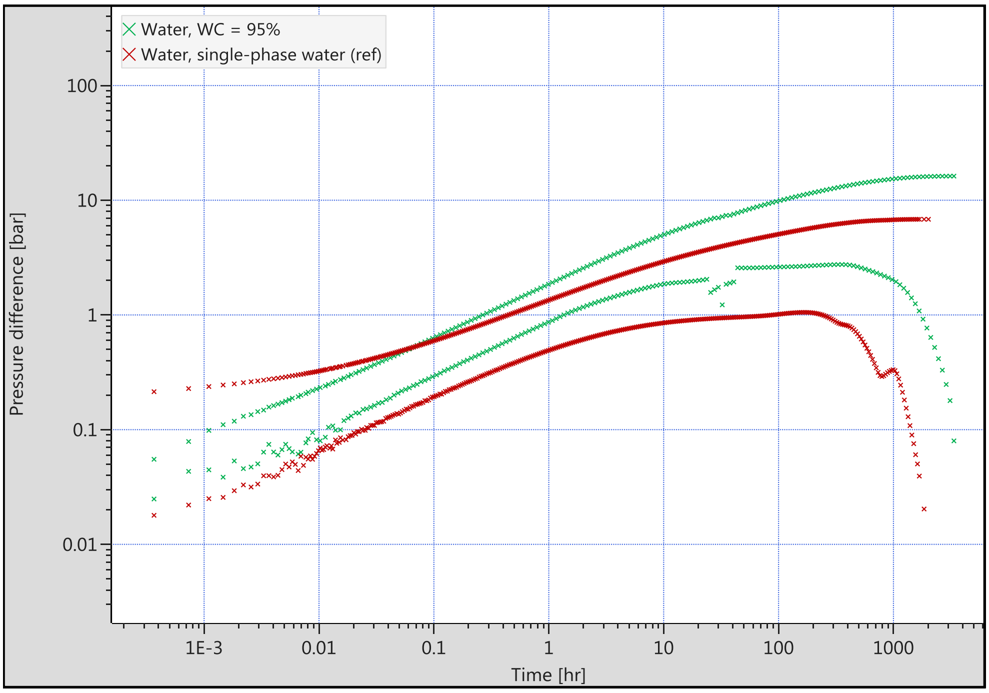

Figure 79 – Comparison of pressure responses from single- and two-phase reservoir models

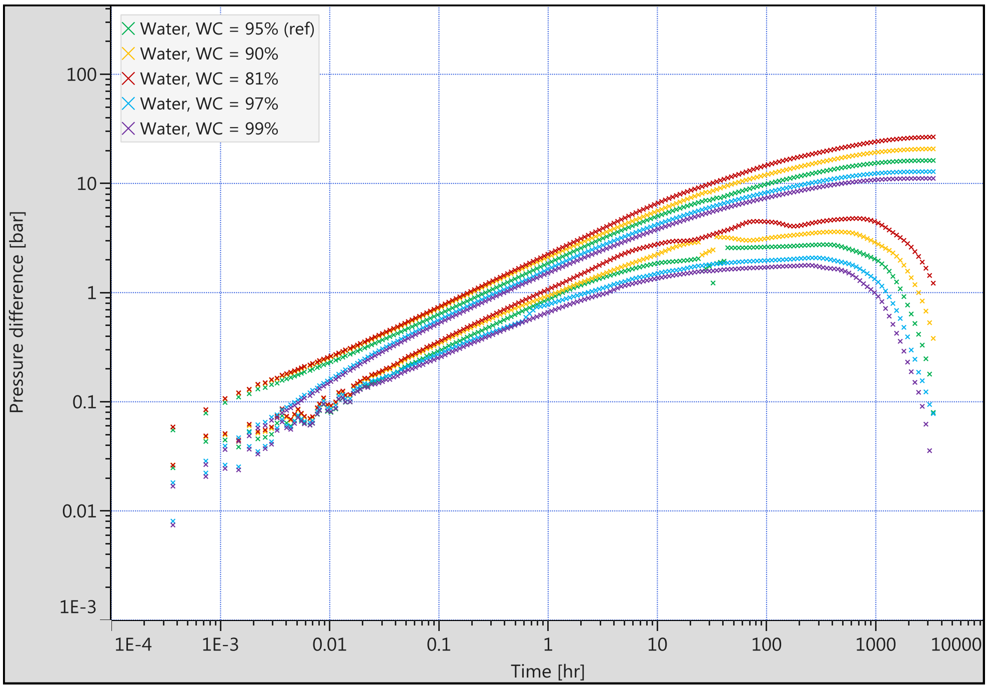

Figure 80 – Pressure transient responses of models with different producing water cuts

Since the average water saturation of each model can be extracted from Petrel, two different approaches have been applied to interpret the late time radial flow stabilization of all responses depicted in Figure 80. Firstly, PTA has been conducted with pure water properties as before and, secondly, based on saturation weighted mixture properties. The results are listed in Table 35 and indicate that neither of the procedures is able to obtain the correct model permeability of 500 mD. Furthermore, it has to be noted that a reasonable match of the data could only be found by adjusting the effective well length in the analytical PTA model.

Table 35 - Extracted horizontal permeability values from various two-phase models

WC_{prod}, %	**S_W**, -	**L_w**, m	Averaged properties	Water properties	
			k_H, mD	**k_H**, mD	**k_H ratio**
99	0.73	940	426	281	0.56
97	0.67	940	483	241	0.48
95	0.61	940	527	180	0.36
90	0.55	940	583	140	0.28
81	0.50	940	625	105	0.21

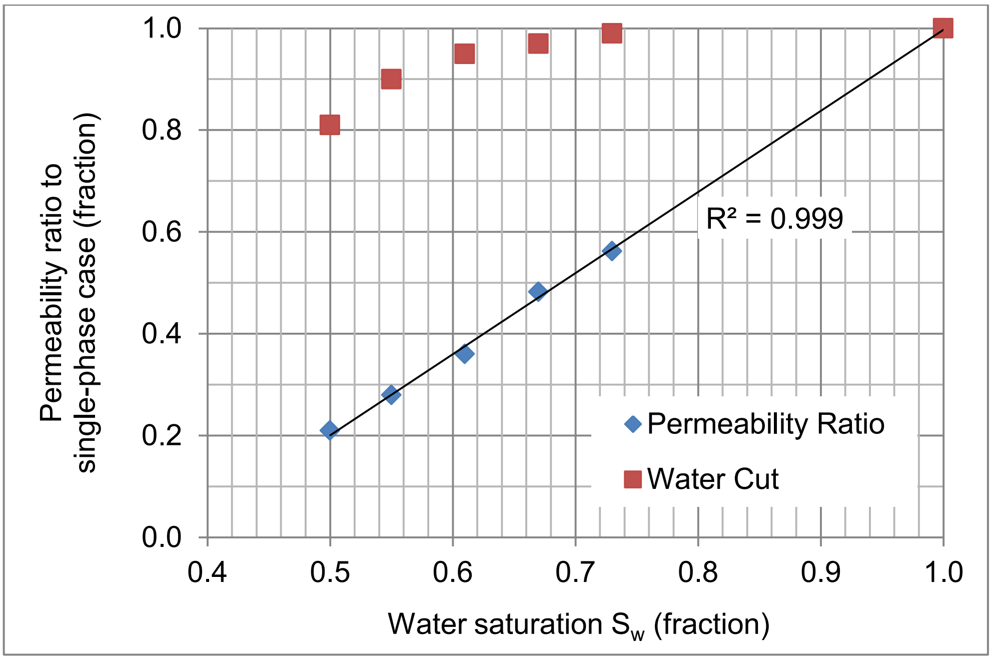

Figure 81 - Average water saturation versus obtained permeability ratio from PTA

Since neither of the fluid sets yields significant improvement over the other, subsequent analyses are focused on PTA based on water properties. The horizontal permeability values for the two-phase models provided in Table 35 have been divided by the absolute permeability of 500 mD obtained from a fall-off test conducted in the single-phase model. The calculated permeability ratios have been subjected to further scrutiny. A correlation between the obtained values and the water relative permeability at the respective water saturation could not be confirmed. Same applies to a correlation with the total effective permeability. Figure 81 provides a plot of the permeability ratio as a function of average water saturation, indicating a clear linear relationship between the two parameters.

Although no relationship could be derived between the obtained permeability ratios and the actual relative permeability curves, this strong correlation between average water saturation and obtained permeability clearly indicates the influence of some relative permeability effect. Hence, a subsequent analysis has been focused on total mobility and the mobility ratio between oil and water in the reservoir. Therefore, in-situ oil viscosities of 3.1 cP, 0.6 cP, and 0.3 cP have been considered. The respective pressure responses originating from the reservoir model producing at 95 % water cut are depicted in Figure 82. It can be obtained that lower oil viscosity is represented by a lower stabilization of the pressure derivative, which indicates an increased mobility. This finding suggests that both phases contribute to the pressure transient as the result of a conducted fall-off test.

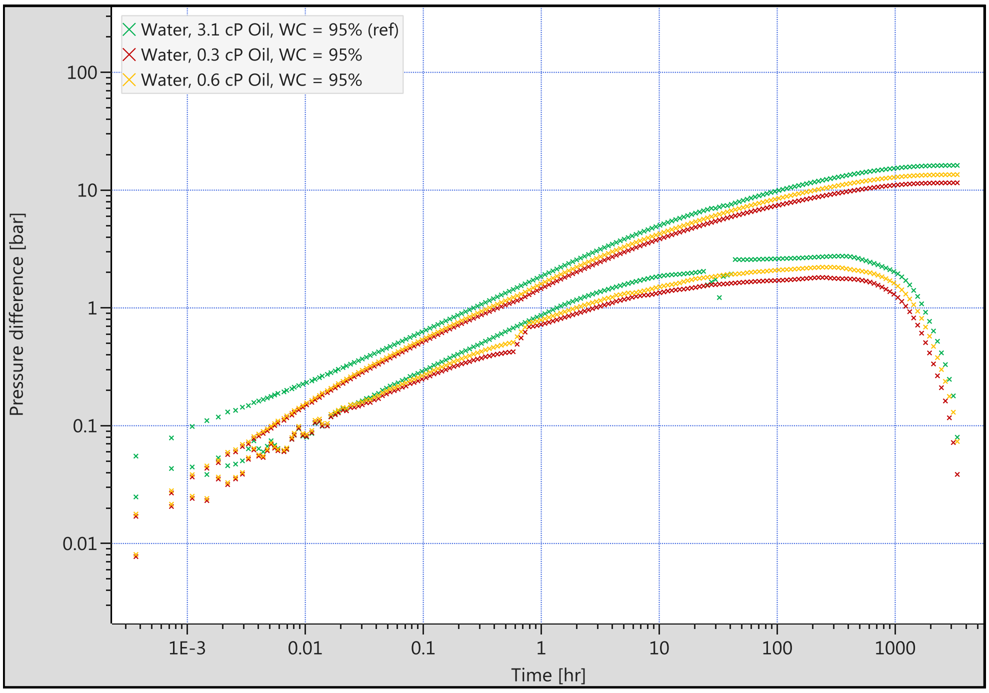

Figure 82 – The influence of different in-situ oil viscosities

This is supported by Figure 83, which compares the pressure transients originating from fall-off tests conducted with pure water, pure oil, and a mixture of a water cut of 95 % into the reservoir model producing at 95 % water cut. It can be seen that all three cases stabilize at a comparable plateau during their late time response, which means that similar mobility values will be obtained, irrespective of the actual injection fluid.

An extension of this analysis including reservoir models producing at different water cuts has revealed that no explicit relationship between total mobility and the observed horizontal permeability from PTA can be derived. Figure 84 illustrates a strong correlation between the parameters; however, the coefficient of determination decreases with decreasing in-situ oil viscosity. This discrepancy might be attributed to a stronger pressure dependency of oil properties compared to the water phase.

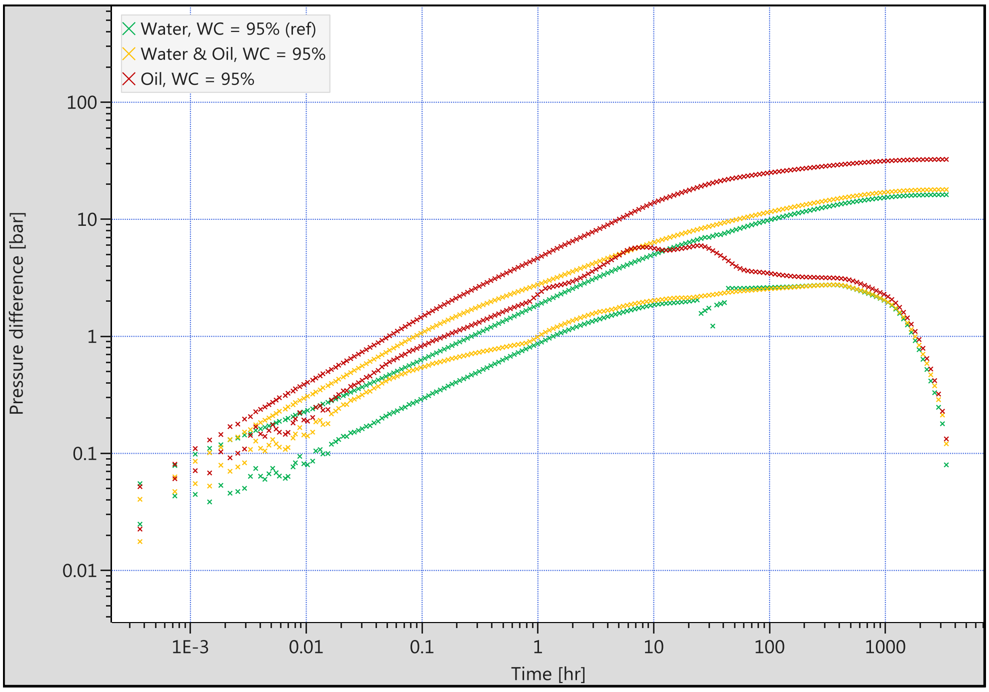

Figure 83 – The influence of different injection fluids

Although no consistent description of the actual model permeability has been attained, the relative interpretation of polymer and water injection fall-off tests in two-phase reservoirs is capable of constraining in-situ polymer viscosity. Figure 85 depicts the pressure transients of fall-off tests conducted with three different polymer solution viscosities together with their water baseline response. PTA of the pure water case has revealed a horizontal permeability of 180 mD and an effective well length of 940 m. By subsequent matching of the linear flow straight line while leaving all remaining analytical model parameters unaltered, apparent polymer viscosity can be calculated and is presented in Table 36. Comparing the results with location parameters of the actual viscosity distribution in the model shows that the mean can be reproduced with reasonable accuracy. While mode and median have been found to be the more representative parameters during single-phase analyses, the obtained apparent viscosity from PTA is decreased towards the mean, which might be an effect of the water and oil phase mutually influencing the pressure response.

Table 36 – Comparison of PTA results for different injected polymer viscosities

		PTA		**Model μ_{Poly} distribution**, cP		
Case	*μ_{inj}, cP*	*2 L_w, m*	*μ_{app}, cP*	*mode*	*median*	*mean*
PLYVISC 1	5.6	347	4.0	5.6	5.4	4.1
PLYVISC 3	12.4	233	9.0	12.4	12.2	9.0
PLYVISC 5	20.4	190	13.5	20.4	20.0	14.5
			MAPE	42.9%	39.6%	3.3%

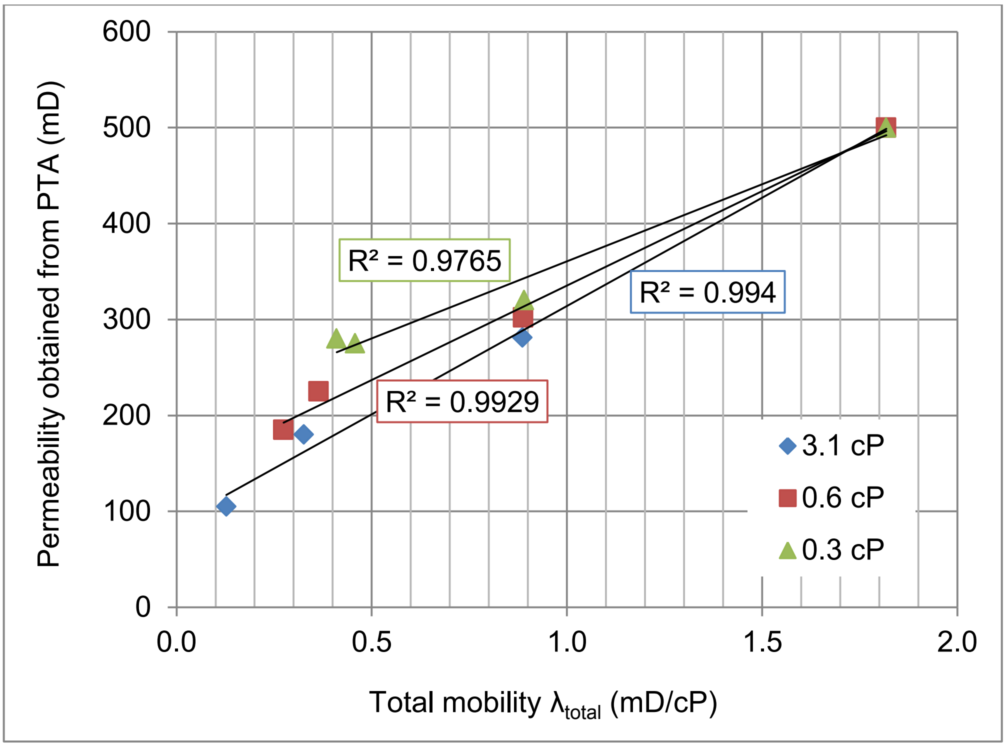

Figure 84 - Permeability derived from PTA versus water mobility

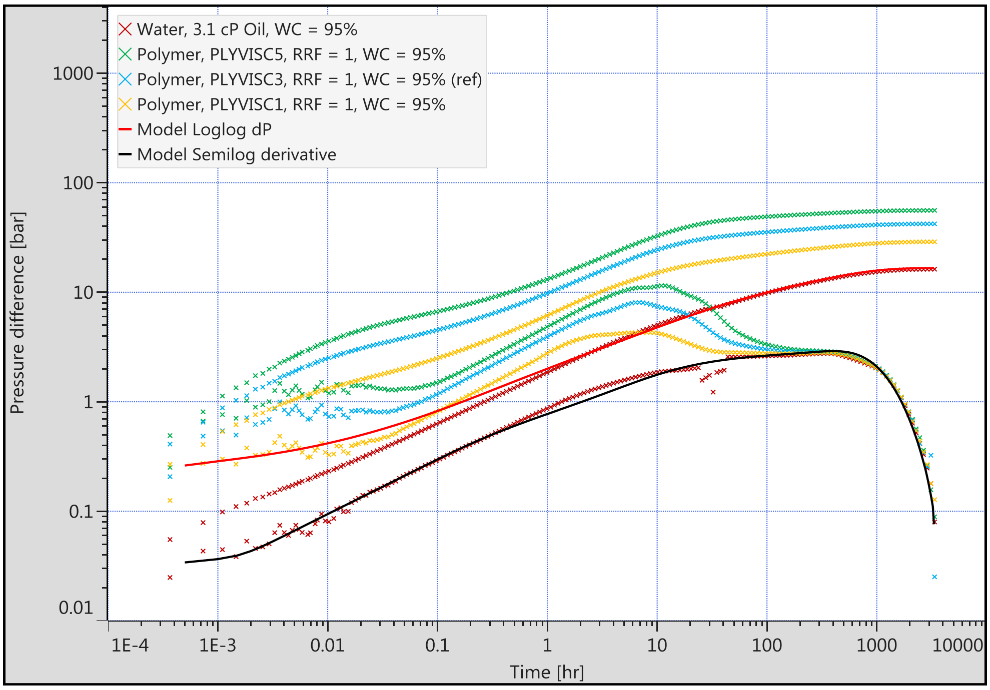

Figure 85 – The influence of different polymer viscosities

Figure 86 depicts the fall-off pressure transients associated with the injection of 12.4 cP polymer solution into reservoir models producing at different water cuts. Although the pure water responses stabilize at different plateaus during late time radial flow, the polymer derivatives share the same linear flow straight line, before diverging towards the respective stabilization. This observation indicates that the early time pressure response is dominated by the formation of a distinct polymer bank. The proposed influence of the oil phase on the magnitude of the derived polymer viscosity might consequently be limited to the contribution of residual oil saturation.

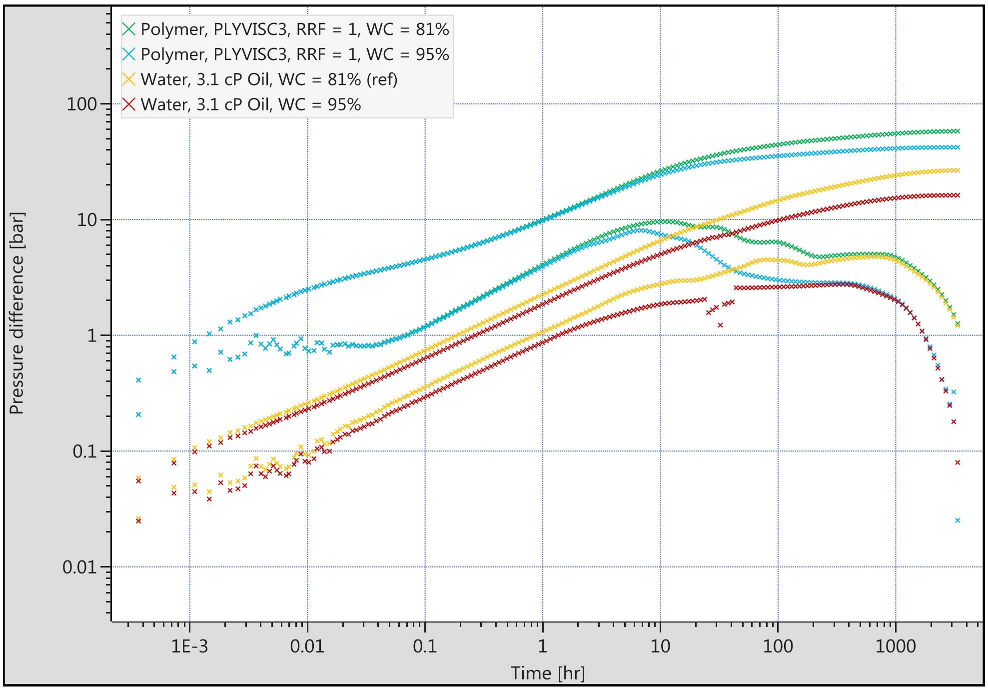

Figure 86 – The influence of different average water saturations during polymer injection

Table 37 - Comparison of PTA results for different polymer adsorption behavior

				Model distribution, cP			
		PTA		**μ_{app}**			**μ_{eff}**
Case	*μ_{inj}, cP*	*L_w, m*	*μ_{app}, cP*	*mode*	*median*	*mean*	*mean*
RRF 1	12.4	233	9.0	12.5	11.8	8.3	8.3
RRF 2	12.4	176	15.7	24.8	23.0	16.7	8.5
RRF 3	12.4	144	23.4	37.0	35.3	25.2	8.7
			MAPE	51.9%	43.0%	7.1%	

Figure 87 depicts the influence of an increasing magnitude of polymer adsorption and the associated water phase permeability reduction. The results derived from the pressure derivatives are summarized in Table 37. As expected, apparent viscosity increases with an increasing RRF. The comparison with actual model values emphasizes that by having a thorough understanding of the in-situ polymer adsorption and actual permeability reduction behavior, effective polymer viscosity can be obtained with reasonable accuracy. This finding is in perfect agreement with observations from the single-phase models; however, stresses the same difficulties. Since polymer adsorption is similarly hard to quantify as in-situ viscosity, gained insights are likely to be limited to the apparent viscosity of in-situ polymer solution.

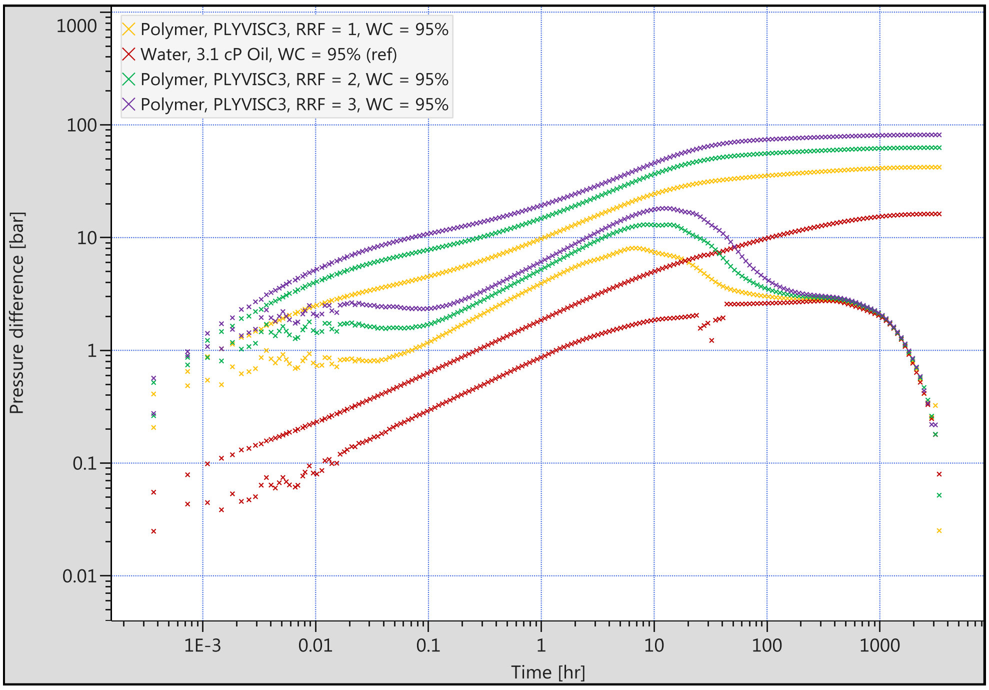

Figure 87 – The influence of different polymer adsorption and permeability reduction

8.2 The Effect of Reservoir Heterogeneity

A similar study on the single-phase models has revealed that no distinction can be made between the responses of layered and vertically sliced reservoirs. Hence, this study is limited to stratified rock type heterogeneity. An overview of all considered rock types as well as implemented polymer - rock interactions is provided in chapter 7.4. Prior to simulating a range of various fall-off test scenarios, all models have been initialized to yield the same producing water cuts as discussed in the previous chapter to ensure meaningful comparisons.

Figure 88 compares water fall-off test pressure transients from a homogeneous formation with responses from a stratified reservoir comprised of several rock types. It can be seen that the pressure derivatives from both models are in acceptable agreement and that higher water cuts improve the match between the curves. This observation can be explained by the increasing dominance of the water phase. While water injection into reservoirs initialized to yield lower water cuts will exhibit distinct discontinuities in the pressure derivative due to immiscible displacement effects, high water saturations increasingly approximate single-phase fluid flow. The close agreement between the responses obtained from the homogeneous and the heterogeneous reservoirs indicates that vertical layering is unlikely to be detected by PTA of water fall-off tests.

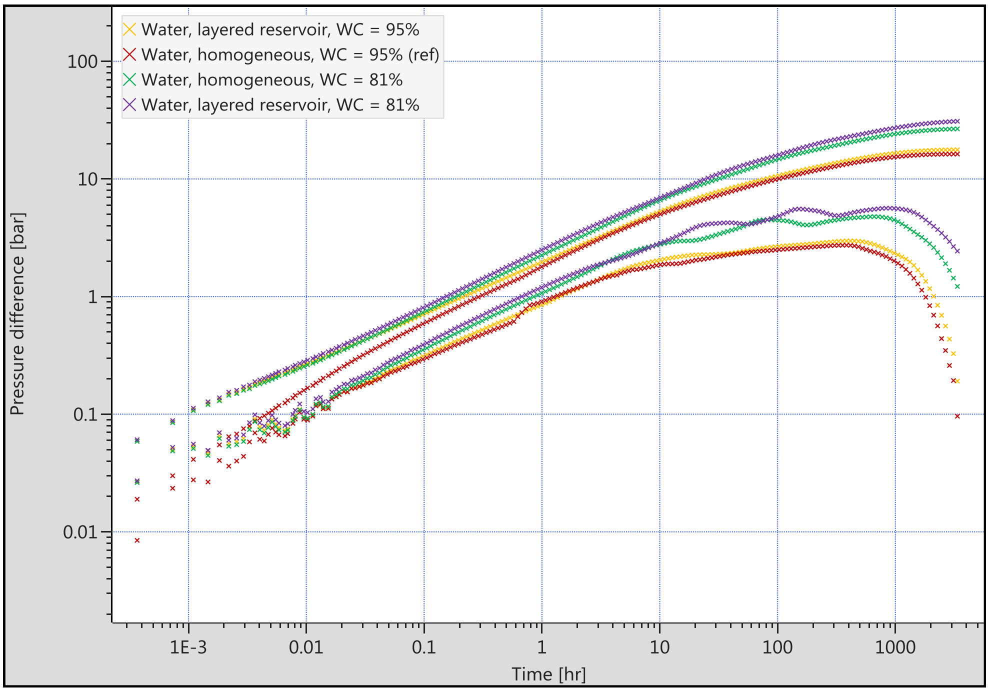

Figure 88 – The influence of stratified rock types on the pure water fall-off test pressure derivative for reservoirs producing at different water cuts

Figure 89 depicts the influence of different polymer viscosity allocations to the various rock types with and without adsorption. The obtained behavior in a two-phase reservoir is identical to observations in the single-phase model. Increased polymer viscosity in high porous and permeable media has a more pronounced influence than high viscous polymer being assigned to low porous and permeable formations. This phenomenon can easily be explained by high porous media allowing for easier penetration of the polymer. Increasing adsorption yields an upward shift of the derivative curve proportional to the actual permeability reduction factor.

In conclusion, Figure 90 once more emphasizes that the determination of apparent viscosity from PTA of polymer injection fall-off tests is not able to yield the polymer’s effective viscosity in the reservoir without detailed knowledge about polymer adsorption and associated permeability reduction.

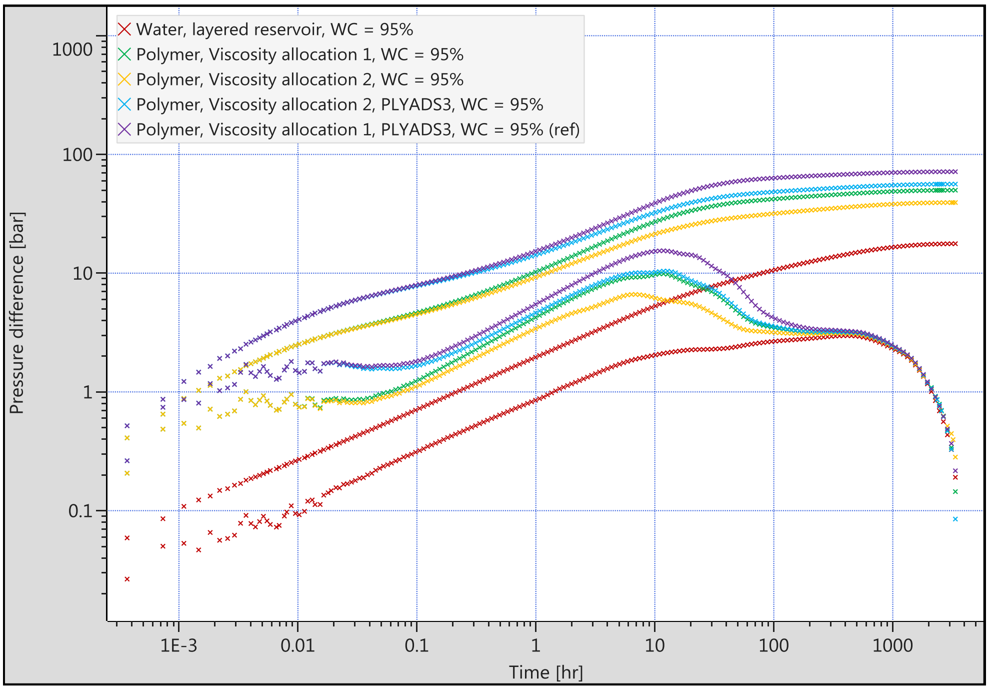

Figure 89 – The influence of different polymer viscosities and adsorption behaviours in a stratified reservoir

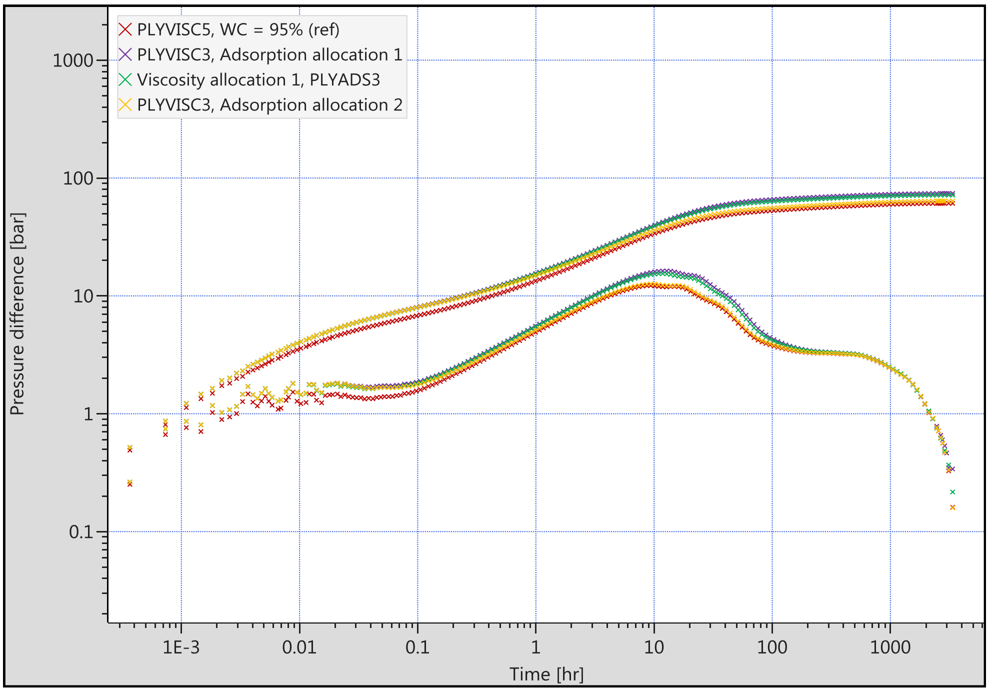

Figure 90 – The challenge of pressure response ambiguity

9 Applicability for Geomodel Screening

PTA has been shown to make a valuable contribution to the characterization of generic single- and two-phase reservoir models for polymer injection into horizontal wells. Eventually, gained insights are applied to elaborate the applicability of PTA for the screening of actual geomodels and discuss its potential to constrain inherent uncertainty associated with both geological and dynamic parameters.

Three different geological realizations currently considered as model centroids in the stochastic reservoir engineering workflow have been subjected to scrutiny with regards to their behavior during PTA. The selected geomodels possess large dissimilarity distances between each other, which corresponds to significant geological differences. Both water and polymer injection fall-off tests have been simulated to study the information content of each of the responses.

A black oil fluid model has been used for simulation with both the water and the oil phase properties being characterized according to previous investigations described in chapter 6.2 and 8.1. Relative permeability and capillary pressure curves have been taken from chapter 8.1. Initial geological screening has been performed with single-phase water models and multi-phase flow has been considered for the subsequent simulation of polymer injection into reservoir models producing at 95 % water cut.

9.1 Geological Screening

All three geomodels describe the reservoir by the same areal extend and account for aquifers attached to the reservoir boundaries. The reservoir top is located at a depth of 1115 m and the average net pay thickness yields approximately 17 m. Distinct layering is inherent in each geological realization and depicted for geomodel 1635 in Figure 91.

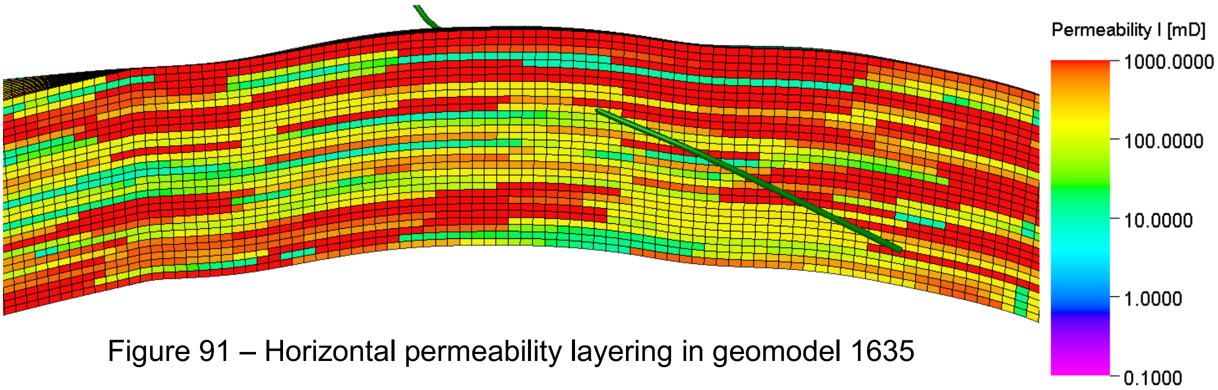

Figure 91 – Horizontal permeability layering in geomodel 1635

Although the distribution of different rock types differs between the geological realizations, all geomodels can be described by an average porosity of approximately 13 %. The permeability distribution of each realization is provided in Table 38. Horizontal permeability is assumed isotropic. According to an actually planned well, a horizontal well of an effective length of 690 m has been placed into the model penetrating various reservoir layers at an approximate depth of 1150 m.

Table 38 - Permeability distribution of the selected geomodels

k_H, mD	**Geomodel**		
	1320	*1551*	*1635*
Min	10	10	10
Mean	450	540	578
Max	6996	6996	6996

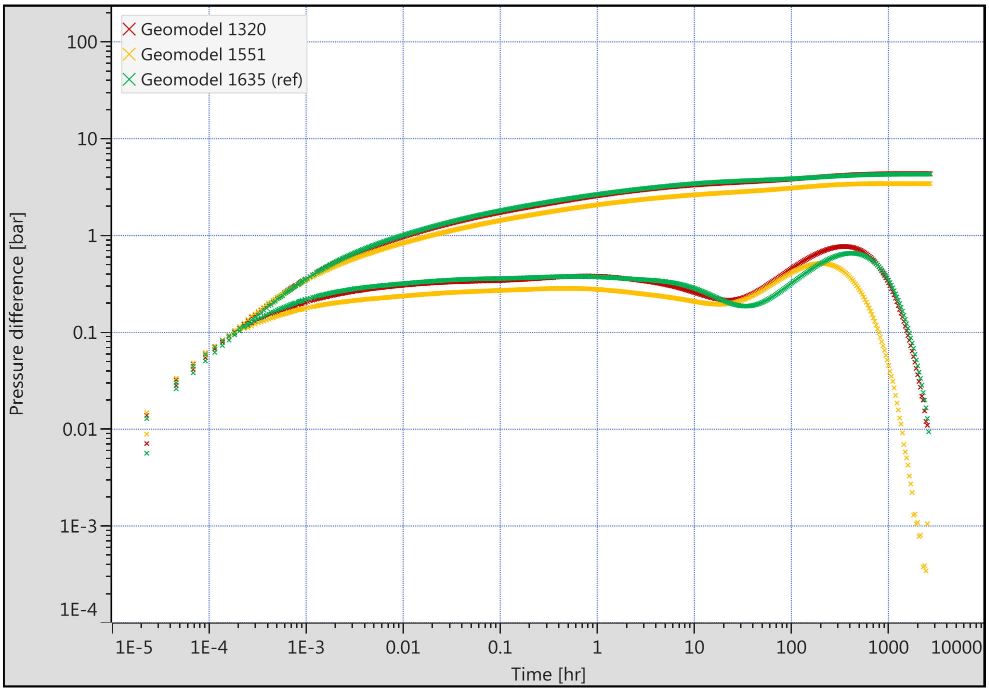

Figure 92 – Water injection fall-off test responses observed in the initial geomodels

Figure 92 depicts the pressure transients associated with a water injection schedule of 2000 scm/d for one week, followed by a shut-in period of 3 months. Although being characterized by large dissimilarity distances in the current parameter space of the stochastic workflow, the pressure responses of all three geomodels appear very similar. Except the features observed at very late times, the derivative appears almost identical to the characteristic shape of a simple horizontal well. None of the characteristic flow regimes of a horizontal well can be identified in the simulated response. Hence, an analysis based on early time vertical radial, middle time linear, and late time horizontal radial flow is not possible.

Figure 93 depicts pressure responses simulated for geomodel 1635 influenced by various boundary implementations, with and without LGR around the well. Although the very-early time response is slightly better resolved, LGR does not yield any significant improvement of the observed pressure signal with regards to the identification of typical horizontal flow geometries. The derivative fluctuation observed during the very-late time can doubtlessly be classified as boundary responses. Hence, the only remaining part for meaningful interpretation is the clear derivative stabilization during middle time. A separate analysis of the injection and the fall-off period has not revealed any further insights, since both periods exhibit similar behavior.

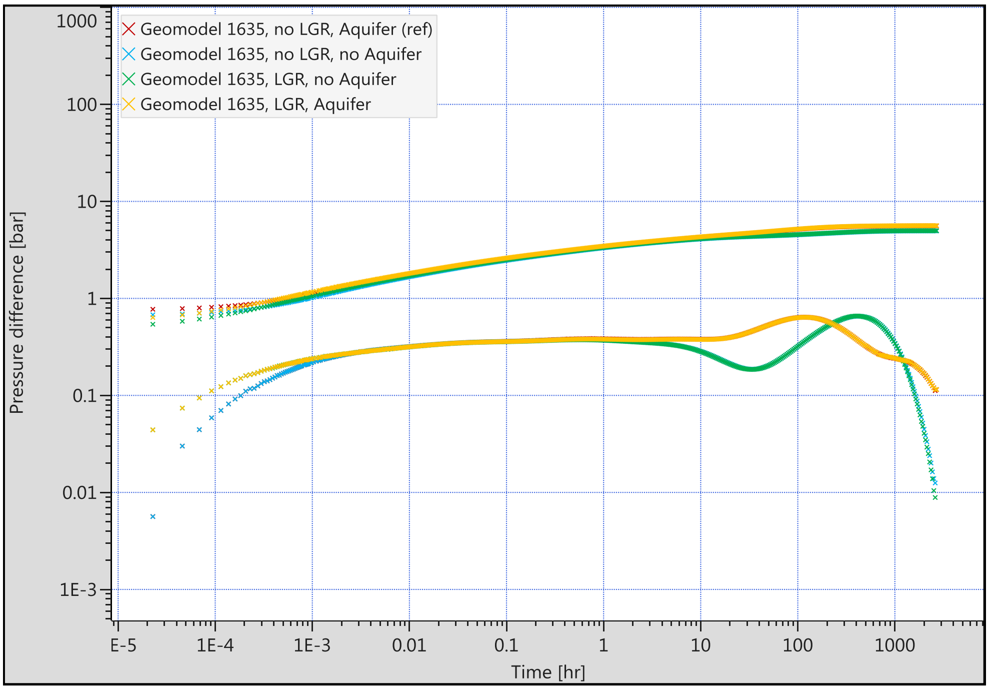

Figure 93 – The influence of LGR and different boundary implementations

In order to improve the understanding of the untypical appearance of the horizontal well, further well paths have been implemented into geomodel 1635. Beside the initial well trajectory, a vertical well and a horizontal well, which perfectly follows one of the reservoir layers, have been considered. Their influence on the simulated BHP response is illustrated in Figure 94. It can be obtained, that the pressure derivative of the vertical and the initial well trajectory coincide during middle and late time. The horizontal well in the reservoir layer exhibits a distinctly different behavior; however, a clear identification of different flow regimes can neither be done. Although there is an indication for a linear flow periods, no radial stabilization can be observed.

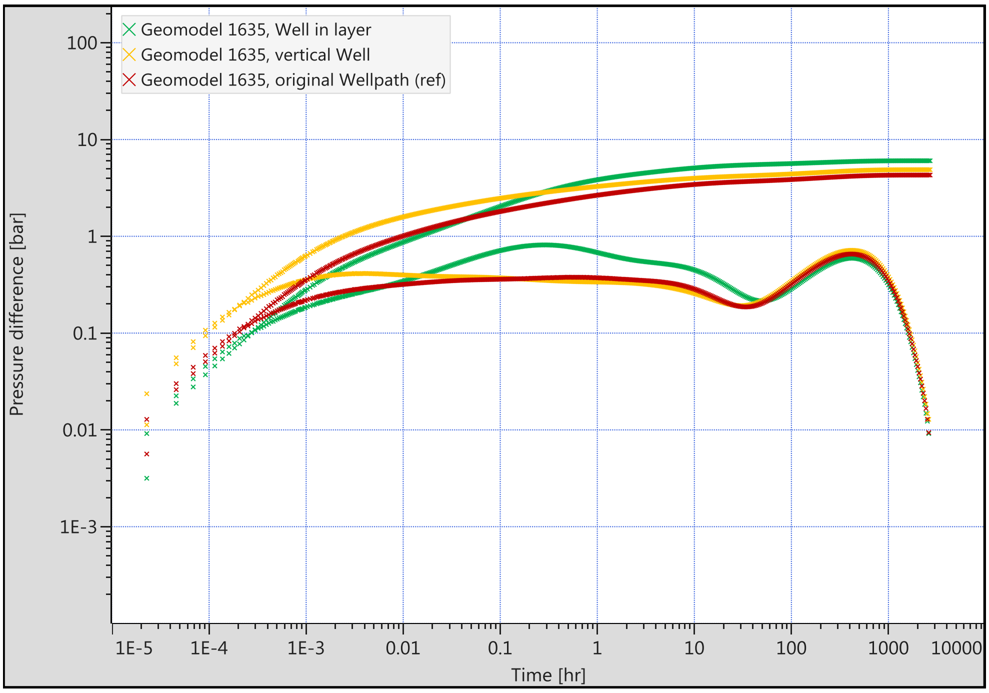

Figure 94 – The influence of differnet well geometries

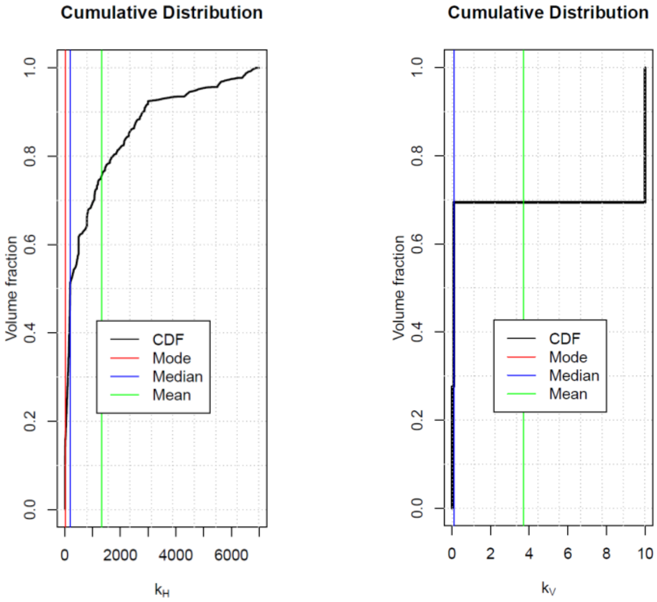

Figure 95 - Distribution of horizontal and vertical permeability (mD) in geomodel 1635

An interpretation of the extended derivative stabilization as observed for the vertical and the initial well revealed a horizontal permeability of 1695 mD. A comparison with Table 38 does not provide any meaningful agreement. Figure 95 provides the gross volume weighted permeability distribution of geomodel 1635, which was computed to account for variable grid block sizes in the reservoir model. The CDF denotes the mean horizontal permeability with a value of 1340 mD. Although this upvalues the result derived from PTA, a discrepancy of almost 300 mD cannot be classified as a satisfying result.

The discontinuous distribution of the vertical permeability is likely to be the reason for the suppression of the establishment of flow regimes typically observed in horizontal wells. The entire distribution consits of three distinct values differing by orders of magnitude only. This leads to negligible vertical flow in the majority of the grid blocks. Furthermore, by penetrating various reservoir layers further resistance to vertical flow is introduced by less permeable intermediate layers.

Figure 96 depicts the pressure responses of the horizontal well placed within one reservoir layer according to different vertical permeabilities. It can be obtained that a homogenous vertical permeability distribution leads to the establishment of a distinct late time radial flow stabilization. Furthermore, with increasing vertical permeability a more pronounced linear flow regime can be observed. Early time vertical flow cannot be identified on the plot, which can be explained by a limited thickness of the reservoir layer.

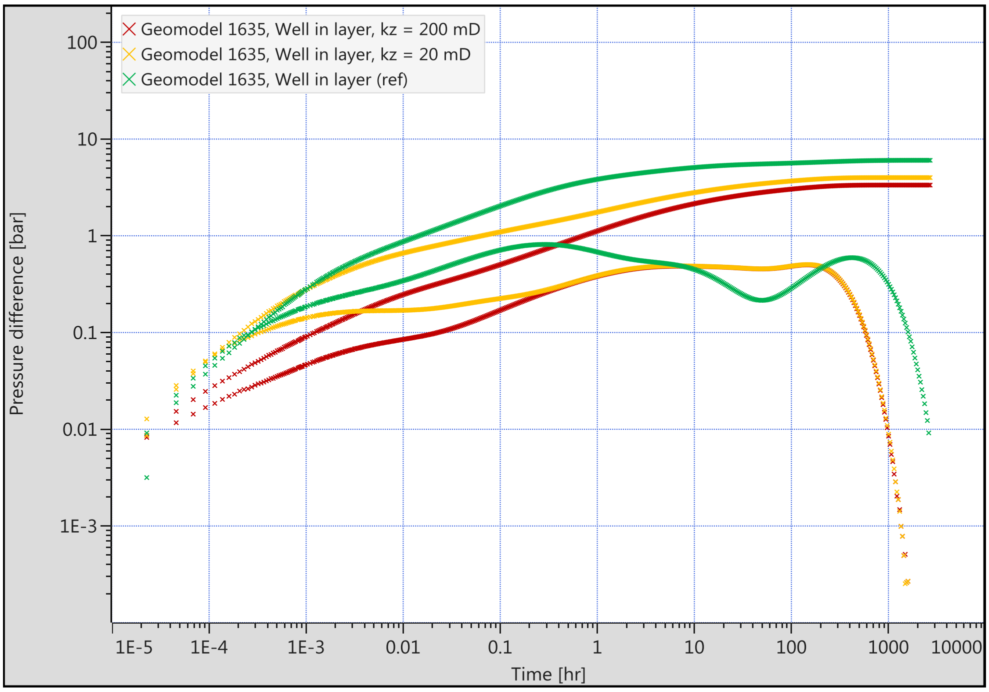

Figure 96 – The influence of vertical permeability on well following the reservoir layer

9.2 Polymer Injection

Although simulated water injection fall-off tests in actual geomodels indicated very limited interpretability, the influence of polymer injection will be discussed briefly for reasons of completeness. Therefore, the geomodels have been initialized as two-phase models producing at a 95 % water cut. The implemented polymer behavior has been introduced in chapter 0. To account for an increased viscosity, the injection rate has been reduced to 200 scm/d.

Figure 97 compares the pressure transients of the injection of pure water with polymers of two different viscosities in geomodel 1635. It can be obtained that increasing fluid viscosity results in an upward shift of the derivative stabilization during middle time before all three responses stabilize at the same plateau during late time. The polymer affected stabilization appears slightly tilted indicating increasing resistance to flow with progressing time. The upward shift of the derivative matches prior expectations; however, no meaningful analysis to determine the in-situ polymer viscosity could be conducted. The responses of the initial well trajectory and the well perfectly aligned within on layer show almost identical behavior.

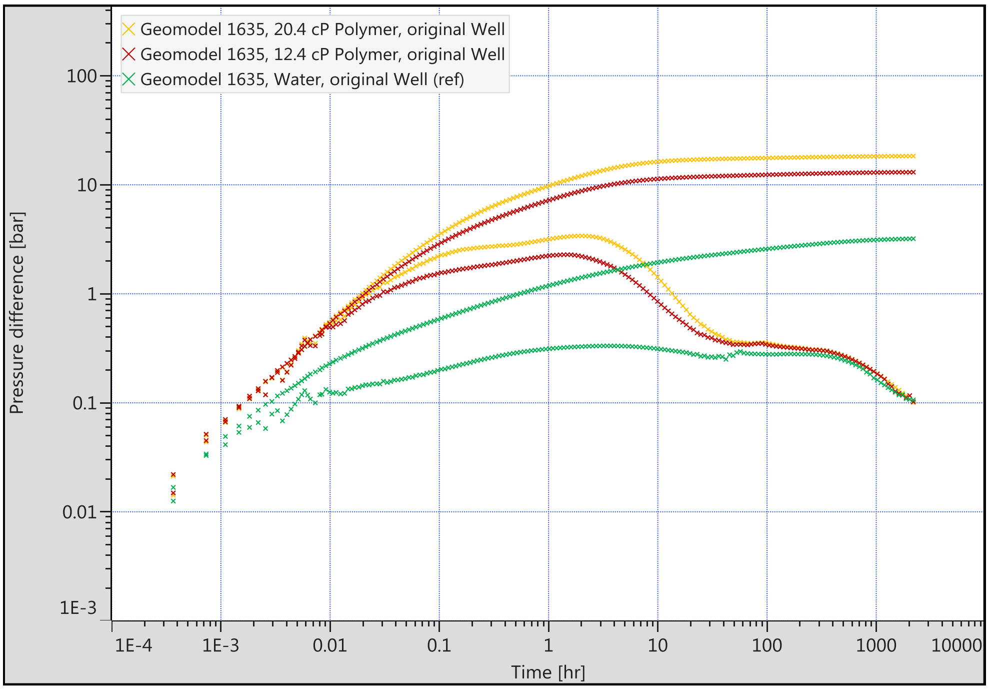

Figure 97 – The influence of polymer viscosity on simulated fall-off tests (geomodel 1635)

The influence of polymer adsorption is depicted in Figure 98. Increasing adsorption and associated permeability reduction leads to a further upward shift of the derivative indicating an increase in apparent polymer viscosity. Although no qualitative analysis was feasible, this observation aligns well with theory and prior findings.

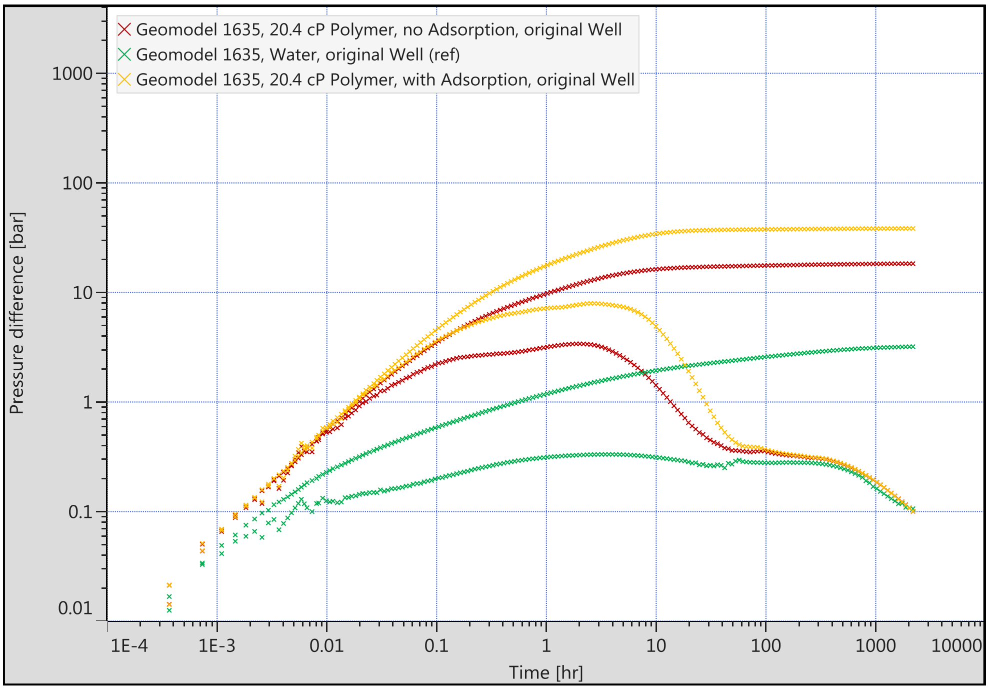

Figure 98 – The influence of polymer adsoprtion on simulated fall-off tests (geomodel 1635)

10 Conclusion

The overall objective of this thesis was to investigate the applicability of pressure fall-off test data to be incorporated into the clustering step of the developed stochastic workflow. Insights gained from PTA could help to constrain uncertainties associated with both geological and dynamic parameters and enhance the current weighting procedure of geological model centroids.

It was shown that PTA provides a valuable tool to enhance reservoir understanding for polymer injection into horizontal wells. For generic single-phase water models, both permeability anisotropy and heterogeneity were successfully determined; however, the degree of reservoir heterogeneity was found to have a strong influence on interpretation reliability. Qualitative type curves were developed for a range of permeability discontinuities within the reservoir.

Several upscaling techniques were investigated with regards to their influence on the pressure response of posterior fall-off tests. Geometric upscaling was found to preserve the maximum of the initial pressure response during permeability upscaling. Arithmetic and harmonic upscaling are associated with a severe upward and downward distortion of the initial parameter distribution, respectively.

An approach was developed to determine the apparent in-situ polymer viscosity by applying PTA techniques. The procedure requires a water injection fall-off test before polymer injection is initiated. The initial water injection fall-off test acts as baseline for subsequently performed polymer injection fall-off tests and provides the reservoir permeability and the effective well length. Both parameters are necessary inputs for a reliable interpretation, since the characteristic change of the linear flow straight line because of polymer injection provides the basis, from which the apparent polymer viscosity can be calculated.

Polymer injection creates two distinct regions in the reservoir, with a polymer bank around the well and an unaltered region further away from the well. This yields a water dominated radial flow stabilization during the later time and a polymer dominated linear flow during early and middle time. The existence of these characteristic derivative features depends on the duration of the injection and the distance to external boundaries. Although apparent polymer viscosity was successfully constrained with reasonable accuracy, no reliable information about the penetration of the polymer into the reservoir could be derived. A simple radius of investigation approach was found to be inapplicable due to the complexity of observed flow regimes.

The reliability of the apparent polymer viscosity derived from PTA was found to be dependent on a well-established late time radial flow stabilization and is highly sensitive towards the effective well length. Hence, a minimum shut-in duration is critical to ensure a meaningful analysis. Furthermore, production logging might be applied during polymer injection tests to determine changes in the effective well length associated with the increased viscosity of the polymer solution, which is prone to divert the injection stream compared to water injection.

This finding is of importance for the operational planning of future fall-off tests in polymer injection wells. Further investigations should be focused on WBS and skin effects on the applicability of the proposed workflow due to their significant influence on the linear flow regime.

The water relative permeability is reduced by polymer injection. Laboratory measurements of the RRF are required to distinguish this effect from behavior related to increased solution viscosity during PTA. Hence, the calculation of effective in-situ polymer viscosity is limited to conditions, where a thorough understanding of the in-situ polymer adsorption and actual permeability reduction behavior has been attained. However, the apparent viscosity derived from PTA can, conversely, help to constrain actual adsorption behavior within the reservoir for cases, where the effective polymer viscosity can be estimated from back-produced polymer solution.

For multi-phase models, the analysis of simulated fall-off tests was not capable of yielding a consistent reservoir description; however, in-situ viscosity could still be approximated with the proposed workflow, if a pure water injection response is provided as baseline. The influence of polymer viscosity and polymer adsorption behavior on the pressure transient did not show any distinct differences between single- and multi-phase flow conditions. Extended polymer injection duration was found to increase the reliability of the apparent viscosity obtained from PTA due to a more pronounce polymer bank.

Gained insights were applied to actual geomodels currently considered in the stochastic modelling workflow. Due to geological complexity, a direct implementation of the proposed workflow could not be confirmed. For geologically complex formations, it is expected that matching procedures for simulated pressure responses produces more reliable results compared to analytical PTA, since all features of the various flow patterns are rigorously taken into account. Furthermore, the entire range of transient data including transition periods between distinct flow geometries are considered, whereas direct analysis is limited to the subset of identifiable flow regimes.

11 References

[1] R. B. Needham and P. H. Doe, “Polymer Flooding Review,” *Journal of Petroleum Technology,* vol. 39, no. 12, 1987.

[2] G. F. Teletzke, R. C. Wattenbarger and J. R. Wilkinson, "Enhanced Oil Recovery Pilot Testing Best Practices," SPE Reservoir Evaluation and Engineering, 2010.

[3] J. Cheng, J. Wei, K. Song and P. Han, “Study on Remaining Oil Distribution After Polymer Flooding,” SPE 133808, 2010.

[4] K. Zaki, “Injectivity and Falloff Testing,” 06 12 2002. [Online]. Available: http://www.advntk.com/pwrijip2003/pwri/toolbox/monitoring/buildup/best_practices_1_falloff.htm#key_issues. [Accessed 21 06 2017].

[5] N. Saad, V. Maroongroge and C. Kalkomey, “Ranking Geostatistical Models Using Tracer Production Data,” SPE 35494, 1996.

[6] J. McLennan and C. V. Deutsch, “Ranking Geostatistical Realizations by Measures of Connectivity,” SPE 98168, 2005.

[7] G. M. Shook and K. M. Mitchell, "A Robust Measure of Heterogeneity for Ranking Earth Models: The F PHI Curve and Dynamic Lorenz Coefficient," SPE 124625, 2009.

[8] C. Scheidt and J. Caers, “Uncertainty Quantification in Reservoir Performance Using Distances and Kernel Methods--Application to a West Africa Deepwater Turbidite Reservoir,” SPE 118740, 2009.

[9] M.-M. Chiotoroiu, J. Peisker, T. Clemens and M. R. Thiele, “Forecasting Incremental Oil Production of a Polymer Pilot Extension in the Matzen Field Including Quantitative Uncertainty Assessment,” SPE 179546 MS, 2016.

[10] A. Laoroongroj, M. Zechner, T. Clemens and A. Gringarten, “Determination of the In-Situ Polymer Viscosity from Fall off Tests,” SPE 154832, 2012.

[11] IHS, “Well Testing Fundamentals,” [Online]. Available: http://cdn.ihs.com/www/images/Fekete-WellTest-Fundamentals.png. [Accessed 02 09 2017].

[12] Schlumberger, “Well Test Interpretation,” Schlumberger, Sugar Land, TX, 2008.

[13] D. Bourdet, Well Test Analysis : The use of Advanced Interpretation Models (Handbook of Petroleum Exploration and Production 3), Amsterdam: Elsevier Science, 2002.

[14] C. S. Matthews and D. G. Russell, Pressure Buildup and Flow Tests in Wells, Richardson, TX: Society of Petroleum Engineers, 1967.

[15] M. M. Kamal, Transient Well Testing, vol. Monograph Series, Richardson, TX: Society of Petroleum Engineers, 2009.

[16] M. Kamal, D. Freyder and M. Murray, "Use of Transient Testing in Reservoir Management," *Journal of Petroleum Technology,* vol. 47, no. 11, 1995.

[17] M. Abbaszadeh and M. Kamal, "Pressure-Transient Testing of Water-Injection Wells," SPE 16744, 1989.

[18] P. Jones, "Reservoir Limit Tests," *Oil and Gas Journal,* vol. 54, no. 59, 1956.

[19] A. U. Chaudhry, Oil Well Testing Handbook, Houston, TX: Elsevier, 2004.

[20] J. Joseph, C. Ehlig-Economides and F. Kuchuk, "The Role of Downhole Flow and Pressure Measurements in Reservoir Testing," SPE 18379, 1988.

[21] C. Ehlig-Economides, P. Hegeman and S. Vik, "Guidelines simplify well test interpretation," *Oil and Gas Journal,* vol. 92, no. 29, 1994.

[22] C. C. Miller, A. B. Dyes and C. Hutchinson Jr., "The Estimation of Permeability and Reservoir Pressure From Bottom Hole Pressure Build-Up Characteristics," SPE 950091, 1950.

[23] J. Moran and E. Finklea, "Theoretical Analysis of Pressure Phenomena Associated with the Wireline Formation Tester," SPE 177, 1962.

[24] A. C. Gringarten, H. J. Ramey Jr. and R. Raghavan, "Unsteady-State Pressure Distributions Created by a Well With a Single Infinite-Conductivity Vertical Fracture," SPE 4051, 1974.

[25] H. Cinco-Ley, F. Samaniego V. and N. Dominguez A., "Transient Pressure Behavior for a Well With a Finite-Conductivity Vertical Fracture," SPE 6014, 1978.

[26] D. Bourdet, J. Ayoub and Y. Pirard, "Use of Pressure Derivative in Well Test Interpretation," SPE 12777, 1989.

[27] Y.-L. Zhao, L.-H. Zhang, J. Chen, L.-X. Li and Y. Zhou, “Analytical solutions for flow of horizontal well in compressible, three-dimensional unconsolidated formations,” *Journal of Geophysics and Engineering,* vol. 11, no. 4, 2014.

[28] I. B. E. Yasin, “Pressure Transient Analysis Using Generated Well Test Data from Simulation of Selected Wells in Norne Field,” Norwegian University of Science and Technology, 2012.

[29] Y. Sun, L. Saleh and B. Bai, “Measurement and Impact Factors of Polymer Rheology in Porous Media,” in *Rheology*, Rijeka, Dr. Juan De Vicente (Ed.), InTech, 2012.

[30] U. Bröckel, W. Meier and G. (. Wagner, Product Design and Engineering, Weinheim: Wiley-VCH, 2013.

[31] W. Gogarty, “Mobility Control With Polymer Solutions,” SPE 1566, 1967.

[32] K. Sorbie, Polymer-improved oil recovery, London: Blackie, 1991.

[33] S. Mishra, A. Bera and A. Mandal, “Effect of Polymer Adsorption on Permeability Reduction in Enhanced Oil Recovery,” *Journal of Petroleum Engineering,* 5 March 2014.

[34] A. Zaitoun and N. Kohler, "Two-Phase Flow Through Porous Media: Effect of an Adsorbed Polymer Layer," *Proceedings of the SPE Annual Technical Conference and Exhibition,* 2-5 October 1988.

[35] L. Zhang and M. Dusseault, “Anisotropic Permeability Estimation by Horizontal Well Tests,” SPE 37071, 1996.

[36] J. Sheng, Modern chemical enhanced oil recovery : theory and practice, Burlington: Gulf Professional Publishing, 2010.

Appendices

Appendix A – Eclipse fluid PVT data

Table 39 - Water PVT properties as implemented in Eclipse (based on standard correlations)

Pressure	**B_w**	**c_w**	**ρ_w**	**μ_w**
bara	m³/sm³	1/bar	kg/m³	cP
100	1.008	4.11E-05	1012.4	0.55
105	1.008	4.11E-05	1012.6	0.55
110	1.008	4.10E-05	1012.8	0.55
115	1.007	4.10E-05	1013.0	0.55
120	1.007	4.09E-05	1013.2	0.55
125	1.007	4.09E-05	1013.4	0.55
130	1.007	4.08E-05	1013.6	0.55
135	1.006	4.08E-05	1013.8	0.55
140	1.006	4.07E-05	1014.0	0.55
145	1.006	4.07E-05	1014.2	0.55
150	1.006	4.06E-05	1014.4	0.55

Table 40 - Oil PVT properties as implemented in Eclipse (based on standard correlations)

Pressure	**B_o**	**c_o**	**ρ_o**	**μ_o**
bara	m³/sm³	1/bar	kg/m³	cP
100	1.107	1.07E-04	817.6	2.97
105	1.106	1.07E-04	818.0	2.99
110	1.106	8.59E-05	818.4	3.02
115	1.105	6.45E-05	818.7	3.04
120	1.105	8.58E-05	819.0	3.07
125	1.104	6.45E-05	819.3	3.10
130	1.104	6.45E-05	819.5	3.13
135	1.104	6.46E-05	819.7	3.16
140	1.104	4.30E-05	820.0	3.19
145	1.103	6.46E-05	820.2	3.22
150	1.103	4.31E-05	820.4	3.26

Appendix B – Horizontal permeability plane type curves

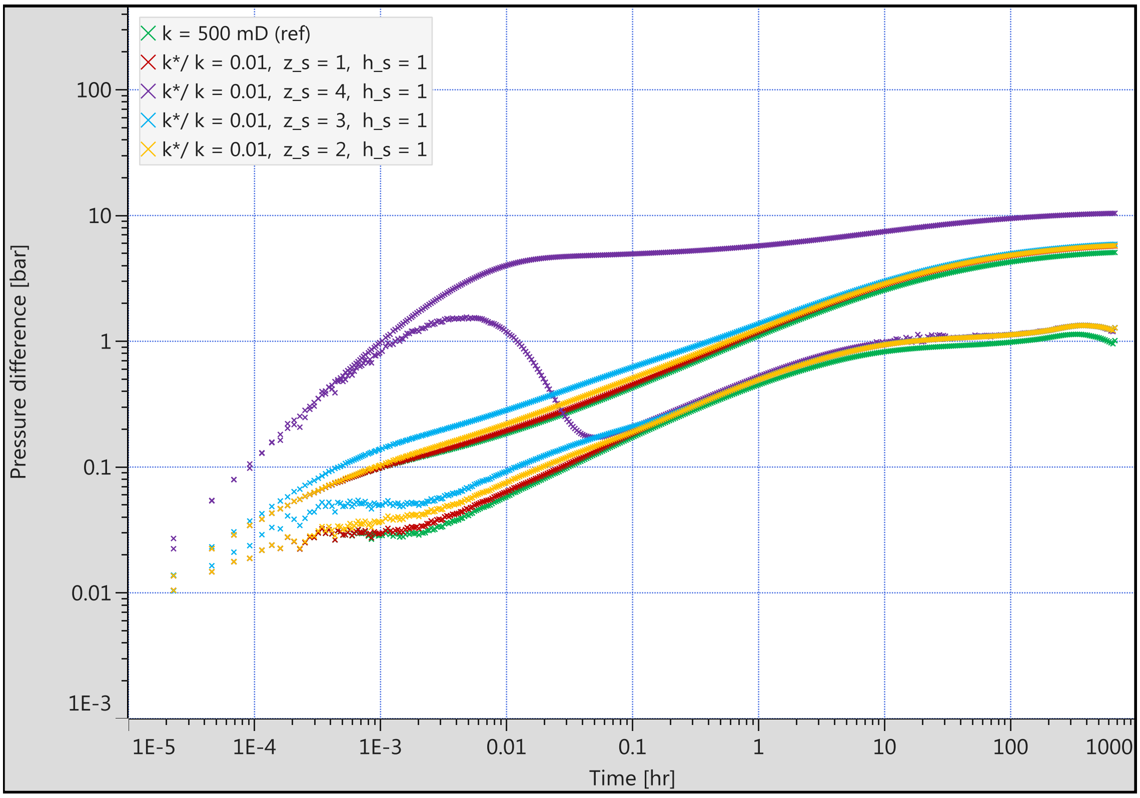

Figure 99 – Effect of thin horizontal streak of low permeability (k*/k = 0.01)

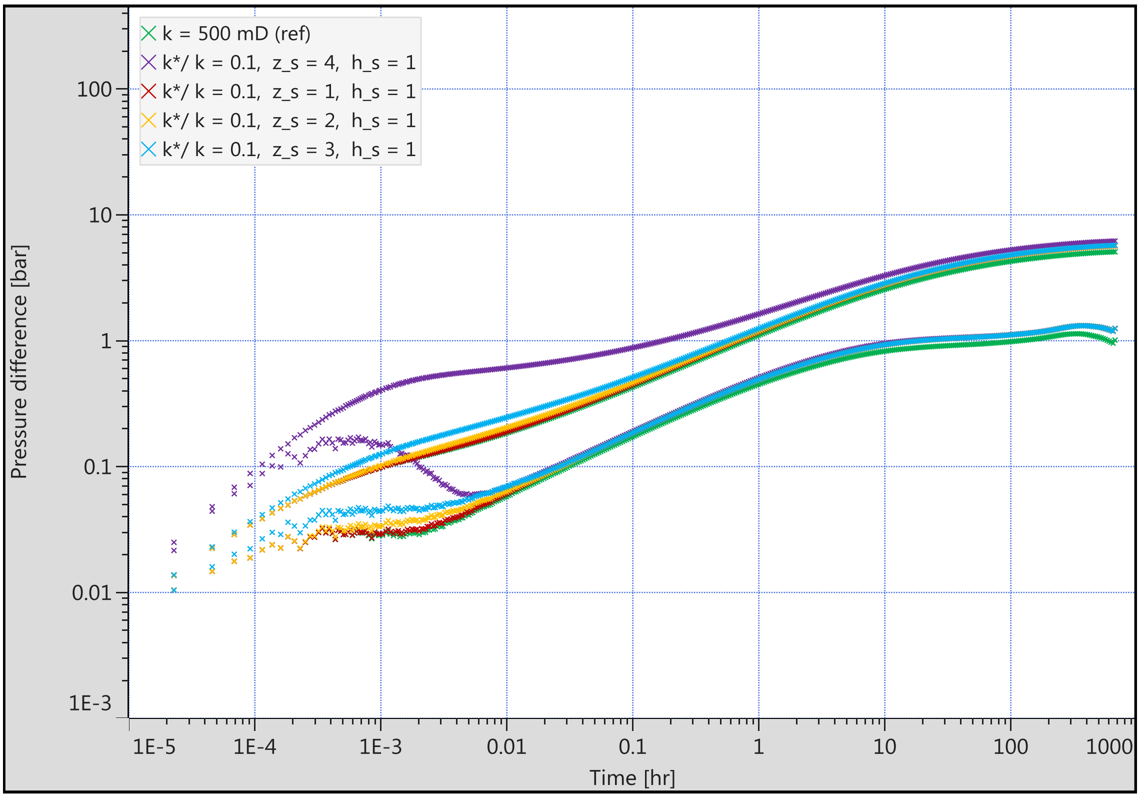

Figure 100 - Effect of thin horizontal streak of low permeability (k*/k = 0.1)

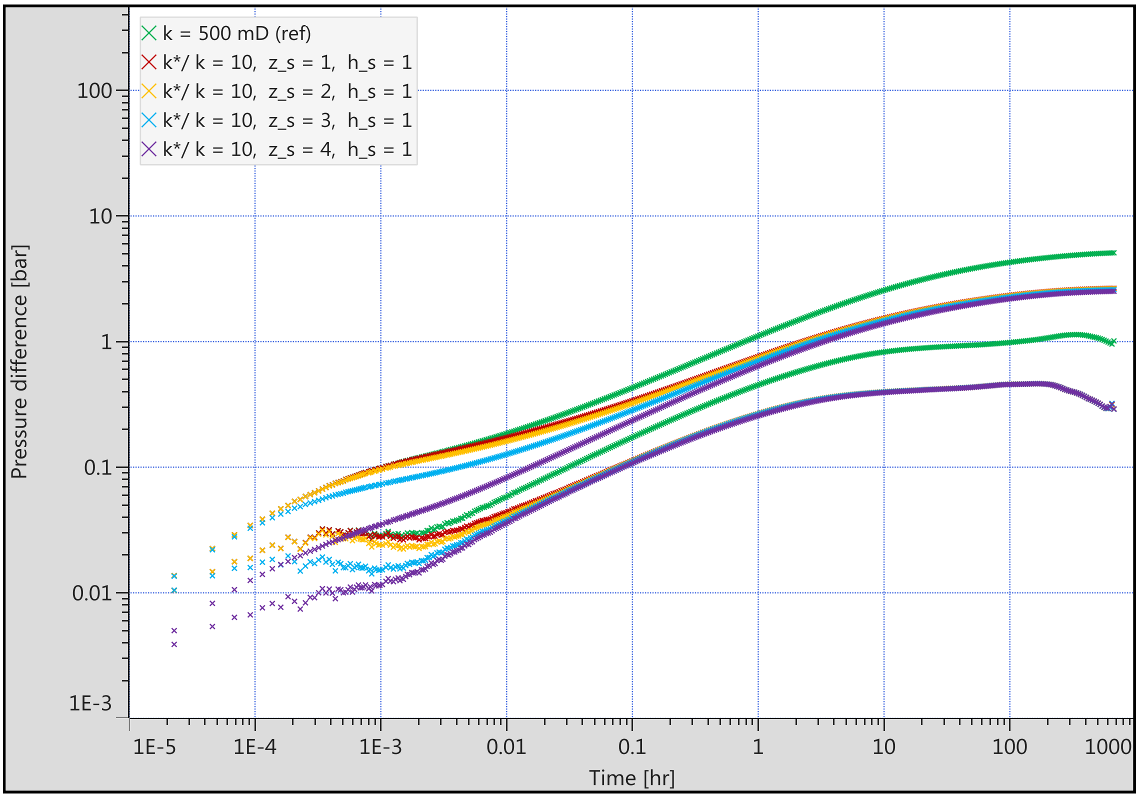

Figure 101 – Effect of thin horizontal streak of high permeability (k*/k = 10)

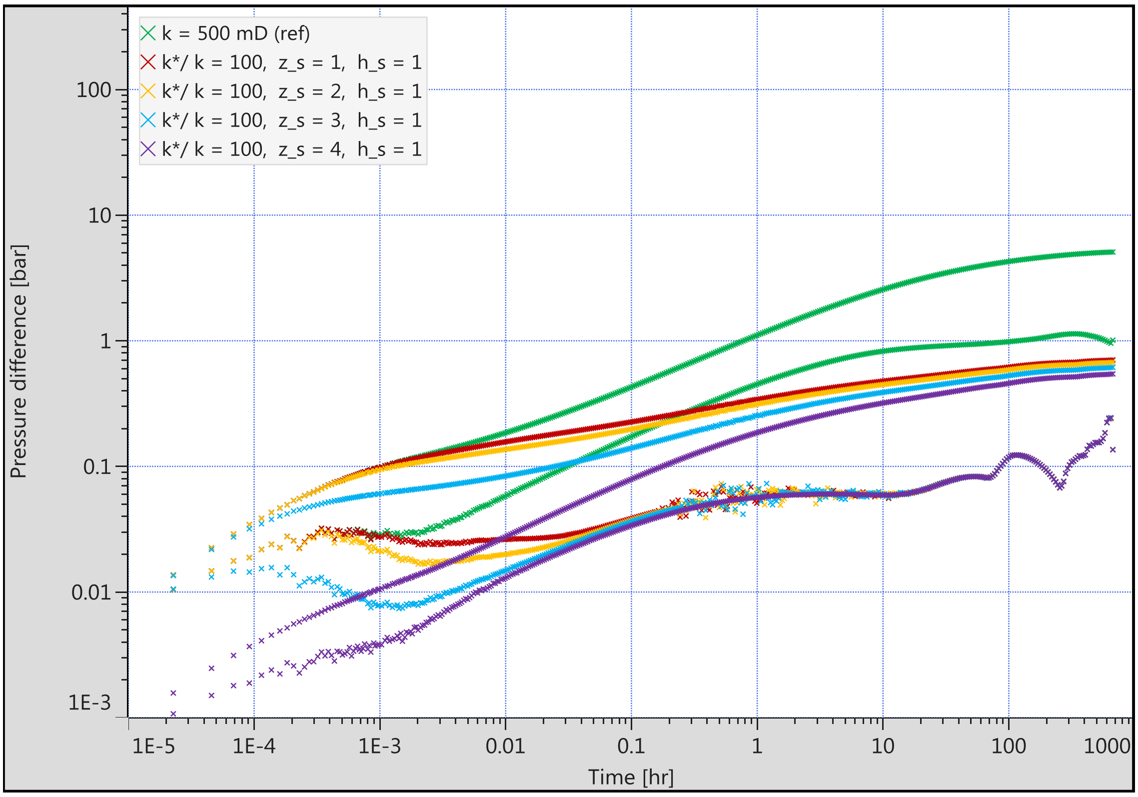

Figure 102 – Effect of thin horizontal streak of high permeability (k*/k = 100)

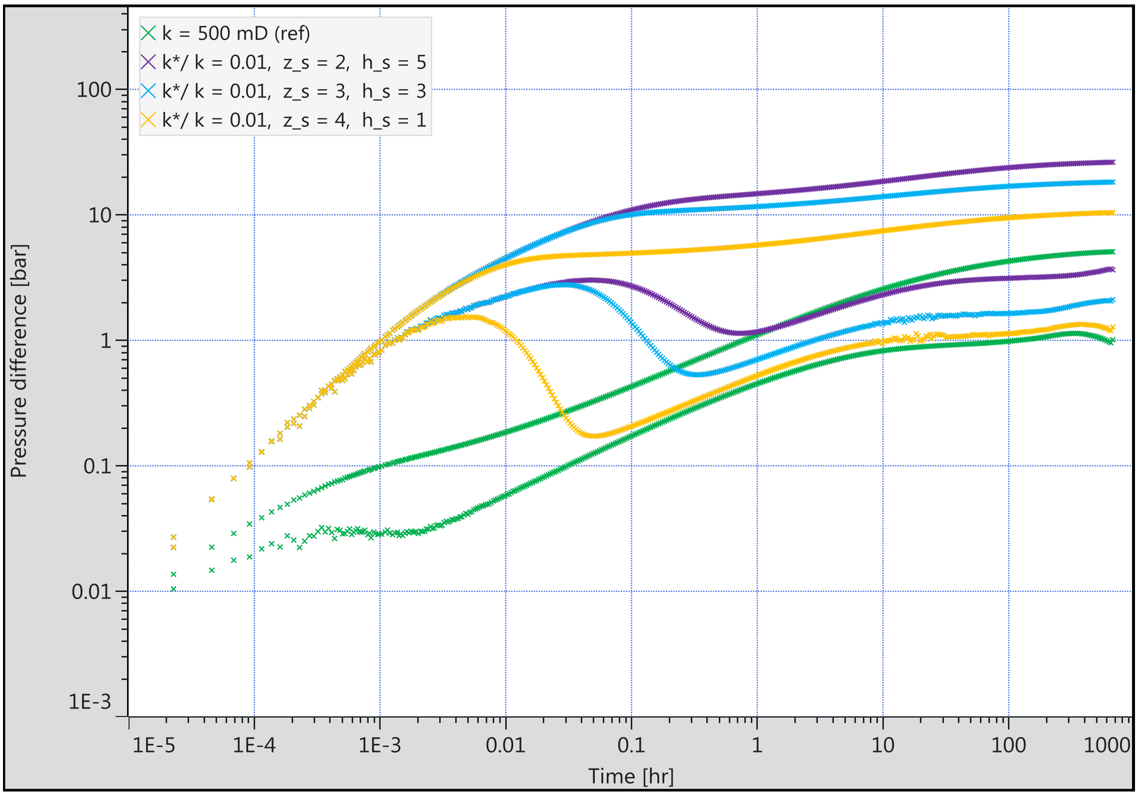

Figure 103 – Influence of thickness of low permeability streak concentrically encompassing the horizontal well (k*/k = 0.01)

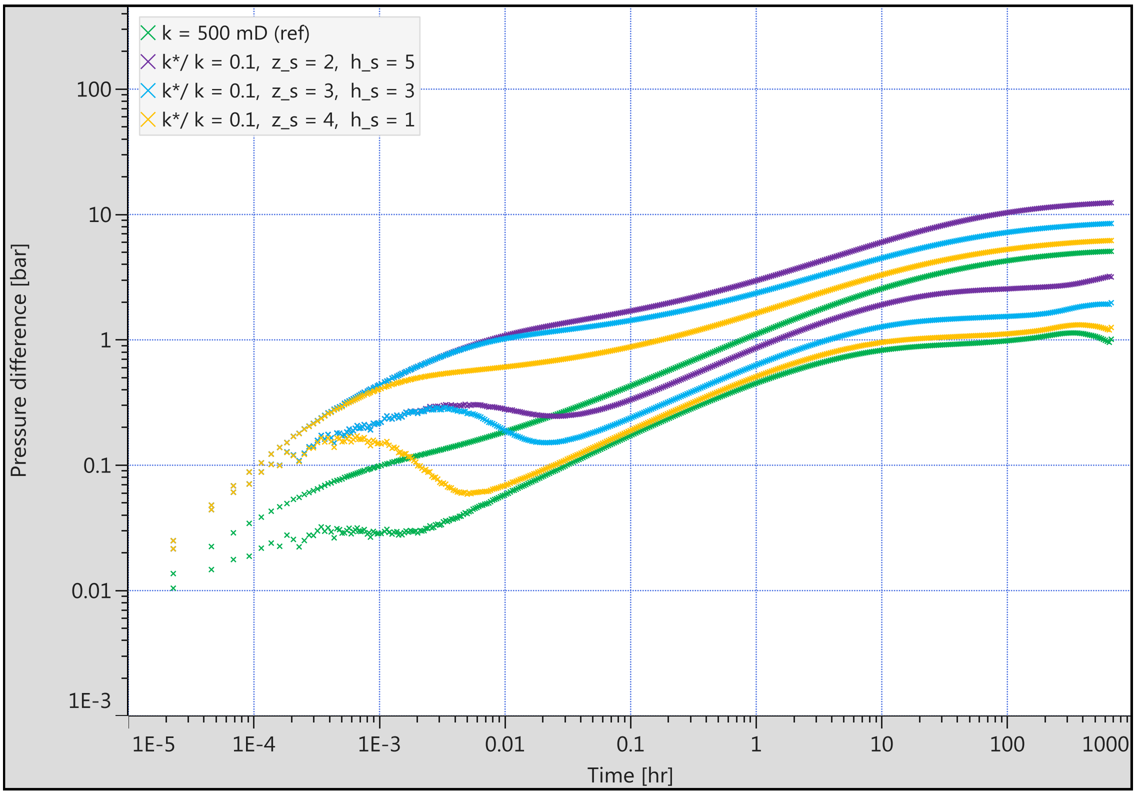

Figure 104 - Influence of thickness of low permeability streak concentrically encompassing the horizontal well (k*/k = 0.1)

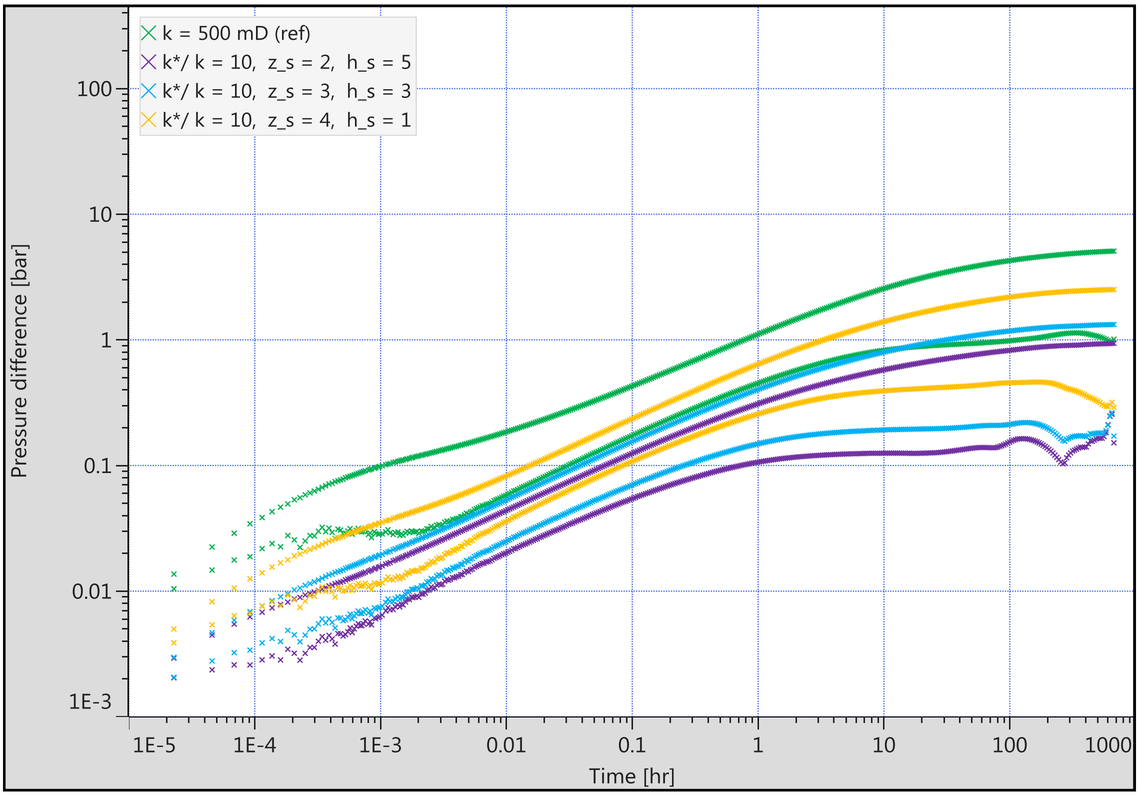

Figure 105 – Influence of thickness of high permeability streak concentrically encompassing the horizontal well (k*/k = 10)

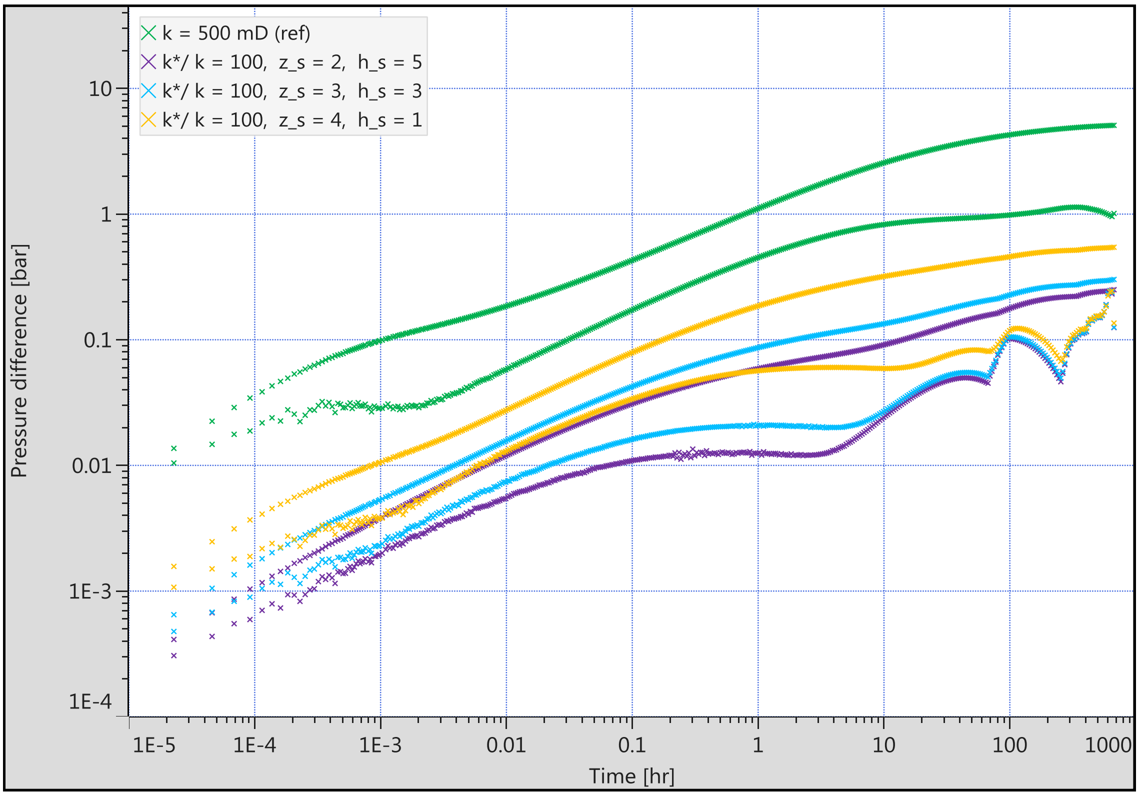

Figure 106 - Influence of thickness of high permeability streak concentrically encompassing the horizontal well (k*/k = 100)

Appendix C – Vertical permeability plane type curves (parallel to well)

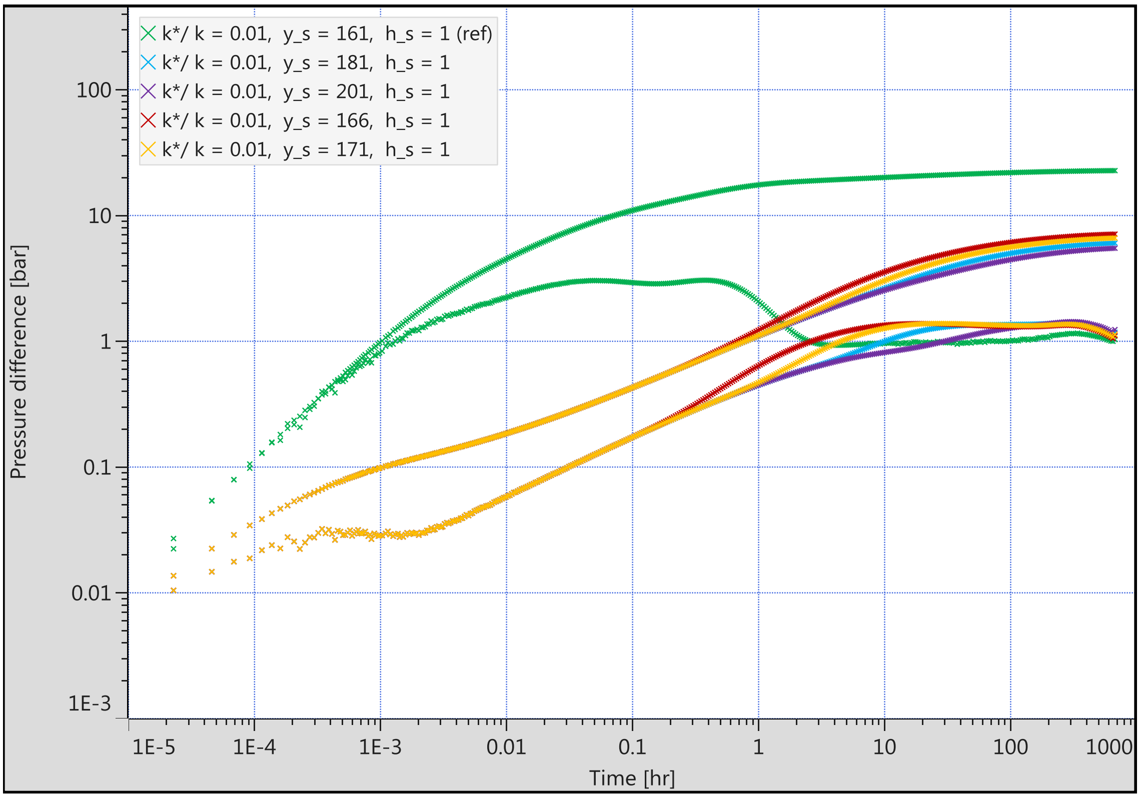

Figure 107 – Effect of thin vertical streak of low permeability parallel to the well (k*/k = 0.01)

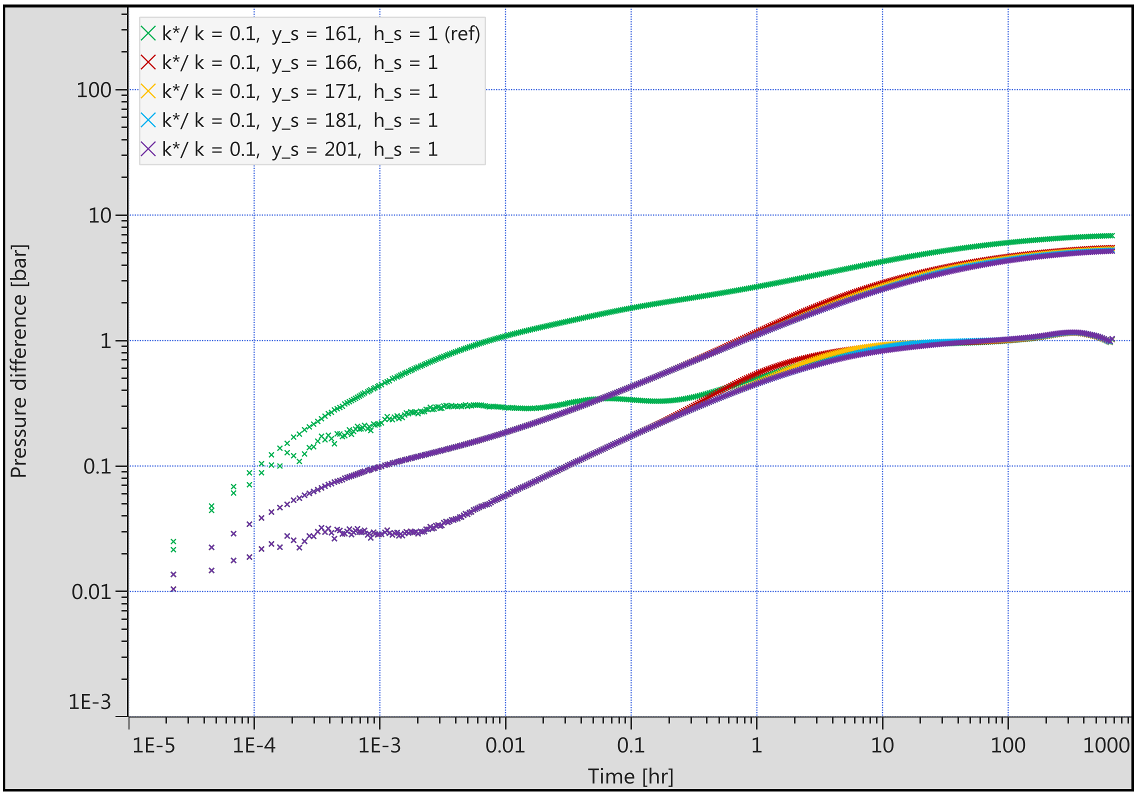

Figure 108 - Effect of thin vertical streak of low permeability parallel to the well (k*/k = 0.1)

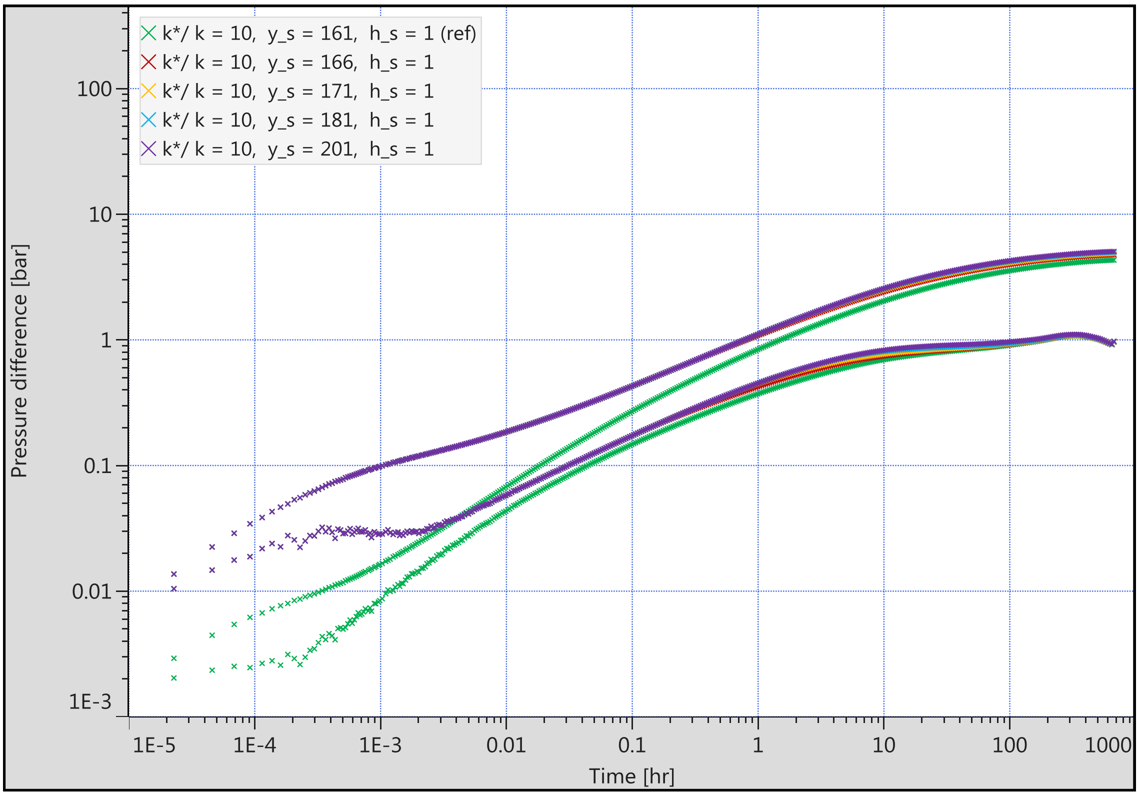

Figure 109 – Effect of thin vertical streak of high permeability parallel to the well (k*/k = 10)

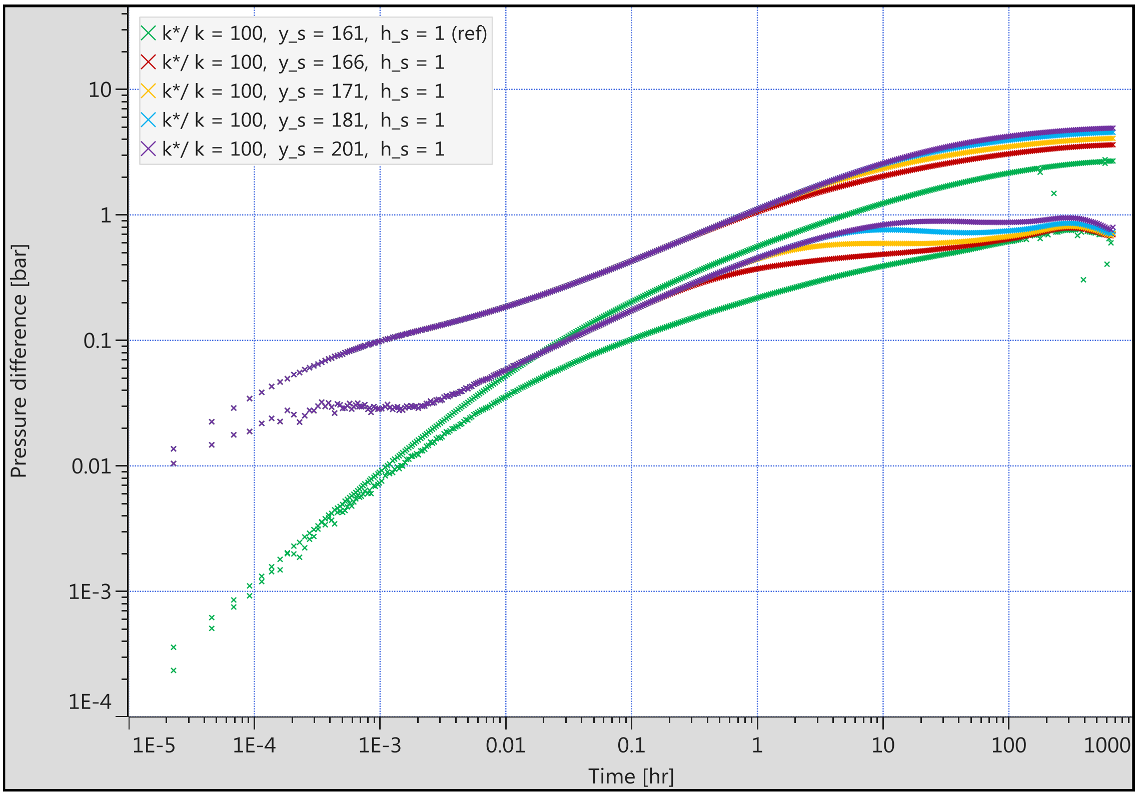

Figure 110 – Effect of thin vertical streak of high permeability parallel to the well (k*/k = 100)

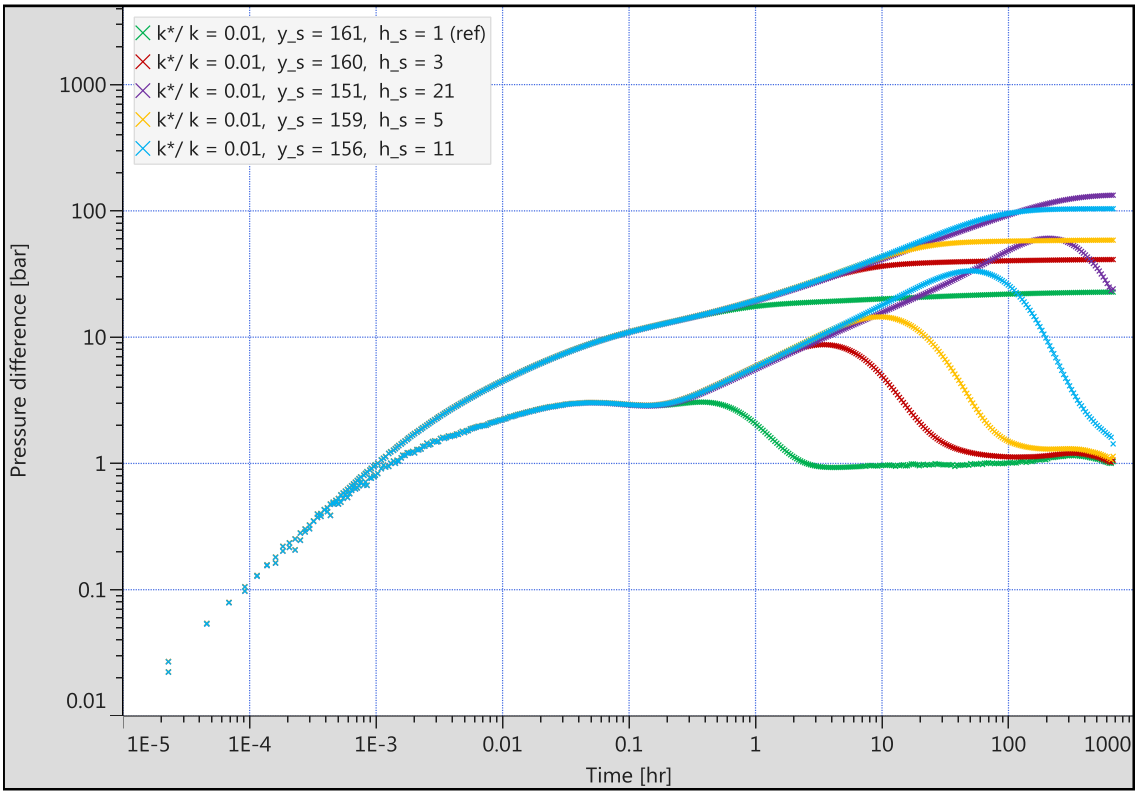

Figure 111 – Influence of width of parallel oriented low permeability streak concentrically encompassing the horizontal well (k*/k = 0.01)

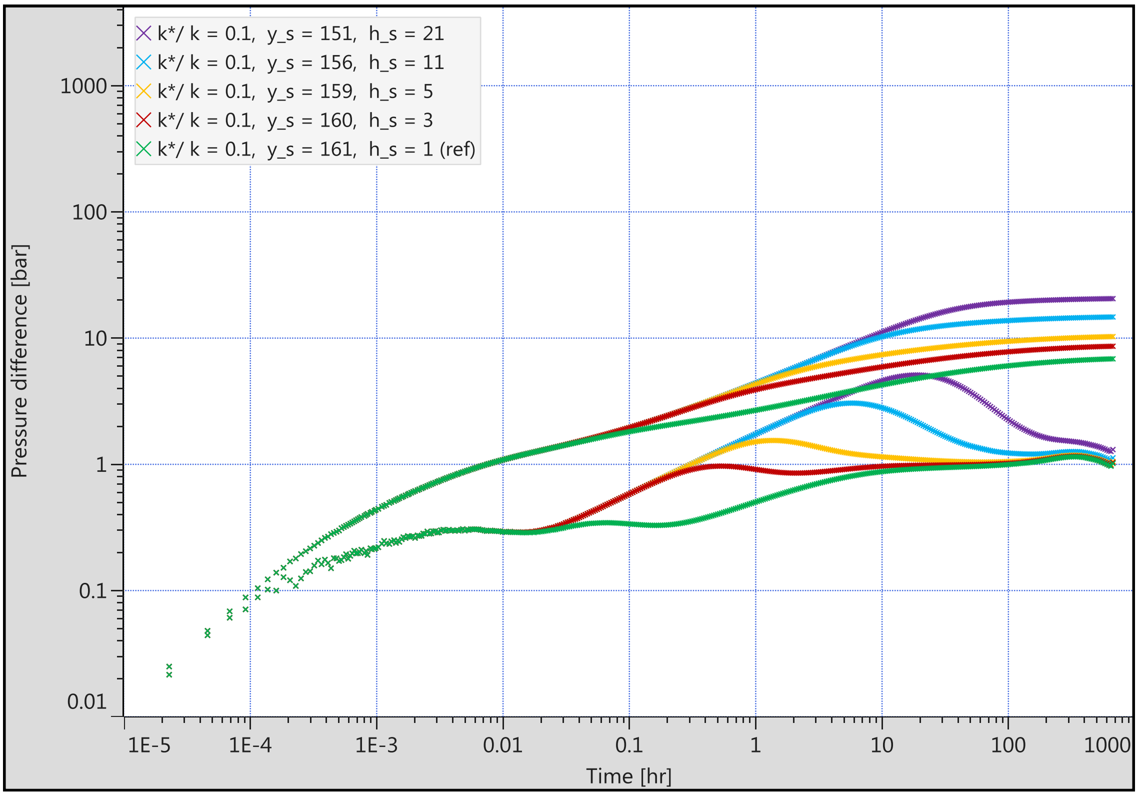

Figure 112 - Influence of width of parallel oriented low permeability streak concentrically encompassing the horizontal well (k*/k = 0.1)

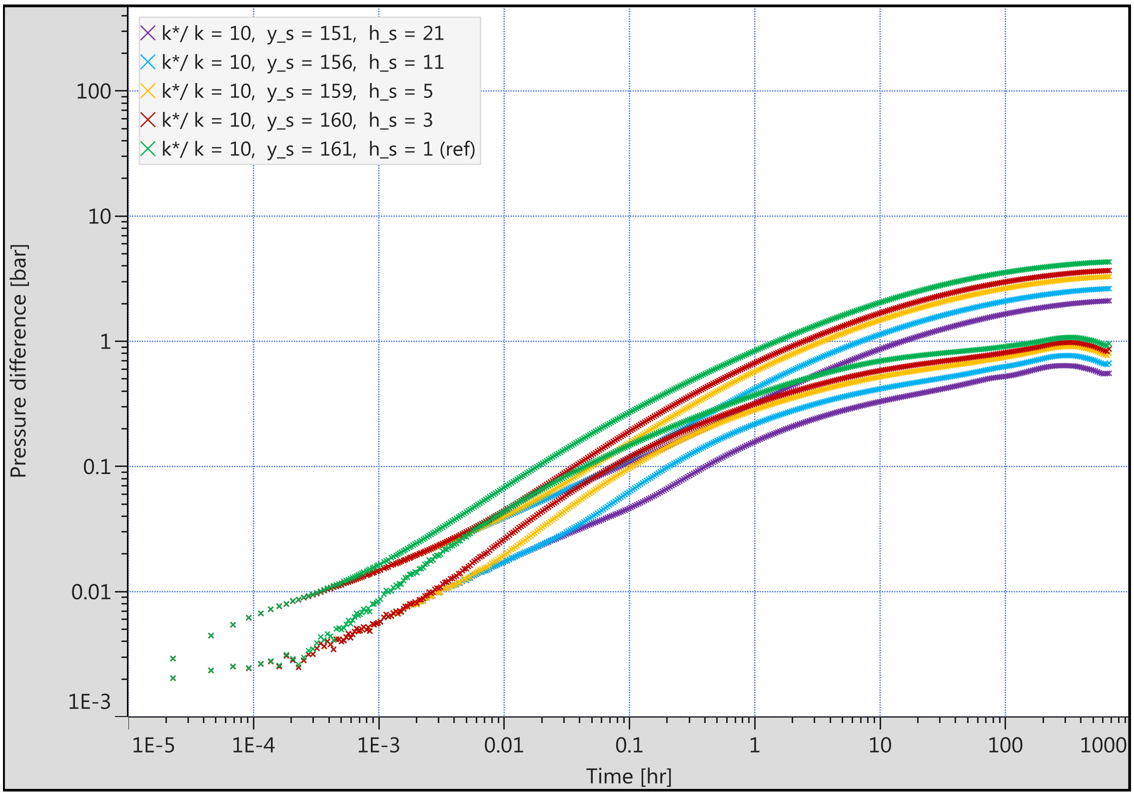

Figure 113 – Influence of width of parallel oriented high permeability streak concentrically encompassing the horizontal well (k*/k = 10)

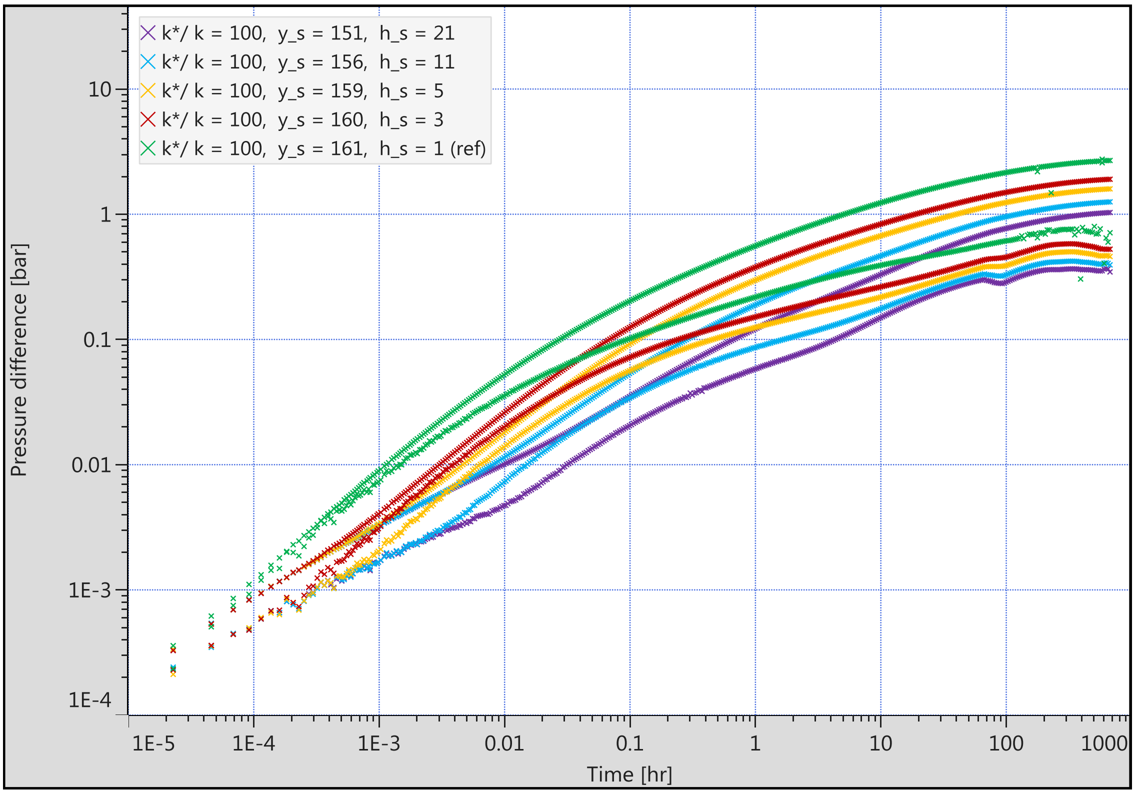

Figure 114 - Influence of width of parallel oriented high permeability streak concentrically encompassing the horizontal well (k*/k = 100)

Appendix D – Vertical permeability plane type curves (perpendicular to well)

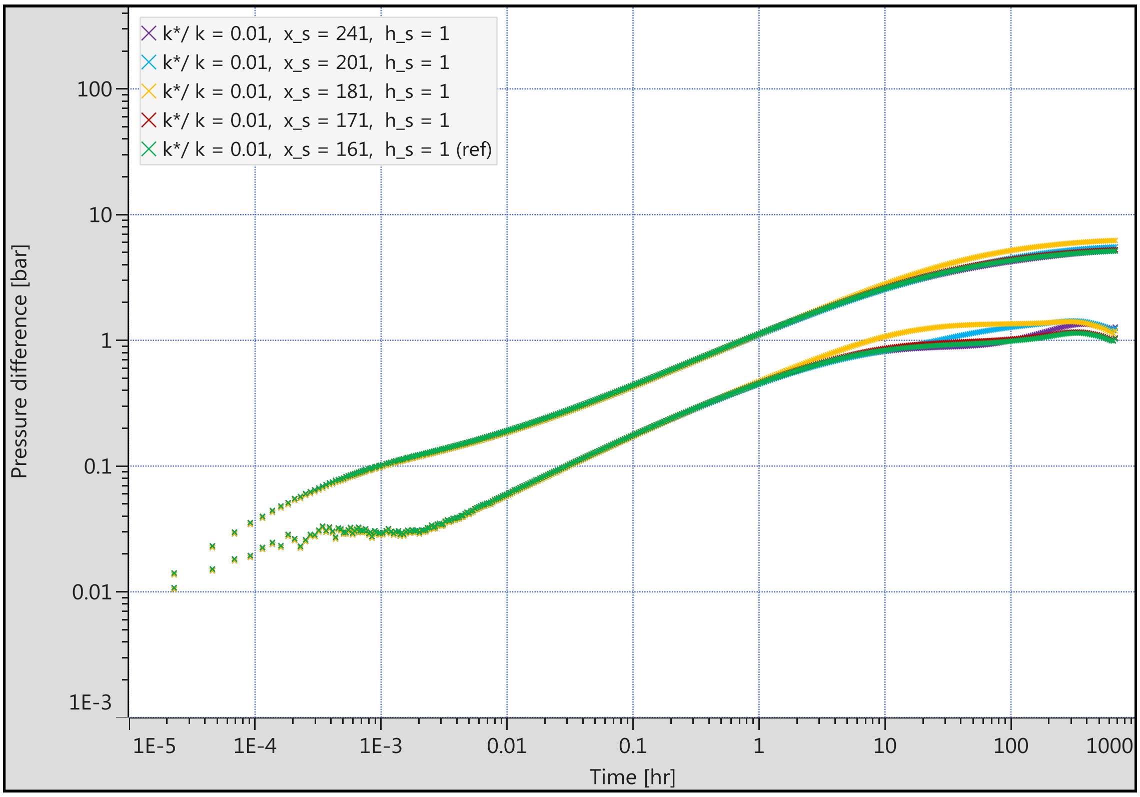

Figure 115 – Vertical low permeability streak perpendicularly intersecting the well (k*/k = 0.01)

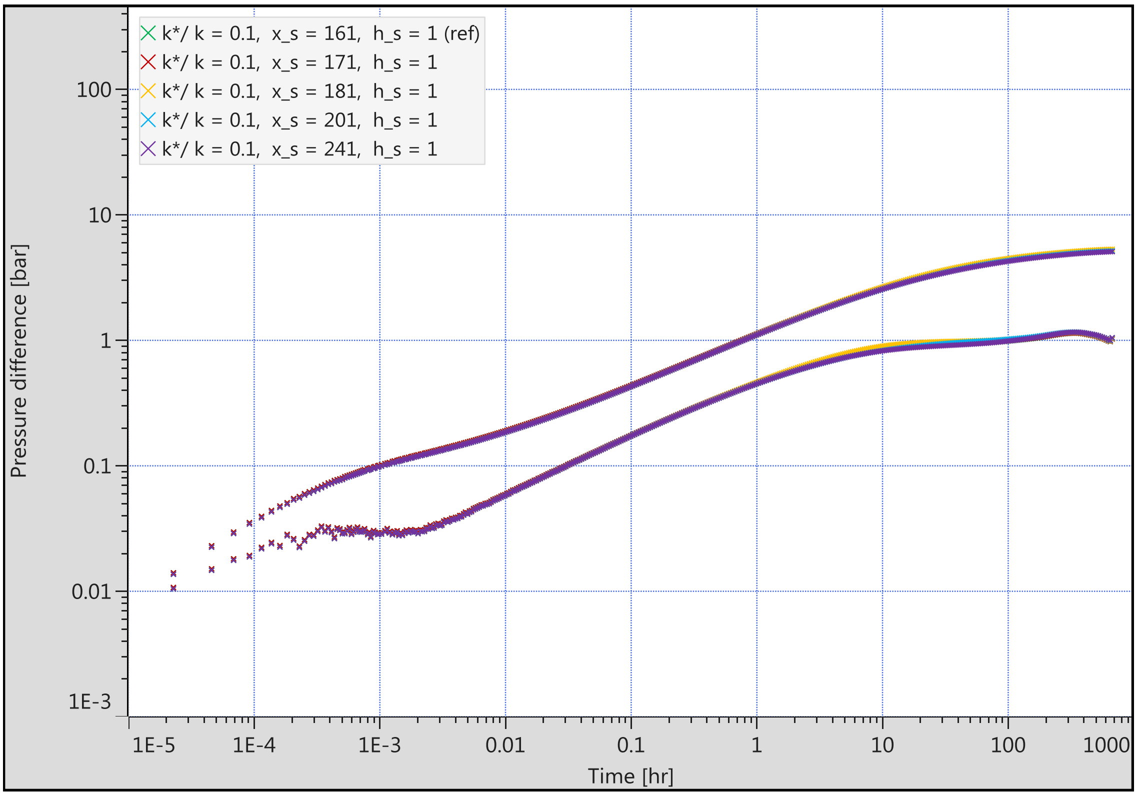

Figure 116 - Vertical low permeability streak perpendicularly intersecting the well (k*/k = 0.1)

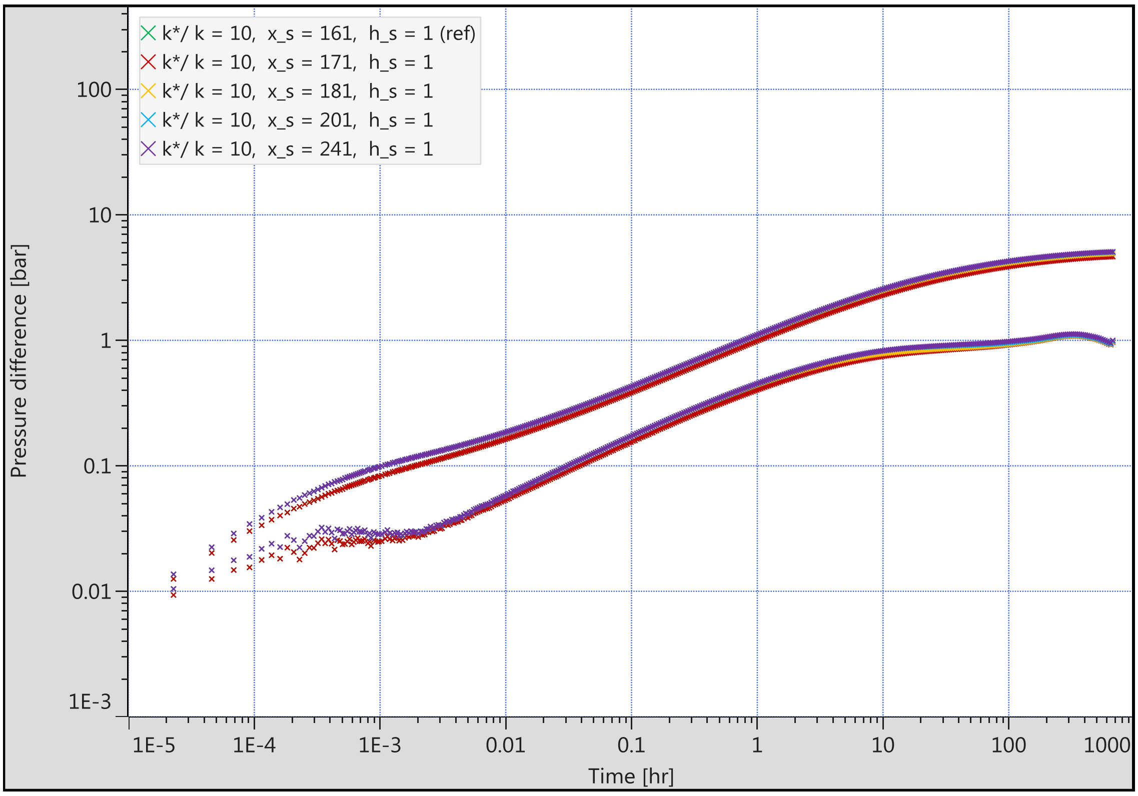

Figure 117 – Vertical high permeability streak perpendicularly intersecting the well (k*/k = 10)

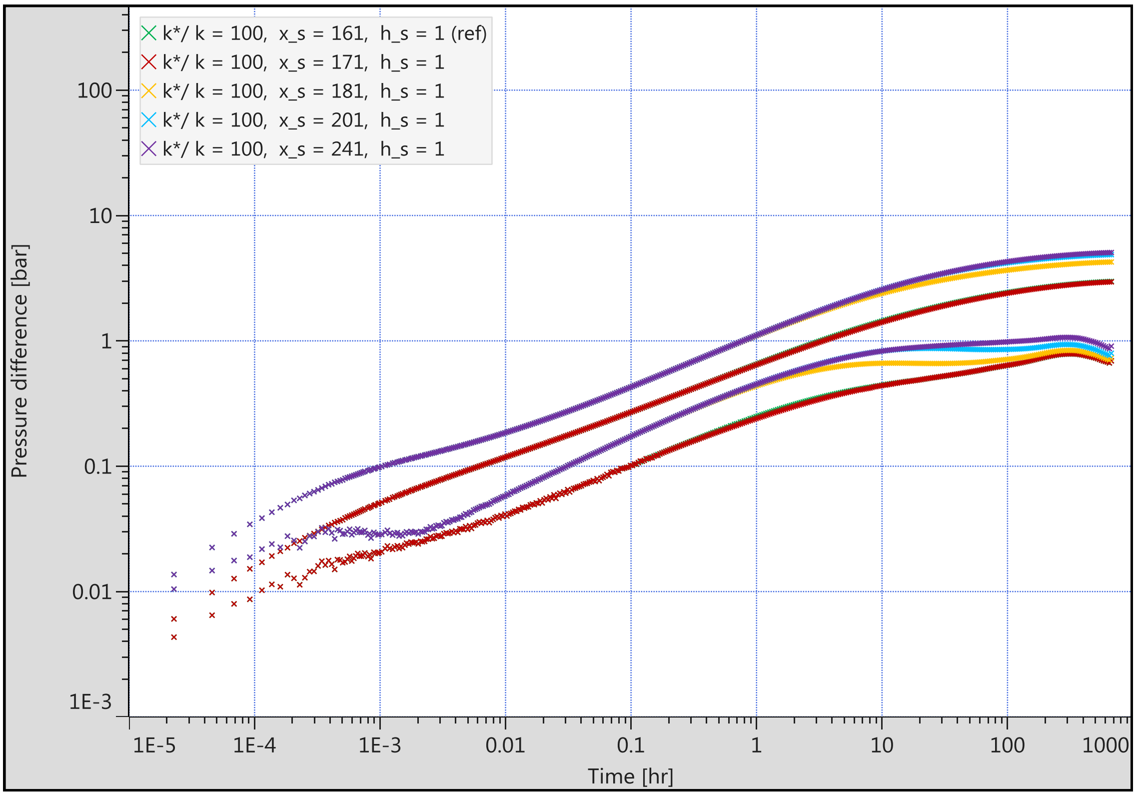

Figure 118 – Vertical high permeability streak perpendicularly intersecting the well (k*/k = 100)

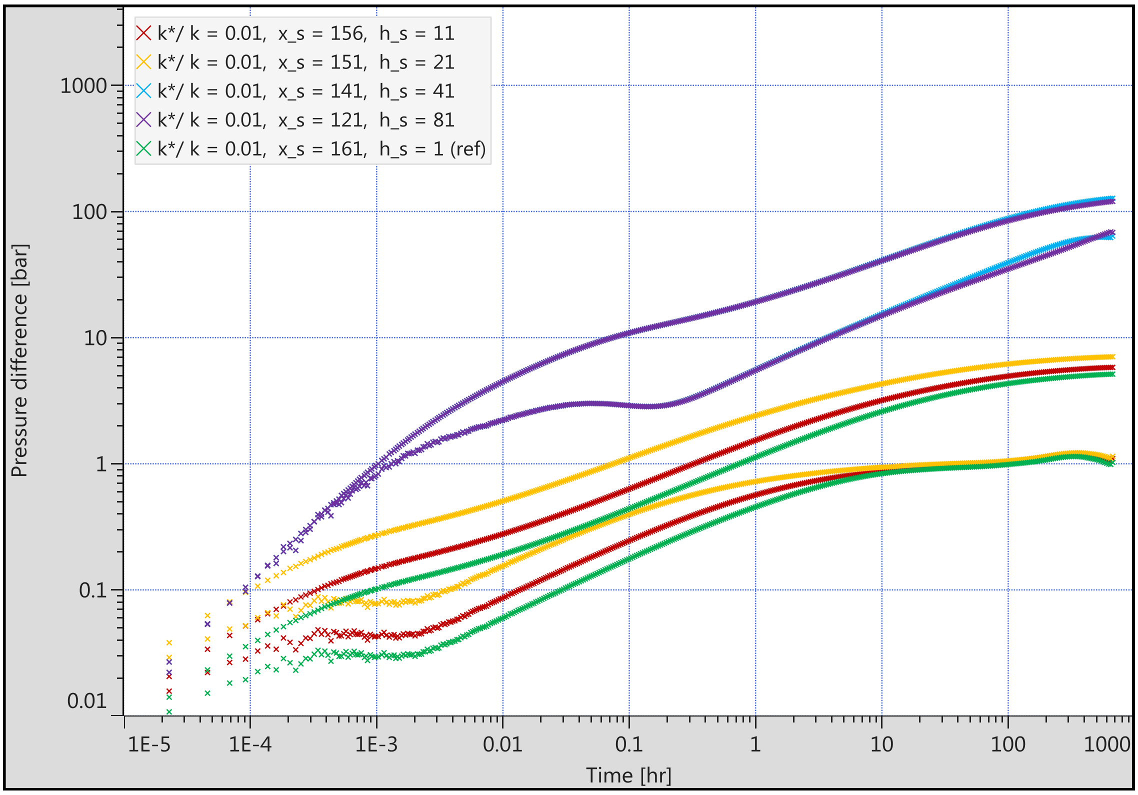

Figure 119 – Influence of width of perpendicularly intersecting low permeability streak concentrically encompassing the horizontal well (k*/k = 0.01)

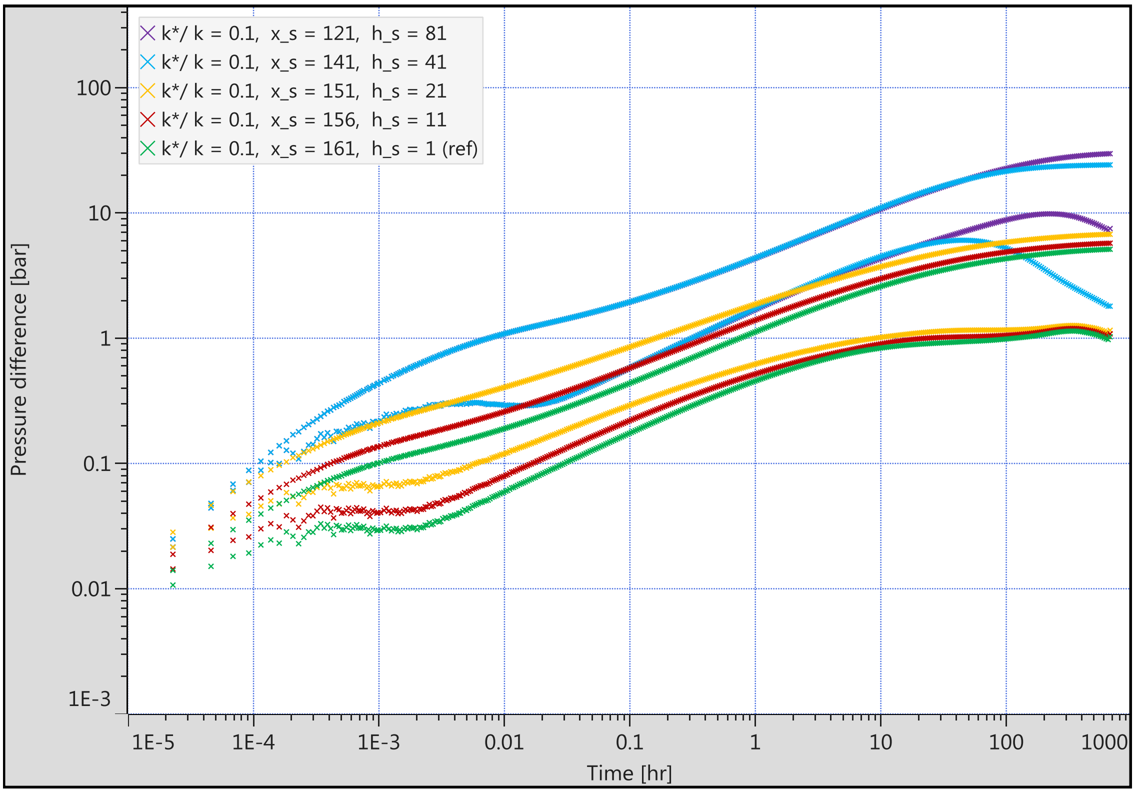

Figure 120 - Influence of width of perpendicularly intersecting low permeability streak concentrically encompassing the horizontal well (k*/k = 0.1)

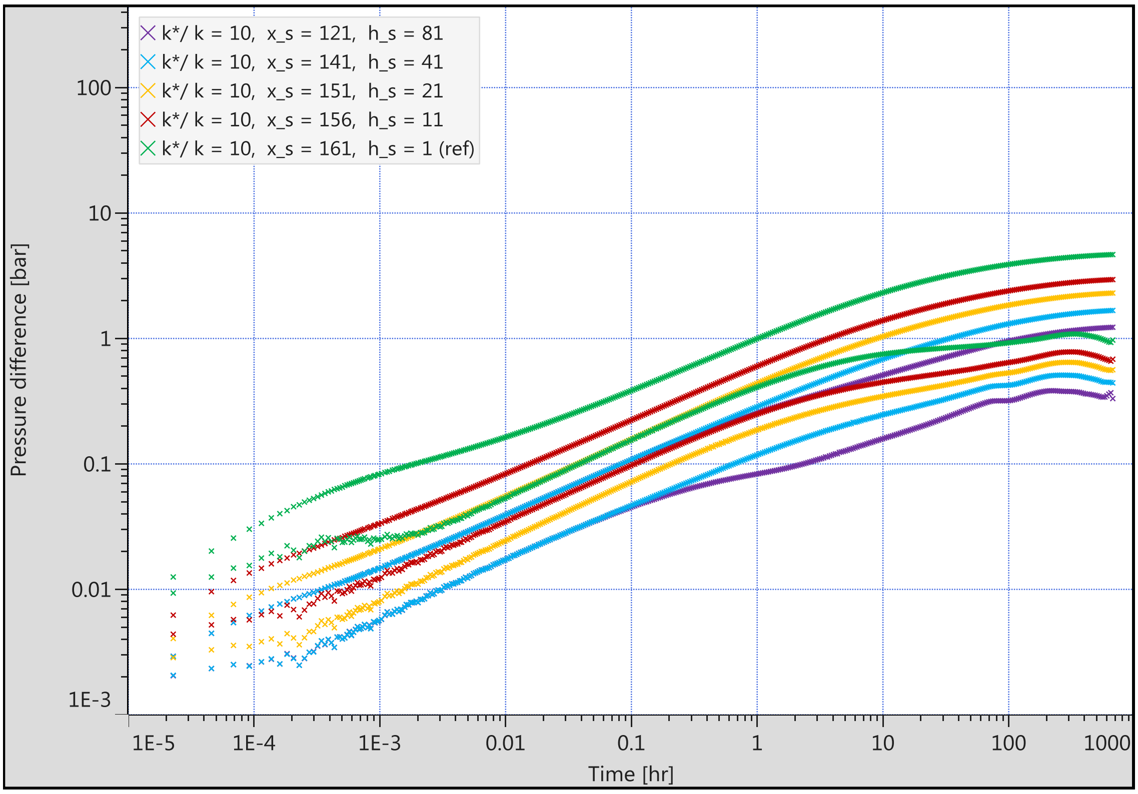

Figure 121 – Influence of width of perpendicularly intersecting high permeability streak concentrically encompassing the horizontal well (k*/k = 10)

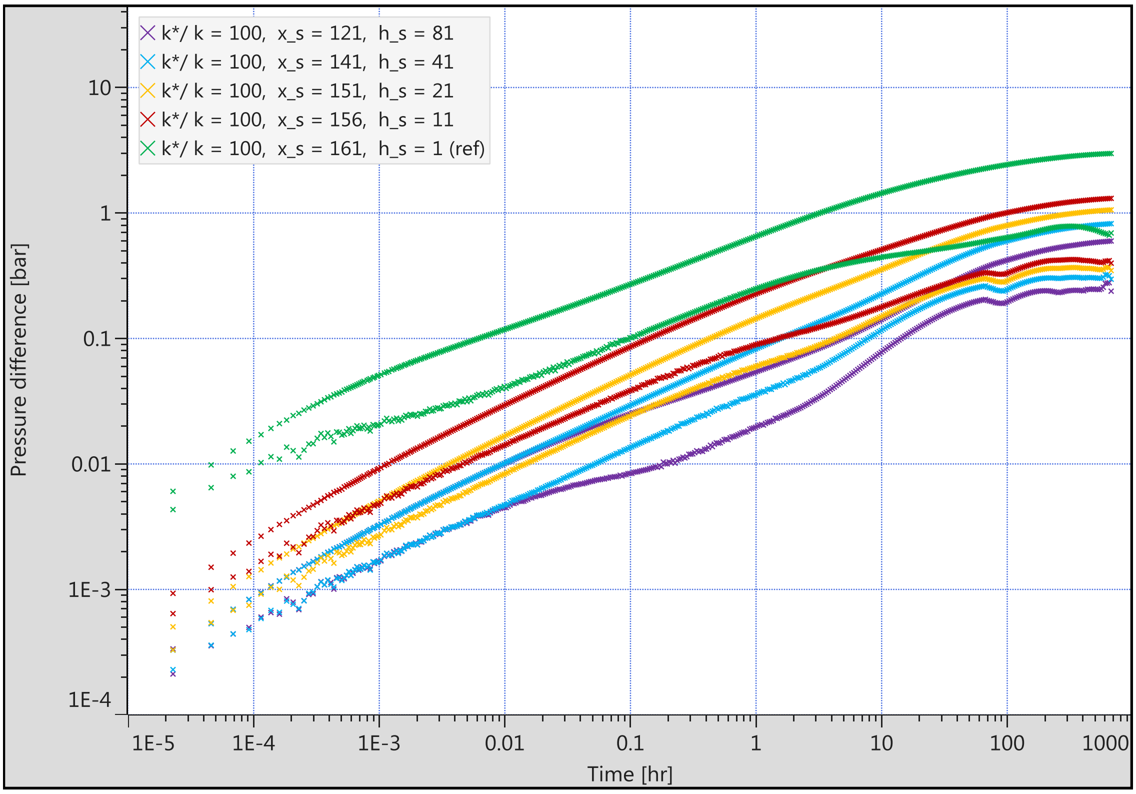

Figure 122 - Influence of width of perpendicularly intersecting high permeability streak concentrically encompassing the horizontal well (k*/k = 100)

Appendix E – Influence of various upscaling techniques on the pressure response for a log-normally distributed permeability (μ = 3, σ = 1.5)

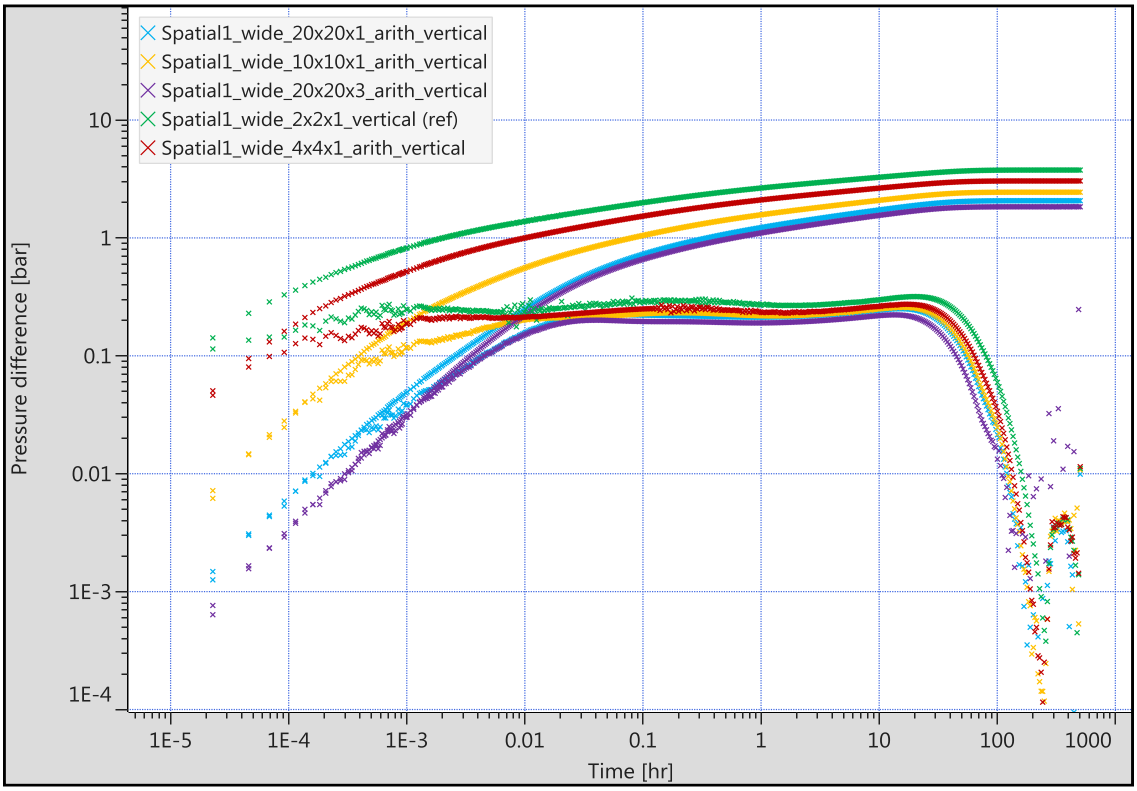

Figure 123 – Pressure response alteration for a vertical well due to arithmetic upscaling

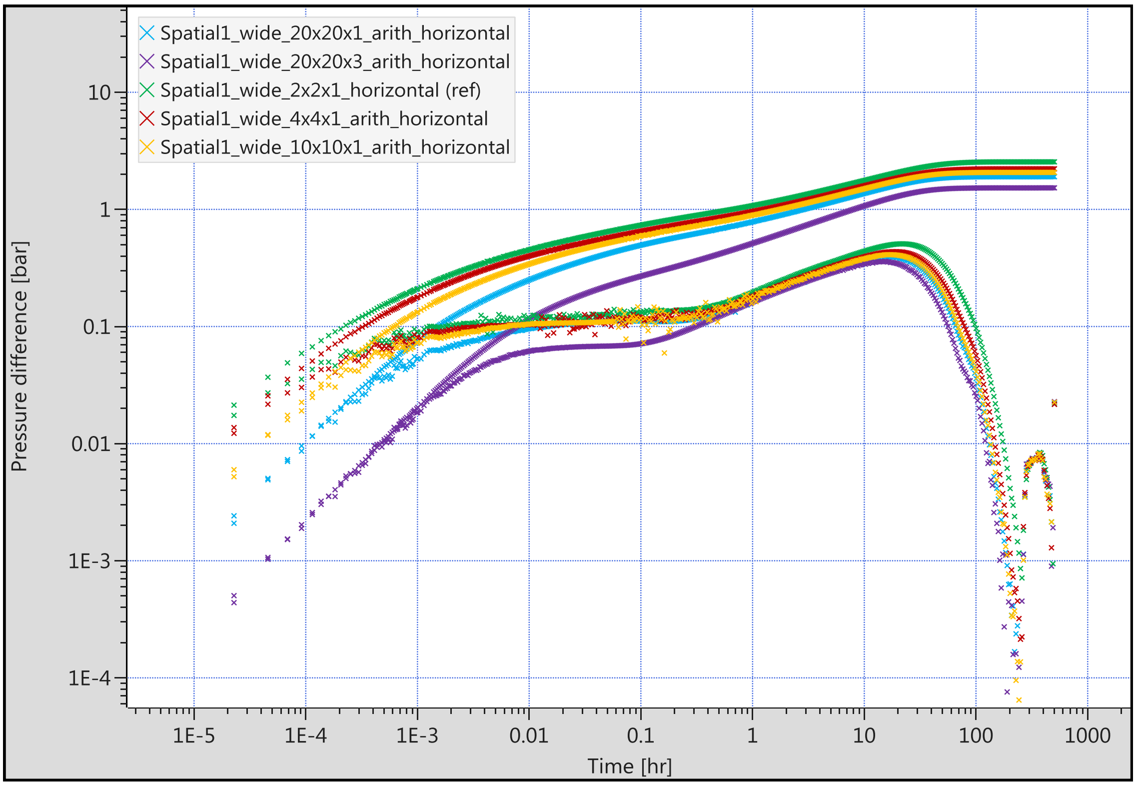

Figure 124 – Pressure response alteration for a horizontal well due to arithmetic upscaling

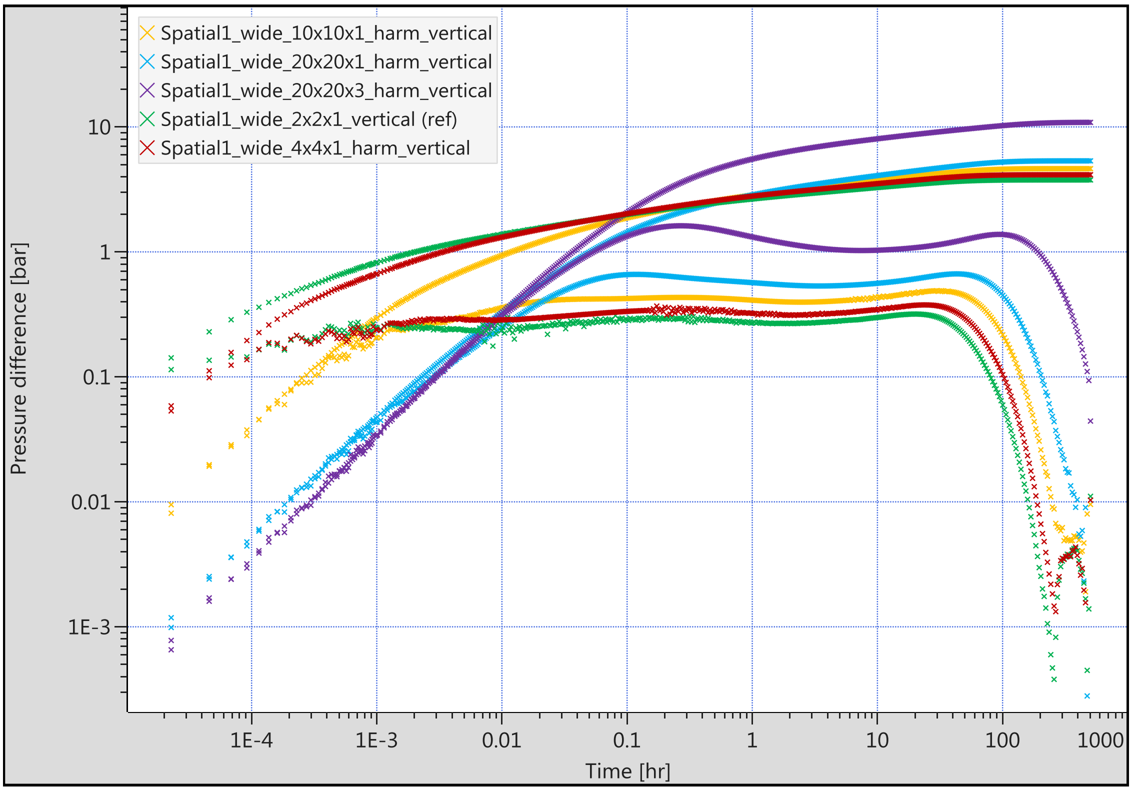

Figure 125 – Pressure response alteration for a vertical well due to harmonic upscaling

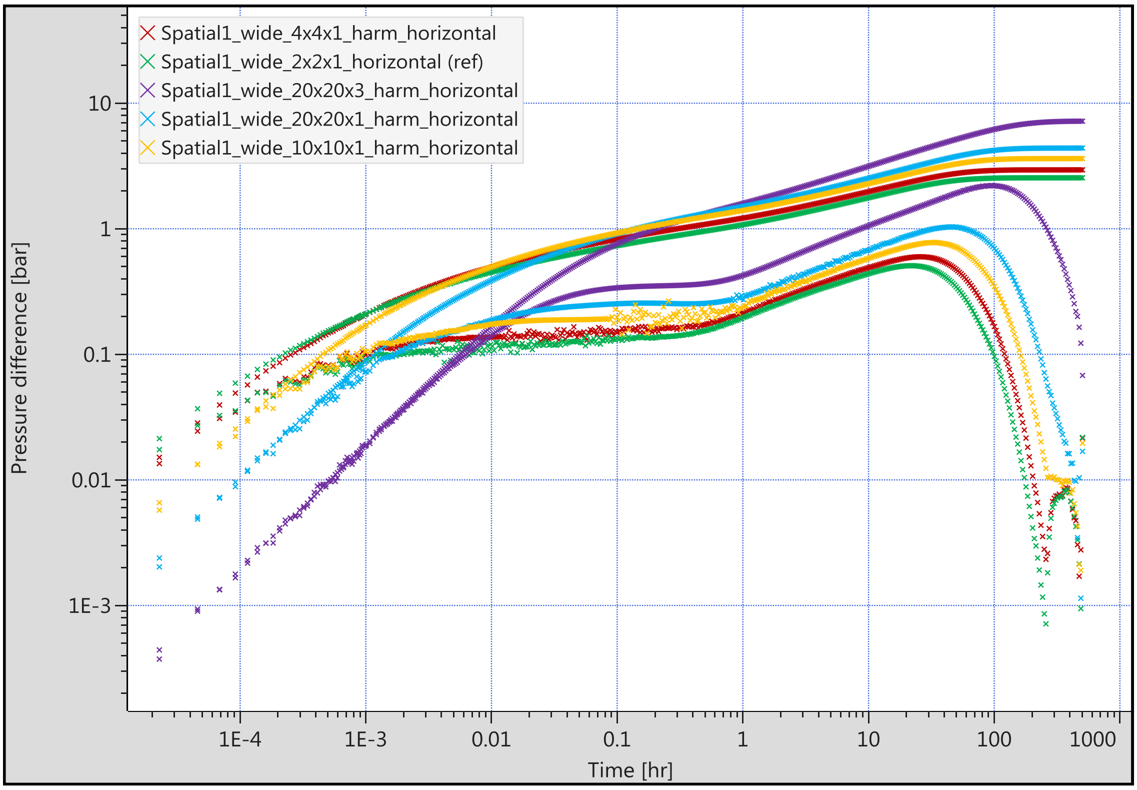

Figure 126 – Pressure response alteration for a horizontal well due to harmonic upscaling

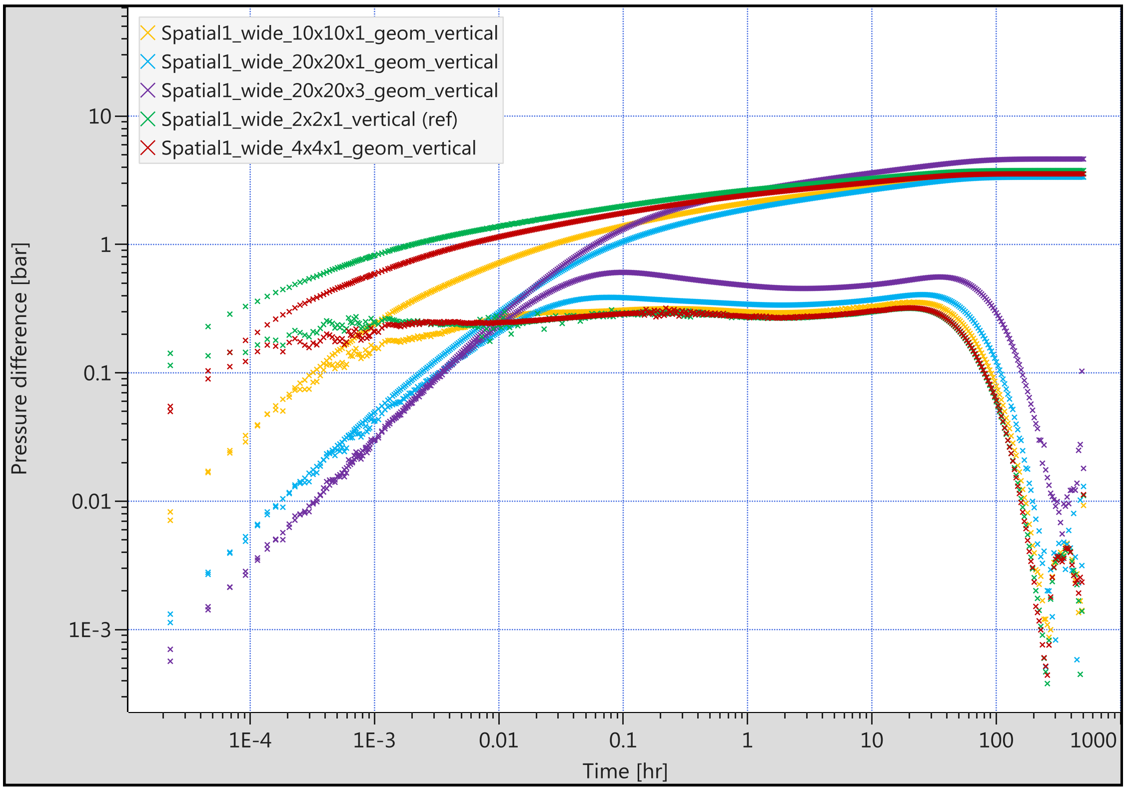

Figure 127 – Pressure response alteration for a vertical well due to geometric upscaling

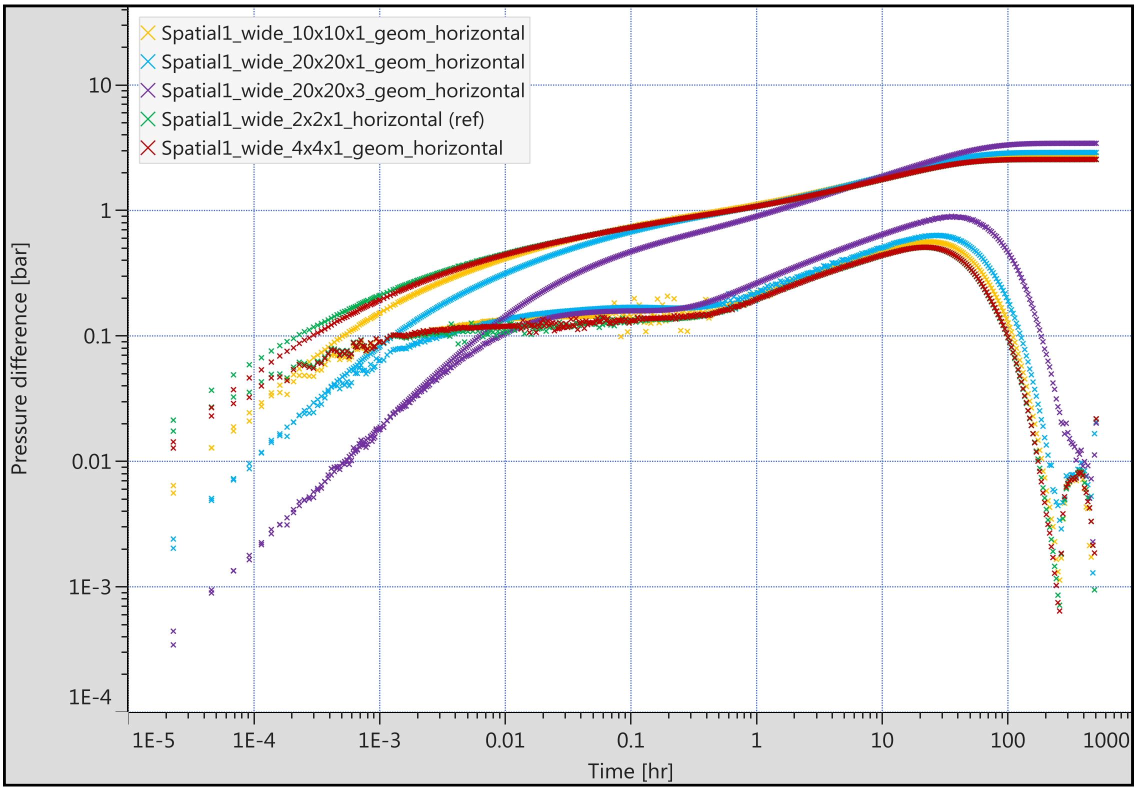

Figure 128 – Pressure response alteration for a horizontal well due to geometric upscaling

Appendix F – Polymer viscosity correlations as implemented into Eclipse

$C_{Polymer}$	$\mu_{Polymer}$				
	PLYVISC 1	PLYVISC 2	PLYVISC 3	PLYVISC 4	PLYVISC 5
kg/scm	cP	cP	cP	cP	cP
0.000	0.550	0.550	0.550	0.550	0.550
0.125	0.828	0.968	1.176	1.385	1.594
0.250	1.110	1.396	1.818	2.241	2.664
0.375	1.398	1.834	2.476	3.118	3.760
0.500	1.691	2.283	3.149	4.015	4.881
0.625	1.989	2.741	3.837	4.933	6.029
0.750	2.293	3.211	4.541	5.871	7.202
0.875	2.601	3.690	5.260	6.830	8.400
1.000	2.915	4.180	5.995	7.810	9.625
1.125	3.234	4.680	6.745	8.810	10.875
1.250	3.558	5.191	7.511	9.831	12.152
1.375	3.887	5.711	8.292	10.873	13.454
1.500	4.221	6.243	9.089	11.935	14.781
1.625	4.561	6.784	9.901	13.018	16.135
1.750	4.905	7.336	10.728	14.121	17.514
1.875	5.255	7.898	11.571	15.245	18.919
2.000	5.610	8.470	12.430	16.390	20.350
2.125	5.970	9.053	13.304	17.555	21.807
2.250	6.335	9.646	14.193	18.741	23.289
2.375	6.706	10.249	15.098	19.948	24.797

Appendix G – Polymer adsorption correlations as implemented into Eclipse

$C_{Polymer}$	Polymer adsorption				
	PLYADS 1	PLYADS 2	PLYADS 3	PLYADS 4	PLYADS 5
kg/scm	$\mu g/g_{rock}$	$\mu g/g_{rock}$	$\mu g/g_{rock}$	$\mu g/g_{rock}$	$\mu g/g_{rock}$
0.000	0.000	0.000	0.000	0.000	0.000
0.125	0.792	2.376	4.753	7.129	9.506
0.250	1.584	4.753	9.506	14.259	19.011
0.375	2.376	7.129	14.259	21.388	28.517
0.500	3.169	9.506	19.011	28.517	38.023
0.625	3.961	11.882	23.764	35.646	47.529
0.750	4.753	14.259	28.517	42.776	57.034
0.875	4.840	14.519	29.037	43.556	58.074
1.000	4.859	14.578	29.155	43.733	58.311
1.125	4.879	14.637	29.273	43.910	58.547
1.250	4.899	14.696	29.392	44.087	58.783
1.375	4.918	14.755	29.510	44.265	59.020
1.500	4.938	14.814	29.628	44.442	59.256
1.625	4.958	14.873	29.746	44.619	59.492
1.750	4.977	14.932	29.864	44.796	59.728
1.875	4.997	14.991	29.982	44.974	59.965
2.000	5.017	15.050	30.100	45.151	60.201
2.125	5.036	15.109	30.219	45.328	60.437
2.250	5.056	15.168	30.337	45.505	60.674
2.375	5.076	15.227	30.455	45.682	60.910
φ_{dead}	0.15	0.175	0.2	0.25	0.3
RRF	1.5	1.75	2	2.5	3
Maximum adsorbed concentration	5.076	15.227	30.455	45.682	60.910

Appendix H – Reservoir models for layered heterogeneity investigation

Case		**00**	**01**	**02**	**03**	**04**	**05**	**06**	**07**	**08**	**09**	**10**
Injected fluid		*Water*	*Polymer*									
Layer 1	h, m	4	4	4	4	4	4	4	4	4	4	4
	φ	0.1	0.1	0.1	0.1	0.1	0.1	0.1	0.1	0.1	0.1	0.1
	k_H, mD	100	100	100	100	100	100	100	100	100	100	100
	k_V/k_H	1	1	1	1	1	1	1	1	1	1	1
	PLYVISC		5	3	1	5	1	5	5	5	3	3
	PLYADS						3	3	5	1	5	1
Layer 2	h, m	4	4	4	4	4	4	4	4	4	4	4
	φ	0.15	0.15	0.15	0.15	0.15	0.15	0.15	0.15	0.15	0.15	0.15
	k_H, mD	300	300	300	300	300	300	300	300	300	300	300
	k_V/k_H	1	1	1	1	1	1	1	1	1	1	1
	PLYVISC		5	3	2	4	2	4	5	5	3	3
	PLYADS						3	3	4	2	4	2
Layer 3	h, m	5	5	5	5	5	5	5	5	5	5	5
	φ	0.2	0.2	0.2	0.2	0.2	0.2	0.2	0.2	0.2	0.2	0.2
	k_H, mD	500	500	500	500	500	500	500	500	500	500	500
	k_V/k_H	1	1	1	1	1	1	1	1	1	1	1
	PLYVISC		5	3	3	3	3	3	5	5	3	3
	PLYADS						3	3	3	3	3	3
Layer 4	h, m	4	4	4	4	4	4	4	4	4	4	4
	φ	0.25	0.25	0.25	0.25	0.25	0.25	0.25	0.25	0.25	0.25	0.25
	k_H, mD	700	700	700	700	700	700	700	700	700	700	700
	k_V/k_H	1	1	1	1	1	1	1	1	1	1	1
	PLYVISC		5	3	4	2	4	2	5	5	3	3
	PLYADS						3	3	2	4	2	4
Layer 5	h, m	4	4	4	4	4	4	4	4	4	4	4
	φ	0.3	0.3	0.3	0.3	0.3	0.3	0.3	0.3	0.3	0.3	0.3
	k_H, mD	900	900	900	900	900	900	900	900	900	900	900
	k_V/k_H	1	1	1	1	1	1	1	1	1	1	1
	PLYVISC		5	3	5	1	5	1	5	5	3	3
	PLYADS						3	3	1	5	1	5
AVERAGE	h, m	21	21	21	21	21	21	21	21	21	21	21
	φ	0.2	0.2	0.2	0.2	0.2	0.2	0.2	0.2	0.2	0.2	0.2
	k_H, mD	500	500	500	500	500	500	500	500	500	500	500

Case		**11**	**12**	**13**	**14**	**15**	**16**	**17**	**18**	**19**	**20**	**21**
Injected fluid		*Water*	*Polymer*									
Layer 1	h, m	4	4	4	4	4	4	4	4	4	4	4
	φ	0.1	0.1	0.1	0.1	0.1	0.1	0.1	0.1	0.1	0.1	0.1
	k_H, mD	100	100	100	100	100	100	100	100	100	100	100
	k_V/k_H	0.1	0.1	0.1	0.1	0.1	0.1	0.1	0.1	0.1	0.1	0.1
	PLYVISC		5	3	1	5	1	5	5	5	3	3
	PLYADS						3	3	5	1	5	1
Layer 2	h, m	4	4	4	4	4	4	4	4	4	4	4
	φ	0.15	0.15	0.15	0.15	0.15	0.15	0.15	0.15	0.15	0.15	0.15
	k_H, mD	300	300	300	300	300	300	300	300	300	300	300
	k_V/k_H	0.1	0.1	0.1	0.1	0.1	0.1	0.1	0.1	0.1	0.1	0.1
	PLYVISC		5	3	2	4	2	4	5	5	3	3
	PLYADS						3	3	4	2	4	2
Layer 3	h, m	5	5	5	5	5	5	5	5	5	5	5
	φ	0.2	0.2	0.2	0.2	0.2	0.2	0.2	0.2	0.2	0.2	0.2
	k_H, mD	500	500	500	500	500	500	500	500	500	500	500
	k_V/k_H	0.1	0.1	0.1	0.1	0.1	0.1	0.1	0.1	0.1	0.1	0.1
	PLYVISC		5	3	3	3	3	3	5	5	3	3
	PLYADS						3	3	3	3	3	3
Layer 4	h, m	4	4	4	4	4	4	4	4	4	4	4
	φ	0.25	0.25	0.25	0.25	0.25	0.25	0.25	0.25	0.25	0.25	0.25
	k_H, mD	700	700	700	700	700	700	700	700	700	700	700
	k_V/k_H	0.1	0.1	0.1	0.1	0.1	0.1	0.1	0.1	0.1	0.1	0.1
	PLYVISC		5	3	4	2	4	2	5	5	3	3
	PLYADS						3	3	2	4	2	4
Layer 5	h, m	4	4	4	4	4	4	4	4	4	4	4
	φ	0.3	0.3	0.3	0.3	0.3	0.3	0.3	0.3	0.3	0.3	0.3
	k_H, mD	900	900	900	900	900	900	900	900	900	900	900
	k_V/k_H	0.1	0.1	0.1	0.1	0.1	0.1	0.1	0.1	0.1	0.1	0.1
	PLYVISC		5	3	5	1	5	1	5	5	3	3
	PLYADS						3	3	1	5	1	5
AVERAGE	h, m	21	21	21	21	21	21	21	21	21	21	21
	φ	0.2	0.2	0.2	0.2	0.2	0.2	0.2	0.2	0.2	0.2	0.2
	k_H, mD	500	500	500	500	500	500	500	500	500	500	500

Appendix I – Reservoir models for sliced heterogeneity investigation

Case		**22**	**23**	**24**	**25**	**26**	**27**	**28**	**29**	**30**	**31**	**32**
Injected fluid		*Water*	*Polymer*									
Slice 1	L, m	160	160	160	160	160	160	160	160	160	160	160
	φ	0.1	0.1	0.1	0.1	0.1	0.1	0.1	0.1	0.1	0.1	0.1
	k_H, mD	100	100	100	100	100	100	100	100	100	100	100
	k_V/k_H	1	1	1	1	1	1	1	1	1	1	1
	PLYVISC		5	3	1	5	1	5	5	5	3	3
	PLYADS						3	3	5	1	5	1
Slice 2	L, m	160	160	160	160	160	160	160	160	160	160	160
	φ	0.15	0.15	0.15	0.15	0.15	0.15	0.15	0.15	0.15	0.15	0.15
	k_H, mD	300	300	300	300	300	300	300	300	300	300	300
	k_V/k_H	1	1	1	1	1	1	1	1	1	1	1
	PLYVISC		5	3	2	4	2	4	5	5	3	3
	PLYADS						3	3	4	2	4	2
Slice 3	L, m	160	160	160	160	160	160	160	160	160	160	160
	φ	0.2	0.2	0.2	0.2	0.2	0.2	0.2	0.2	0.2	0.2	0.2
	k_H, mD	500	500	500	500	500	500	500	500	500	500	500
	k_V/k_H	1	1	1	1	1	1	1	1	1	1	1
	PLYVISC		5	3	3	3	3	3	5	5	3	3
	PLYADS						3	3	3	3	3	3
Slice 4	L, m	160	160	160	160	160	160	160	160	160	160	160
	φ	0.25	0.25	0.25	0.25	0.25	0.25	0.25	0.25	0.25	0.25	0.25
	k_H, mD	700	700	700	700	700	700	700	700	700	700	700
	k_V/k_H	1	1	1	1	1	1	1	1	1	1	1
	PLYVISC		5	3	4	2	4	2	5	5	3	3
	PLYADS						3	3	2	4	2	4
Slice 5	L, m	160	160	160	160	160	160	160	160	160	160	160
	φ	0.3	0.3	0.3	0.3	0.3	0.3	0.3	0.3	0.3	0.3	0.3
	k_H, mD	900	900	900	900	900	900	900	900	900	900	900
	k_V/k_H	1	1	1	1	1	1	1	1	1	1	1
	PLYVISC		5	3	5	1	5	1	5	5	3	3
	PLYADS						3	3	1	5	1	5
AVERAGE	L, m	800	800	800	800	800	800	800	800	800	800	800
	φ	0.2	0.2	0.2	0.2	0.2	0.2	0.2	0.2	0.2	0.2	0.2
	k_H, mD	500	500	500	500	500	500	500	500	500	500	500

Case		**33**	**34**	**35**	**36**	**37**	**38**	**39**	**40**	**41**	**42**	**43**
Injected fluid		*Water*	*Polymer*									
Slice 1	L, m	160	160	160	160	160	160	160	160	160	160	160
	φ	0.1	0.1	0.1	0.1	0.1	0.1	0.1	0.1	0.1	0.1	0.1
	k_H, mD	100	100	100	100	100	100	100	100	100	100	100
	k_V/k_H	0.1	0.1	0.1	0.1	0.1	0.1	0.1	0.1	0.1	0.1	0.1
	PLYVISC		5	3	1	5	1	5	5	5	3	3
	PLYADS						3	3	5	1	5	1
Slice 2	L, m	160	160	160	160	160	160	160	160	160	160	160
	φ	0.15	0.15	0.15	0.15	0.15	0.15	0.15	0.15	0.15	0.15	0.15
	k_H, mD	300	300	300	300	300	300	300	300	300	300	300
	k_V/k_H	0.1	0.1	0.1	0.1	0.1	0.1	0.1	0.1	0.1	0.1	0.1
	PLYVISC		5	3	2	4	2	4	5	5	3	3
	PLYADS						3	3	4	2	4	2
Slice 3	L, m	160	160	160	160	160	160	160	160	160	160	160
	φ	0.2	0.2	0.2	0.2	0.2	0.2	0.2	0.2	0.2	0.2	0.2
	k_H, mD	500	500	500	500	500	500	500	500	500	500	500
	k_V/k_H	0.1	0.1	0.1	0.1	0.1	0.1	0.1	0.1	0.1	0.1	0.1
	PLYVISC		5	3	3	3	3	3	5	5	3	3
	PLYADS						3	3	3	3	3	3
Slice 4	L, m	160	160	160	160	160	160	160	160	160	160	160
	φ	0.25	0.25	0.25	0.25	0.25	0.25	0.25	0.25	0.25	0.25	0.25
	k_H, mD	700	700	700	700	700	700	700	700	700	700	700
	k_V/k_H	0.1	0.1	0.1	0.1	0.1	0.1	0.1	0.1	0.1	0.1	0.1
	PLYVISC		5	3	4	2	4	2	5	5	3	3
	PLYADS						3	3	2	4	2	4
Slice 5	L, m	160	160	160	160	160	160	160	160	160	160	160
	φ	0.3	0.3	0.3	0.3	0.3	0.3	0.3	0.3	0.3	0.3	0.3
	k_H, mD	900	900	900	900	900	900	900	900	900	900	900
	k_V/k_H	0.1	0.1	0.1	0.1	0.1	0.1	0.1	0.1	0.1	0.1	0.1
	PLYVISC		5	3	5	1	5	1	5	5	3	3
	PLYADS						3	3	1	5	1	5
AVERAGE	L, m	800	800	800	800	800	800	800	800	800	800	800
	φ	0.2	0.2	0.2	0.2	0.2	0.2	0.2	0.2	0.2	0.2	0.2
	k_H, mD	500	500	500	500	500	500	500	500	500	500	500

Appendix J – The influence of reservoir and PVT heterogeneity

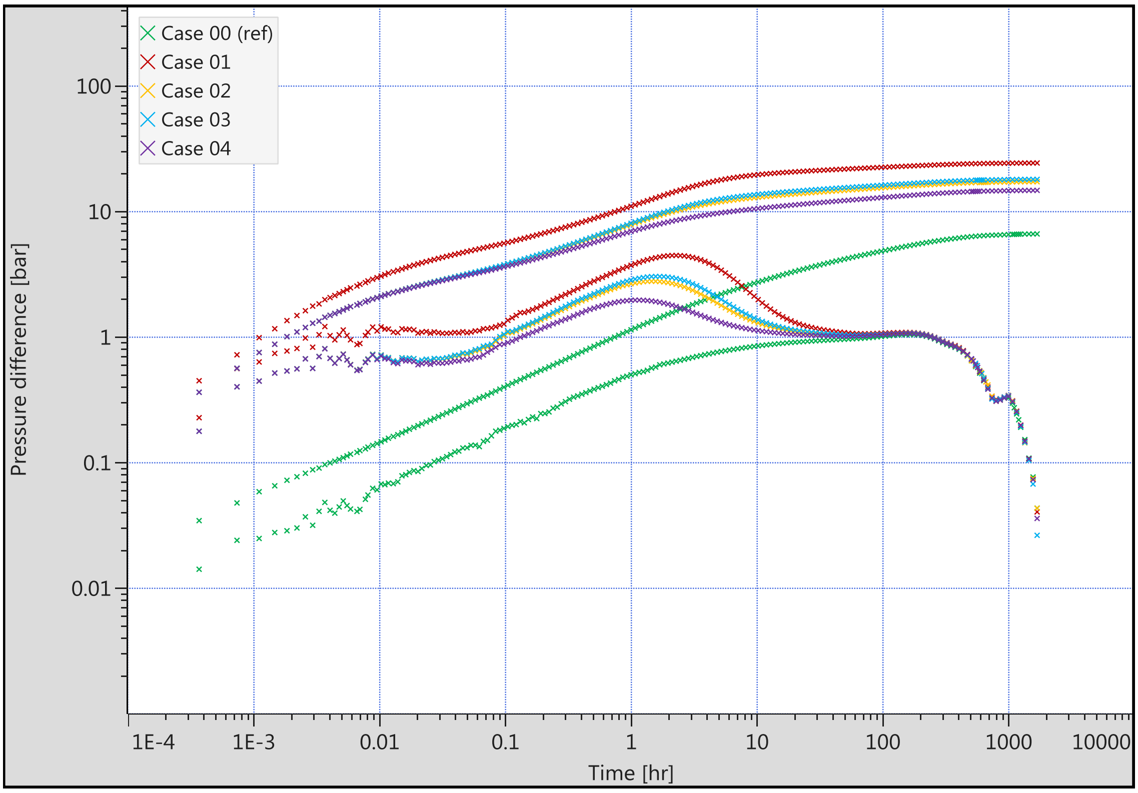

Figure 129 – Influence of different polymer viscosity correlations within a layered reservoir

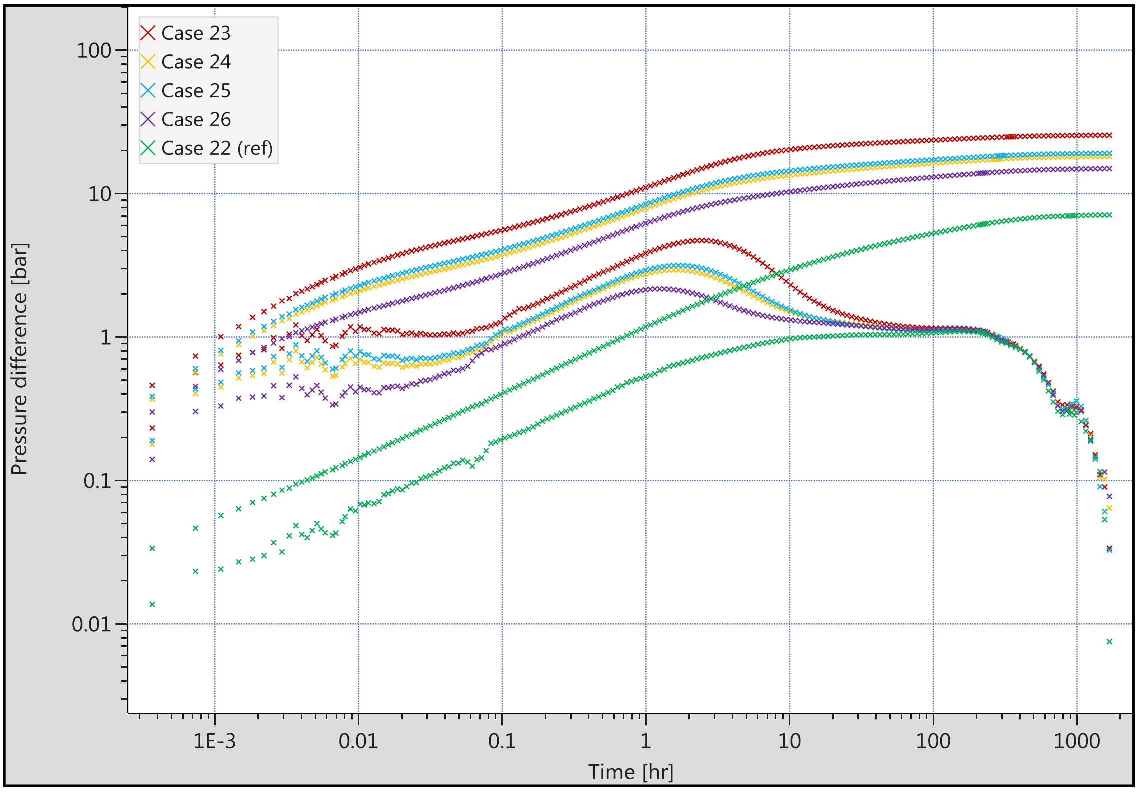

Figure 130 - Influence of different polymer viscosity correlations within a sliced reservoir

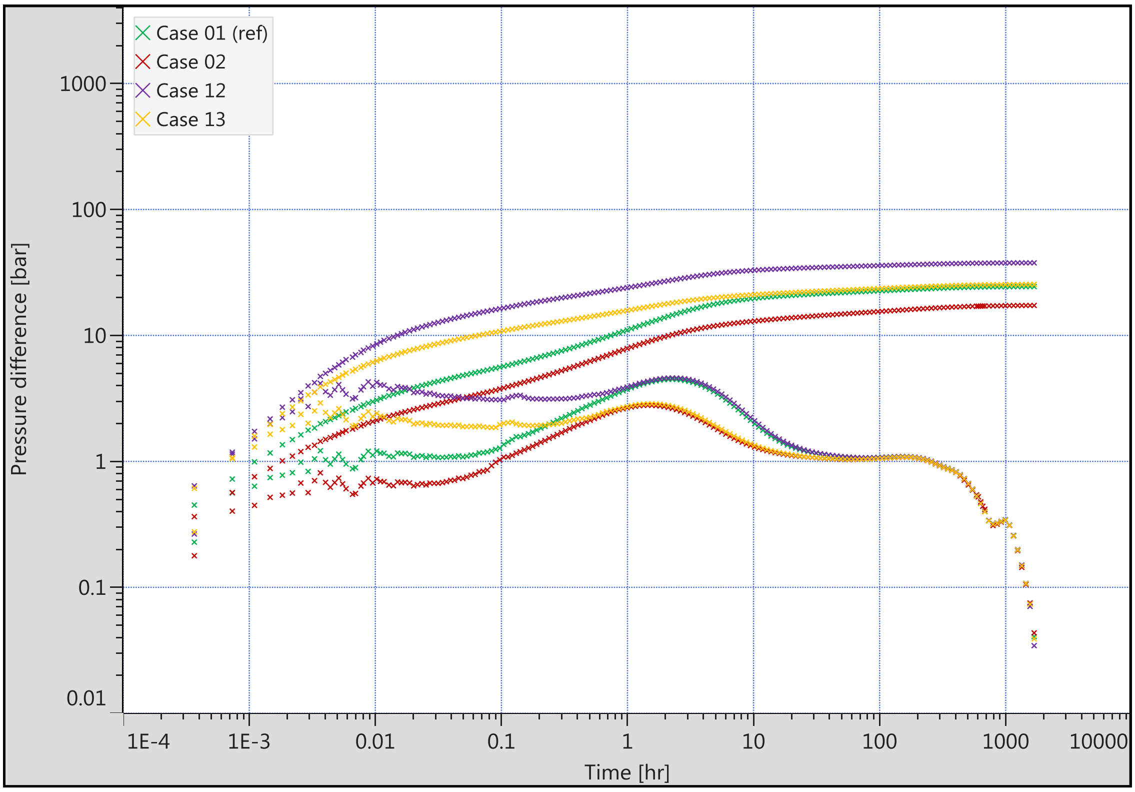

Figure 131 – The influence of vertical permeability anisotropy in a layered reservoir

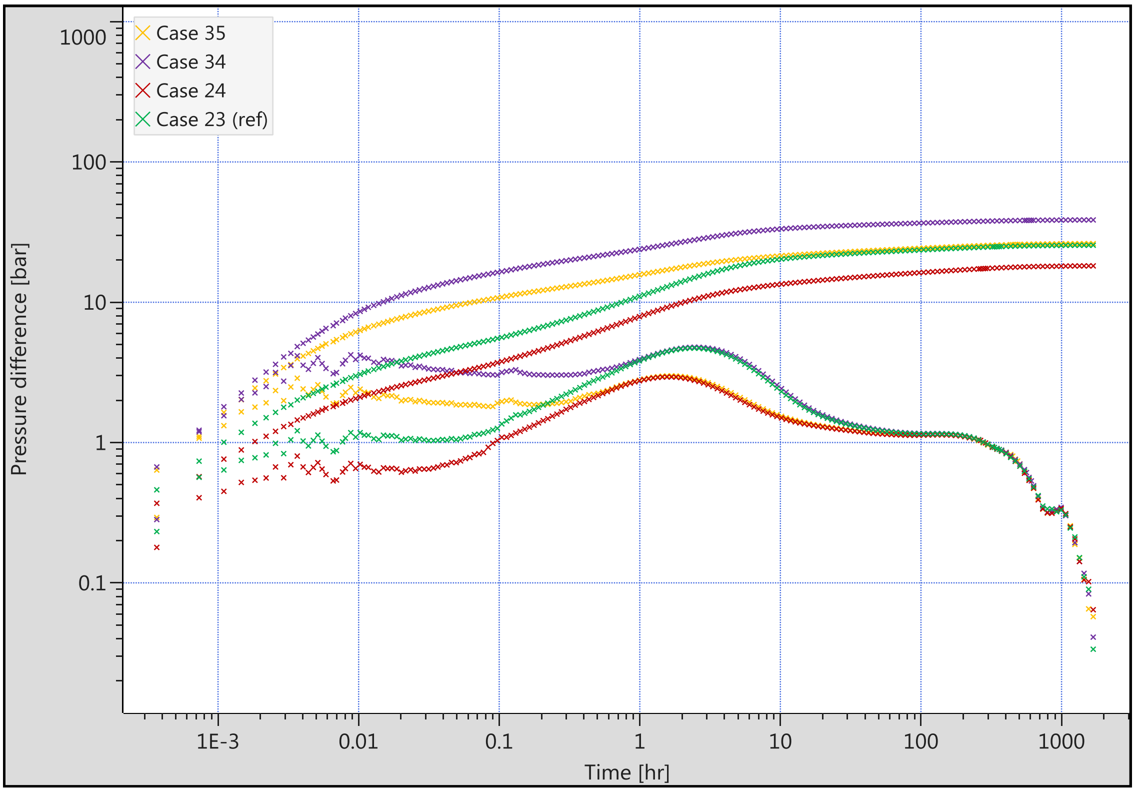

Figure 132 – The influence of vertical permeability anisotropy in a sliced reservoir

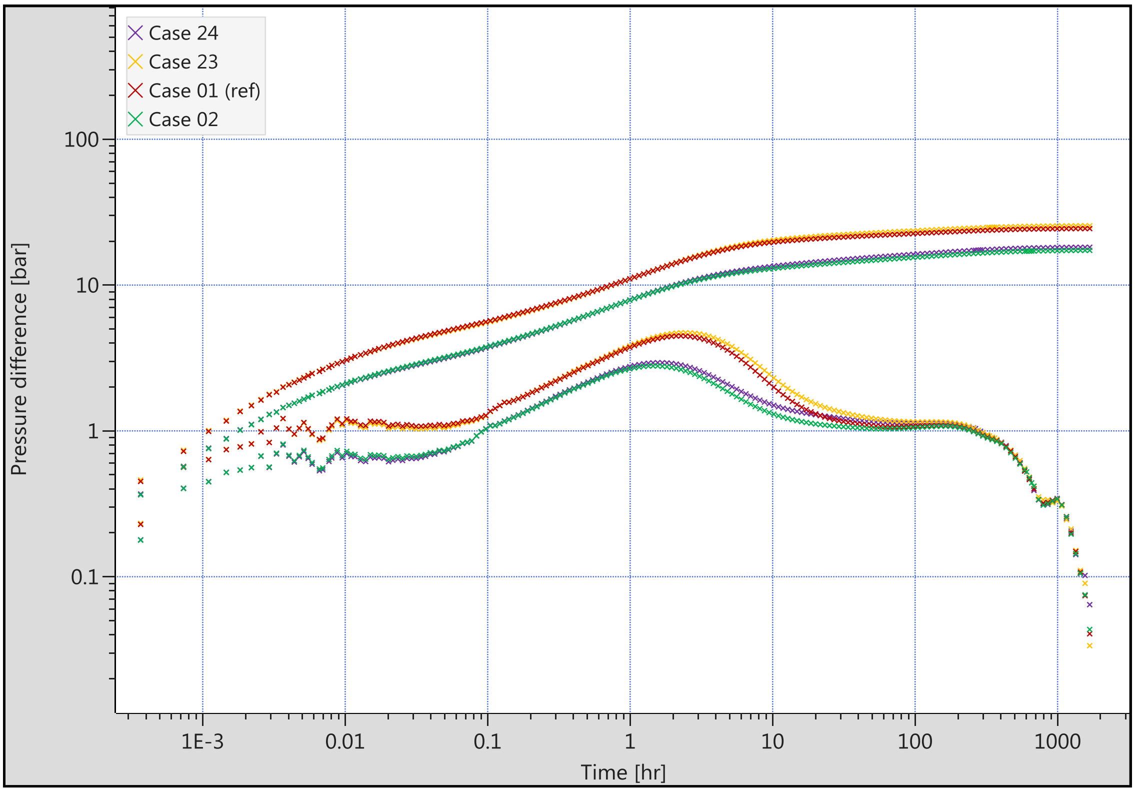

Figure 133 – The influence of spatial orientation of rock and PVT heterogeneities ($k_V/k_H = 1$)

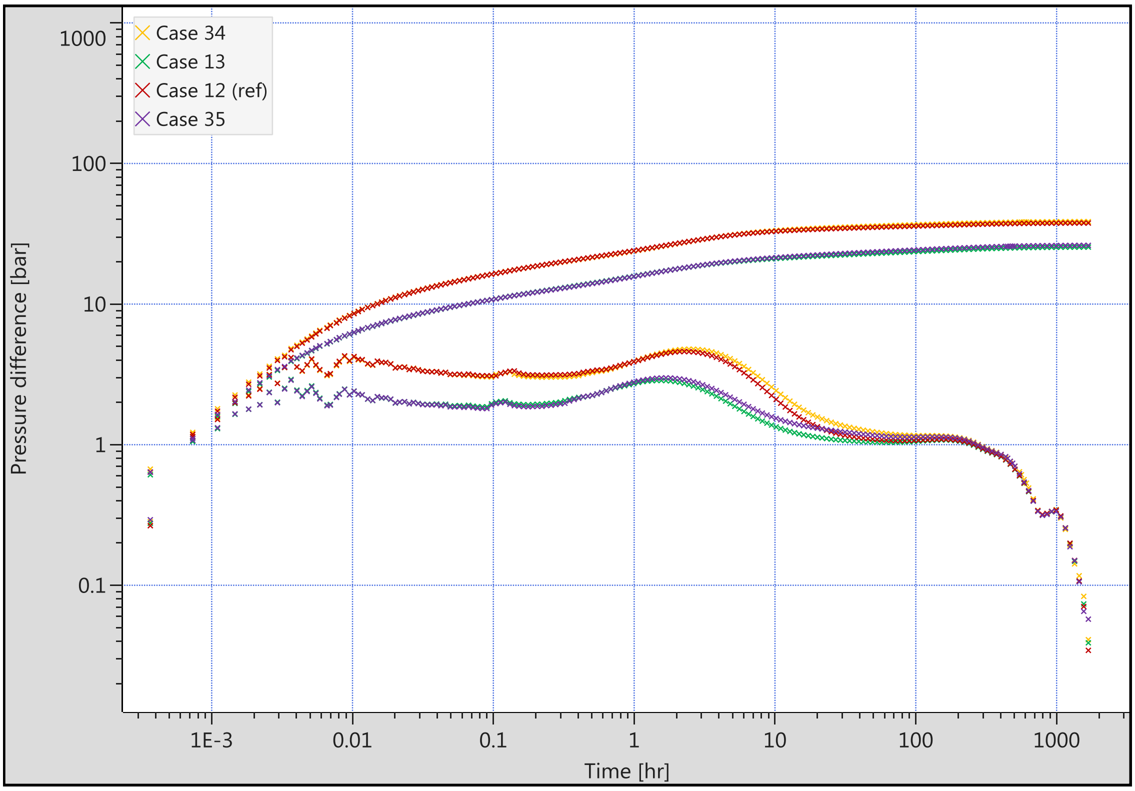

Figure 134 – The influence of spatial orientation of rock and PVT heterogeneities ($k_V/k_H = 0.1$)

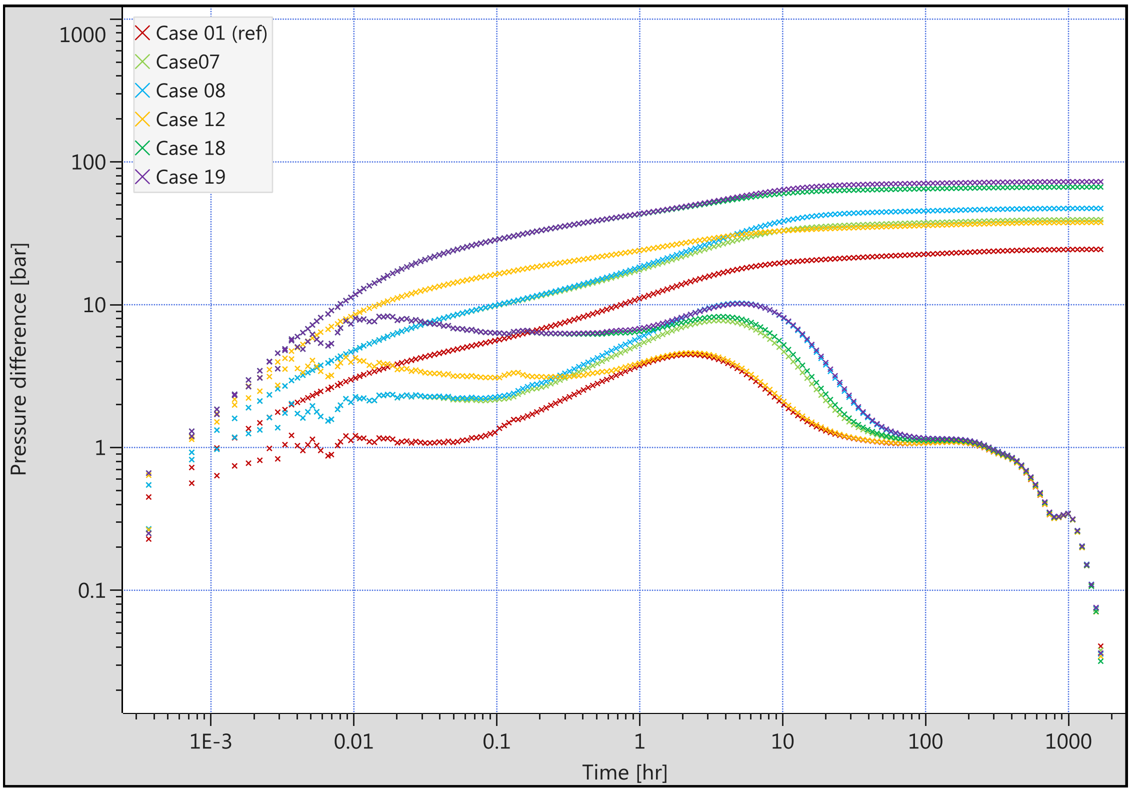

Figure 135 – The influence of different adsorption behavior allocation in a layered model

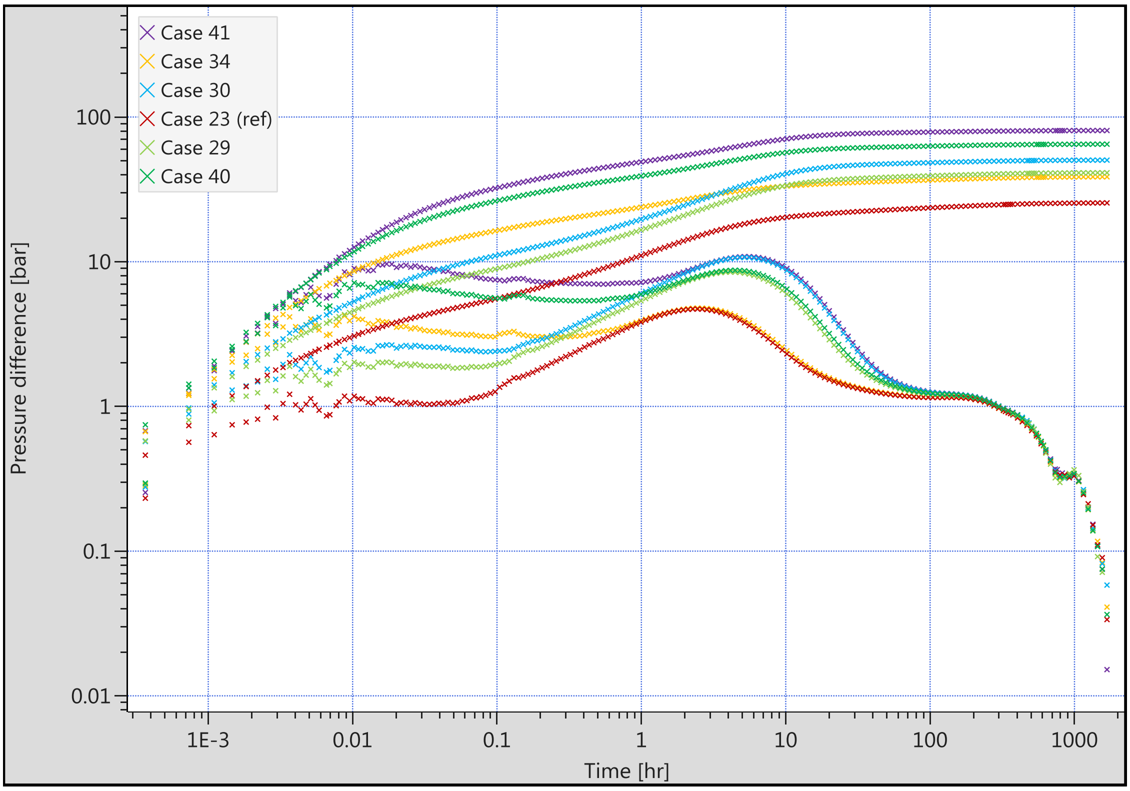

Figure 136 – The influence of different adsorption behavior allocation in a sliced model